Simulation and Design Optimization of Wave Propagation in Heterogeneous Materials

by
Joel Saa-Seoane
MSc. Computation for Design and Optimization - MIT (2011)
Eng. Camins, Canals i Ports - UPCBarcelonaTech (2010)
Llic. Matemàtiques - UPCBarcelonaTech (2008)

Submitted to the Department of Aeronautics and Astronautics
in partial fulfillment of the requirements for the degree of
Doctor of Philosophy
at the
MASSACHUSETTS INSTITUTE OF TECHNOLOGY
September 2014

Signature redacted

Author .....
Department of Aeronautics and Astronautics
July 2, 2014

Certified by ..... Signature redacted
Thesis supervisor: **Jaume Peraire**
H.N. Slater Professor and Department Head

Certified by ..... Signature redacted
Thesis supervisor: **Cuong N. Nguyen**
Research Scientist

Certified by ..... Signature redacted
Thesis committee member: **Robert M. Freund**
Theresa Seley Professor in Management Science

Certified by ..... Signature redacted
Thesis committee member: **Raul Radovitzky**
Professor of Aeronautics and Astronautics

Accepted by ..... Signature redacted
Paulo C. Lozano
Chair, Graduate Program Committee

Simulation and Design Optimization of Wave Propagation in Heterogeneous Materials

by

Joel Saa-Seoane

Submitted to the Department of Aeronautics and Astronautics
on July 2, 2014, in partial fulfillment of the
requirements for the degree of
Doctor of Philosophy

Abstract

Propagation of waves through heterogeneous structured materials has been the focus of considerable research in recent years. These materials consist of quasi periodic geometries combining two or more piecewise homogeneous component media. The interest in these materials stems from the fact that when waves propagate through them one can observe phenomena, such as bandgaps, which cannot be obtained with any single homogeneous medium. The design of structured materials aims to identify patterns which have desirable features regarding wave propagation applications.

The range of applications is very broad. In the context of electromagnetic waves, governed by Maxwell's equations, one may be interested in the design of low-loss waveguides, invisibility cloaks, superlenses or light frequency filters. For acoustic applications one may consider the design of passive noise filters or sound beams.

The physics governing the propagation of waves is well understood and the existing mathematical models often provide excellent predictions. For this reason, the design of structured materials can greatly benefit from the use of numerical simulation and optimization techniques. Accurate numerical simulations can describe the propagation of waves through heterogeneous materials once the geometry and material properties are defined. Optimization methods can help determine arrangements of component materials and their properties in order to optimally accomplish a desired outcome.

The work presented in this thesis includes a collection of multiscale high order accurate numerical simulation methods capable of simulating wave propagation in piecewise homogeneous media for two types of problems of interest: the source and the eigenvalue problems. In particular, we introduce the multiscale continuous Galerkin and multiscale hybridizable discontinuous Galerkin methods which exploit the inherent structure of the problem by reusing information from repeated subdomains. The efficiency that these approaches provide (reducing degrees of freedom by a factor of 20 to 100) allows for the numerical solution of large acoustic and electromagnetic wave problems, even in 3d, with a greatly reduced need for computational resources.

Furthermore, a discrete topological optimization procedure enhanced with reduced basis approximations is developed in order to facilitate the automated design of these materials. The combination of both methods, simulation and optimization, yields enhanced capabilities for the design of optimal patterns for multiple applications. The design of invisibility cloaks and high transmission waveguide bends in 2d and 3d are considered.

Thesis supervisor: **Jaume Peraire**
Title: H.N. Slater Professor and Department Head

Thesis supervisor: **Cuong N. Nguyen**
Title: Research Scientist

Acknowledgments

I would love to thank all those who helped me get, in some way or another, this PhD. First, I would like to thank my advisor, Prof. Jaume Peraire, for giving me the opportunity to come to MIT and work with him. He has been a unique source of ideas and creativity and he has always been willing to kindly share his knowledge and experience on computational engineering with those around him. I am also very grateful to Dr. Cuong Nguyen, who also as a thesis supervisor has inspired me through his technical knowledge. In addition, I also want to thank my thesis committee members Prof. Robert M. Freund and Prof. Raul Radovitzky for caring about my work and continuosly providing useful feedback. I would also like to recognise the contributions of my thesis readers Prof. Nicholas X. Fang and Prof. Qiqi Wang, who greatly helped improve the final shape of this work.

I would also like to thank the dayly contributions of my research group colleagues and friends. It has been a great pleasure to work and collaborate with Dr. Abby Men, who opened the research path on computational Photonics for our group. Also, Dr. Xevi Roca has not only been a priceless source of knowledge and fruitful research discussions, but also a unique source of energy in both fun but also hard moments. Jean Sofronas and Joyce Light have been extremely nice, efficient and helpful when dealing with any logistics. My fellow PhD students and friends Ferran, Hemant and David have made this long journey a lot easier and entertaining. It has been a real pleasure sharing this fantastic experience with you all, and I hope there are yet many more stories to come.

I am also very grateful to many others who have shaped the past four and a half years. In particular, there have been many inspiring colleagues in ACDL –Andrew, Patrick, Eric, Xun, Nikhil, Matt– that have been able to create a productive yet fun work and research environment. In addition, this accomplishment would have not been possible without the unconditional support of my *not work related* friends both in the Boston area -Carmen, Christie, Enrique, Maite, Noel, Paula, Xabi- but also back in Barcelona -Monto, Edu, Gupi, Nacho, Rata, Pacho, Elena-.

Last, but not least, I want to thank my family -Raul, Gloria, Raul, Ana- for their continuous support and love, without which I would have definitely not gotten this far. This experience has been unforgettable thanks to my partner, Cristina, who has always been very supportive and positive, despite the distance. It has been 4+ years of hard and -mostly apart- work but the synchronized outcomes for both of us have been extraordinary.

Finally, I would like to acknowledge the financial support provided through a fellowship by 'la Caixa' foundation, the AFOSR grant No. FA9550-11-1-0141 and the Singapore-MIT alliance.

to my family

Contents

List of Figures

List of Tables

Chapter 1

Introduction

> *Cogito ergo sum.*
>
> **–René Descartes**

The design of materials that exhibit desirable features has always been of considerable scientific interest. First, humans tried to understand and exploit properties that materials found in nature could offer. Later on, we discovered that the mixture of several natural materials could create new ones with improved capabilities, such as alloys or steel. Nowadays, with the rapid pace of technological advances we can manufacture materials with specific structures at the *nano*scale to obtain useful *macro*scopic properties, like Photonic Crystals. In fact, in the case of the recently discovered *meta*materials, some of their capabilities (e.g. invisibility [122]) cannot be attained through any other known natural material that is homogeneous.

In order to illustrate how structure can provide materials with very particular properties, we consider the one dimensional propagation of a linear wave through a homogeneous medium. For this problem, we know the solution field, which consists of a wave of constant shape that propagates at a speed determined by the medium, as shown in figure 1.1-top. However, if in a region of the domain the host material is replaced by a material with different wave propagation properties, the propagation speed of the wave in the alternative medium becomes different. Moreover, at the

interfaces, reflections will appear. In fact, for the case of only one interface, both the reflected and the transmitted fields can be obtained analytically.

Similarly, if a second interface is introduced in the structure, a decaying but non zero field keeps reflecting back and forth between the two interfaces. Every time this bouncing wave reaches an interface, a fraction of it will be transmitted (constructively -if in phase- or destructively -if out of phase- adding to the already existing waves in that medium) and another portion will reflect back, as shown in the third scenario of figure 1.1. Hence, the analytical expression for the resulting wave at every point of the space can be expressed as an infinite sum of terms, or series.

If more interfaces are considered, it is then possible to create configurations in which the total transmitted field is canceled, or *viceversa*, *i.e.* all the field is transmitted and the internal reflections are canceled out. Moreover, if an infinitely periodic material is considered, there will exist broad bands of frequencies for which wave propagation is not allowed. This phenomenon is known as bandgap and was discovered for electromagnetic waves by Lord Rayleigh [131] in the 19th century.

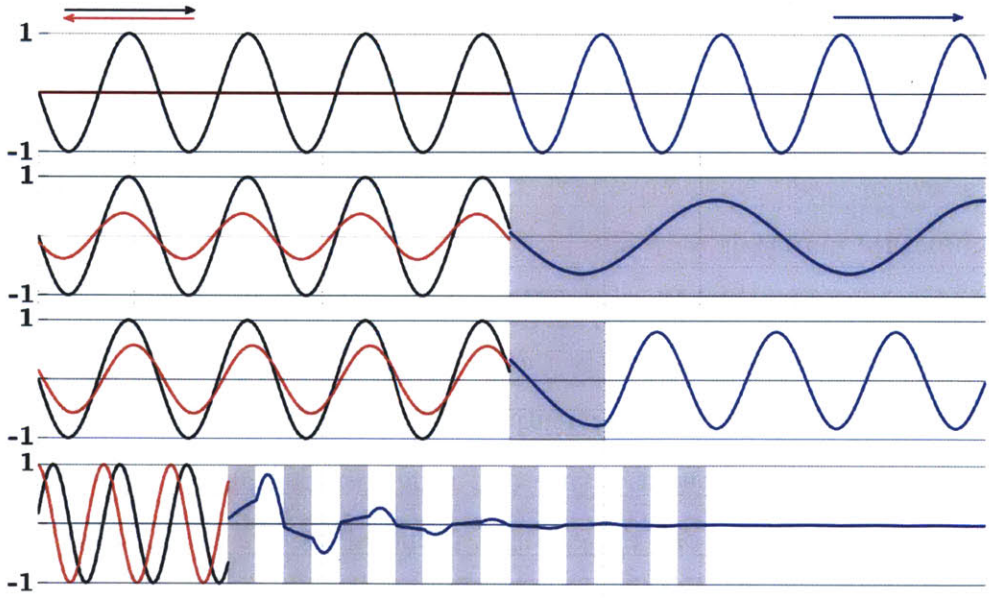

Figure 1.1: Effect of structured materials for filtering wave propagation.

To sum up, figure 1.1 shows the propagation pattern of the incident (black), reflected (red) and transmitted (blue) waves for several configurations of two materials

having different propagation speeds. Note that the total wave is obtained as the addition of the incident, reflected and transmitted fields. The wave interactions can change from being in phase to out of phase through small perturbations of the material distributions. Furthermore, the effects that a small material inclusion can have are global and thus it may affect the total wave field far away in the domain.

Wave equations also govern the propagation of electromagnetic, acoustic and elastic waves in 2d and 3d. However, in multiple dimensions wave fronts interact with material interfaces in a more complex and less intuitive manner. These ideas can be exploited to manipulate electromagnetic, acoustic, elastic and surface waves. The research presented in this thesis focuses on the design of structured materials for applications in acoustics and electromagnetics.

1.1 Applications of interest

The problem of designing a material that can be used to coat an object in order to render it invisible has received considerable attention in recent years. Back in 2006, an exact solution to the cylindrical cloak was proposed by Pendry et al. in [122]. The solution was based on transformation optics but presented two major obstacles: the material properties of the resulting coating layer varied continuously, and singular values of such properties were attained at the inner surface of the cloak. An experimental design of the transformation optics approach was then introduced in [142] for electromagnetic waves, where the inhomogeneous and anisotropic material properties were manufactured through periodically arranged *micro*structures providing a reasonable reduction of the scattered field. More recently, Landy and Smith [86] proposed and built a low loss solution based on transformation optics, valid for one direction and a single microwave frequency. For acoustic waves, the first approach to a theoretical cloak was introduced in [130], improved in [48] and a practical multilayered solution was proposed in [152]. The transformation optics theory has also been extended to the problem of designing a carpet cloak in [87].

Further analysis and specific designs of the cylinder cloak problem are presented in [64, 80, 101, 104, 136], based on the transformation optics approach. However, these

solutions do not address the two main fabricability issues. More recently, different alternatives have been introduced in order to obtain manufacturable cloaking devices: replicating a unit cell with a host dielectric and a metal wire [25], or with a clever array distribution of capacitors and inductors [164], depending on the regime of waves to cloak.

Optimization techniques using genetic algorithms [163] or nonlinear optimization methods [129] have also been used to determine the optimal permittivity values for a collection of layers around the object to be cloaked. These theoretical cloaks show good reductions of the scattered field in simulations, but their manufacturability is questionable since the permittivity values for each layer might not be given by an accessible homogeneous material. Furthermore, cloaking devices for broad bands of frequencies are particularly desirable and some effective solutions are provided in [57, 59, 145], although once more, they exhibit critical fabrication issues. Most recently, topology optimization approaches have been successfully used to determine graded [4] but also discrete [3] cylinder cloak patterns that work for a single frequency and direction with over 95% of optimality.

In addition to invisibility cloaks, we are also interested in the design of waveguides. The development of 3d optical waveguides has been crucial for telecommunications. Optical fibers provide the ability of propagating confined light signals for long distances. The first fibers were based on the index guiding principle and thanks to total internal reflection (TIR) most of the energy would never leave the higher refractive index material core [137].

Later, 1d multilayer structures (such as Bragg fibers [158]) and 2d Photonic Crystal [78] fibers were developed. These are structures where a cladding surrounding the core was designed with patterns for which the frequencies of interest fell inside one of their bandgaps. In this way, most of the energy would be confined in the core.

More recently waveguides based on 2d Photonic Crystal structures have been designed on slabs [62,75]. These particular type of waveguides, experimentally tested in [22,30], offer some advantages with respect to fibers [137]: a higher quality factor [1] and lower losses for sharp bends [31].

The efficient design of sharp bends within all kinds of waveguides is of considerable interest [60] since they account for the majority of the losses accumulated along large distances. The local performance of sharp bends has been improved by the addition of extra rods of various radii in the corner regions [8, 94] as well as using topology optimization methods in [72, 73].

Photonic Crystals waveguides can also be enhanced with optical *nano*cavities that trap light in very small volumes for a long period of time and for a very narrow frequency range. The strong confinement of electromagnetic waves in PC *nano*cavities can dramatically increase light-matter and photon-photon interactions, which are important for a wide range of applications including optical communications [74], biosensing [157] and lasers [2, 151].

Besides the design of cloaks and waveguides, there are many other potential applications for structured materials in photonics and optics. One example is the design of flat superlenses [121, 166], which are lenses that are able to capture arbitrarily small (subwavelength) scale features without dissipation, in contrast to regular lenses. Additionally, negative refraction objects [90, 91, 154] or energy harvesting devices [29, 49] can be designed. Moreover, non-intrusive damage detectors through electromagnetic pulses and directional frequency filters have also been successfully designed in [138].

1.2 Problem Description

The numerical design of structured materials requires an efficient forward simulation tool that accurately predicts wave fields. In addition, we also need an optimization methodology that is able to identify effective material patterns. Solutions of equation 1.1 for given boundary conditions provide the spatial component $u(\mathbf{x})$ of the total wave field $U(\mathbf{x}, t) = u(\mathbf{x})e^{i\omega t}$. All in all, let $\Omega \subset \mathbb{R}^n$ be a domain of interest. We seek to study the steady behavior of the second order linear wave equation, which can be seen as the solution of the Helmholtz equation:

$$\nabla \cdot (a(\mathbf{x})\nabla u) + k^2 b(\mathbf{x})u = 0 \qquad \text{in } \Omega, \tag{1.1}$$

where k is the wavenumber and $a(\mathbf{x}), b(\mathbf{x})$ are functions of the material properties that may vary spatially.

Alternatively, we are interested in frequency domain solutions of Maxwell's equations, which read:

$$\begin{aligned} \nabla \times \mathbf{H} - (i\omega a(\mathbf{x}) + b(\mathbf{x}))\mathbf{E} = \mathbf{J} \quad \text{in } \Omega, \\ \nabla \times \mathbf{E} + i\omega c(\mathbf{x})\mathbf{H} = 0 \quad \text{in } \Omega, \end{aligned} \tag{1.2}$$

where $\mathbf{E}, \mathbf{H}$ represent the electric and magnetic field, respectively, and $\mathbf{J}$ is the input current. The material properties are denoted by $a(\mathbf{x}), b(\mathbf{x}), c(\mathbf{x})$ (permittivity, permeability and conductivity). Also, $i = \sqrt{-1}$ and ω corresponds to the frequency. Solutions of equation 1.2 with the corresponding boundary conditions provide the spatial component of the electric and magnetic fields.

We consider the following related problems:

1- **Forward simulation problem**: Given $a(\mathbf{x}), b(\mathbf{x}), (c(\mathbf{x})), k, (\omega)$ and boundary conditions, compute the solution fields $u, (\mathbf{E}, \mathbf{H})$. Here we seek to solve equations 1.1 or 1.2 in order to provide the solution field across the domain of interest Ω. Furthermore, additional outcomes of the simulation problem are the sensitivities of the solution with respect to the design parameters (a, b, c). To this end, we will develop a multiscale technique that exploits the repetition of geometry and structures within the domain in order to avoid the redundant computational work.

2- **Eigenvalue simulation problem**: Given $a(\mathbf{x}), b(\mathbf{x}), (c(\mathbf{x}))$ and boundary condition type, find $k_n, (\omega_n)$ and $u_n, (\mathbf{E}_n, \mathbf{H}_n)$. In this case we look for eigenpairs (wave eigenfield and eigenfrequency) as well as identifying band diagrams for structured materials, also under periodicity assumptions. In addition, we are interested in their sensitivities with respect to the design parameters (a, b, c). The multiscale technique adapted to the eigenproblem results in a nonlinear eigenvalue formulation that can still be efficiently solved, exploiting the geometric structure.

3- **Design optimization problem**: Find distributions $a(\mathbf{x}), b(\mathbf{x}), (c(\mathbf{x}))$ that optimize a functional J. Typically, this functional depends on the state variables $u, (\mathbf{E}, \mathbf{H})$, the parameters $k, (\omega)$ and the design variables $a, b, (c)$. In particular, we

look at discrete distributions of materials since this is a rather common, yet complex, manufacturing constraint. The choice of J as well as the set of constraints corresponding to the governing equation will determine whether we design for a source problem (1-) or an eigenvalue problem (2-).

Each of the three problems introduced above will be tackled separately. However, combining either of the simulation problems with the optimization method results in an approach for the design of materials for the control of wave propagation.

1.3 Main Challenges and Scope

The numerical design of structured materials presents several computational challenges. On the one hand, the simulation of the forward problem can already be expensive to obtain, especially for large three dimensional settings. Some state-of-the-art methodologies, such as MEEP [117] for PC simulations, have had a great impact in their communities but they are developed for specific equations (Maxwell's in case of MEEP) and require advanced computational resources and parallel implementations for large settings. On the other hand, when design is sought through binary optimization, many forward solves are required, which very often leads to intractable problems.

First, the wave equation is non coercive which means that it may lead to indefinite systems of equations after the discretization process. The solution of indefinite systems is difficult, especially for large problems. Moreover, wave phenomena in structured materials are particularly challenging to resolve since problems often involve complex geometries with details at very different scales. Furthermore, very high material contrasts might be present.

Additionally, the numerical simulation of problems with high frequencies pose serious difficulties. Over the last few years, efficient methodologies have been proposed to simulate wave propagation at both ends of the frequency spectrum. At the low end, the aforementioned methodologies already provide successful results. Similarly, sophisticated solvers based on geometrical optics have been designed to deal with problems at infinite frequencies [5, 76]. However, direct numerical simulation remains

difficult for high frequencies that are not infinite. The fundamental difficulty is the fact that the required accuracy level is proportional to the wavelength. Typically about ten degrees of freedom are required per wavelength and direction, so the size of the problem scales poorly.

Boundary conditions for wave propagation problems are also complicated to handle. Although most numerical methods require finite domains, wave problems are often defined on open, unbounded regions. As a result, techniques to avoid reflections at far field boundaries need to be introduced. First order absorbing boundary conditions work well for simple problems but if higher accuracy is sought, perfectly matched layers (PMLs) need to be considered. The use of PMLs increases significantly the size of the domain and thereby the computational cost of solving the problem of interest.

Figure 1.2 shows the geometry (left) and wave field (right) on a two dimensional waveguide. In this problem, a point source is placed at the beginning of the waveguide. Furthermore, cylinder rods of a different material have been included in the domain in a quasi-periodic arrangement. The propagation of waves with the frequency considered is not allowed throughout the periodic arrangement of rods in any direction, because of the bandgap phenomenon that will be later discussed. As a result, wave propagation is only allowed within the line defect and outside the quasi periodic distribution of rods. In addition, several PML layers are considered around the domain of interest to artificially damp the solution without reflecting any energy back into the domain.

This example already shows some of the challenges of numerically solving these classes of problems, albeit small and 2d. A very fine discretization is required to accurately capture the geometric details, leading to very large systems of equations and thus higher costs both in terms of time and memory. Also, the computational domain is significantly larger than the region of interest because of the boundary conditions. In addition, besides all the preceding challenges, there is a need not only for an accurate but also very efficient simulation capability since a large number of numerical simulations will be required for design optimization purposes.

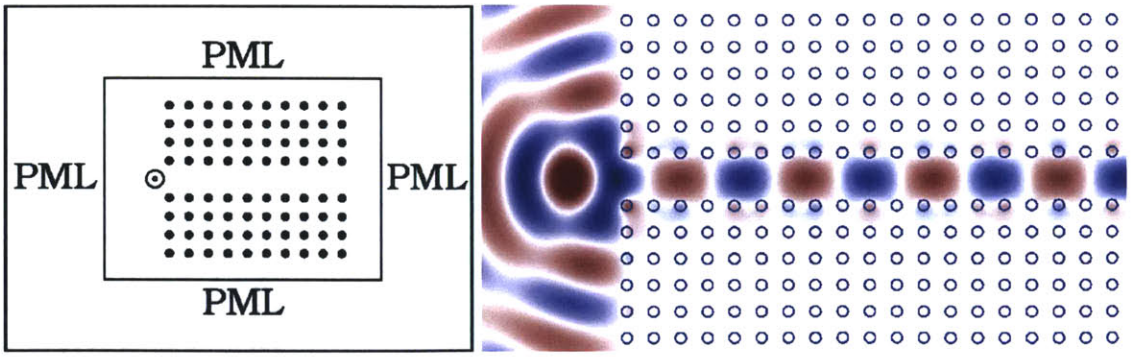

Figure 1.2: Geometry (left) and Wave propagation (right) through a two dimensional waveguide.

Although physical and mathematical intuition has been able to identify many practical patterns for certain applications, it can be insufficient to design structured materials, especially when trying to obtain manufacturable and realizable designs. As a result, considering optimization-based approaches for the design process might be helpful. However, the optimization problems that arise are often of a discrete nature, leading to binary or mixed-integer optimization models. In our setting, we consider the spatial domain discretized into pixels, and thus the design optimization problem that we are interested in solving consists of choosing between two given materials for each pixel, which leads to large binary optimization models.

In general, solving discrete optimization problems is NP hard. More specifically, the set of design variables in our problems is large (in the order of 10^3) and the cost of an NP hard algorithm is (in the worst case) exponential in the size of the variable set, so deterministic branch and bound-like algorithms can be computationally intractable. Moreover, objective functions will typically be nonlinear and nonconvex. It is also observed that in many cases, continuous relaxations of discrete formulations do not provide either binary solutions or close guesses.

For all these reasons, the numerical design of structured materials for wave propagation problems is computationally challenging. Nevertheless, this is a field of active research because of the relevance and practical impact of the potential applications involved.

1.4 Proposed approach

In this work we present multiscale high order finite element methods implemented on unstructured meshes. Far field boundary conditions are represented through PMLs or alternatively first-order absorbing characteristic methods. When solving Helmholtz's equations, the multiscale MSCG method is presented as an extension of classical continuous Galerkin (CG) for simplicity; however, when electromagnetic waves are sought through solutions to Maxwell's equations, the multiscale MSHDG extends the hybridized discontinuous Galerkin (HDG) method. More specifically, the extension of the HDG method as a solver for the local problems in the multiscale setting for Maxwell's equation becomes crucial since this method can capture the rotational derivatives in a very natural way, without the consideration of H(curl)-elements as other continuous FEM approaches would require [102]. This property, together with a natural treatment of the boundary conditions, will simplify both the formulation and the implementation. Additionally, the multiscale continuous Galerkin method is extended for eigenvalue problems resulting in a nonlinear scheme (NMSCG).

These forward solvers are particularly suitable for the numerical simulation of waves in structured materials since they take advantage of the geometric repetition. In fact, after a judicious decomposition of the domain into subregions, only one representative of each class of subproblems is solved (there are as many classes as different sets of geometries). Then, local information is reused and assembled into a global system of smaller size. This formulation helps decrease the computational cost of the simulation problem but it also significantly reduces the cost of the optimization process, even permitting the design of structures for large problems, as we shall see later. Overall, the multiscale methodologies introduced in this thesis are especially well suited for the resolution of relatively large wave problems with high frequencies without the use of automated domain decomposition and parallelization techniques. In particular, we are capable of solving tens to hundreds of wavelengths, even in 3d.

For the design optimization of discrete patterns we present a binary gradient coordinate descent heuristic method. This approach considers only binary sensitivities

and uses the numerical simulation tools to obtain estimates of the objective function value. Although it is heuristic and computing a global optimum cannot be guaranteed, we have been able to find binary patterns with the desired performance in practice. This method also exploits the physics of the problem by introducing reduced basis approximations for the forward solution of neighboring states. Actually, wave fields corresponding to similar material states are close. As a result, one can use reduced basis approximations to cheaply obtain solutions with a certain level of accuracy.

1.5 Literature Review

This section provides a summary of previous work relevant for the numerical design of structured materials.

1.5.1 Forward wave simulation techniques

The simulation of wave phenomena in heterogeneous media has been a very active field of research and therefore the range of available methods is very diverse. Most of wave propagation problems of interest require unbounded domains. Boundary Integral Methods are able to deal with open domains in a natural manner. They were first used for the wave equation in [144]. The main disadvantage of Boundary Integral Methods is that they lead to systems of equations which are dense. These systems of equations are therefore hard to solve, especially for large problems.

Other methods such as finite difference or finite elements, discretize the differential equations directly, and the unbounded domains are truncated by introducing artificial computational boundaries and imposing radiation (or non-reflecting) boundary conditions. There is a number of ways in which radiation conditions can be imposed, ranging from first order characteristic methods [53, 112] to Perfectly Matched Layers or PMLs [17, 83]. More specifically, PMLs are a set of artificial layers that surround the computational domain of interest. In these layers, the governing equations are modified in order to numerically dissipate solutions that are supposed to leave the domain without reflecting.

Finite difference methods using regular grids, although simple and cost efficient,

are not well suited for the geometries of interest in this research. In order to adapt these methods to problems involving irregular domains and complex geometries, some *ad-hoc* modifications have been proposed which avoid the need for very fine discretizations [117]. These solutions however do not result in high order accurate methods. Alternatively, Yu *et al.* [162] have introduced a method that modifies the governing equations to smoothly handle the small geometric heterogeneities.

Often, the numerical simulation of large wave propagation problems requires advanced computational resources with parallel implementations and iterative solvers. Sparse factorizations can be prohibitively expensive, algebraic preconditioners are also expensive and do not generalize, and multigrid methods scale poorly. Nevertheless, in the case of time domain wave equations, successful methodologies have been devised including parallelized finite and spectral element methods (SPECFEM3d [82]), which have been derived and implemented for elastic waves [81], seismic simulations [11, 92, 127], and waves in porous media [100]. Similarly, the FDTD method has also been implemented in parallel using the MPI library in [66], allowing for the simulation of wave propagation problems with scalability. None of this methods, however, provides a practical paradigm for the design of structured materials, which is the main objective of this thesis.

Finally, the use of unstructured meshes allows complex geometries to be represented accurately but when used with low order methods they lead to dispersion errors. These numerical errors can be reduced through the use of high order methods.

Continuous and Discontinuous Galerkin Methods

The finite element method is a popular technique for the spatial discretization of wave propagation problems due to its ability to handle complex geometries and inhomogeneous materials. It also provides high-order accuracy. There are several spatial discretization strategies within the finite element method, which include continuous Galerkin methods, spectral element methods, mixed finite element methods, and discontinuous Galerkin methods. Each of these methods has its own strengths and weaknesses that make it ideally suited for specific applications.

For instance, discontinuous Galerkin methods [10,13,14,44,45,50,51] work well on arbitrary meshes, result in stable high-order accurate (low dispersion) discretizations of hyperbolic systems, allow for a simple and unambiguous imposition of boundary conditions, and are very flexible to parallelization and adaptivity. One major criticism of many DG methods is that they have too many degrees of freedom due to nodal duplication at the element boundary interfaces.

In order to overcome some of the drawbacks of DG methods, the Local and Compact Discontinuous Galerkin (LDG, CDG) methods were introduced in [44, 124], respectively. The Hybridizable Discontinuous Galerkin (HDG) method was then introduced for diffusion-reaction problems [36,43] and later analyzed in [33,37,40]. Several HDG methods are subsequently developed for biharmonic equations [34], linear and non-linear convection-diffusion problems [35, 107, 108], linear elasticity [147], Stokes flows [39, 109, 110], incompressible Navier Stokes equations [111, 115], compressible Euler and NavierStokes equations [113, 123] and continuum mechanics [106]. More recently, the HDG method has been also developed for the time-harmonic Maxwell's equations [114] and for the wave equation in acoustics and elastodynamics [112].

The HDG methods are fully implicit, unstructured, and high-order accurate in both space and time; yet they are computationally attractive because the only globally coupled unknown is the numerical trace of the solution field. Since the numerical trace is only defined on the elemental faces and single-valued, the HDG methods may have significantly less global degrees of freedom than other DG methods [70]. Another attractive feature of the HDG methods is that they yield optimal convergence of order $k+1$ in the L^2-norm for all the approximate variables and possess superconvergence $k+2$ properties for elliptic problems.

Note that the main advantage of hybridized methods lies on the organization of the degrees of freedom and the sparsification of the system matrix for a reduction of the globally coupled degrees of freedom. Actually, the larger the polynomial approximation order, the bigger the contrast of degrees of freedom between statically condensed problems (like HDG or MSCG/MSHDG) and non-hybrid methods (like CG), as shown in [70]. The simplified reason is that the traces are defined on 2d

elements but the volumetric variables take values over entire volumes.

In particular, the HDG method has been here developed and implemented for a multimaterial frequency domain wave simulation through Helmholtz's equation in [139, 140] as part of this thesis. This equation is solved using an HDG discretization on an unstructured grid together with first order absorbing boundary conditions and Perfectly Matched Layers.

Multiscale methods for the source problem

Most of the problems that we are interested in solving have geometric details and solution patterns with different length scales. Moreover, geometries often appear repeatedly throughout the domain. In these cases, the efficiency of simulation methods that use domain decompositions can be improved by reusing information corresponding to subdomains with repeated patterns.

Our approaches, the multiscale continuous Galerkin (MSCG) and multiscale hybridizable discontinuous Galerkin (MSHDG) methods, are an extension of the hybridized continuous Galerkin (HCG) and hybridized DG (HDG) methods introduced in [41] and [37] respectively, which in turn have their root in hybridized mixed finite element methods [36]. The extension lies in the definition of the local subproblems: while the HCG/HDG methods define the subproblems at the discretization element level, the multiscale methods define the subproblems at a subdomain level. This subtle extension is crucial because it provides further reduction in the global degrees of freedom and better efficiency in parallelization. In fact, our approach is particularly attractive for problems with repeated, piecewise-constant, or periodic coefficients, since in such cases the number of local subproblems can be significantly reduced by a judicious choice of subdomains and associated approximation spaces.

These multiscale methods also bear some similarity to the mortar element method [18, 19]. The underlying idea here is twofold. First, the original problem is broken into several smaller subproblems which are formulated on subdomains and they are less expensive to solve than the original problem. Second, a framework for stitching together the solutions of the subproblems is carried out by relaxing the intersubdo-

main continuity requirements and imposing it 'weakly' through the introduction of a so-called flux Lagrange multiplier. However, different from our approach, the mortar element method imposes weak continuity on the approximation to the solution instead of enforcing the continuity of the approximation to the fluxes. As a result, the two approaches differ from both the local subproblems and the final variational formulation for the multiplier.

Our approach also has a variational multiscale interpretation since, instead of using conventional polynomial functions, it employs basis functions that are adaptive to the local properties of the differential operator. We note that the idea of using problem-specific basis has been widely applied to the numerical solution of PDEs with multiple scales. Examples include the special finite element method [9], the multiscale finite element method [69], and reduced basis methods [105]. Our multiscale methods differ from these alternatives in several important ways. The special finite element method is based on the particular property of the harmonic average in one-dimensional elliptic problems and thereby is restricted to problems with the coefficient varying locally in one dimension. Like our approach, the multiscale FEM constructs its basis functions by solving a number of local subproblems on subdomains. The difference between the introduced methods and the multiscale FEM approach lies in the boundary conditions for the local subproblems, as we shall see later.

Similarly to our proposed method, a hybridized multiscale DG method (HMDG) was introduced in [103] for Eurler and Navier-Stokes equations. Also, a geometric multiscale finite element method has been developed for structured materials in [28]. However, unlike the multiscale methods presented in this thesis, these approaches do not reuse any information from repeated local subelements.

Multiscale methods for the eigenvalue problem

Analogously, the multiscale techniques are extended to eigenvalue formulations of the wave equation. These problems are of high interest since they characterize physical phenomena like photonic or phononic bandgaps. Hence, a thorough analysis of eigenmodes allows for the design of waveguides, resonators and many more applications

in acoustics and electromagnetics. In addition, geometric repetition is often present and thus the use of multiscale techniques can also be helpful.

The use of Schur complement techniques for the eigenvalue Helmholtz's equation has been previously analyzed in [38], where the HDG method is extended to Thomas-Raviart equations. Numerical schemes that exploit a dimensional reduction for eigenvalue problems have also been developed in [26] for computational chemistry, and more generally through mixed finite element methods in [99]. The result of static condensation on linear source problems provide a reduced globally coupled yet still linear system of equations. However, these family of techniques turn an eigenvalue problem $\mathcal{A}u = \gamma u$ into a formulation with nonlinear dependence on γ. Nevertheless, the nonlinear nature of the eigenvalue reduced equations does not pose any computational issues. In fact, close approximations can be found through a natural eigenvalue problem and convergence from them is guaranteed [38] through Newton's method.

1.5.2 Design Optimization

Physical and mathematical intuition have been used to successfully design many structured materials. However, these approaches often lead to solutions that are not fully optimal and/or not binary. As a result, several optimization techniques have been developed and successfully applied for design problems. In particular, semidefinite programming techniques characterized in [119, 132] have been used with a high degree of success for the design of materials under eigenvalue like governing equations such as the maximization of photonic bandgaps [96, 97]. Furthermore, convex optimization techniques introduced in [160, 161] as well as the use of the adjoint method [27, 54, 139] to obtain information about the sensitivities have also been used. Additionally, nonlinear optimization techniques have also led to cloaking patterns [163] as well as to the design of *micro*cavities [88]. One of the main drawbacks of all these methods is the fact that they do not take into account manufacturability constraints in the structured material design: in general, material properties cannot attain a continuous distribution of values, but only discrete.

Some optimization methods that successfully address the discrete nature of the

material properties can already be found in the literature. In fact, both topology optimization through non integer penalization [16,60,62,67,72,73] and level set methods [143,167] have been applied to a broad range of problems with remarkable results. These methods use information from continuous gradients: the former penalizes non-integer values of new candidates and the latter continuously evolves the interfaces between different materials.

Topology optimization can lead to quite suboptimal solutions since it is seldom the case that the optimum under binary constraints lays close to the continuous optimum. Moreover, topological optimization methods based on penalization often suffer from numerical instabilities and extreme sensitivity to the penalization procedure considered. In addition, since problems modeled through the wave equation are typically sensitive to material perturbations, convergence of topology optimization algorithms to good and robust local optima can be hard.

On the other hand, the main problem with level set methods for the design of structured materials is the high cost incurred in the presence of complex structures involving multiple boundaries. These methods have been proven to work well for shape optimization design problems, where the shape of a given material or component needs to be identified. However, more general structured materials might not have known boundaries to evolve or, even more challenging for level set methods, the size of some connected components of the pattern might be on the order of the numerical resolution.

Finally, genetic algorithms and simulated annealing are some of the heuristic methods that have been used for some applications, such as granular composite protectors [61]. They have shown relatively good performance for small problems although the main drawback is that these methods typically do not exploit the underlying physics and therefore offer a poor scalability with respect to the size pixel set.

Reduced Basis methods

When we seek to design structured materials through optimization, many simulation problems need to be solved. The resolution of each simulation problems is already

computationally expensive and therefore there is the need for an alternative numerical capability that is able to provide accurate enough solutions at a cheaper cost.

In this context, for the faster numerical resolution of the wave equation, a reduced basis approach is introduced. Reduced basis methods were initially used with success for incompressible viscous flow calculations in [128] and later analyzed more deeply in [12]. Approximate solutions can be obtained at a cheaper cost since they are expressed as linear combinations of orthogonalized solutions within the parametric set. The accuracy of the approximations offered by the reduced basis relies on a good choice of the basis as well as a smooth behavior of the solution field with respect to small perturbations of the different parameters.

In contrast to Proper Orthogonal Decomposition methods (PODs) or other singular value decomposition based methods, the reduced basis approach just computes a few (expensive) solutions that are all included in the basis after orthogonalization. These alternative methods compute all possible solutions before orthonormalization and then truncate the most relevant components to form the basis.

Reduced basis approximations work particularly well for elliptic equations that are coercive and therefore dissipative. As it is well characterized in [12], the approximation error can be *a priori* accurately bounded and therefore the convergence and practicality of this approach is guaranteed. However, although the Helmholtz equation is elliptic, it is non coercive and thus accurate bounds of reduced basis interpolation errors are harder to determine or very conservative. Equivalently, Maxwell's equation also describe waves and thus the sensitivities of the solution fields with respect to changes on the geometry are large and not localized.

1.6 Thesis Objectives

The main objective of this thesis is to develop, implement and validate an efficient methodology for numerically modeling, optimizing, and thereby designing structured heterogeneous materials of practical use for wave applications. To that end, the following objectives are to be pursued:

1. Develop a numerical simulation method for wave propagation problems in het-

erogeneous media.

- Formulate and implement a multiscale CG method for the simulation of structured materials under finite repetition of geometries for Helmholtz's equation in 2d and 3d.
- Formulate and implement a multiscale HDG method for the simulation of structured materials under finite repetition of geometries for Maxwell's equation in 2d and 3d.
- Extend the formulation and implementation of the nonlinear multiscale CG method for the numerical simulation of eigenvalue Helmholtz's problems in heterogeneous media with repeated patterns in 2d and 3d.
- Assess the accuracy and efficiency of the previous methods and how they compare to other state-of-the-art simulation tools in the field.
- Validate the numerical solutions provided by the multiscale methods with experimental results reported in the literature.

Overall, the MSCG, MSHDG and NMSCG methods will be developed for the simulation of wave propagation in heterogeneous media with repeated patterns. A global, coarse and structured grid will split the physical domain into several subproblems that will be solved through a CG/HDG discretization method on unstructured meshes that accurately define the geometries. Weak continuity of the fluxes will be imposed on the interelement boundary conditions and PMLs or first-order absorbing conditions will be used for the exterior boundaries.

2. Investigate and implement a practical design optimization capability for structured materials.

   - Develop a binary gradient coordinate descent optimization method.
   - Develop a reduced basis approach for the faster computations of approximate solutions in a given neighborhood, ensuring a threshold of accuracy.
   - Assess the quality of the optimal patterns obtained as well as their robustness and manufacturability.

All in all, we present here a binary descent algorithm [140] that, while heuristic, exploits the physics of the wave equation. In addition, solutions will always be feasible and sensitivities are obtained only from binary information, not continuous.

We finally assess the performance of this methodology through the design of relevant applications. In particular, invisibility cloaks and efficient waveguide and fiber bends will be designed in 2d and also in 3d.

1.7 Outline

This thesis consists of seven chapters. This first chapter has motivated, introduced and formulated the problem. We have also described the main challenges and objectives of this research, carefully reviewing the previous and current work in these areas of research. The second chapter introduces the multiscale CG method for wave propagation problems modeled through Helmholtz's equation. The performance of this method is shown through several acoustic and electromagnetic examples in 2d and 3d. Chapter 3 extends the methodology to a multiscale HDG method that can model Maxwell's equation, also in 3d. Similarly, chapter 4 derives a nonlinear extension of the multiscale methods for the numerical resolution of eigenvalue wave problems. This capability is applied for 2d and 3d Helmholtz's eigenproblems and extended for periodic settings. Chapter 5 presents a binary optimization heuristic algorithm for the design of structured materials within the wave propagation context. Chapter 6 shows the power of bringing together the simulation methods and the binary optimization technique through the design of cloaks and low loss sharp bends in PC waveguides and fibers. Finally, a summary of contributions and a thorough analysis of the future work is provided in chapter 7.

Chapter 2

Multiscale Continuous Galerkin Method for Helmholtz's equation

> *Make everything as simple as possible, but not simpler*
>
> **–Albert Einstein**

In this chapter we introduce a class of multiscale methods for the numerical simulation of waves. Firstly, we develop a multiscale continuous Galerkin method (MSCG) that will be used for problems governed by Helmholtz's equation in 2d and 3d. These methodologies will be then extended in chapter 3 to solve general 3d problems governed by Maxwell's equations through a multiscale hybridized discontinuous Galerkin method (MSHDG).

These multiscale methodologies become crucial for the efficient simulation of wave propagation problems in heterogeneous media, especially for high frequencies and in presence of geometric details with very different sizes. These methods first decompose the governing equation on a bounded polygonal or polyhedral domain into a set of local subproblems on non-overlapping polygonal or polyhedral subdomains. These subproblems are then solved using either a continuous Galerkin or a hybridizable discontinuous Galerkin method and the boundary conditions are taken to be elements of a traced continuous or discontinuous finite element space defined on the subdo-

main boundaries. Solutions to these subproblems are then used as basis functions in a variational formulation of the underlying equation in order to determine the Lagrange multiplier that approximates the exact solution on the subdomain boundaries. Finally, the approximate solution can be post-processed from the solutions of the subproblems and the Lagrange multiplier. For problems with piecewise-constant coefficients and repeated patterns, the number of subproblems can be reduced significantly by a judicious choice of subdomains and associated approximation spaces.

2.1 Multiscale framework

Most of the problems we are interested in involve heterogeneous media with small-scale features such as rods, fibers, stiffeners etc. It is therefore required that the equations considered take into account these features. Let us then consider general linear elliptic partial differential equations:

$$\left.\begin{aligned} -\nabla \cdot (a(\mathbf{x})\nabla u) + k^2 b(\mathbf{x}) u &= f, \quad \text{in } \Omega \\ u &= g_D, \quad \text{on } \Gamma_D \\ a\nabla u \cdot \mathbf{n} &= g_N, \quad \text{on } \Gamma_N \end{aligned}\right\} \tag{2.1}$$

Here $\Omega \subset \mathbb{R}^d$ is the physical domain with boundary $\partial\Omega = \Gamma_D \cap \Gamma_N$, $f \in L^2(\Omega)$, $a(\mathbf{x})$ and $b(\mathbf{x})$ are functions defined on Ω that determine the material distribution, and k is the wavevector. We assume that $a(\mathbf{x})$ and $b(\mathbf{x})$ are bounded. The boundary conditions are given by functions g_D and g_N on disjoint subsets Γ_D and Γ_N of $\partial\Omega$. Here $\mathbf{n}$ denotes the unit outward normal on the boundary of a given domain.

To model media with small-scale features, we assume that the material coefficients $a(\mathbf{x})$ and $b(\mathbf{x})$ have the smallest scale of length, which is of course finite but very small relative to the size of the total domain Ω. A scale resolution of the smallest features may require an enormous computational effort. It is therefore of considerable interest to develop a numerical method that can allow for the scale resolution and at the same time have the computational efficiency in terms of both memory storage and CPU time.

The multiscale methods presented in this thesis provide a computationally efficient

numerical scheme for the resolution of these kind of problems. The key concept is to develop two levels of discretization: a highly parallelizable and reusable local set of problems that are fine enough to capture all geometric details; and a global system formed by assembling the local information on a higher order but much coarser discretization that is just able to resolve the frequencies of interest accurately.

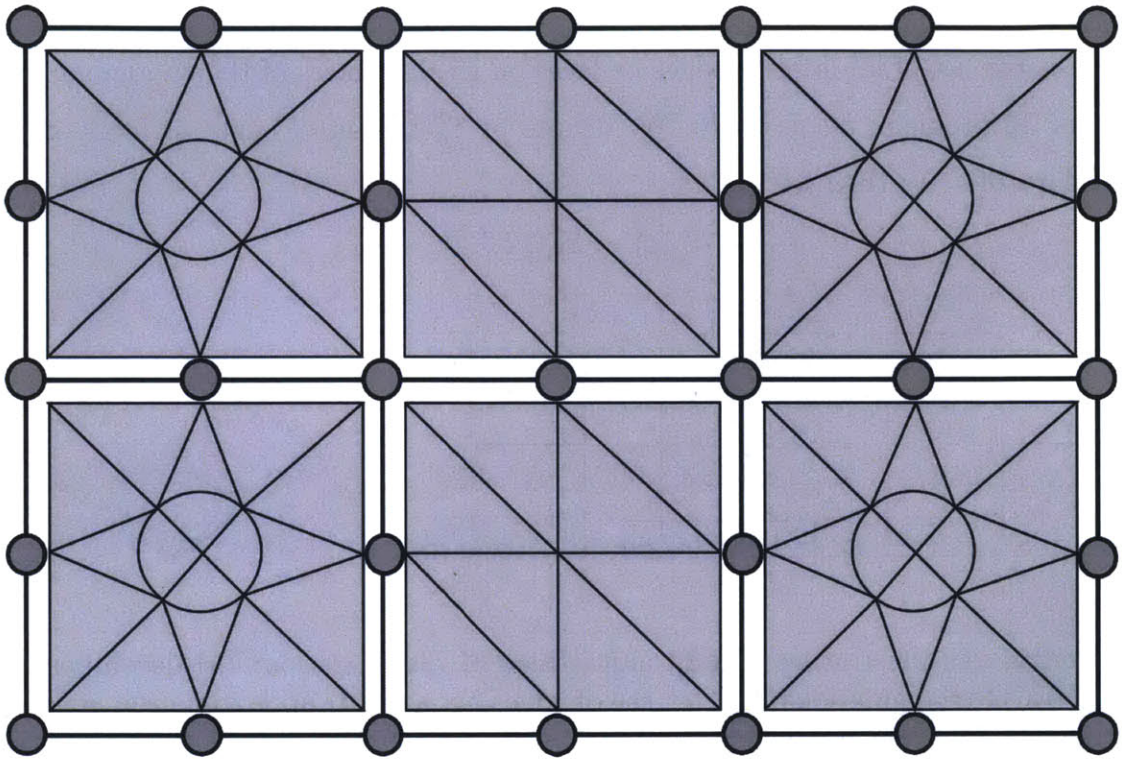

Figure 2.1: An illustration of a *macro* discretization with two families of subelements *micro* discretized using CG.

In particular, let us discretize the domain Ω into a *macro* decomposition $\{\Omega^m\}_{m=1}^M$. Each subdomain will then be *micro* discretized with a regular continuous Galerkin (CG) method as shown in figure 2.1.

We then denote by $\mathcal{T}_\Omega = \{\Omega^m, 1 \leq m \leq M\}$ the *macro* decomposition of the polygonal/polyhedral domain Ω into non-overlapping polygonal/polyhedral subdomains such that

$$\overline{\Omega} = \bigcup_{m=1}^{M} \overline{\Omega^m}, \quad \text{and} \quad \Omega^m \cap \Omega^k = \emptyset \text{ for } m \neq k. \tag{2.2}$$

Let $\mathcal{T}_h^m$ denote a *micro* regular CG (or HDG in next chapter) triangulation of each

subdomain Ω^m. We assume that

$$\bigcup_{m=1}^{M} \mathcal{T}_h^m = \mathcal{T}_h, \tag{2.3}$$

where $\mathcal{T}_h$ is the fine triangulation of our physical domain Ω. We next define

$$\mathcal{E}_h^i = \{e : e \text{ is an interface of } K^- \in \mathcal{T}_h^i \text{ and } K^+ \in \mathcal{T}_h^j \text{ for } i \neq j\} \tag{2.4}$$

which is the set of all interior edges or faces on the interfaces of the subdomains for a 2d or 3d problem, respectively. We denote by $\mathcal{E}_h^\partial$ the set of edges or faces on the boundary $\partial\Omega$. We then set

$$\mathcal{E}_h = \mathcal{E}_h^i \cup \mathcal{E}_h^\partial. \tag{2.5}$$

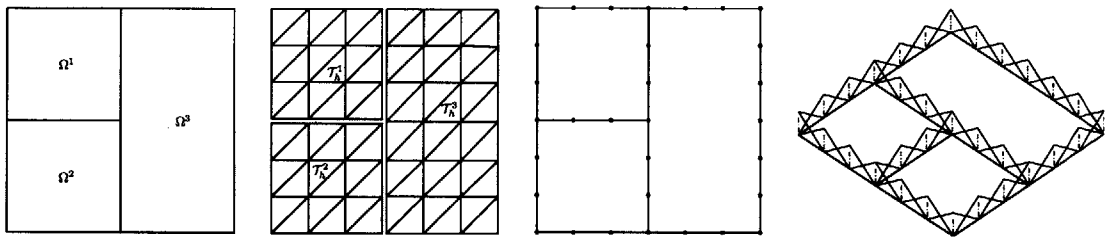

Figure 2.2: An illustration of a 2d multiscale CG discretization: (a) decomposition Ω^m; (b) CG triangulations $\mathcal{T}_h^m$; (c) set of edges $\mathcal{E}_h$; and (d) approximation space V_h for polynomial order $p = 1$.

Besides the geometrical decomposition, we also need to define the finite element approximation spaces for both levels of discretization. At the local level, they will depend on the discretization chosen therein and will thus be described later for each case. For the global problem we will define a set of Lagrange multipliers λ that will take values on the approximation space V_h defined as follows:

$$V_h = \{\mu \in C^0(\mathcal{E}_h) \ : \ \mu|_e \in \mathcal{P}_p(e), \forall e \in \mathcal{E}_h\}. \tag{2.6}$$

Furthermore, we set $V_h(g_D) = \{\mu \in V_h \ : \ \mu = \mathsf{P}g_D \text{ on } \Gamma_D\}$ in order to meet the Dirichlet boundary conditions. Figure 2.2 depicts an example of Ω^m and $\mathcal{T}_h^m$, $1 \leq m \leq M$ and also illustrates $\mathcal{E}_h$ and the approximation space V_h for $p = 1$ in the same example.

2.2 The multiscale CG method

In order to motivate the discussion of the multiscale CG technique, we firstly describe the classical continuous Galerkin (CG) method for solving 2.1. Let $\mathcal{T}_h$ denote a finite element (FE) triangulation of the domain Ω with a mesh size h. We then define the space

$$X_h = \{v \in C^0(\Omega) \ : \ v|_K \in \mathcal{P}_p(K) \text{ for } K \in \mathcal{T}_h\}, \tag{2.7}$$

where $C^0(D)$ denotes the space of continuous functions on a domain D and $\mathcal{P}_p(K)$ denotes the space of polynomials of order less than or equal to p on K. We then set

$$X_h(g_D) = \{v \in X_h \ : \ v = \mathsf{P}g_D \text{ on } \Gamma_D\}, \tag{2.8}$$

where P represents the L^2-projection into the space of traces on Γ_D of functions in X_h. The CG method provides an approximate solution $u_h \in X_h(g_D)$ that satisfies

$$(a\nabla u_h, \nabla v)_\Omega + (bk^2 u_h, v)_\Omega = (f, v)_\Omega + \langle g_N, v\rangle_{\Gamma_N}, \quad \forall v \in X_h(0). \tag{2.9}$$

Here, for $w, v \in L^2(D)$ and $r, t \in L^2(B)$, we define the finite element standard Lebesgue inner products on a domain D or a boundary B as:

$$(w, v)_D = \int_D wv\, dx; \quad \langle r, t\rangle_B = \int_B rt\, ds. \tag{2.10}$$

Note that $L^2(D)$ and $L^2(B)$ are the spaces of square integrable functions on $D \subset \mathbb{R}^d$ and $B \subset \mathbb{R}^{d-1}$, respectively. We can assume that both the continuous problem 2.1 and the CG discretized counterpart 2.9 have a unique solution.

If small geometric features want to be captured in the CG discretization, the size of the mesh elements has to be smaller than the size of such details and thus we require at least $O(\kappa^{-d})$ degrees of freedom for scale resolution, being κ the size of the smallest geometric features and d the dimension of the problem: 2 or 3. Since $\kappa \ll 1$, the direct solution of the linear system of the CG method might be extremely expensive, especially for large problems in 3d. As a consequence, we present an alternative numerical methodology that will be efficient and will hold improved scalability: a multiscale continuous Galerkin method, or MSCG.

We thus structure this section in three parts: First, we introduce the required additional notation and describe the formulation of the MSCG method for linear elliptic PDEs. Then, a weak trace formulation is derived whereby the set of Lagrange multipliers corresponds to the unique solution of the variational formulation on the traced space V_h. In addition, we include an implementation guide of the algorithm.

2.2.1 Formulation of the MSCG

Let us first introduce the approximation space Y_h where the solution field will lay.

$$Y_h = \{v \in L^2(\Omega) \ : \ v \in C^0(\Omega^m), \text{ and } v|_K \in \mathcal{P}_p(K), \forall K \in \mathcal{T}_h^m, 1 \leq m \leq M\}, \quad (2.11)$$

which consists of polynomials which are continuous in each subdomain but doubled-valued at the subdomain interfaces. Note that $\mathcal{P}_p(K)$ is the space of polynomials of order at most p on K.

One of the key features of the MSCG method is that we shall relax the continuity restriction at the subdomain interfaces and impose it back through the Lagrange multiplier λ. To enforce the continuity of the approximate solution $U_h \in Y_h$ across the subdomain interfaces we force the values of U_h corresponding to the degrees of freedom on the boundary of each subdomain to be equal to the Lagrange multiplier λ, which we take in the traced approximation space V_h. This is equivalent to imposing Dirichlet boundary conditions at every subdomain if λ is known.

The continuity of the solution field U_h relies on the continuity of the Lagrange multipliers. Note that if $\mu \in V_h$ is continuous over $\mathcal{E}_h$, then any function $w \in Y_h$ where $w_{\mathcal{E}_h} = \mu$, is continuous over Ω.

We now introduce an auxiliary variable denoted by q_h which approximates $a\nabla u \cdot \boldsymbol{n}$ on $\partial\Omega^m$. This additional variable resides in the space

$$W_h = \{w \in L^2(\{\partial\Omega^m \ : \ \Omega^m \in \mathcal{T}_\Omega\}) \ : \ w|_{\partial\Omega^m} = v|_{\partial\Omega^m} \text{ for } v \in Y_h\}. \quad (2.12)$$

Note that $w \in W_h$ is a function defined on the edges or faces of the subdomain and thus will be double-valued in the interior boundaries of $\Omega^m \in \mathcal{T}_\Omega$. Moreover, on each subdomain Ω^m we will introduce local subproblems, in which the approximate

solutions (U_h, q_h) belong to the following spaces, respectively:

$$\begin{aligned} X_h^m &= \{v \in C^0(\Omega^m) \ : \ v|_K \in \mathcal{P}_p(K) \text{ for } K \in \mathcal{T}_h^m\}, \\ W_h^m &= \{w \in C^0(\partial\Omega^m) \ : \ w|_{\partial\Omega^m} = v|_{\partial\Omega^m} \text{ for } v \in X_h^m, \forall K \in \mathcal{T}_h^m\}. \end{aligned} \tag{2.13}$$

Finally, we define $X_h^m(\eta) = \{v \in X_h^m \ : v = \eta \text{ on } \partial\Omega^m\}$ for some $\eta \in V_h$ in order to account for the Dirichlet boundary conditions.

We can now define the MSCG primal problem as seeking an approximation $(U_h, \lambda, q_h) \in Y_h \times V_h(g_D) \times W_h$ such that:

$$(a\nabla U_h, \nabla v)_\Omega + \left(bk^2 U_h, v\right)_\Omega - \sum_{m=1}^{M} \langle q_h, v\rangle_{\partial\Omega^m} = (f, v)_\Omega, \qquad \forall v \in Y_h, \tag{2.14a}$$

$$U_h = \lambda, \qquad \text{on } \mathcal{E}_h, \tag{2.14b}$$

$$\langle [\![q_h]\!], \mu\rangle_{\mathcal{E}_h} = \langle g_N, \mu\rangle_{\Gamma_N}, \quad \forall \mu \in V_h(0). \tag{2.14c}$$

Here $[\![q_h]\!]$ is the jump of the normal component of the flux defined as

$$[\![q_h]\!] = \begin{cases} q_h|_{\partial\Omega^m} + q_h|_{\partial\Omega^k} & \text{on the interface } \partial\Omega^m \cap \partial\Omega^k, \\ q_h & \text{on the interface } \partial\Omega^m \cap \partial\Omega. \end{cases} \tag{2.15}$$

We thus see that equation 2.14c enforces a weak continuity of the auxiliary variable across the interfaces of the subdomains. In addition, it can be proved (see theorem B.1 in appendix B) that the solution $(U_h, \lambda, q_h) \in Y_h \times V_h(g_D) \times W_h$ exists and is unique and also that $U_h = u_h$ in Ω and $\lambda = u_h$ on $\mathcal{E}_h$, being u_h the solution of the CG discretization obtained by 2.9. As a consequence, the approximate solution U_h has the order of convergence of $O(h^p)$ in the energy norm and of $O(h^{p+1})$ in the L^2 norm under certain assumptions on the smoothness and regularity of the continuous problem 2.1 according to the standard approximation result given in [32].

2.2.2 Weak trace formulation of the Lagrange multiplier

We now show how to eliminate the unknowns U_h and q_h to obtain a weak formulation only for λ. We begin by introducing two sets of local subproblems formulated at the subdomain level. For each Ω^m the first local subproblem associates to the function

$f \in L^2(\Omega)$ the pair of functions $(U_f|_{\Omega^m}, q_f|_{\Omega^m}) \in X_h^m \times W_h^m$ defined by

$$(a\nabla U_f, \nabla v)_{\Omega^m} + \left(bk^2 U_f, v\right)_{\Omega^m} - \langle q_f, v\rangle_{\partial\Omega^m} = (f, v)_{\Omega^m}, \quad \forall v \in X_h^m, \tag{2.16a}$$

$$U_f = 0, \qquad \text{on } \partial\Omega^m. \tag{2.16b}$$

It is clear that the pair $(U_f|_{\Omega^m}, q_f|_{\Omega^m})$ is the approximate solution of

$$-\nabla \cdot (a\nabla u_f) + bk^2 u_f = f, \quad \text{in } \Omega^m, \tag{2.17a}$$

$$u_f = 0, \quad \text{on } \partial\Omega^m. \tag{2.17b}$$

Note that problems 2.16 and 2.17 are defined on the subdomains $\Omega^m, 1 \leq m \leq M$. In addition, the second local subproblem associates to each $\eta \in V_h$ the pair of functions $(U_\eta|_{\Omega^m}, q_\eta|_{\Omega^m}) \in X_h^m \times W_h^m$ such that

$$(a\nabla U_\eta, \nabla v)_{\Omega^m} + \left(bk^2 U_\eta, v\right)_{\Omega^m} - \langle q_\eta, v\rangle_{\partial\Omega^m} = 0, \quad \forall v \in X_h^m, \tag{2.18a}$$

$$U_\eta = \eta, \quad \text{on } \partial\Omega^m. \tag{2.18b}$$

The pair $(U_\eta|_{\Omega^m}, q_\eta|_{\Omega^m})$ is thus the approximate solution of

$$-\nabla \cdot (a\nabla u_\eta) + bk^2 u_\eta = 0, \quad \text{in } \Omega^m, \tag{2.19a}$$

$$u_\eta = \eta, \quad \text{on } \partial\Omega^m. \tag{2.19b}$$

A key property of this decomposition lays on the fact that both continuous subproblems have the same differential operator despite the forcing term as well as the Dirichlet boundary conditions being different. By linearity and superposition we can claim (see theorem B.2) that $u_{f\eta} := u_f + u_\eta$ is the solution of

$$-\nabla \cdot (a\nabla u_{f\eta}) + bk^2 u_{f\eta} = f, \quad \text{in } \Omega^m, \tag{2.20a}$$

$$u_{f\eta} = \eta, \quad \text{on } \partial\Omega^m. \tag{2.20b}$$

As a result, $U_\lambda + U_f$ is nothing but an approximation to the solution of problem 2.1 for $\eta = \lambda$, where the Lagrange multiplier λ satisfies its weak formulation. More formally, we can prove (see B.3 in appendix B) that for (U_h, λ, q_h) solution of the primal problem 2.14, $U_h = U_\lambda + U_f$ and $q_h = q_\lambda + q_f$. In addition, it can also be

proved that $\lambda \in V_h(g_D)$ is the unique solution of the formulation:

$$(a\nabla U_\lambda, \nabla U_\mu)_\Omega + (bk^2 U_\lambda, U_\mu)_\Omega = (f, U_\mu)_\Omega + \langle g_N, \mu \rangle_{\Gamma_N}, \quad \forall \mu \in V_h(0). \tag{2.21}$$

As a consequence, the Lagrange multiplier λ is determined as a solution of the weak formulation 2.21. This characterization result allows for an efficient implementation of the MSCG method, which we describe in detail in the next section.

2.2.3 Implementation

Let us now describe the steps for constructing a discrete algebraic system associated with the weak formulation for the Lagrange multiplier. Firstly, we show that the MSCG has a variational multiscale interpretation which allows us to draw some remarks on its connection with other methods.

We note from the weak formulation 2.21 that we do not need to compute the auxiliary variable q_h to construct the matrix equations for the multiplier λ. Indeed, it follows from the local subproblem 2.16 that $U_f|_{\Omega^m} \in X_h^m(0)$ is the solution of

$$(a\nabla U_f, \nabla v)_{\Omega^m} + \left(bk^2 U_f, v\right)_{\Omega^m} = (f, v)_{\Omega^m}, \quad \forall v \in X_h^m(0). \tag{2.22}$$

Similarly, we have from 2.18 that $U_\eta|_{\Omega^m} \in X_h^m(\eta)$ for $\eta \in V_h$ is the solution of

$$(a\nabla U_\eta, \nabla v)_{\Omega^m} + \left(bk^2 U_\eta, v\right)_{\Omega^m} = 0, \quad \forall v \in X_h^m(0). \tag{2.23}$$

Clearly, the discrete subproblems 2.22 and 2.23 are the usual CG formulations of 2.17 and 2.19, respectively. Moreover, the two discrete subproblems differ from each other only in the right-hand side.

We next consider solving for λ. Let us assume that the space V_h is spanned by:

$$V_h = \text{ span } \{\varphi_i, 1 \leq i \leq N\}, \tag{2.24}$$

where $\varphi_i, 1 \leq i \leq N$, are the nodal basis functions on $\mathcal{E}_h$. These basis functions satisfy $\varphi_i(\mathbf{x}_j) = \delta_{ij}$, where $\mathbf{x}_j \in \mathcal{E}_h, 1 \leq j \leq N$, are the nodal points of $\mathcal{E}_h$. By equation 2.21, we have:

$$\lambda(\mathbf{x}) = \sum_{j=1}^{N} \Lambda_j \varphi_j(\mathbf{x}), \tag{2.25}$$

where $\Lambda \in \mathbb{R}^N$ represents the degrees of freedom of λ and provides the solution to the following linear system of equations:

$$\mathbb{A}\Lambda = \mathbb{F}. \tag{2.26}$$

Here $\mathbb{A} \in \mathbb{R}^{N\times N}$ and $\mathbf{F} \in \mathbb{R}^N$ are given by

$$\mathbb{A}_{ij} = a_h(\varphi_i, \varphi_j) = (a\nabla U_{\varphi_i}, \nabla U_{\varphi_j})_\Omega + (bk^2 U_{\varphi_i}, U_{\varphi_j})_\Omega, \quad 1 \le i,j \le N, \tag{2.27a}$$

$$\mathbf{F}_i = b_h(\varphi_i) = (f, U_{\varphi_i})_\Omega + \langle g_N, \varphi_i\rangle_{\Gamma_N}, \quad 1 \le i \le N. \tag{2.27b}$$

Of course, the Dirichlet boundary condition must also be enforced when solving 2.26 for Λ. Note that U_{φ_i} is the solution of 2.23 for $\eta = \varphi_i$ and that to compute U_{φ_i} we need to solve the local subproblem 2.23 only on the subdomains for which φ_i is non-zero. We then compute U_λ from the definition of the first local subproblem and apply superposition of the solutions to obtain the following decomposition:

$$U_\lambda = \sum_{j=1}^{N} \Lambda_j U_{\varphi_j}. \tag{2.28}$$

If we now set

$$H_h = \text{span}\,\{U_{\varphi_i}, 1 \le i \le N\}, \tag{2.29}$$

then it follows from 2.26-2.29 that $U_\lambda \in H_h$ satisfies

$$(a\nabla U_\lambda, \nabla v)_\Omega + (bk^2 U_\lambda, v)_\Omega = (f, v)_\Omega + \langle g_N, v\rangle_{\Gamma_N}, \quad \forall v \in H_h. \tag{2.30}$$

Note that this formulation is equivalent to the weak formulation 2.21 of the Lagrange multiplier λ and therefore yields to the same algebraic system. However, this variational formulation allows us to draw several important remarks detailed in the next four paragraphs.

First of all, we can see that the approximate solution $U_h = U_\lambda + U_f$ has a variational multiscale interpretation in the sense that it is computed by introducing and solving the local subproblems on the subdomains. We first construct the basis functions in 2.29 that capture the local properties of the differential operator at the fine scale. Then, we solve formulation 2.30 using the newly constructed local basis functions instead of conventional polynomial functions. The purpose of the subproblems is

thus to eliminate the fine-scale degrees-of-freedom for u_h in favor of the coarse-scale degrees-of-freedom for λ. This concept can also be interpreted as a static condensation of the many degrees of freedom inside each subdomain into the coarser set of degrees of freedom on the interfaces. Furthermore, since λ is the exact restriction of U_h on $\mathcal{E}_h$, the computation of only λ may be sufficient for some applications that require the knowledge of the solution on the boundaries or interfaces.

Secondly, we note that when the material coefficients $a(x)$ and $b(x)$ are distributed in a repeated manner (say subelements $j \in \mathcal{J} \subset \{m\}_{m=1}^{M}$ have the same geometry), the approximation spaces are such that $X_h^{j_1} = X_h^{j_2}, \forall j_1, j_2 \in \mathcal{J}$. That is, all subdomains that belong to a given class, have the same geometry, triangulation, and polynomial basis. As a consequence, all subdomains in a given class provide the same solution to problem 2.23 and therefore we need to solve the corresponding local subproblem only once. For problems with piecewise-constant or periodic coefficients, we can exploit this observation to greatly reduce the number of local subproblems by a judicious choice of subdomains and associated approximation spaces. We shall discuss this key advantage in greater detail in the examples presented later on.

It is also important to note that the weak formulation 2.30 reveals a connection between the MSCG method and the multiscale FE method [69]. Indeed, we note that when the subdomains are linear triangular or rectangular elements (in 3d, tetrahedra or hexahedra) and $\mathcal{E}_h$ is redefined as the set of all edges or faces of the subdomains, we recover the multiscale FE method with linear boundary conditions. However, in such case, the crucial property $U_h = u_h$ does not hold true except only when the *micro* triangulation $\mathcal{T}_h^m$ coincides with the subdomain Ω^m for $1 \leq m \leq M$. In general, the multiscale FE method does not yield the same solution as the CG method, in contrast to the MSCG.

Finally, the MSCG method can be extended to variable-degree approximation spaces and meshes with hanging nodes by redefining the set of interface edges or faces $\mathcal{E}_h$ and the approximation spaces $V_h(g)$, X_h^m, and W_h^m in a suitable way. We shall discuss this extension in a future section. Moreover, the conservative approximation $\boldsymbol{Q}_h$ to the flux $\boldsymbol{q} = a\nabla u$ can be efficiently constructed by a local element-by-element

post-processing of the MSCG solution U_h. The implementation of such techniques is discussed, for instance in [42].

At this stage, we are certainly able to describe the assembly of the global stiffness matrix $\mathbb{A}$ and load vector $\mathbf{F}$ in equation 2.27. We begin by solving the subproblems on the particular subdomain Ω^m. In the basis set $\{\varphi_j\}_{j=1}^N$ of V_h there exists a subset of $N^m \leq N$ basis functions which have non-zero support on $\partial\Omega^m$. Let $\{\psi_j\}_{j=1}^{N^m}$ be such subset, which means that $\psi_j^m(\boldsymbol{s}_i^m) = \delta_{ij}, 1 \leq i, j \leq N^m$, where $\boldsymbol{s}_i^m, 1 \leq n \leq N^m$, are the nodal points of $\mathcal{E}_h$ on $\partial\Omega^m$.

Discretizing the first local subproblem 2.22 and applying the boundary conditions we obtain the linear system of equations:

$$\mathbb{K}^m \boldsymbol{u}_{f^m} = \boldsymbol{f}^m, \tag{2.31}$$

where $\boldsymbol{u}_{f^m}$ is the vector of degrees of freedom for $U_f|_{\Omega^m}$. Similarly, discretizing the second local subproblem 2.23 with $\eta = \psi_j^m$ and applying the boundary conditions we obtain the linear system of equations:

$$\mathbb{K}^m \boldsymbol{u}_{\psi_j^m} = \mathbb{G}^m \boldsymbol{d}_{\psi_j^m}, \quad 1 \leq j \leq N^m, \tag{2.32}$$

where $\boldsymbol{u}_{\psi_i^m}$ and $\boldsymbol{d}_{\psi_j^m}$ are the vectors of degrees of freedom for $U_{\psi_j^m}|_{\Omega^m}$ and ψ_j^m, respectively. Note that equations 2.32 and 2.31 have the same left-hand-side matrix and differ only in their right-hand-side vector.

The local stiffness matrix $\mathbb{A}^m \in \mathbb{R}^{N^m \times N^m}$ and load vector $\boldsymbol{F}^m \in \mathbb{R}^{N^m}$ can then be computed as

$$\mathbb{A}_{ij}^m = \boldsymbol{u}_{\psi_i^m}^T \mathbb{K}^m \boldsymbol{u}_{\psi_j^m}, \quad 1 \leq i, j \leq N^m, \tag{2.33a}$$

$$\boldsymbol{F}_i^m = \boldsymbol{u}_{\psi_i^m}^T \boldsymbol{f}^m + \boldsymbol{g}_i^m, \quad 1 \leq i \leq N^m, \tag{2.33b}$$

where $\boldsymbol{g}_i^m = \langle g_N, \psi_i^m \rangle_{\Gamma_N}, i = 1, \ldots, N^m$. Note that the specific forms for $\mathbb{K}^m, \mathbb{G}^m, \boldsymbol{f}^m$, and $\boldsymbol{g}^m$ depend on the approximation spaces used in the discretization process. Furthermore, the dimensions of these quantities as well as both $\mathbb{A}^m$ and $\boldsymbol{F}^m$ vary from subdomain to subdomain. Finally, the global stiffness matrix $\mathbb{A}$ and load vector $\boldsymbol{F}$ are assembled through the standard assembly procedure. Table 2.1 summarizes the

implementation steps.

Table 2.1: Implementation steps of MSCG method

1. For a representative of each subdomain $\Omega^m, 1 \leq m \leq M$,
   a. Compute the matrices $\mathbb{K}^m$, $\mathbb{G}^m$, and vectors $\boldsymbol{f}^m$, $\boldsymbol{g}^m$
   b. Solve for $\boldsymbol{u}_{fm}$ from 2.31
   c. Solve for $\boldsymbol{u}_{\psi_j^m}, 1 \leq j \leq N^m$, from 2.32
   d. Compute the local stiffness matrix $\mathbb{A}^m$ and load vector $\boldsymbol{F}^m$ from 2.33
2. Assemble $\mathbb{A}$ and $\boldsymbol{F}$ according to the standard assembly procedure
3. Solve $\mathbb{A}\Lambda = \boldsymbol{F}$ considering $\lambda = \mathsf{P}g_D$ on Γ_D into account
4. Compute U_λ according to 2.28 and postprocess $U_h = U_\lambda + U_f$

Also note that in order to recover U_h after the global problem has been solved, the local problems do not need to be resolved each one with different Dirichlet boundary conditions corresponding to the values of λ on their boundary degrees of freedom. It is enough to use the decomposition $U_h = U_f + U_\lambda$ at each subdomain level where $U_\lambda = \sum_{j=1}^{N} \Lambda_j U_{\varphi_j}$, so in terms of computational cost, we need to perform a matrix-matrix multiplication for each subelement in contrast to a matrix inverse or a system resolution.

2.3 Convergence test and cost analysis

We now perform a numerical test for which the exact solution is known to confirm the convergence and accuracy of the method presented. We consider solving 2.1 in 2d on the regular square $\Omega = (0,1) \times (0,1)$ for the non-coercive elliptic (Helmholtz) problem with homogeneous material properties $a = b = 1$. The force term f and boundary data g_D are chosen such that the exact solution is given by the function

$$u(x,y) = x^2 + y^2 + \sin(k(x\cos\theta + y\sin\theta))$$

This solution field represents a plane wave propagating in the θ-direction, where k is the wavenumber and θ is the streamline direction of the planar wave. Below we report numerical results for $\theta = \pi/4$ and $k = 8$.

Let us now consider triangular meshes obtained by splitting a regular $n \times n$ Cartesian grid into a total of $2n^2$ triangles, with uniform element sizes of $h = 1/n$. The

original domain is decomposed evenly into $M = q \times q$ rectangular subdomains so that each subdomain has $2n^2/q^2$ elements. Note that q needs to be a divisor of n. On these subdomains, we consider solutions of polynomial degree p represented using a nodal basis within each triangle, with the nodes uniformly distributed.

We present $L^2(\Omega)$ errors in the solution for both the MSCG method with $q = 1, 2, 4, 8$ and the CG method on five different meshes $n = 8, 16, 32, 64, 128$ in table 2.2 for $p = 1$ and in table 2.3 for $p = 2$. As expected, the MSCG method yields exactly the same $L^2(\Omega)$ error in the solution as the CG method. Furthermore, a convergence rate of $O(h^{p+1})$ is expected for this example since the analytical solution is smooth.

Table 2.2: Convergence history of the MSCG method and the CG method for $p = 1$: $L^2(\Omega)$ error in the solution as a function of n.

Mesh	MSCG				CG	
n	$q = 1$ error	$q = 2$ error	$q = 4$ error	$q = 8$ error	error	order
8	$9.27 \cdot 10^{-1}$	$9.27 \cdot 10^{-1}$	$9.27 \cdot 10^{-1}$	$9.27 \cdot 10^{-1}$	$9.27 \cdot 10^{-1}$	—
16	$1.63 \cdot 10^{-1}$	$1.63 \cdot 10^{-1}$	$1.63 \cdot 10^{-1}$	$1.63 \cdot 10^{-1}$	$1.63 \cdot 10^{-1}$	2.51
32	$4.00 \cdot 10^{-2}$	$4.00 \cdot 10^{-2}$	$4.00 \cdot 10^{-2}$	$4.00 \cdot 10^{-2}$	$4.00 \cdot 10^{-2}$	2.02
64	$9.87 \cdot 10^{-3}$	$9.87 \cdot 10^{-3}$	$9.87 \cdot 10^{-3}$	$9.87 \cdot 10^{-3}$	$9.87 \cdot 10^{-3}$	2.02
128	$2.44 \cdot 10^{-3}$	$2.44 \cdot 10^{-3}$	$2.44 \cdot 10^{-3}$	$2.44 \cdot 10^{-3}$	$2.44 \cdot 10^{-3}$	2.02

Table 2.3: Convergence history of the MSCG method and the CG method for $p = 2$: $L^2(\Omega)$ error in the solution as a function of n.

Mesh	MSCG				CG	
n	$q = 1$ error	$q = 2$ error	$q = 4$ error	$q = 8$ error	error	order
8	$2.37 \cdot 10^{-2}$	$2.37 \cdot 10^{-2}$	$2.37 \cdot 10^{-2}$	$2.37 \cdot 10^{-2}$	$2.37 \cdot 10^{-2}$	—
16	$1.70 \cdot 10^{-3}$	$1.70 \cdot 10^{-3}$	$1.70 \cdot 10^{-3}$	$1.70 \cdot 10^{-3}$	$1.70 \cdot 10^{-3}$	3.80
32	$1.63 \cdot 10^{-4}$	$1.63 \cdot 10^{-4}$	$1.63 \cdot 10^{-4}$	$1.63 \cdot 10^{-4}$	$1.63 \cdot 10^{-4}$	3.38
64	$1.85 \cdot 10^{-5}$	$1.85 \cdot 10^{-5}$	$1.85 \cdot 10^{-5}$	$1.85 \cdot 10^{-5}$	$1.85 \cdot 10^{-5}$	3.14
128	$2.23 \cdot 10^{-6}$	$2.23 \cdot 10^{-6}$	$2.23 \cdot 10^{-6}$	$2.23 \cdot 10^{-6}$	$2.23 \cdot 10^{-6}$	3.05

Note that not only the same convergence rate is obtained but also the exact same error for equivalent discretizations. This is due to the fact that actually the MSCG solution U_h and the CG solution u_h in 2.9 are the same: $U_h = u_h$, as proven in theorem B.1.

Finally, it is also relevant to compare the degrees of freedom for the MSCG and CG methods. This analysis will focus on the 2d problem with structured meshes just considered for simplicity. Unstructured discretizations as well as 3d problems could be analyzed in an analogous fashion. In order assess the cost, let us note that the $\mathcal{T}_h$ has $2n^2$ uniform triangles and $(np+1)^2$ nodes. The total degrees of freedom for the CG method is thus:

$$\mathcal{N}_{\text{dof}}^{\text{cg}} = (np+1)^2. \tag{2.34}$$

For the MSCG method, there are $M = q^2$ micro triangulations $\mathcal{T}_h^m, 1 \leq m \leq M$, each of which has $2(n/q)^2$ uniform triangles and $(np/q+1)^2$ nodes. Hence, each subproblem has $\mathcal{K}_{\text{dof}}^{\text{mscg}}$ unknowns with

$$\mathcal{K}_{\text{dof}}^{\text{mscg}} = (np/q+1)^2. \tag{2.35}$$

Moreover, since the Lagrange multiplier is defined only on the boundary interfaces of the subdomains, it has $\mathcal{N}_{\text{dof}}^{\text{mscg}}$ degrees of freedom with

$$\mathcal{N}_{\text{dof}}^{\text{mscg}} = (q+1)(2np-q+1). \tag{2.36}$$

We show in tables 2.4 and 2.5 the results for for $p = 1$ and $p = 2$, respectively. It can be seen that for all choices of q, both $\mathcal{K}_{\text{dof}}^{\text{mscg}}$ and $\mathcal{N}_{\text{dof}}^{\text{mscg}}$ are significantly smaller than $\mathcal{N}_{\text{dof}}^{\text{cg}}$. Moreover, the finer the discretization, the bigger the difference. In particular, $\mathcal{K}_{\text{dof}}^{\text{mscg}} = 1,089$, $\mathcal{N}_{\text{dof}}^{\text{mscg}} = 4,545$, and $\mathcal{N}_{\text{dof}}^{\text{cg}} = 66,049$ for the case $p = 2$ and $n = 128$.

Table 2.4: Comparison of the degrees of freedom between the MSCG method and the CG method using uniform meshes for $p = 1$.

	MSCG									CG
n	$q=2$			$q=4$			$q=8$			
	M	$\mathcal{K}_{\text{dof}}^{\text{mscg}}$	$\mathcal{N}_{\text{dof}}^{\text{mscg}}$	M	$\mathcal{K}_{\text{dof}}^{\text{mscg}}$	$\mathcal{N}_{\text{dof}}^{\text{mscg}}$	M	$\mathcal{K}_{\text{dof}}^{\text{mscg}}$	$\mathcal{N}_{\text{dof}}^{\text{mscg}}$	$\mathcal{N}_{\text{dof}}^{\text{cg}}$
8	4	25	45	16	9	65	64	4	81	81
16	4	81	93	16	25	145	64	9	225	289
32	4	289	189	16	81	305	64	25	513	1,089
64	4	1,089	381	16	289	625	64	81	1,089	4,225
128	4	4,225	765	16	1,089	1,265	64	289	2,241	16,641

Table 2.5: Comparison of the degrees of freedom between the MSCG method and the CG method using uniform meshes for $p = 2$.

	MSCG									CG
n	$q = 2$			$q = 4$			$q = 8$			
	M	$\mathcal{K}_{\text{dof}}^{\text{mscg}}$	$\mathcal{N}_{\text{dof}}^{\text{mscg}}$	M	$\mathcal{K}_{\text{dof}}^{\text{mscg}}$	$\mathcal{N}_{\text{dof}}^{\text{mscg}}$	M	$\mathcal{K}_{\text{dof}}^{\text{mscg}}$	$\mathcal{N}_{\text{dof}}^{\text{mscg}}$	$\mathcal{N}_{\text{dof}}^{\text{cg}}$
8	4	81	93	16	25	145	64	9	225	289
16	4	289	189	16	81	305	64	25	513	1,089
32	4	1089	381	16	289	625	64	81	1,089	4,225
64	4	4,225	765	16	1,089	1,265	64	289	2,241	16,641
128	4	16,641	1,533	16	4,225	2,545	64	1,089	4,545	66,049

It is important to point out that since the MSCG method solves a number of subproblems with multiple right-hand sides, it may have the same or even more computational cost than the CG method when the computation is carried out on a serial computer and/or without reusing the information from the local problems. However, if each subproblem is solved in parallel and we reuse information from every subdomain given the pattern repetition, then the cost of the MSCG method can be assumed to be proportional to solving only one of the local problems as well as the global problem in serial, which is significantly less computationally demanding than solving the system corresponding to the CG method.

2.4 Extension to non-conforming discretizations

The method presented so far assumes that the degrees of freedom on the boundaries of the local subdomains coincide with the degrees of freedom for the Lagrange multipliers on the traced space. This assumption has considerable limitations if complex geometries are sought to be represented across the subproblems. It also requires the resolution of both local and global discretizations to be equivalent, although that might lead to an excessive amount of degrees of freedom.

For all these reasons, we now extend the MSCG method to treat variable-degree approximation spaces with hanging nodes. The extension provides more flexibility for mesh generation and h/p adaptive refinement. Interestingly, the extension enables further reduction in the global coupled unknowns of the Lagrange multiplier. The

following observations are key. First, since the local subproblem on one subdomain is independent of the other subproblems on other subdomains, the approximation space for that local subproblem may have a different polynomial degree with the approximation spaces for the other subproblems. This will provide treatment of meshes with hanging nodes and render h/p adaptive refinement easier. Second, since the Lagrange multiplier is defined on the boundaries of the subdomains and serves as gluing the solutions between the subdomains, we may use polynomials of higher degrees to represent it and reduce the number of nodal points at the same time. This non-conforming MSCG approach will reduce the density and size of the discrete matrix of the global problem. Let us describe more specifically this approach.

We begin by introducing the notion of a minimal edge or face. An edge or face E of a subdomain Ω^m is said to be a minimal edge or face of the *macro* decomposition $\mathcal{T}_\Omega$ if it coincides with either $\partial\Omega^m \cap \partial\Omega$ or $\partial\Omega^m \cap \partial\Omega^k$, where Ω^k is any subdomain other than Ω^m such that $E \cap \partial\Omega^k$ has nonzero Lebesgue measure. Recall that the *macro* decomposition $\mathcal{T}_\Omega = \{\Omega^m, 1 \leq m \leq M\}$ is the set of non-overlapping polygonal subdomains which decompose the physical domain Ω. We denote by

$$\mathcal{E}_\Omega = \left\{ E^\ell \in \bigcup_{m=1}^{M} \partial\Omega^m \ : \ E^\ell \text{ is a minimal edge of } \mathcal{T}_\Omega, 1 \leq \ell \leq L \right\} \tag{2.37}$$

a collection of non-overlapping minimal edges or faces of $\mathcal{T}_\Omega$ such that

$$\bigcup_{m=1}^{M} \overline{\partial\Omega^m} = \bigcup_{\ell=1}^{L} \overline{E^\ell}, \quad \text{and} \quad E^\ell \cap E^k = \emptyset \text{ for } \ell \neq k. \tag{2.38}$$

Furthermore, we subdivide each edge $E^\ell \in \mathcal{E}_\Omega$ into n_ℓ microscopic (smaller) edges $\mathsf{e}_i, 1 \leq i \leq n_\ell$; note that $n_\mathsf{e} = \sum_{\ell=1}^{L} n_\ell$ is the total number of microscopic edges. We then define

$$\mathcal{E}_\mathsf{e} = \{\mathsf{e}_j, 1 \leq j \leq n_\mathsf{e}\}. \tag{2.39}$$

An illustration of $\mathcal{E}_\Omega$ and $\mathcal{E}_\mathsf{e}$ is given figure 2.3-(a). In this figure, note that BE and EG are minimal edges and thus belong to $\mathcal{E}_\Omega$; whereas BG of $\partial\Omega^3$ does not belong to $\mathcal{E}_\Omega$ since it is not a minimal edge. The figure also shows that the edge CH of $\mathcal{E}_\Omega$ is subdivided into two edges CI and IH to form $\mathcal{E}_\mathsf{e} = \{AB, BC, CI, IH, HG, GF, FD, DA,$

$BE, EG, ED\}$.

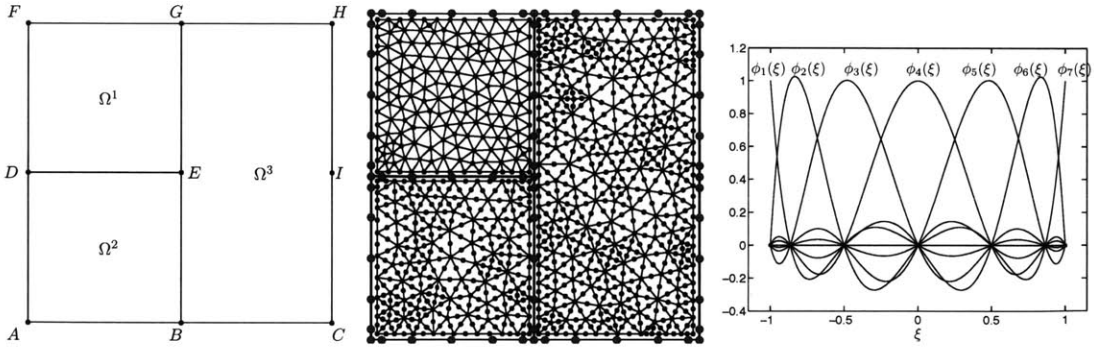

(a) (b) (c)

Figure 2.3: An illustration of (a) $\mathcal{E}_\Omega$ and $\mathcal{E}_\mathsf{e}$, (b) V_h^{non} and $X_h^{m,\text{non}}, 1 \leq m \leq M$, and (c) basis functions of $\mathcal{P}_{p(\mathsf{e})=6}(\mathsf{e}_r)$ on a reference edge $\mathsf{e}_r \equiv (-1, 1)$ with order 6.

We next introduce the approximation spaces as follows:

$$
\begin{aligned}
Y_h^{\text{non}} &= \{v \in L^2(\Omega) \ : \ v \in C^0(\Omega^m), v|_K \in \mathcal{P}_{p(\Omega^m)}(K), \forall K \in \mathcal{T}_h^m, 1 \leq m \leq M\}, \\
V_h^{\text{non}} &= \{\mu \in C^0(\mathcal{E}_\mathsf{e}) \ : \ \mu|_\mathsf{e} \in \mathcal{P}_{p(\mathsf{e})}(\mathsf{e}), \forall \mathsf{e} \in \mathcal{E}_\mathsf{e}\}, \\
W_h^{\text{non}} &= \{w \in L^2(\{\partial\Omega^m \ : \ \Omega^m \in \mathcal{T}_\Omega\}) \ : \ w|_{\partial\Omega^m} = v|_{\partial\Omega^m} \text{ for } v \in Y_h^{\text{non}}\},
\end{aligned}
\tag{2.40}
$$

where $\mathcal{P}_{p(\Omega^m)}(K)$ is the space of polynomials of (low) degree at most $p(\Omega^m)$ on $K \in \mathcal{T}_h^m$ and $\mathcal{P}_{p(\mathsf{e})}(\mathsf{e})$ is the space of polynomials of (high) degree at most $p(\mathsf{e})$ on $\mathsf{e} \in \mathcal{E}_\mathsf{e}$. It is important to note that $p(\Omega^m)$ can vary with Ω^m and that $p(\mathsf{e})$ can vary with e. Next let us define the traced space $V_h^{\text{non}}(g_D)$:

$$
V_h^{\text{non}}(g_D) = \{\mu \in V_h \ : \ \mu = \mathsf{P}^{V_h^{\text{non}}} g_D \text{ on } \Gamma_D\}, \tag{2.41}
$$

where $\mathsf{P}^{V_h^{\text{non}}}$ denotes the L^2-projection into the space of functions in V_h^{non} on Γ_D. Here we consider spectral elements [120] for our traced approximation space V_h^{non}.

Finally, on each subdomain Ω^m we introduce the approximation space for the solution field:

$$
X_h^{m,\text{non}} = \{v \in C^0(\Omega^m) \ : \ v|_K \in \mathcal{P}_{p(\Omega^m)}(K) \text{ for } K \in \mathcal{T}_h^m\}, \tag{2.42}
$$

where, once more, the Dirichlet boundary conditions modify this space as $X_h^{m,\text{non}}(\eta) =$

$\{v \in X_h^{m,\text{non}} : v = \mathsf{P}^{X_h^{m,\text{non}}}\eta \text{ on } \partial\Omega^m\}$ for some $\eta \in V_h$, where $\mathsf{P}^{X_h^{m,\text{non}}}$ denotes the L^2-projection into the space of traces on $\partial\Omega^m$ of functions in $X_h^{m,\text{non}}$.

Figure 2.3-(b) shows an example of V_h^{non} and $X_h^{m,\text{non}}, 1 \leq m \leq M$, for the domain decomposition depicted subfigure (a). The larger nodes represent the degrees of freedom of V_h and the smaller ones represent the degrees of freedom of $X_h^{m,\text{non}}, 1 \leq m \leq M$. We can also see that $X_h^{1,\text{non}}$ (respectively, $X_h^{2,\text{non}}$ and $X_h^{3,\text{non}}$) is a linear (respectively, quadratic) finite element approximation space and that there are many hanging nodes along the interior minimal edges of $\mathcal{E}_\text{e}$. Furthermore, for each $e \in \mathcal{E}_\text{e}$ that $\mathcal{P}_{p(\mathsf{e})}(\mathsf{e})$ is the space of polynomials of degree $p(\mathsf{e}) = 6$ as shown in subfigure (c), which shows the Lagrange interpolation polynomials at the Chebyshev nodes [120]. Note how on any edge $e \in \mathcal{E}_\text{e}$, the number of greater nodes is significantly smaller than the number of interior nodes.

In addition, we can show that the approximate solution of the non-conforming MSCG method is the same as that of a non-conforming CG method in a very similar way to the conforming case. In this case, we seek an approximation $(U_h^{\text{non}}, \lambda^{\text{non}}, q_h^{\text{non}}) \in Y_h^{\text{non}} \times V_h^{\text{non}}(g_D) \times W_h^{\text{non}}$ such that

$$\begin{aligned}
(a\nabla U_h^{\text{non}}, \nabla v)_\Omega + (bk^2 U_h^{\text{non}}, v)_\Omega - & \\
- \sum_{m=1}^{M} \langle q_h^{\text{non}}, v\rangle_{\partial\Omega^m} &= (f, v)_\Omega, && \forall v \in Y_h^{\text{non}}, \\
U_h^{\text{non}} &= \mathsf{P}^{X_h^{m,\text{non}}}\lambda^{\text{non}}, && \text{on } \mathcal{E}_\text{e}, \\
\langle [\![q_h^{\text{non}}]\!], \mu\rangle_{\varepsilon_h} &= \langle g_N, \mu\rangle_{\Gamma_N}, && \forall \mu \in V_h^{\text{non}}(0).
\end{aligned} \tag{2.43}$$

And equivalently to the conforming case, we can prove (see theorem B.4 in appendix B) that there exists a unique set of functions $(U_h^{\text{non}}, \lambda^{\text{non}}, q_h^{\text{non}})$ in the spaces $Y_h^{\text{non}} \times V_h^{\text{non}}(g_D) \times W_h^{\text{non}}$ satisfying the primal formulation 2.14 and also that $U_h^{\text{non}} = u_h^{\text{non}}$ on Ω, $\lambda^{\text{non}} = u_h^{\text{non}}$ on $\mathcal{E}_\text{e}$, where $u_h \in X_h(g_D)$ is the solution to the CG problem 2.9.

We now eliminate the unknowns U_h^{non} and q_h^{non} to obtain a weak formulation only for λ^{non}. To this end, we introduce two local subproblems for each $\Omega^m \in \mathcal{T}_\Omega$. The first local subproblem maps the function $f \in L^2(\Omega)$ to $U_f^{\text{non}}|_{\Omega^m} \in X_h^{m,\text{non}}(0)$ defined

by

$$\left(a\nabla U_f^{\text{non}}, \nabla v\right)_{\Omega^m} + \left(bk^2 U_f^{\text{non}}, v\right)_{\Omega^m} = (f, v)_{\Omega^m}, \quad \forall v \in X_h^{m,\text{non}}(0). \tag{2.44}$$

The second local subproblem maps $\eta \in V_h^{\text{non}}$ to $U_\eta^{\text{non}}|_{\Omega^m} \in X_h^{m,\text{non}}(\eta)$ that satisfies

$$\left(a\nabla U_\eta^{\text{non}}, \nabla v\right)_{\Omega^m} + \left(bk^2 U_\eta^{\text{non}}, v\right)_{\Omega^m} = 0, \quad \forall v \in X_h^{m,\text{non}}(0). \tag{2.45}$$

Note once more that the two subproblems have the same bilinear form and only the right hand sides are different. Analogously to the conforming case, a Lagrange multiplier λ^{non} can be introduced as the solution of a variational formulation. All in all, it can be proved (see theorem B.5) that if $(U_h^{\text{non}}, \lambda^{\text{non}}, q_h^{\text{non}})$ is the solution of the primal formulation 2.14, then $U_h^{\text{non}} = U_{\lambda^{\text{non}}}^{\text{non}} + U_f^{\text{non}}$. Moreover, the Lagrange multiplier $\lambda^{\text{non}} \in V_h^{\text{non}}(g_D)$ is the unique solution of:

$$(a\nabla U_{\lambda^{\text{non}}}^{\text{non}}, \nabla U_\mu^{\text{non}})_\Omega + \left(bk^2 U_{\lambda^{\text{non}}}^{\text{non}}, U_\mu^{\text{non}}\right)_\Omega, = (f, U_\mu^{\text{non}})_\Omega + \langle g_N, \mu\rangle_{\Gamma_N}, \quad \forall \mu \in V_h^{\text{non}}(0) \tag{2.46}$$

Once more, thanks to this trace characterization, the implementation of the non-conforming MSCG method can be carried out efficiently. Indeed, it follows the same steps as the implementation of the conforming MSCG method, which has already been described in detail previously. The non-conforming MSCG can reduce the density and size of the discrete global matrix since it allows for a flexible tuning of the subelement meshes as well as the polynomial order used in the traced space. Furthermore, it allows for an absolute geometric flexibility across subelements. For these reasons, all the subsequent simulation examples will consider this approach.

2.5 Numerical results

In this section we present some physical applications where the proposed multiscale CG methodology is particularly helpful and suitable. The objective is to show a set of problems in the context of wave propagation that can be efficiently and accurately solved with the MSCG method. We focus on the simulation of electromagnetic waves in 2d and acoustic waves in 3d, which are all modeled by Helmholtz's equations and suitable choices of the design parameters $a(\mathbf{x})$ and $b(\mathbf{x})$ in 2.1.

2.5.1 Superlenses

Classical optical lenses use wave diffraction at a convex lens to focus a given image. However, this approach has important limitations discovered by Ernst Abbe back in 1873. Since evanescent subwavelength waves decay exponentially in a medium with positive permittivity and permeability (like a lens), all the information that the image contains at a subwavelength scale is lost, hence arbitrary sharpness of an image cannot be obtained.

Because of this limitation, there is little room for improvement in classical lenses. Nevertheless, Photonic Crystals (PC) and/or metamaterials open new possibilities. J.B. Pendry introduced in [121] the concept of superlens: a slab that could provide negative refraction index and thus preserve the evanescent subwavelength information.

The practical design of superlenses rose a lot of research interest and a first PC solution that doesn't involve negative index materials but that already saves some of the evanescent information for very thin ranges of frequencies was theoretically introduced in [90] and later matched with experiments in [47]. Similarly, Fang *et al.* designed a silver superlens that could capture subwavelength information in [56].

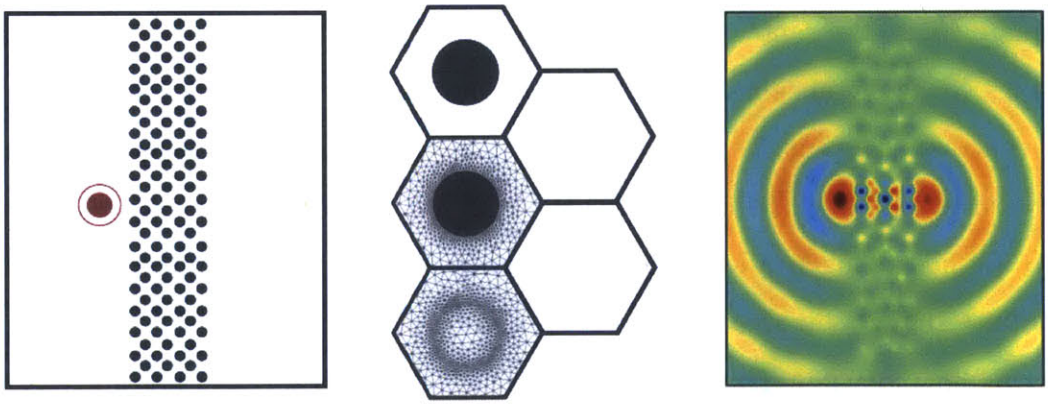

Figure 2.4: Geometry setting, MSCG discretization and numerical simulation of the TM superlens in [90]. Frequency $\omega_0 a/2\pi c = 0.2$, $\varepsilon = 12$ and radius $0.45a$.

In order to numerically simulate a Photonic Crystal superlens using MSCG we consider a subdomain decomposition into hexagons. Seven layers of these hexagons form the lens in the central vertical axis. Each hexagon has a rod centered in the

subdomain. Furthermore, a point source is introduced at the left side of the superlens. According to [90], this structure will create a superlens for TM modes (choose, $a(\mathbf{x}) = \varepsilon$, $b(\mathbf{x}) = 1$) around the frequency $\omega_0 a/2\pi c = 0.20$, when rods of permittivity $\varepsilon = 12$ and radius $r = 0.45a$ are considered. The host material is chosen to be air ($\varepsilon = 1$). Note that a is the period of the hexagonally symmetric PC structure. Figure 2.4 shows the computational domain, the subdomain decomposition and discretization around the rods as well as the solution field for ω_0.

2.5.2 2d Photonic Crystal waveguides with square symmetry

Photonic Crystals can be used for many applications. Here, we focus on PC waveguides, which can be used for telecommunications and optical wave control. The MSCG methodology introduced in this chapter works particularly well for structures with a finite repetition of small patterns and will thus be suitable for the numerical simulation of PC waveguides. The physical phenomenon that gives rise to PC waveguides is the Photonic Bandgap. Certain periodic structures prevent propagation of given ranges of frequencies in any direction, see for instance [74,96] for detailed descriptions. In particular, when a collection of rods is distributed respecting the symmetries of the square (place the center of the rods at every corner of a square grid) these gaps of frequencies where transmission is prohibited are opened. Depending on the permittivity contrast and thus the material of the rods as well as their radius, these ranges are placed at different frequencies and have different widths. The extension of the MSCG method to eigenvalue problems is carried out in chapter 4 and a methodology to compute these band structures will be thereby provided.

Let us now focus on Transverse Magnetic (TM) modes for 2d Photonic Crystals. In this case, if we consider rods made out of silicon ($\varepsilon = 11.8$) and with a radius $r = 0.2a$, being a the periodicity, the lowest bandgap shows up for frequencies $\omega a/2\pi c \in (0.27, 0.41)$ and the second gap for $\omega a/2\pi c \in (0.70, 0.73)$. As a consequence, if we define a material that is composed of this structure but one line of rods is removed, a waveguide is created. Energy propagation is not permitted in any direction within the PC structure and thus the wave only travels through the waveguide. Figure 2.5

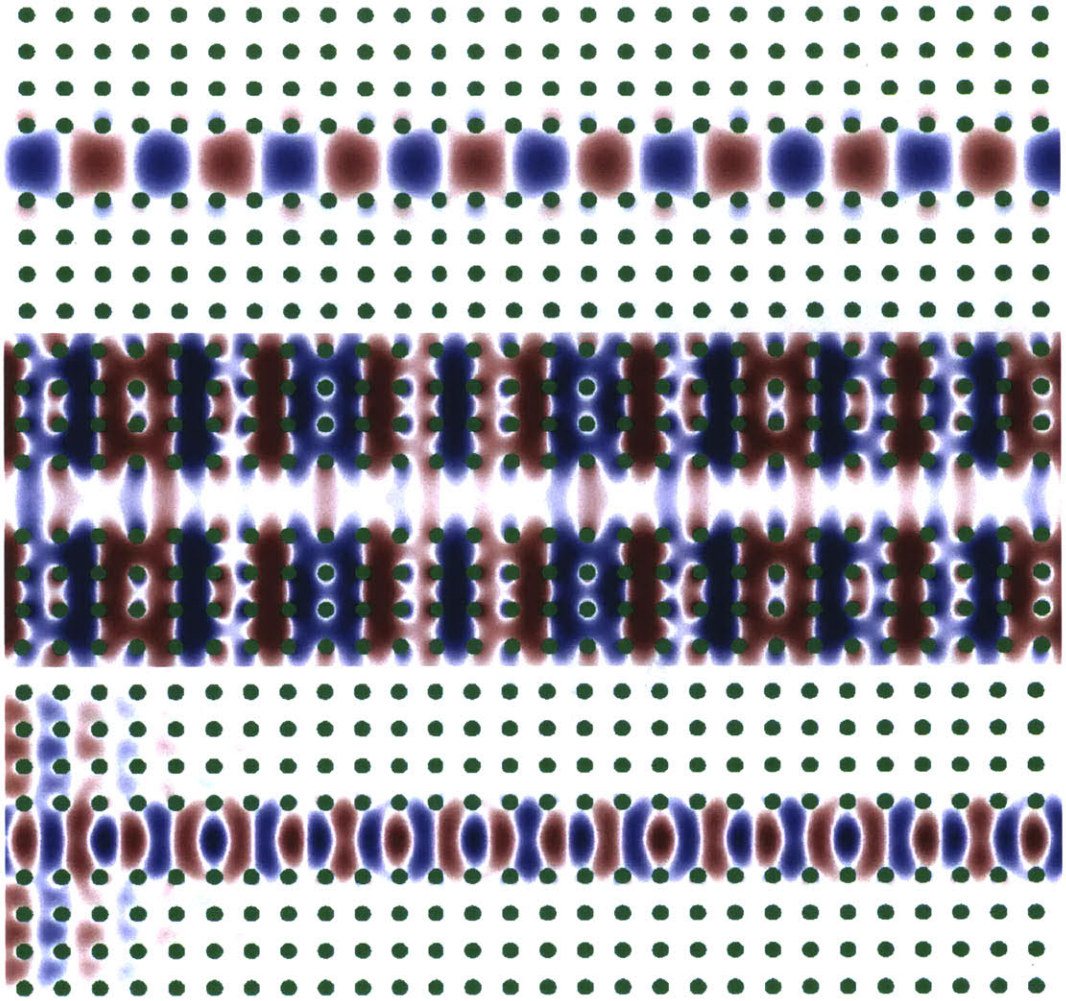

Figure 2.5: TM wave propagation field for a 2d PC with a planar incoming wave from the left side for $\omega a/2\pi c = 0.30$ (top), $\omega a/2\pi c = 0.47$ (center), $\omega a/2\pi c = 0.71$ (bottom). Silicon rods ($\varepsilon = 11.8$) with radius $r = 0.2a$.

shows the propagation patterns of the described PC waveguide for a frequency inside the first gap, one between the two lowest bandgaps, and another one in the second propagation prohibited range.

Similarly, Photonic Crystals can also be used to build optical nanocavities that trap light in very small volumes for a long period of time and for very narrow frequency ranges. These cavities can also be used as frequency filters when combined with a PC waveguide as the one just presented. If the resonance frequency of the cavity is inside one bandgap of the surrounding PC, the cavity will let it go through; however, if we slightly modify the frequency, although still in the bandgap, the cavity will mostly

reflect it back and the transmission will decrease significantly. These narrow band filters can be very useful for optical communication [79], biosensing [157] and laser design [2], among others.

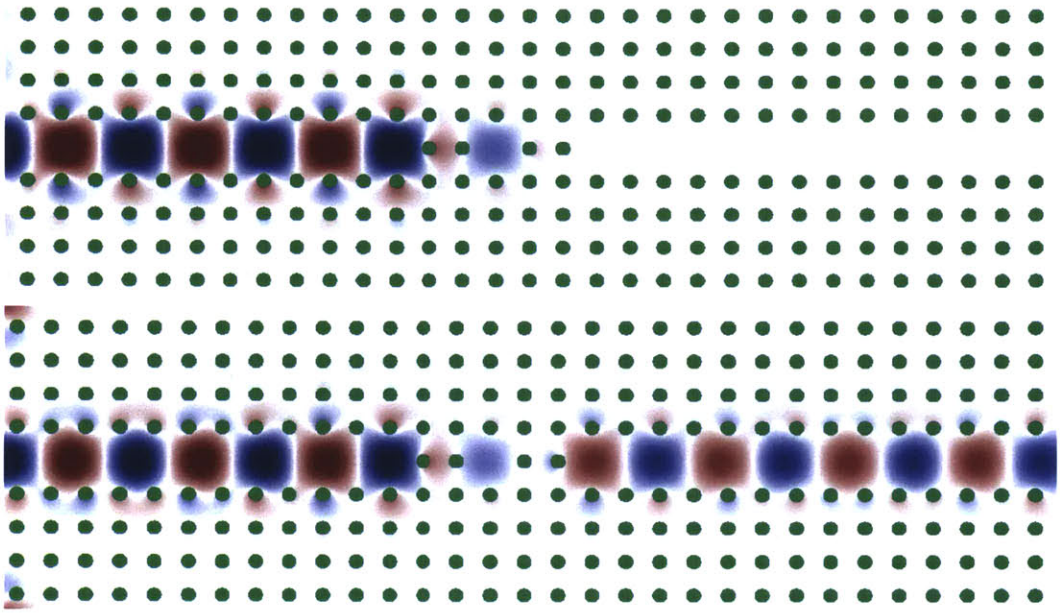

Figure 2.6: Waveguide-cavity-waveguide narrow filter for the TM wave field for. Planar wave incoming from the left side of the boundary. Frequencies are $\omega a/2\pi c = 0.375$ (top) and $\omega a/2\pi c = 0.381$ (bottom). Silicon rods ($\varepsilon = 11.8$) with radius $r = 0.2a$.

For the same PC structure that produces the waveguide previously analyzed, a nanocavity can be created by just removing one single rod and the corresponding resonance frequency is $\omega a/2\pi c = 0.38$. So, if a waveguide-cavity-waveguide structure is created, we can have very close frequencies providing different responses. Figure 2.6 shows the propagation patterns for frequencies $\omega a/2\pi c = 0.375$, which essentially filters out all propagation within the waveguide, and $\omega a/2\pi c = 0.381$, which mostly preserves the propagation pattern of the original waveguide. Further details on this specific waveguide-cavity-waveguide structure can be found in [74].

The main goal of waveguides is to transport electromagnetic energy for long distances. However, the paths that waveguides take are seldom straight and often have to face bends, sometimes sharp. A desired feature of a waveguide is that it does not have high losses when it suffers a bend. In particular, for the PC waveguide that we have been analyzing so far, a 90 degrees bend can be created in a natural way given

the square symmetry of the pattern. The effectiveness of this natural bend will be assessed in section 6.2 as well as the design of optimal bends.

The bottom center of figure 2.7 shows the propagation pattern for a frequency of $\omega a/2\pi c = 0.34$ obtained numerically using MSCG. Let us describe the simulation procedure for this example and the preceding PC waveguide cases can be derived similarly.

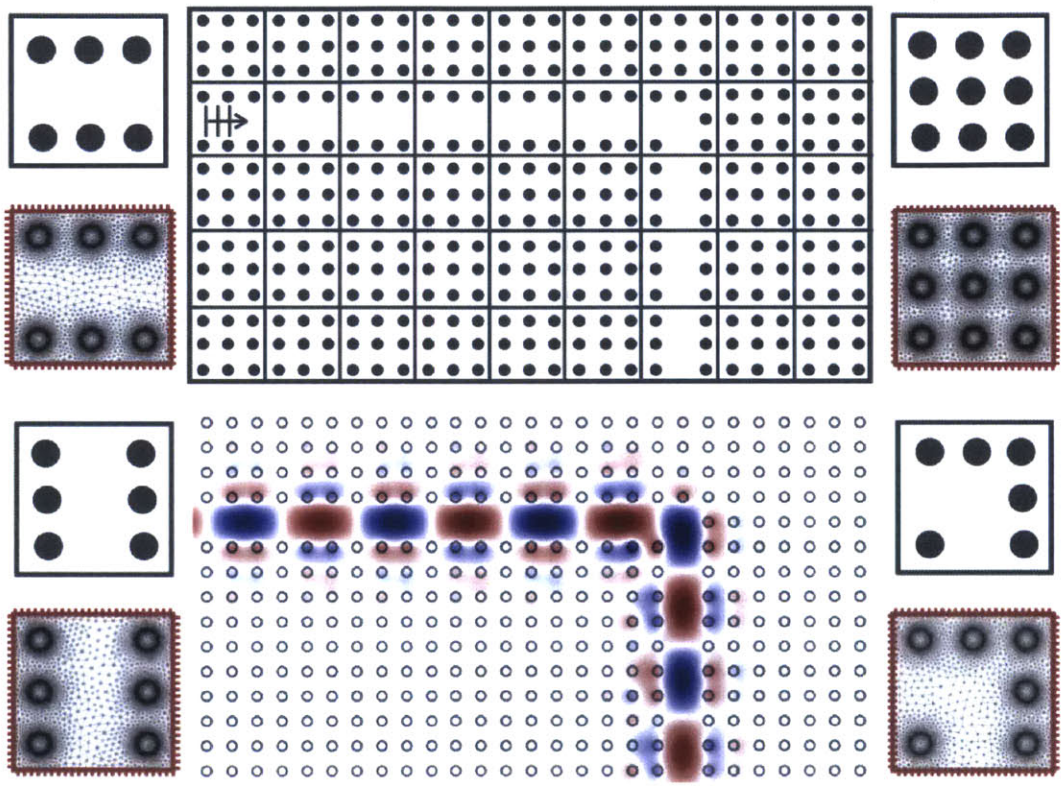

Figure 2.7: MSCG simulation of a TM 90 degrees waveguide bend on a square latticed PC. Computational domain with subdomain decomposition (top), numerical solution (bottom) and different subdomains with their discretization (sides). PML regions are not shown. Frequency $\omega a/2\pi c = 0.34$. Silicon rods ($\varepsilon = 11.8$) with radius $r = 0.2a$.

First of all, the MSCG method requires the definition of the computational domain as well as a clever choice of the subdomain decomposition. We want the subdomains to be invariant with respect to translation and rotation, so that we can reduce the number of subproblems to be solved. Furthermore, the size of the subdomains should not be too small, because that would increase the size of the global problem; but it should not be too big either, because that would make the local problem very large.

The size of the subdomains together with the frequency of interest determine the polynomial approximation order chosen at the *macro* discretization. Similarly, the geometric detail and the frequency of interest will define the size of the *micro* mesh as well as the local approximation order. Note that the levels of discretization and the local polynomial orders may differ from one subelement to another. Moreover, Perfectly Matched Layers (PML) need to be included in the computational domain to avoid reflections.

In particular, for the waveguide bend that is shown in figure 2.7 we have chosen a subdomain discretization that contains sets of 3×3 rods. In this way, there are only four different subdomain types (plus those for the PML) as shown on both sides of the figure with their corresponding local discretizations. In this case, we want every subdomain to be able to accurately solve problems where they contain up to two wavelengths so we use polynomial order of 20. The local polynomial order is 2 and the local meshes are quite fine because they approximate the geometry linearly.

Note that in terms of computational cost, the most limiting part of the algorithm is the resolution of the global system hence the local problem should never be jeopardizing the overall accuracy. This typically implies that the local problem is designed to resolve higher frequencies than the global.

Table 2.6 summarizes the degrees of freedom of the different discretizations for the numerical simulation of the waveguide bend shown in figure 2.7. Note that if this problem was solved using a classic CG approach, the total system of equations would have around $500K$ degrees of freedom.

Table 2.6: Degrees of freedom count for 2d PC waveguide bend

problem	elements	order	$\#DOF$
subdomain #1	7,817	2	$20K$
subdomain #2	5,396	2	$15K$
subdomain #3	5,375	2	$15K$
subdomain #4	5,375	2	$15K$
homogeneous	800	2	$2K$
Global MSCG	96	20	$5K$

2.5.3 2d Photonic Crystal waveguides with hexagonal symmetry

Triangular PC lattices can be designed using the symmetries of a hexagon. The practical implementation of the MSCG method for these lattices is slightly different and the main point of these lines is to describe the procedure. Note that the symmetries of the hexagon lead to a positioning of the rods at the vertices of a grid built of equilateral triangles.

We now focus on a particular example and compute the wave propagation pattern using MSCG. Let us choose the rods to be made of silicon ($\varepsilon = 11.8$) and with radius $r = 0.2a$, being a the periodicity of the Photonic Crystal. For this specific structure, the band diagram is computed in chapter 4 and shown in figure 4.6. A bandgap is opened for frequencies within the range $\omega a/2\pi c \in (0.29, 0.44)$, hence no propagation in any direction will be allowed within the crystal for these frequencies. However, if a linear defect is opened by removing one row of rods, the energy will only travel throughout it. In fact, a waveguide can be split in two channels and later reunified in a very natural way through Y shaped bends as shown in figure 2.8.

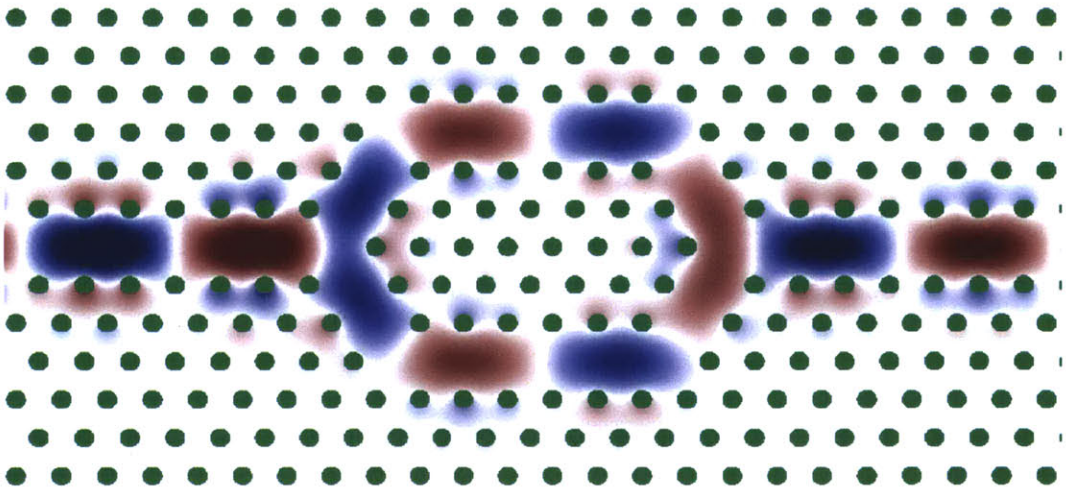

Figure 2.8: TM wave propagation pattern for $\omega a/2\pi c = 0.36$ through a double Y shaped hexagonal lattice waveguide. Silicon rods ($\varepsilon = 11.8$) with radius $r = 0.2a$. PML is not shown.

In order to maximize the benefit of using the MSCG method for this particular application we want to choose the subdomain decomposition cleverly. We need to

decide what shapes are given to different subdomains in order to be able to identify repeated patterns. Given the hexagonal symmetry, one could choose an equilateral triangle as a unit cell, as well as a hexagon or a rhombus.

After we have the whole computational domain decomposed into rhombi we still need to decide how many rods we include in each rhombus. Similarly to the square lattice case, a balance needs to be found between too small subdomains or too big ones. Once more, a 3×3 array of rods in each subdomain seems to provide a good equilibrium between the density of the global problem and its size. Figure 2.9 shows a schematic description of the geometry and the discretization. It shows the discretization of each subdomain, how it fits the geometry and some of the rods removed to form the first Y bend.

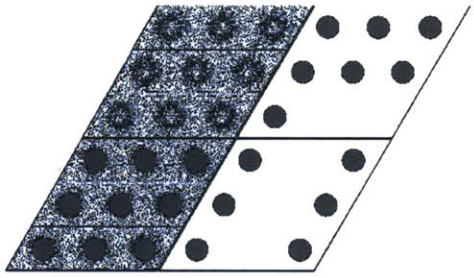

Figure 2.9: Schematic description of the geometry and its MSCG discretization.

Table 2.7: Degrees of freedom count for 2d PC Y waveguide bend

problem	elements	order	$\#DOF$
subdomains with rods	$8,121$	2	$23K$
homogeneous subdomains	800	2	$2K$
Global MSCG	105	20	$6K$

Equivalently to the case of the square lattice, the use of MSCG drastically reduces the total computational cost of the problem due to the reuse of information and condensation of it into the subelement skeleton level. For this specific problem and discretization, the count of degrees of freedom of the different problems are summarized in table 2.7. Note that if we were to solve this problem using classic CG, the size of the global system of equations to solve would be $740K \times 740K$. Figure 2.10 shows the solution pattern for $\omega a/2\pi c = 0.41$, including the solution in the PML.

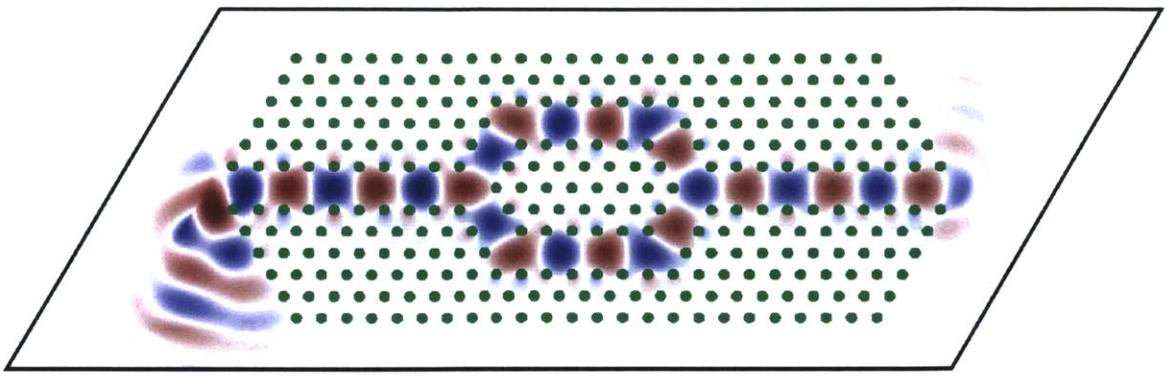

Figure 2.10: TM wave propagation pattern for $\omega a/2\pi c = 0.41$ through a double Y shaped hexagonal lattice waveguide. Silicon rods ($\varepsilon = 11.8$) with radius $r = 0.2a$.

Equivalently, TE polarized modes can be simulated with the MSCG method in order to obtain the H field. For this case, the material parameters are specified as $a(\mathbf{x}) = 1/\varepsilon$ and $b(\mathbf{x}) = 1$, where ε is the permittivity of each piece of material. Structures that provide broad bandgaps for the H field under a TE polarization are, for instance, hexagonally periodically air holes drilled on a higher index material, as discussed in the following analysis.

The state-of-the-art numerical methodology for electromagnetic waves simulation on Photonic Crystals is a Finite Difference Time Domain (FDTD) software [117]. In order to validate the results given by the MSCG method we will compare the results from both methodologies.

In particular, let us consider a 2d PC with a host material of $\varepsilon = 11.8$ and air holes of radii $r = 0.3a$ drilled respecting a triangular symmetry of period a. For this geometry, a TE bandgap shows up for frequencies $\omega a/2\pi c \in (0.20, 0.28)$. In addition, we consider a waveguide obtained by line defects that shape a Y bend/splitter. Figure 2.11 shows the H_z transmission fields for two different frequencies in the gap. If we now compute the transmission fractions for each frequency using both methodologies, we observe a match up to the accuracy considered in each case as shown in figure 2.12.

More specifically, the top subfigures in 2.11 show the H_z field obtained using the FDTD method whereas the bottom ones present their corresponding MSCG simulation. The FDTD simulation is time dependent and therefore the results shown are

obtained after several periods, once we do not observe any change from period to period. The solution obtained with the MSCG method is frequency domain and thus provides the final solution (up to $e^{i\omega t}$) directly.

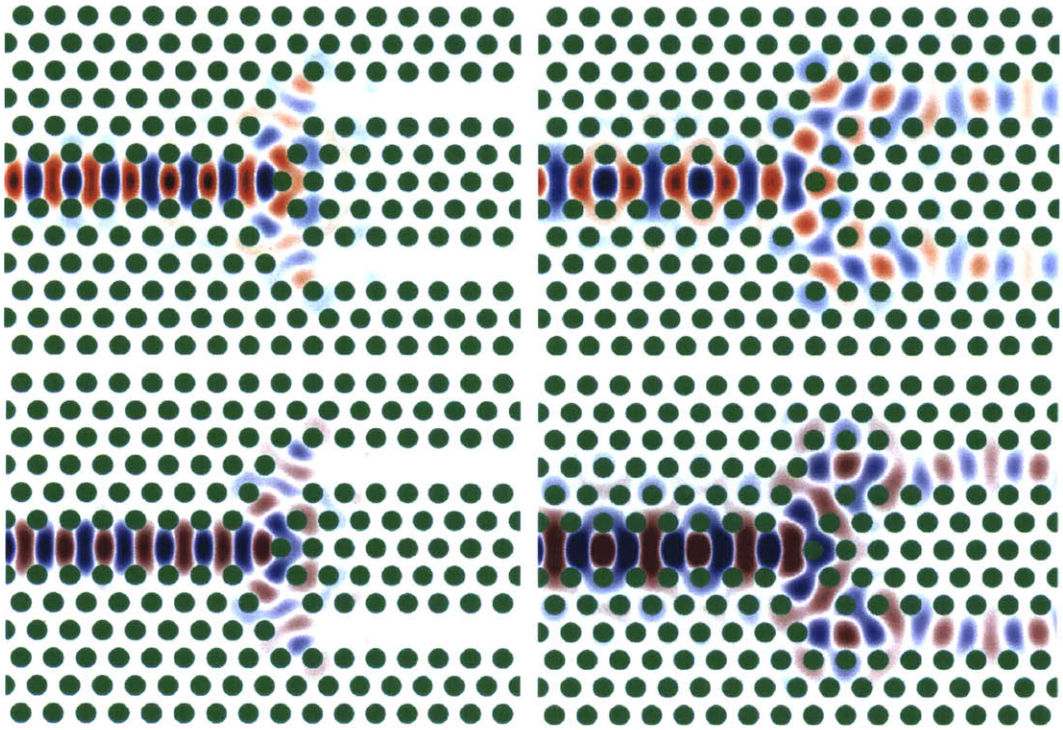

Figure 2.11: H_z propagation fields obtained using FDTD (top) and MSCG (bottom). Y bend on a $\varepsilon = 11.8$ slab with air holes of radii $r = 0.3a$ -in green- for frequencies in the bandgap: $\omega a/2\pi c = 0.26$ (left) and $\omega a/2\pi c = 0.225$ (right).

We now show in figure 2.12 the convergence of the transmission fraction value for the geometry given above and frequency $\omega a/2\pi c = 0.225$ (adding the contributions from both channels it adds up to around $T = 0.94$). Particularly, we show how the value of such fraction converges as the discretization is refined from $h = a/5$ to $h = a/20$, where h is the size of the elements and a the period of the structure. The figure shows the convergence curves for the FDTD method (dashed) as well as the MSCG method with different choices of polynomial approximation order at the *macro* discretization level. The results are compared to the solution obtained using the MSCG method for $k = 30$ and also 30 local elements per period and direction.

First of all, we note how the numerical results obtained with both methods are matched, validating the MSCG method. Secondly, we see that if the resolution of the

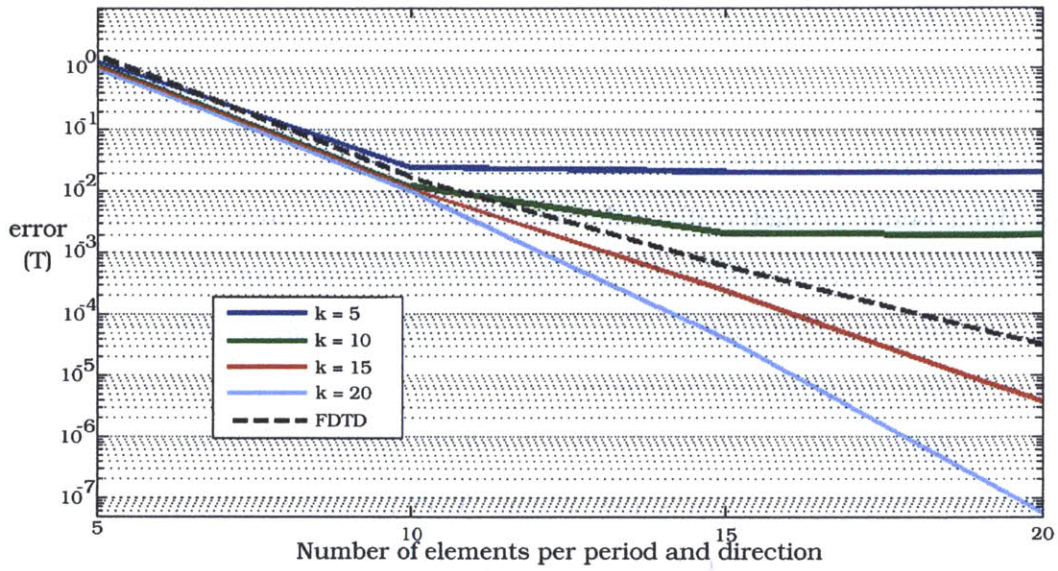

Figure 2.12: Grid convergence of the transmission fraction (error of T vs. a/h) for different *macro* discretization approximation orders of MSCG and FDTD.

global level and the local level are very different, the accuracy is limited by the least resolved mesh. In fact, we see how the accuracy of the solution for $k = 5$ does not improve after $h = a/10$ but it actually makes sense to go slightly beyond $a/h = 5$ since the global variables are of higher order. Equivalently, we see how for local discretizations of $a/h = 5$ or $a/h = 10$ there is almost no difference in the accuracy among the cases $k = 5$ to $k = 20$ because the solution is limited by the local solver. Given that only a few local problems are solved and they are totally parallelizable (the computational cost is limited by the global problem), we see that the best result is typically obtained by picking *macro* discretization order k that is enough for the frequencies of interest and then choosing a finer local grid size h to exploit all the power of k. Finally, figure 2.12 also shows that the MSCG method provides more accurate solutions for the same level of discretization and with a faster convergence rate, given the higher order. Moreover, in terms of wall-clock time, FDTD and MSCG discretizations of the same order take similar times in 2d.

2.5.4 3-dimensional waves

One of the most attractive properties of the multiscale methodology is its high efficiency for solving problems that can be decomposed into subdomains with only a few of them being geometrically different. The notable condensation of degrees of freedom provides this method with the capability of solving very large problems. In particular, some 3d applications become numerically tractable without the need of very advanced computational resources.

In order to show the computational power of the multiscale method, the numerical solution of a very large problem is now sought. More specifically, figure 2.13 shows the wave propagation pattern of a 3d vibration wave in a domain of size $10\lambda \times 10\lambda \times 100\lambda$, being λ the wavelength. The simulation of high frequency waves (or lower frequency in large domains) is computationally challenging because it requires a large number of degrees of freedom given that these scale with the wavelengths per dimension. Particularly, this problem has been divided into $10 \times 10 \times 100$ local subelements, each one of which has $6K$ order 2 local elements that perfectly capture one wavelength. All in all, the total number of degrees of freedom exceeds $200m$ for a CG approach. Nevertheless, we only solve for the condensed global system of equations, which has $\mathcal{N}_{dof}^{mscg} = 1,572,900$, since a polynomial approximation order of 6 has been chosen on the faces. Note that this global system of equations, equivalent to up to $200m$ degrees of freedom, has been solved without the consideration of iterative solvers nor any sort of parallelization technique. Once more, first-order absorbing boundary conditions have been used and the solution is converged to machine precision.

Figure 2.13: Acoustic wave propagation pattern for a 3d homogeneous rectangular prism. The domain size is $10 \times 10 \times 100$ wavelengths.

2.6 Concluding Remarks

In this chapter we have presented the first member of a set of multiscale methods for the simulation of wave propagation problems: the multiscale continuous Galerkin method. The MSCG takes advantage of hybridization beyond the fact that the local problems can be solved in parallel. All subelements are chosen such that there are only a handful of different classes. Then, only one representative of each class is solved, in parallel. Finally, the global system of equations is assembled and solved, but it is much smaller -yet denser- than the original.

All in all, we are able to solve problems, the CG discretization of which would require up to several hundred million degrees of freedom in 3d. This is especially encouraging since a single 8 core machine has been used with a sparse direct solver. In particular, we have used the MSCG method for the forward direct simulation of electromagnetic problems in 2d (since Maxwell's equations for TE/TM modes can be reduced to Helmholtz's equation) as well as acoustic wave problems both in 2d and 3d.

Chapter 3

Multiscale Hybridizable DG method for the time-harmonic Maxwell's equations

Through science we prove, but we discover through intuition

–Henri Poincare

Helmholtz's equation can model in 2d both acoustic and TM/TE modes of electromagnetic waves. Nevertheless, Maxwell's equations modeling EM in 3d can not be reduced to Helmholtz's since the polarizations are coupled. It is therefore desirable to extend the multiscale method introduced in the previous section to Maxwell's equations in 3d.

We consider the time-harmonic Maxwell's equations as:

$$\left.\begin{aligned} \nabla \times \mathbf{H} - (i\omega a(\mathbf{x}) + b(\mathbf{x}))\mathbf{E} &= \mathbf{J}, && \text{in } \Omega \\ \nabla \times \mathbf{E} + i\omega c(\mathbf{x})\mathbf{H} &= 0, && \text{in } \Omega \\ \mathbf{n} \times \mathbf{E} &= g_D, && \text{on } \Gamma_D \\ \mathbf{n} \times \mathbf{H} &= g_N, && \text{on } \Gamma_N \end{aligned}\right\} \tag{3.1}$$

Note that $a(\mathbf{x}), b(\mathbf{x})$ and $c(\mathbf{x})$ are parameters that will be determined by the material at each point of the domain. More specifically, $a = \varepsilon$ is the permittivity of the material, $b = \sigma$ is the conductivity of the medium (considered 0 for simplicity)

and $c = \mu$ corresponds to the permeability, considered to be 1, since most materials of interest show such value. $\mathbf{J}$ is the impressed current density, $\mathbf{E}, \mathbf{H}$ correspond to the frequency domain electric and magnetic fields respectively, and ω corresponds to the frequency. Boundary conditions are considered in the last two equations. These formulations model a wide range of problems of interest within electromagnetics.

Computational electromagnetics in 3d brings up several additional challenges. Firstly, there is a poor scalability of the degrees of freedom since the TE/TM modes are now coupled and we need to simultaneously solve for $\mathbf{E}$ and $\mathbf{H}$. In addition, vector field solutions to Maxwell's equations satisfy a divergence free condition leading to the consideration of $\mathbf{H}^{curl}$ approximation spaces [52]. The finite element implementation of these spaces is challenging for classic CG methods but becomes more natural if a hybridizable discontinuous Galerkin (HDG) discretization is used.

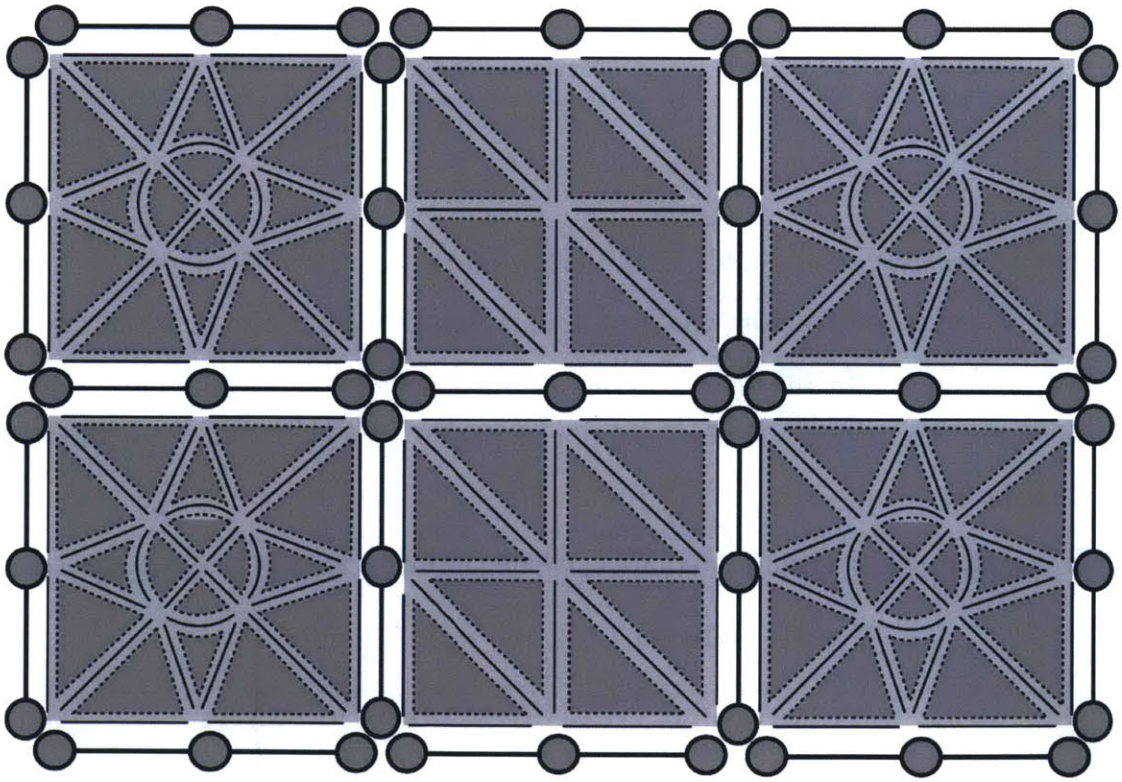

Figure 3.1: An illustration of a MSHDG *macro* discretization with subelements discretized using HDG.

In this chapter we first adapt the HDG methods presented in [114] for 3d problems. Then, we extend the multiscale methodology with global discontinuous spaces

using HDG as a solver for the subelement problems, providing a guide for the implementation and a convergence-cost analysis. Finally, simulation results are provided.

3.1 The HDG method for Maxwell's equations

The set of equations 3.1 provide the frequency domain solutions for an electromagnetics problem. Let us first introduce the additional notation required, describe the HDG discretization procedure and define the approximation spaces.

We denote by $\mathcal{T}_h$ a collection of disjoint regular elements K that partition the domain $\Omega \subset \mathbb{R}^d, d \in \{2,3\}$. The set $\partial\mathcal{T}_h := \{\partial K; K \in \mathcal{T}_h\}$ is then a collection of boundaries of the discretization elements. For a given element $K \in \mathcal{T}_h$, $F = \partial K \cap \partial\Omega$ is a boundary face if the d Lebesgue measure of F is zero but the $d-1$ measure is not. For two elements K^+ and K^- of the collection $\mathcal{T}_h$, $F = \partial K^+ \cap \partial K^-$ is the interior face between K^+ and K^- again if the d Lebesgue measure is zero but the $d-1$ is not. If $d = 2$, such faces will be called edges. Equivalently to the notation introduced for the MSCG method, we denote by $\mathcal{E}_h^i$ and by $\mathcal{E}_h^\partial$ the set of interior and boundary edges/faces respectively. And we finally set $\mathcal{E}_h = \mathcal{E}_h^i \cup \mathcal{E}_h^\partial$.

Let now $\mathbf{n}^+$ and $\mathbf{n}^-$ be the outward unit normal vectors on two neighboring elements K^+ and K^-, respectively. We use $\mathbf{v}^\pm$ to denote the trace of $\mathbf{v}$ on F from the interior of $K^\pm$, where $\mathbf{v} \in \mathbf{L}^2(\Omega) \equiv [L^2(\Omega)]^d$. Then, we define the jumps $[\![\cdot]\!]$ as follows: for $F \in \mathcal{E}_h^i$ we set

$$[\![\mathbf{v} \odot \mathbf{n}]\!] = \mathbf{v}^+ \odot \mathbf{n}^+ + \mathbf{v}^- \odot \mathbf{n}^-. \tag{3.2}$$

Here $\odot$ is either $\cdot$ or $\times$, depending on which is required for each equation. For $F \in \mathcal{E}_h^\partial$, the set of boundary edges on which $\mathbf{v}$ is single valued, we set

$$[\![\mathbf{v} \odot \mathbf{n}]\!] = \mathbf{v} \odot \mathbf{n}, \tag{3.3}$$

where $\mathbf{n}$ is the unit outward normal to $\partial\Omega$. We further set

$$\mathbf{v}^t := \mathbf{n} \times (\mathbf{v} \times \mathbf{n}), \qquad \mathbf{v}^n := \mathbf{n}(\mathbf{v} \cdot \mathbf{n}), \tag{3.4}$$

where $\mathbf{v}^t$ and $\mathbf{v}^n$ represent the tangential and normal components of $\mathbf{v}$, respectively.

Note that the total vector field can be obtained as $\mathbf{v} = \mathbf{v}^t + \mathbf{v}^n$.

After the additional notation has been introduced, we are ready to define the particular approximation spaces that will be required for the HDG formulation. Also, since Maxwell's equations in 2d can be decomposed into TE or TM polarized modes and modeled through Helmholtz's equation, we will now focus only on 3d problems. Let D be an open domain in $\mathbb{R}^3$. We introduce the following curl-conforming space:

$$\mathbf{H}^{curl}(D) = \{\mathbf{v} \in \mathbf{L}^2(D) : \nabla \times \mathbf{v} \in [L^2(D)]^3\}. \tag{3.5}$$

Recall that $L^2(D)$ is the space of square integrable functions on D. The $\mathbf{H}^{curl}$-norm associated with this space is then defined as:

$$||\mathbf{v}||_{\mathbf{H}^{curl}(D)} = \left(\int_D |\mathbf{v}|^2 + |\nabla \times \mathbf{v}|^2\right)^{1/2}. \tag{3.6}$$

Let $P_m(D)$ denote the space of complex-valued polynomials of degree at most m on D. We also introduce the following approximation spaces $\mathbf{X}_h$ and $\mathbf{M}_h$ for the solution fields and the traces respectively.

$$\begin{aligned} \mathbf{X}_h = &\ \{\mathbf{v} \in \mathbf{L}^2(\mathcal{T}_h) : \mathbf{v}|_K \in [P_k(K)]^d, \forall K \in \mathcal{T}_h\}, \\ \mathbf{M}_h = &\ \{\boldsymbol{\eta} \in \mathbf{L}^2(\mathcal{E}_h) : \boldsymbol{\eta}|_F \in \mathbf{M}(F), \forall F \in \mathcal{E}_h\}, \end{aligned} \tag{3.7}$$

where the local space is defined as $\mathbf{M}(F) = \{\boldsymbol{\eta} \in [P_k(F)]^d : \boldsymbol{\eta} \cdot \mathbf{n}|_F = \mathbf{0}\}$. In order to naturally include the $\mathbf{H}^{curl}$ nature of the solutions let us define $\mathbf{t}_1$ and $\mathbf{t}_2$ as the tangent vectors on face F. We then have,

$$\mathbf{M}(F) = P_k(F)\mathbf{t}_1 \oplus P_k(F)\mathbf{t}_2 \tag{3.8}$$

and thus $\mathbf{M}(F)$ consists of functions, the normal component of which vanishes on F.

Finally, we define various hermitian products for the previously introduced finite element spaces. Let η, ξ be scalar functions defined on a given volume $D \subset \mathbb{R}^3$ and $(\eta, \xi)_D$ denote the integral of $\eta\xi^*$ over such domain. We then define the volumetric hermitian products. Note that the asterisk represents the complex conjugate.

$$(\eta, \xi)_{\mathcal{T}_h} := \sum_{K \in \mathcal{T}_h} (\eta, \xi)_K \quad \text{and} \quad (\boldsymbol{\eta}, \boldsymbol{\xi})_{\mathcal{T}_h} := \sum_{i=1}^{3} (\eta_i, \xi_i)_{\mathcal{T}_h}. \tag{3.9}$$

Analogously, if $\langle \eta, \xi \rangle_D$ denotes the 2d integral of $\eta \xi^*$ over a domain $D \subset \mathbb{R}^2$, the hermitian products on the faces are defined as:

$$\langle \eta, \xi \rangle_{\partial \mathcal{T}_h} := \sum_{K \in \mathcal{T}_h} \langle \eta, \xi \rangle_{\partial K} \quad \text{and} \quad \langle \boldsymbol{\eta}, \boldsymbol{\xi} \rangle_{\partial \mathcal{T}_h} := \sum_{i=1}^{3} \langle \eta_i, \xi_i \rangle_{\partial \mathcal{T}_h}. \tag{3.10}$$

3.1.1 Formulation

At this stage we can introduce the HDG method formulation for the 3d Maxwell's equations. This method will seek a solution $(\mathbf{E}_h, \mathbf{H}_h, \widehat{\mathbf{E}}_h) \in \mathbf{X}_h \times \mathbf{X}_h \times \mathbf{M}_h$ such that the following discretized system holds for all $(\mathbf{R}, \mathbf{W}, \boldsymbol{\Theta}) \in \mathbf{X}_h \times \mathbf{X}_h \times \mathbf{M}_h$:

$$\begin{aligned} (i\omega c \mathbf{H}_h, \mathbf{R})_{\mathcal{T}_h} + (\mathbf{E}_h, \nabla \times \mathbf{R})_{\mathcal{T}_h} + \left\langle \mathbf{n} \times \widehat{\mathbf{E}}_h, \mathbf{R} \right\rangle_{\partial \mathcal{T}_h} &= 0 \\ (\mathbf{H}_h, \nabla \times \mathbf{W})_{\mathcal{T}_h} + \left\langle \mathbf{n} \times \widehat{\mathbf{H}}_h, \mathbf{W} \right\rangle_{\partial \mathcal{T}_h} + ((i\omega a + b)\mathbf{E}_h, \mathbf{W})_{\mathcal{T}_h} &= (\mathbf{J}, \mathbf{W})_{\mathcal{T}_h} \\ \left\langle \mathbf{n} \times \widehat{\mathbf{H}}_h, \boldsymbol{\Theta} \right\rangle_{\partial \mathcal{T}_h \backslash \Gamma_D} + \left\langle (\widehat{\mathbf{E}}_h - \mathbf{g}_D) \times \mathbf{n}, \boldsymbol{\Theta} \right\rangle_{\Gamma_D} &= 0 \end{aligned} \tag{3.11}$$

The number of degrees of freedom on the faces will determine the computational cost of the global system of equations. In order to reduce them, we consider the traces for the magnetic field as a stabilized combination of the other variables.

$$\widehat{\mathbf{H}}_h = \mathbf{H}_h + \tau(\mathbf{E}_h - \widehat{\mathbf{E}}_h) \times \mathbf{n} \tag{3.12}$$

Note that $\widehat{\mathbf{E}}_h$ is an approximation to the tangential electric field $\mathbf{E}_h^t = \mathbf{n} \times \mathbf{E}_h \times \mathbf{n}$ that is single-valued across inter-element boundaries and satisfies the boundary conditions imposed through the last equation. If we now substitute 3.12 into 3.11, we obtain the final HDG discretization for Maxwell's equations:

$$\begin{aligned} (i\omega c \mathbf{H}_h, \mathbf{R})_{\mathcal{T}_h} + (\mathbf{E}_h, \nabla \times \mathbf{R})_{\mathcal{T}_h} + \left\langle \mathbf{n} \times \widehat{\mathbf{E}}_h, \mathbf{R} \right\rangle_{\partial \mathcal{T}_h} &= 0 \\ (\nabla \times \mathbf{H}_h, \mathbf{W})_{\mathcal{T}_h} + \left\langle \tau(\mathbf{n} \times \mathbf{E}_h \times \mathbf{n} - \widehat{\mathbf{E}}_h), \mathbf{W} \right\rangle_{\partial \mathcal{T}_h} + ((i\omega a + b)\mathbf{E}_h, \mathbf{W})_{\mathcal{T}_h} &= (\mathbf{J}, \mathbf{W})_{\mathcal{T}_h} \\ \left\langle \mathbf{n} \times \mathbf{H}_h + \tau(\mathbf{n} \times \mathbf{E}_h \times \mathbf{n} - \widehat{\mathbf{E}}_h), \boldsymbol{\Theta} \right\rangle_{\partial \mathcal{T}_h \backslash \Gamma_D} + \left\langle (\widehat{\mathbf{E}}_h - \mathbf{g}_D) \times \mathbf{n}, \boldsymbol{\Theta} \right\rangle_{\Gamma_D} &= \langle \mathbf{g}_N, \boldsymbol{\Theta} \rangle_{\Gamma_N} \end{aligned} \tag{3.13}$$

Note how the first two equations correspond to the weak formulation of the governing equations 3.1. The third one enforces continuity of the tangential component of $\mathbf{H}_h$ across the inter-element faces and also imposes the boundary conditions weakly.

3.1.2 Implementation

Let us now describe the implementation steps of this method. First, we write system 3.13 in terms of bilinear and linear forms. The HDG for Maxwell's equation finds $(\mathbf{E}_h, \mathbf{H}_h, \widehat{\mathbf{E}}_h) \in \mathbf{X}_h \times \mathbf{X}_h \times \mathbf{M}_h$ such that:

$$\begin{aligned} i\omega c\mathcal{A}(\mathbf{H}_h, \mathbf{R}) &+ \mathcal{B}(\mathbf{E}_h, \mathbf{R}) &+ \mathcal{C}(\widehat{\mathbf{E}}_h, \mathbf{R}) &= \mathcal{F}_1(\mathbf{R}) \\ \mathcal{B}(\mathbf{H}_h, \mathbf{W}) &+ [\mathcal{D}\mathcal{A}](\mathbf{E}_h, \mathbf{W}) &- \tau\mathcal{F}(\widehat{\mathbf{E}}_h, \mathbf{W}) &= \mathcal{F}_2(\mathbf{W}) \\ -\mathcal{C}(\mathbf{H}_h, \boldsymbol{\Theta}) &+ \tau\mathcal{H}(\mathbf{E}_h, \boldsymbol{\Theta}) &+ (1-\tau)\mathcal{I}(\widehat{\mathbf{E}}_h, \boldsymbol{\Theta}) &= \mathcal{F}_3(\boldsymbol{\Theta}) \end{aligned} \tag{3.14}$$

for all $(\mathbf{R}, \mathbf{W}, \boldsymbol{\Theta}) \in \mathbf{X}_h \times \mathbf{X}_h \times \mathbf{M}_h$. Note that $[\mathcal{D}\mathcal{A}](\cdot) := [\tau\mathcal{D} + (i\omega a + b)\mathcal{A}](\cdot)$. The bilinear forms $\mathcal{A} - \mathcal{I}$ as well as the linear forms $\mathcal{F}_j$ for $j = \{1, 2, 3\}$ are defined, for $(\mathbf{E}, \mathbf{H}, \boldsymbol{\Upsilon}) \in \mathbf{X}_h \times \mathbf{X}_h \times \mathbf{M}_h$ as follows:

$$\begin{aligned} &\mathcal{A}(\mathbf{H}, \mathbf{R}) = (\mathbf{H}, \mathbf{R})_{\mathcal{T}_h} && \mathcal{B}(\mathbf{E}, \mathbf{R}) = (\mathbf{E}, \nabla \times \mathbf{R})_{\mathcal{T}_h} \\ &\mathcal{C}(\boldsymbol{\Upsilon}, \mathbf{R}) = \langle \mathbf{n} \times \boldsymbol{\Upsilon}, \mathbf{R} \rangle_{\partial\mathcal{T}_h} && \mathcal{D}(\mathbf{E}, \mathbf{W}) = \langle (\mathbf{n} \times \mathbf{E} \times \mathbf{n}), \mathbf{W} \rangle_{\partial\mathcal{T}_h} \\ &\mathcal{F}(\boldsymbol{\Upsilon}, \mathbf{W}) = \langle \boldsymbol{\Upsilon}, \mathbf{W} \rangle_{\partial\mathcal{T}_h} && \mathcal{H}(\mathbf{E}, \boldsymbol{\Theta}) = \langle (\mathbf{n} \times \mathbf{E} \times \mathbf{n}, \boldsymbol{\Theta} \rangle_{\partial\mathcal{T}_h \setminus \partial\Omega} \\ &\mathcal{I}(\boldsymbol{\Upsilon}, \boldsymbol{\Theta}) = \langle \boldsymbol{\Upsilon} \times \mathbf{n}, \boldsymbol{\Theta} \rangle_{\partial\mathcal{T}_h} && \mathcal{F}_1(\mathbf{R}) = \mathbf{0} \\ &\mathcal{F}_2(\mathbf{W}) = (\mathbf{J}, \mathbf{W})_{\mathcal{T}_h} && \mathcal{F}_3(\boldsymbol{\Theta}) = \langle -\mathbf{g}_D \times \mathbf{n}, \boldsymbol{\Theta} \rangle_{\Gamma_D} + \langle \mathbf{g}_N, \boldsymbol{\Theta} \rangle_{\Gamma_N} \end{aligned} \tag{3.15}$$

For the implementation of the HDG method we need to discretize the formulation just introduced. To that end, let us first define $\varphi_n, 1 \leq n \leq N$ to be the basis functions of $P_k(K)$. Similarly, let $\phi_m, 1 \leq m \leq M$ be the basis functions of $\{P_k(F), \forall F \in \partial K\}$. The following matrices $\mathbb{A}^k$ to $\mathbb{I}^k$ represent the discretization of the corresponding bilinear forms.

$$\mathbb{A}^k = \begin{bmatrix} \mathbb{M}^k & 0 & 0 \\ 0 & \mathbb{M}^k & 0 \\ 0 & 0 & \mathbb{M}^k \end{bmatrix} \quad \mathbb{B}^k = \begin{bmatrix} 0 & \mathbb{B}^k_{12} & -\mathbb{B}^k_{13} \\ -\mathbb{B}^k_{12} & 0 & \mathbb{B}^k_{23} \\ \mathbb{B}^k_{13} & -\mathbb{B}^k_{23} & 0 \end{bmatrix}$$

$$\mathbb{C}^k = \begin{bmatrix} \mathbb{C}^k_{11} & \mathbb{C}^k_{12} \\ \mathbb{C}^k_{21} & \mathbb{C}^k_{22} \\ \mathbb{C}^k_{31} & \mathbb{C}^k_{32} \end{bmatrix} \quad \mathbb{D}^k = \begin{bmatrix} \mathbb{D}^k_{11} & -\mathbb{D}^k_{12} & -\mathbb{D}^k_{13} \\ -\mathbb{D}^k_{12} & \mathbb{D}^k_{22} & -\mathbb{D}^k_{23} \\ -\mathbb{D}^k_{13} & -\mathbb{D}^k_{23} & \mathbb{D}^k_{33} \end{bmatrix} \tag{3.16}$$

$$\mathbb{F}^k = \begin{bmatrix} \mathbb{F}^k_{11} & \mathbb{F}^k_{12} \\ \mathbb{F}^k_{21} & \mathbb{F}^k_{22} \\ \mathbb{F}^k_{31} & \mathbb{F}^k_{32} \end{bmatrix} \quad \mathbb{H}^k = \begin{bmatrix} \mathbb{H}^k_{11} & \mathbb{H}^k_{12} & \mathbb{H}^k_{13} \\ \mathbb{H}^k_{21} & \mathbb{H}^k_{22} & \mathbb{H}^k_{32} \end{bmatrix} \quad \mathbb{I}^k = \begin{bmatrix} \mathbb{I}^k_{11} & \mathbb{I}^k_{12} \\ \mathbb{I}^k_{21} & \mathbb{I}^k_{22} \end{bmatrix} \tag{3.17}$$

where the different blocks of each elemental matrix can be obtained according to the following rules. Firstly, for $1 \leq i, j \leq N$, $1 \leq r, s \leq M$ and $1 \leq l \leq 3$, we obtain the mass matrices as $\mathbb{M}^k_{ij} = (\varphi_i, \varphi_j)_K$; the different components of convection curl-like matrices as $\mathbb{B}^k_{12,ij} = (\partial_{x_3}\varphi_i, \varphi_j)_K$, $\mathbb{B}^k_{13,ij} = (\partial_{x_2}\varphi_i, \varphi_j)_K$ and $\mathbb{B}^k_{23,ij} = (\partial_{x_1}\varphi_i, \varphi_j)_K$; and the matrices for the traces corresponding to the first equation as $\mathbb{C}^k_{l1,ir} = \langle(\mathbf{n} \times \mathbf{t}_1)_l\varphi_i, \phi_r\rangle_{\partial K}$ and $\mathbb{C}^k_{l2,ir} = \langle(\mathbf{n}\times\mathbf{t}_2)_l\varphi_i, \phi_r\rangle_{\partial K}$. The tangent vectors are defined in terms of the normal vector $\mathbf{n} = (n_1, n_2, n_3)$ such that the if n_1 is the largest component, then $\mathbf{t}_1 = (-n_2/n_1, 1, 0)$ and $\mathbf{t}_2 = (-n_3/n_1, 0, 1)$. If n_2 or n_3 are the largest components the tangent vectors are obtained analogously.

Similarly, we obtain the submatrices for $\mathbb{D}$ as $\mathbb{D}^k_{11,ij} = ((n_2^2 + n_3^2)\varphi_i, \varphi_j)_K$, $\mathbb{D}^k_{22,ij} = ((n_1^2 + n_3^2)\varphi_i, \varphi_j)_K$, $\mathbb{D}^k_{33,ij} = ((n_1^2 + n_2^2)\varphi_i, \varphi_j)_K$, and $\mathbb{D}^k_{ab,ij} = ((n_a n_b)\varphi_i, \varphi_j)_K$ for $ab \in \{12, 13, 23\}$. Then, $\mathbb{F}^k_{l1,ir} = \langle(\mathbf{t}_1)_l\varphi_i, \phi_r\rangle_{\partial K}$ and $\mathbb{F}^k_{l2,ir} = \langle(\mathbf{t}_2)_l\varphi_i, \phi_r\rangle_{\partial K}$. Also, for the $\mathbb{H}$ components, $\mathbb{H}^k_{ab,ir} = \langle\alpha_{ab}\varphi_i, \phi_r\rangle_{\partial K}$, where the values of α_{ab} are:

$$\begin{aligned} \alpha_{11} &= (n_2^2 + n_3^2)t_{11} - n_1n_2t_{12} - n_1n_3t_{13}, \quad \alpha_{12} = (n_1^2 + n_3^2)t_{12} - n_1n_2t_{11} - n_2n_3t_{13} \\ \alpha_{13} &= (n_1^2 + n_2^2)t_{13} - n_1n_3t_{11} - n_2n_3t_{12}, \quad \alpha_{21} = (n_2^2 + n_3^2)t_{21} - n_1n_2t_{22} - n_1n_3t_{23} \\ \alpha_{22} &= (n_1^2 + n_3^2)t_{22} - n_1n_2t_{21} - n_2n_3t_{23}, \quad \alpha_{23} = (n_1^2 + n_2^2)t_{23} - n_1n_3t_{21} - n_2n_3t_{22} \end{aligned} \tag{3.18}$$

Finally, the submatrices for $\mathbb{I}$ can be obtained as $\mathbb{I}^k_{ab,rs} = \langle\beta_{ab}\phi_r, \phi_s\rangle_{\partial K}$, where β_{ab} are given by:

$$\begin{aligned} \beta_{11} &= (t_{11}t_{11} + t_{12}t_{12} + t_{13}t_{13}), \quad \beta_{12} = (t_{11}t_{21} + t_{12}t_{22} + t_{13}t_{23}) \\ \beta_{21} &= (t_{11}t_{21} + t_{12}t_{22} + t_{13}t_{23}), \quad \beta_{22} = (t_{21}t_{21} + t_{22}t_{22} + t_{23}t_{23}) \end{aligned} \tag{3.19}$$

As for the linear forms $\mathcal{F}_i, i = 1, 2, 3$, their corresponding discretization can be written as $\mathbf{F}^k_1 = 0$, $\mathbf{F}^k_2 = [\mathbf{F}^k_{2_1}; \mathbf{F}^k_{2_2}; \mathbf{F}^k_{2_3}]$ and $\mathbf{F}^k_3 = [\mathbf{F}^k_{3_1}; \mathbf{F}^k_{3_2}]$, where the component

vectors are respectively:

$$\mathbf{F}^k_{2_{l,i}} = (J, \varphi_i) \qquad \mathbf{F}^k_{3_{l,r}} = (g_1 t_{l1} + g_2 t_{l2} + g_3 t_{l3}, \phi_r) \tag{3.20}$$

with $(g_1, g_2, g_3) = \mathbf{g}_D \times \mathbf{n}$. All in all, if we drag into the matrices the constants in front, i.e. $\mathbb{A} \longleftarrow i\omega c\mathbb{A}$, $\{\mathbb{D}, \mathbb{F}, \mathbb{H}\} \longleftarrow \tau\{\mathbb{D}, \mathbb{F}, \mathbb{H}\}$, $\mathbb{E} \longleftarrow (i\omega a + b)\mathbb{A}$ and $\mathbb{I} \longleftarrow (1-\tau)\mathbb{I}$, the HDG system of equations can be written as:

$$\begin{bmatrix} \mathbb{A} & \mathbb{B} & \mathbb{C} \\ \mathbb{B}^t & \mathbb{D}+\mathbb{E} & \mathbb{F} \\ -\mathbb{C}^t & \mathbb{H} & \mathbb{I} \end{bmatrix} \begin{bmatrix} \mathbf{H} \\ \mathbf{E} \\ \boldsymbol{\Upsilon} \end{bmatrix} = \begin{bmatrix} \mathbf{F_1} \\ \mathbf{F_2} \\ \mathbf{F_3} \end{bmatrix} \tag{3.21}$$

where $\mathbf{E}, \mathbf{H}$ represent the value of the electric and magnetic fields at the degrees of freedom defined in each discretization element, whereas $\boldsymbol{\Upsilon}$ corresponds to the traces on the degrees of freedom on the interfaces.

After the discretized system of equations is formed, it is now time to solve it. However, instead of directly solving 3.21, we will take advantage of its sparsity pattern. Note that the upper left 2×2 submatrix formed by $\mathbb{A}, \mathbb{B}$ and $\mathbb{D} + \mathbb{E}$ is block diagonal since the information from each element K only has nonzero entries for the local degrees of freedom of the same element K. Hence, using the Schur complement, one can easily write $\mathbf{H} = \mathbf{H}(\boldsymbol{\Upsilon})$ and $\mathbf{E} = \mathbf{E}(\boldsymbol{\Upsilon})$ and finally use the last equation to solve the system for $\boldsymbol{\Upsilon}$. After the fact, if the local solution is desired, it can be again recovered in a fully parallel way, element by element. We can write,

$$\begin{bmatrix} \mathbf{H} \\ \mathbf{E} \end{bmatrix} = \begin{bmatrix} \mathbb{A} & \mathbb{B} \\ \mathbb{B}^t & \mathbb{D}+\mathbb{E} \end{bmatrix}^{-1} \left(\begin{bmatrix} \mathbf{F}_1 \\ \mathbf{F}_2 \end{bmatrix} - \begin{bmatrix} \mathbb{C} \\ \mathbb{F} \end{bmatrix} \boldsymbol{\Upsilon} \right) \tag{3.22}$$

where the inverse can be computed very efficiently since it is block diagonal and each block can be inverted separately. Then we solve the global system $\mathbb{K}\boldsymbol{\Upsilon} = \mathbf{T}$, where:

$$\begin{aligned} \mathbb{K} &= \mathbb{I} - \begin{bmatrix} -\mathbb{C}^t & \mathbb{H} \end{bmatrix} \begin{bmatrix} \mathbb{A} & \mathbb{B} \\ \mathbb{B}^t & \mathbb{D}+\mathbb{E} \end{bmatrix}^{-1} \begin{bmatrix} \mathbb{C} \\ \mathbb{F} \end{bmatrix} \\ \mathbf{T} &= \mathbf{F}_3 - \begin{bmatrix} -\mathbb{C}^t & \mathbb{H} \end{bmatrix} \begin{bmatrix} \mathbb{A} & \mathbb{B} \\ \mathbb{B}^t & \mathbb{D}+\mathbb{E} \end{bmatrix}^{-1} \begin{bmatrix} \mathbf{F}_1 \\ \mathbf{F}_2 \end{bmatrix} \end{aligned} \tag{3.23}$$

3.2 Multiscale HDG formulation

For the efficient simulation of electromagnetic wave propagation problems in 3d, we want to extend the multiscale method presented in chapter 2 to Maxwell's equations using the HDG method just presented at the local problem level and discontinuous spaces at the global multiscale level in order to impose the tangential nature of the solutions easily. As a result, in this section we will present the multiscale hybrid discontinuous Galerkin method (MSHDG) as the merge of the HDG solver locally together with the multiscale global decomposition presented in the previous chapter.

Let us first introduce the additional approximation spaces that will be required for the formulation. First of all, we need to introduce the spaces for each one of the subdomains $\Omega^m, 1 \leq m \leq M$. To that end, $\mathbf{X}_h^m$ and $\mathbf{M}_h^m, \forall m = 1..M$ are defined as follows for the volumetric variables and the HDG traces respectively as follows:

$$\begin{aligned} \mathbf{X}_h^m &= \{\mathbf{R} \in \mathbf{L}^2(\mathcal{T}_h^m) : \mathbf{R}|_K \in [P_k(K)]^d, \forall K \in \mathcal{T}_h^m\}, \\ \mathbf{M}_h^m &= \{\boldsymbol{\Theta} \in \mathbf{L}^2(\mathcal{E}_h^m) : \boldsymbol{\Theta}|_F \in \mathbf{M}(F), \forall F \in \mathcal{E}_h^m\}. \end{aligned} \tag{3.24}$$

In addition, the union of all them together will form the approximation space for the solution fields $\mathbf{E}_h$ and $\mathbf{H}_h$. Spaces $\mathbf{Y}_h$ and $\mathbf{N}_h$ are the global extension by union of $\mathbf{X}_h^m$ and $\mathbf{M}_h^m$, respectively. Finally, at a global level an approximation space for the multiscale traces is also required:

$$\begin{aligned} \mathbf{Y}_h &= \{\mathbf{r} \in [L^2(\mathcal{T}_h)]^d : \mathbf{r}|_{K^m} \in \mathbf{X}_h^m, \forall K^m \in \mathcal{T}_h^m, 1 \leq m \leq M\}, \\ \mathbf{N}_h &= \{\boldsymbol{\theta} \in \mathbf{L}^2(\mathcal{E}_h) : \boldsymbol{\theta}|_{F^m} \in \mathbf{M}_h^m, \forall F^m \in \mathcal{E}_h^m, 1 \leq m \leq M\}, \\ \mathbf{V}_h &= \{\boldsymbol{\mu} \in \mathbf{L}^2(\mathcal{E}_h^g) : \boldsymbol{\mu}|_f \in \mathbf{V}(f), \forall f \in \mathcal{E}_h^g\} \end{aligned} \tag{3.25}$$

where $\mathcal{E}_h^g$ is formed by all the interfaces at the multiscale level, *i.e.* the union of all the boundary faces of each subdomain. Furthermore, $\mathbf{V}(f) = \{\boldsymbol{\mu} \in [P_p(f)]^d : \boldsymbol{\mu} \cdot \mathbf{n} = 0\}$.

Note that each subdomain will be solved using the HDG method presented previously with an approximation order k according to the inherent definition of $\mathbf{X}_h^m$ and $\mathbf{M}_h^m$. Similarly, the *macro* discretization for multiscale purposes will use a polynomial approximation order p as given by $\mathbf{V}_h$. This traced space is defined over the faces of the *macro* discretization and hence it is discontinuous. All in all, the degrees of

freedom on the vertices (in 2d) and on the vertices and edges (in 3d) are duplicated.

We now consider the numerical multiscale global trace $\boldsymbol{\lambda} \in \mathbf{V}_h$ which is an approximation to the tangential electric field $\mathbf{E}^t$ (two linearly independent components) on the set of faces of the *macro* discretization. These are the only globally coupled degrees of freedom and will thus ultimately form the global system. In addition, for each subelement $\Omega^m \in \mathcal{T}_\Omega$ with discretization $\mathcal{T}_h^m$ we need to define a corresponding local problem, for which we use the HDG method presented in the previous section only with Dirichlet boundary conditions imposed by $\boldsymbol{\lambda}$. For the local problems we seek an approximation $(\mathbf{E}_h^m, \mathbf{H}_h^m, \widehat{\mathbf{E}}_h^m) \in \mathbf{X}_h^m \times \mathbf{X}_h^m \times \mathbf{M}_h^m$ such that the following system of equations holds for all $(\mathbf{R}, \mathbf{W}, \widehat{\boldsymbol{\Theta}}) \in \mathbf{X}_h^m \times \mathbf{X}_h^m \times \mathbf{M}_h^m$:

$$\begin{aligned}
(i\omega c\mathbf{H}_h^m, \mathbf{R})_{\mathcal{T}_h^m} + (\mathbf{E}_h^m, \nabla \times \mathbf{R})_{\mathcal{T}_h^m} + \left\langle \mathbf{n} \times \widehat{\mathbf{E}}_h^m, \mathbf{R} \right\rangle_{\partial \mathcal{T}_h^m} &= 0, \\
(\mathbf{H}_h^m, \nabla \times \mathbf{W})_{\mathcal{T}_h^m} + \left\langle \mathbf{n} \times \widehat{\mathbf{H}}_h^m, \mathbf{W} \right\rangle_{\partial \mathcal{T}_h^m} + ((i\omega a + b)\mathbf{E}_h^m, \mathbf{W})_{\mathcal{T}_h^m} &= (\mathbf{J}, \mathbf{W})_{\mathcal{T}_h^m}, \\
\left\langle \mathbf{n} \times \widehat{\mathbf{H}}_h^m, \boldsymbol{\Theta} \right\rangle_{\partial \mathcal{T}_h^m \setminus \partial \Omega^m} + \left\langle (\widehat{\mathbf{E}}_h^m - \boldsymbol{\lambda}) \times \mathbf{n}, \boldsymbol{\Theta} \right\rangle_{\partial \Omega^m} &= 0.
\end{aligned} \tag{3.26}$$

Note that the above problem can be solved at the subelement level whenever the global numerical trace $\boldsymbol{\lambda}$ is known. In other words, the local problem defines $(\mathbf{E}_h^m, \mathbf{H}_h^m, \widehat{\mathbf{E}}_h^m)$ as a function of $\boldsymbol{\lambda}$. Also, note that this problem is nothing but the HDG discretization -given by equations 3.13- of each of the subproblems defined by $\mathcal{T}_\Omega$ with a Dirichlet boundary condition $\mathbf{E}_h^m = \boldsymbol{\lambda}|_{\partial \Omega^m}$ imposed on $\partial \Omega^m$.

The numerical flux $\widehat{\mathbf{H}}_h^m$ still needs to be defined in a way that it guarantees the stability of the local problem. Similarly to [103], where a multiscale HDG method is introduced for Euler and Navier-Stokes equations, the numerical flux can be chosen as $\widehat{\mathbf{H}}_h^m = \mathbf{H}_h^m + \tau(\mathbf{E}_h^m - \widehat{\mathbf{E}}_h^m) \times \mathbf{n}$, where τ represents the stabilization parameter. Note that the actual value of the numerical flux $\widehat{\mathbf{H}}_h^m$ is coupled and intrinsically depends on $\boldsymbol{\lambda}$ through the last equation in 3.26.

Finally, the global problem needs to be defined in order to determine $\boldsymbol{\lambda}$. This is done by requiring an extra equation that imposes the full problem boundary conditions on the global numerical traces. We seek an approximation trace $\boldsymbol{\lambda} \in \mathbf{V}_h$ such

that:

$$\left\langle \mathbf{n} \times \widehat{\mathbf{h}}_h(\boldsymbol{\lambda}), \boldsymbol{\mu} \right\rangle_{\partial \mathcal{T}_h \setminus \partial\Omega} + \left\langle \widehat{\mathbf{b}}(\boldsymbol{\lambda}), \boldsymbol{\mu} \right\rangle_{\partial\Omega} = 0, \qquad \forall \boldsymbol{\mu} \in \mathbf{V}_h \tag{3.27}$$

Here, $\widehat{\mathbf{b}}(\boldsymbol{\lambda})$ is the boundary flux, the precise definition of which depends on the Neumann or Robin boundary conditions. Also, $\widehat{\mathbf{h}}_h \in \mathbf{Y}_h$ is formed by the union of all $\widehat{\mathbf{H}}_h^m$ and is thus equivalently defined. Note that this equation is only defined for the degrees of freedom on the *macro* discretization faces.

Finally, when equations 3.26 and 3.27 are considered together and the numerical flux is inserted in the equations, we obtain the formulation of the MSHDG method. In conclusion, we seek a solution $(\mathbf{e}_h, \mathbf{h}_h, \widehat{\mathbf{e}}_h, \boldsymbol{\lambda}) \in \mathbf{Y_h} \times \mathbf{Y_h} \times \mathbf{N_h} \times \mathbf{V}_h$ such that:

$$\begin{aligned}
(i\omega c \mathbf{h}_h, \mathbf{r})_{\mathcal{T}_h} + (\mathbf{e}_h, \nabla \times \mathbf{r})_{\mathcal{T}_h} + \langle \mathbf{n} \times \widehat{\mathbf{e}}_h, \mathbf{r} \rangle_{\partial \mathcal{T}_h^m} &= 0, \\
(\nabla \times \mathbf{h}_h, \mathbf{w})_{\mathcal{T}_h} + \langle \tau(\mathbf{n} \times \mathbf{e}_h \times \mathbf{n} - \widehat{\mathbf{e}}_h), \mathbf{w} \rangle_{\partial \mathcal{T}_h} + ((i\omega a + b)\mathbf{e}_h, \mathbf{w})_{\mathcal{T}_h} &= (\mathbf{J}, \mathbf{w})_{\mathcal{T}_h}, \\
\langle \mathbf{n} \times \mathbf{h}_h + \tau(\mathbf{n} \times \mathbf{e}_h \times \mathbf{n} - \widehat{\mathbf{e}}_\mathbf{h}), \boldsymbol{\theta} \rangle_{\partial \mathcal{T}_h \setminus \bigcup_m \partial\Omega^m} + \langle (\widehat{\mathbf{e}}_h - \boldsymbol{\lambda}) \times \mathbf{n}, \boldsymbol{\theta} \rangle_{\bigcup_m \partial\Omega^m} &= 0, \\
\langle \mathbf{n} \times \mathbf{h}_h + \tau(\mathbf{n} \times \mathbf{e}_h \times \mathbf{n} - \widehat{\mathbf{e}}_\mathbf{h}), \boldsymbol{\theta} \rangle_{\partial \mathcal{T}_h \setminus \partial\Omega} + \left\langle \widehat{\mathbf{b}}, \boldsymbol{\mu} \right\rangle_{\partial\Omega} &= 0,
\end{aligned} \tag{3.28}$$

holds for all $(\mathbf{r}, \mathbf{w}, \boldsymbol{\theta}, \boldsymbol{\mu}) \in \mathbf{Y_h} \times \mathbf{Y_h} \times \mathbf{N_h} \times \mathbf{V_h}$.

The two levels of hybridization that this method uses will be exploited in the actual implementation of the MSHDG. Note that the degrees of freedom corresponding to $\mathbf{e}_h \in \mathbf{Y}_h$ and $\mathbf{h}_h \in \mathbf{Y}_h$ are only coupled within each *micro* discretization element. Furthermore, the HDG traces $\widehat{\mathbf{e}}_h$ are only coupled within a given subdomain. The only globally coupled degrees of freedom are those related to $\boldsymbol{\lambda}$.

3.3 Implementation

The purpose of this section is to present a guide for the implementation of the MSHDG method, exploiting the structure of this discretization. The efficient implementation of the MSCG method introduced in the previous chapter relied on breaking down the local solver into a collection of Dirichlet problems at each representative of the subdomains, so that we were able to reuse information. In the MSHDG case and given the linear nature of Maxwell's equations, the very same technique can be used.

Let us begin by considering $(\mathbf{E}_\mathbf{J}^m, \mathbf{H}_\mathbf{J}^m, \widehat{\mathbf{E}}_\mathbf{J}^m) \in \mathbf{X}_h^m \times \mathbf{X}_h^m \times \mathbf{M}_h^m$ to be the solution

of the following HDG system of equations:

$$\begin{aligned}(i\omega c\mathbf{H}_{\mathbf{J}}^m,\mathbf{R})_{\mathcal{T}_h}+(\mathbf{E}_{\mathbf{J}}^m,\nabla\times\mathbf{R})_{\mathcal{T}_h}+\left\langle\mathbf{n}\times\widehat{\mathbf{E}}_{\mathbf{J}}^m,\mathbf{R}\right\rangle_{\partial\mathcal{T}_h}&=0,\\(\nabla\times\mathbf{H}_{\mathbf{J}}^m,\mathbf{W})_{\mathcal{T}_h}+\left\langle\tau(\mathbf{n}\times\mathbf{E}_{\mathbf{J}}^m\times\mathbf{n}-\widehat{\mathbf{E}}_{\mathbf{J}}^m),\mathbf{W}\right\rangle_{\partial\mathcal{T}_h}+((i\omega a+b)\mathbf{E}_{\mathbf{J}}^m,\mathbf{W})_{\mathcal{T}_h}&=(\mathbf{J},\mathbf{W})_{\mathcal{T}_h},\\\left\langle\mathbf{n}\times\mathbf{H}_{\mathbf{J}}^m+\tau(\mathbf{n}\times\mathbf{E}_{\mathbf{J}}^m\times\mathbf{n}-\widehat{\mathbf{E}}_{\mathbf{J}}^m),\boldsymbol{\Theta}\right\rangle_{\partial\mathcal{T}_h\setminus\partial\Omega}+\left\langle\widehat{\mathbf{E}}_{\mathbf{J}}^m\times\mathbf{n},\boldsymbol{\Theta}\right\rangle_{\partial\Omega}&=0,\end{aligned}\tag{3.29}$$

for all $(\mathbf{R},\mathbf{W},\boldsymbol{\Theta})\in\mathbf{X}_h^m\times\mathbf{X}_h^m\times\mathbf{M}_h^m$. These equations correspond to the homogeneous Dirichlet Maxwell's problem given by:

$$\left.\begin{aligned}\nabla\times\mathbf{H}_{\mathbf{J}}^m-(i\omega a(\mathbf{x})+b(\mathbf{x}))\mathbf{E}_{\mathbf{J}}^m&=\mathbf{J},\quad\text{in }\Omega^m\\\nabla\times\mathbf{E}_{\mathbf{J}}^m+i\omega c(\mathbf{x})\mathbf{H}_{\mathbf{J}}^m&=0,\quad\text{in }\Omega^m\\\mathbf{n}\times\mathbf{E}_{\mathbf{J}}^m&=0,\quad\text{on }\partial\Omega^m\end{aligned}\right\}.\tag{3.30}$$

Similarly, we consider $(\mathbf{E}_{\boldsymbol{\eta}}^m,\mathbf{H}_{\boldsymbol{\eta}}^m,\widehat{\mathbf{E}}_{\boldsymbol{\eta}}^m)\in\mathbf{X}_h^m\times\mathbf{X}_h^m\times\mathbf{M}_h^m$ to be the solution of the following HDG system of equations:

$$\begin{aligned}\left(i\omega c\mathbf{H}_{\boldsymbol{\eta}}^m,\mathbf{R}\right)_{\mathcal{T}_h}+(\mathbf{E}_{\boldsymbol{\eta}}^m,\nabla\times\mathbf{R})_{\mathcal{T}_h}+\left\langle\mathbf{n}\times\widehat{\mathbf{E}}_{\boldsymbol{\eta}}^m,\mathbf{R}\right\rangle_{\partial\mathcal{T}_h}&=0,\\(\nabla\times\mathbf{H}_{\boldsymbol{\eta}}^m,\mathbf{W})_{\mathcal{T}_h}+\left\langle\tau(\mathbf{n}\times\mathbf{E}_{\boldsymbol{\eta}}^m\times\mathbf{n}-\widehat{\mathbf{E}}_{\boldsymbol{\eta}}^m),\mathbf{W}\right\rangle_{\partial\mathcal{T}_h}+((i\omega a+b)\mathbf{E}_{\boldsymbol{\eta}}^m,\mathbf{W})_{\mathcal{T}_h}&=0,\\\left\langle\mathbf{n}\times\mathbf{H}_{\boldsymbol{\eta}}^m+\tau(\mathbf{n}\times\mathbf{E}_{\boldsymbol{\eta}}^m\times\mathbf{n}-\widehat{\mathbf{E}}_{\boldsymbol{\eta}}^m),\boldsymbol{\Theta}\right\rangle_{\partial\mathcal{T}_h\setminus\partial\Omega}+\left\langle(\widehat{\mathbf{E}}_{\boldsymbol{\eta}}^m-\boldsymbol{\eta})\times\mathbf{n},\boldsymbol{\Theta}\right\rangle_{\partial\Omega}&=0,\end{aligned}\tag{3.31}$$

for all $(\mathbf{R},\mathbf{W},\boldsymbol{\Theta})\in\mathbf{X}_h^m\times\mathbf{X}_h^m\times\mathbf{M}_h^m$. These equations correspond to a Maxwell's problem with inhomogeneous $\mathbf{g}_D=\boldsymbol{\eta}$ Dirichlet boundary conditions without source term given by:

$$\left.\begin{aligned}\nabla\times\mathbf{H}_{\boldsymbol{\eta}}^m-(i\omega a(\mathbf{x})+b(\mathbf{x}))\mathbf{E}_{\boldsymbol{\eta}}^m&=0,\quad\text{in }\Omega^m\\\nabla\times\mathbf{E}_{\boldsymbol{\eta}}^m+i\omega c(\mathbf{x})\mathbf{H}_{\boldsymbol{\eta}}^m&=0,\quad\text{in }\Omega^m\\\mathbf{n}\times\mathbf{E}_{\boldsymbol{\eta}}^m&=\boldsymbol{\eta},\quad\text{on }\partial\Omega^m\end{aligned}\right\}.\tag{3.32}$$

Now, we proceed equivalently to the MSCG method. Hence, consider the space for the multiscale traces as $\mathbf{V}_h=\left[\cup_{f=1}^F V_h^f\right]^d$ where $V_h^f=span\{\varphi_i,1\leq i\leq N^f\}$, being φ_i each of the N^f nodal basis functions on face $f\in\mathcal{E}_h$. Then we can write each component of $\boldsymbol{\lambda}$ as some linear combination of the basis functions φ_i. This decomposition will let us also write the solution fields $(\mathbf{E}_{\boldsymbol{\lambda}}^m,\mathbf{H}_{\boldsymbol{\lambda}}^m,\widehat{\mathbf{E}}_{\boldsymbol{\lambda}}^m)$ as a linear combination of the fields $(\mathbf{E}_{\boldsymbol{\varphi}_i}^m,\mathbf{H}_{\boldsymbol{\varphi}_i}^m,\widehat{\mathbf{E}}_{\boldsymbol{\varphi}_i}^m)$ for each of the $\{\boldsymbol{\varphi}_i\}_{i=1}^{N^f}$. Note that the discontinuous nature

of the *macro* scale space leads to a definition of the global degrees of freedom face by face. All in all, a given subelement $1 \leq m \leq M$ will only communicate with 6 faces f^m and thus with the degrees of freedom therein.

According to the HDG decomposition described in the previous section, we can solve each collection of subproblems (3.30 and 3.32) at a given subdomain for the local traces $\widehat{\mathbf{E}}_{\mathbf{J}}^m$ as:

$$\mathbb{K}^m \boldsymbol{\Upsilon}_{\mathbf{J}}^m = \mathbf{T}_{\mathbf{J}}^m, \tag{3.33}$$

where $\boldsymbol{\Upsilon}_{\mathbf{J}}^m$ represents the degrees of freedom for $\widehat{\mathbf{E}}_{\mathbf{J}}^m$ with $1 \leq m \leq M$. Equivalently, the local HDG discretization for each one of the $\left\{\{\boldsymbol{\varphi}_i\}_{i=1}^{N^f}\right\}_{f=1}^{F}$ problems yields to the following algebraic system of equations:

$$\mathbb{K}^m \boldsymbol{\Upsilon}_{\boldsymbol{\varphi}_i}^m = \mathbf{T}_{\boldsymbol{\varphi}_i}^m, \quad 1 \leq i \leq N^{f^m}, \tag{3.34}$$

where similarly, $\boldsymbol{\Upsilon}_{\boldsymbol{\varphi}_i}^m$ represents the value of the HDG solution on the degrees of freedom of the local traces for the Dirichlet problem with boundary condition $\boldsymbol{\varphi}_i$.

Note that the system matrix $\mathbb{K}^m$ required for all of the $N+1$ HDG problems at every subdomain is the same. When considering the problem for $\mathbf{J}$ as well as each one corresponding to a given $\{\boldsymbol{\varphi}_i\}_{i=1}^{N^{f^m}}$, the only changes in 3.21 correspond to the right hand side terms $\mathbf{F}_2$ and $\mathbf{F}_3$. This means that only $\mathbf{T}^m$ in equations 3.23 will take different values for each problem, denoted by $\mathbf{T}_{\mathbf{J}}^m$ and $\mathbf{T}_{\boldsymbol{\varphi}_i}^m$, leading to different solutions $\boldsymbol{\Upsilon}_{\mathbf{J}}^m$ and $\boldsymbol{\Upsilon}_{\boldsymbol{\varphi}_i}^m$, respectively.

This decomposition, together with the HDG static condensation provided by 3.23, gives us a way to compute all the matrix inversions at the local HDG level as well as at the subelement level in a very efficient manner -the local ones ($\mathbb{A}, \mathbb{B}, \mathbb{D}$ and $\mathbb{E}$) as given by 3.22; as well as the subdomain ones ($\mathbb{K}$) as just explained-.

Finally, let us algebraically write the the global problem given by the last equation in 3.28, as:

$$\mathbb{L}\mathbf{H} + \mathbb{M}\mathbf{E} + \mathbb{N}\boldsymbol{\Upsilon} + \mathbb{O}\boldsymbol{\Lambda} = \mathbf{F}_4, \tag{3.35}$$

where $\mathbf{H}$ and $\mathbf{E}$ provide values for the magnetic and electric fields respectively at the degrees of freedom defined by $\mathbf{Y}_h$; $\boldsymbol{\Upsilon}$ corresponds to $\widehat{\mathbf{e}}_h \in \mathbf{N}_h$ and $\boldsymbol{\Lambda}$ takes values on

the multiscale interfaces, where $\boldsymbol{\lambda} \in \mathbf{V}_h$ is defined. In addition, matrices $\mathbb{L}, \mathbb{M}$ and $\mathbb{N}$ are obtained equivalently to $\mathbb{C}, \mathbb{H}$ and $\mathbb{I}$ in 3.16 but where the shape functions ϕ_r are chosen in the *macro* discretization interfaces instead of the local faces.

We now want to write equation 3.35 only in terms of $\boldsymbol{\Lambda}$ as we have already argued that all the other degrees of freedom can be statically condensed in two steps: first using HDG to go from $\mathbf{H}^m, \mathbf{E}^m$ to $\boldsymbol{\Upsilon}^m$ and then the multiscale decomposition to take these three subelement by subelement into $\boldsymbol{\Lambda}$. Let us recall that the latter decomposition is such that $\mathbf{H}_h^m = \mathbf{H}_{\mathbf{J}}^m + \mathbf{H}_{\boldsymbol{\lambda}}^m$, $\mathbf{E}_h^m = \mathbf{E}_{\mathbf{J}}^m + \mathbf{E}_{\boldsymbol{\lambda}}^m$ and $\boldsymbol{\Upsilon}_h^m = \boldsymbol{\Upsilon}_{\mathbf{J}}^m + \boldsymbol{\Upsilon}_{\boldsymbol{\lambda}}^m$ where:

$$\mathbf{H}_{\boldsymbol{\lambda}}^m = \sum_{i=1}^{N^m} \Lambda_i \mathbf{H}_{\boldsymbol{\varphi}_i}^m, \quad \mathbf{E}_{\boldsymbol{\lambda}}^m = \sum_{i=1}^{N^m} \Lambda_i \mathbf{E}_{\boldsymbol{\varphi}_i}^m, \quad \boldsymbol{\Upsilon}_{\boldsymbol{\lambda}}^m = \sum_{i=1}^{N^m} \Lambda_i \boldsymbol{\Upsilon}_{\boldsymbol{\varphi}_i}^m. \tag{3.36}$$

All in all, we first use 3.22 to write $(\mathbf{H}_{\mathbf{J}}^m, \mathbf{E}_{\mathbf{J}}^m)$ and $(\mathbf{H}_{\boldsymbol{\varphi}_i}^m, \mathbf{E}_{\boldsymbol{\varphi}_i}^m)$, for $1 \leq i \leq N^m$ as a function of $\boldsymbol{\Upsilon}_{\mathbf{J}}^m$ and $\boldsymbol{\Upsilon}_{\boldsymbol{\varphi}_i}^m$, respectively. In other words, we write:

$$\begin{bmatrix} \mathbf{H}_\alpha^m \\ \mathbf{E}_\alpha^m \end{bmatrix} = \begin{bmatrix} \mathbb{A}^m & \mathbb{B}^m \\ (\mathbb{B}^m)^t & \mathbb{D}^m + \mathbb{E}^m \end{bmatrix}^{-1} \left(\begin{bmatrix} \mathbf{F}_1^m \\ \mathbf{F}_2^m(\alpha) \end{bmatrix} - \begin{bmatrix} \mathbb{C}^m \\ \mathbb{F}^m \end{bmatrix} \boldsymbol{\Upsilon}_\alpha^m \right) \tag{3.37}$$

for a representative of each element $1 \leq m \leq M$ and $\alpha \in \{\mathbf{J}, \{\boldsymbol{\varphi}_i\}_{i=1}^{N^m}\}$. Note that the inverse involved is cheap since the matrix is block diagonal at the discretization element level.

Now we use 3.37 to obtain $\mathbb{K}^m$ as well as the right hand sides $\mathbf{T_J}^m$ and $\mathbf{T}_{\boldsymbol{\varphi}_i}^m$ as:

$$\begin{aligned} \mathbb{K}^m &= \mathbb{I}^m - \begin{bmatrix} (-\mathbb{C}^m)^t & \mathbb{H}^m \end{bmatrix} \begin{bmatrix} \mathbb{A}^m & \mathbb{B}^m \\ (\mathbb{B}^m)^t & \mathbb{D}^m + \mathbb{E}^m \end{bmatrix}^{-1} \begin{bmatrix} \mathbb{C}^m \\ \mathbb{F}^m \end{bmatrix}, \\ \mathbf{T}_\alpha^m &= \mathbf{F}_3(\alpha) - \begin{bmatrix} (-\mathbb{C}^m)^t & \mathbb{H}^m \end{bmatrix} \begin{bmatrix} \mathbb{A}^m & \mathbb{B}^m \\ (\mathbb{B}^m)^t & \mathbb{D}^m + \mathbb{E}^m \end{bmatrix}^{-1} \begin{bmatrix} \mathbf{F}_1 \\ \mathbf{F}_2(\alpha) \end{bmatrix}. \end{aligned} \tag{3.38}$$

If we now bring together all the preceding decompositions we end up firstly with a system of equations for the degrees of freedom on the HDG and global traces $(\boldsymbol{\Upsilon}, \boldsymbol{\Lambda})$ that can be expressed as:

$$\mathbb{P} \left(\boldsymbol{\Upsilon}_{\mathbf{J}} + \sum_{i=1}^{N^m} \boldsymbol{\Upsilon}_{\boldsymbol{\varphi}_i^m} \Lambda_i^m \right)_{m=1}^{M} + \mathbb{O}\boldsymbol{\Lambda} = \mathbf{Q} \tag{3.39}$$

where $\mathbb{P}$ and $\mathbf{Q}$ are given by:

$$\begin{aligned}\mathbb{P} &= \mathbb{N} - \begin{bmatrix} \mathbb{L} & \mathbb{M} \end{bmatrix} \begin{bmatrix} \mathbb{A} & \mathbb{B} \\ \mathbb{B}^t & \mathbb{D}+\mathbb{E} \end{bmatrix}^{-1} \begin{bmatrix} \mathbb{C} \\ \mathbb{F} \end{bmatrix} \\ \mathbf{Q} &= \mathbf{F}_4 - \begin{bmatrix} \mathbb{L} & \mathbb{M} \end{bmatrix} \begin{bmatrix} \mathbb{A} & \mathbb{B} \\ \mathbb{B}^t & \mathbb{D}+\mathbb{E} \end{bmatrix}^{-1} \begin{bmatrix} \mathbf{F}_1 \\ \mathbf{F}_2(\mathbf{J}) \end{bmatrix}\end{aligned} \tag{3.40}$$

Note that only $\mathbf{F}_2(\mathbf{J})$ is required since $\mathbf{F}_2(\boldsymbol{\varphi}_i) = 0, \forall i$. To conclude, we use the subelement information $\mathbb{K}^m \boldsymbol{\Upsilon}_{\mathbf{J}} = \mathbf{T}_{\mathbf{J}}^m$ and $\mathbb{K}^m \boldsymbol{\Upsilon}_{\boldsymbol{\varphi}_i} = \mathbf{T}_{\boldsymbol{\varphi}_i}^m$ together with $\boldsymbol{\Upsilon}^m = \boldsymbol{\Upsilon}_{\mathbf{J}}^m + \boldsymbol{\Upsilon}_{\boldsymbol{\varphi}}^m \boldsymbol{\Lambda}$ to obtain the final system of equations only for $\boldsymbol{\Lambda}$ as $\mathbb{Z}\boldsymbol{\Lambda} = \mathbf{W}$, where:

$$\begin{aligned}\mathbb{Z} &= \mathbb{O} - \mathbb{P}\mathbb{K}^{-1}\mathbb{T}_{\boldsymbol{\varphi}} \\ \mathbf{W} &= \mathbf{Q} - \mathbb{P}\mathbb{K}^{-1}\mathbf{T}_{\mathbf{J}}\end{aligned} \tag{3.41}$$

where $\mathbb{K}^{-1}\mathbb{T}_{\boldsymbol{\varphi}}$ and $\mathbb{K}^{-1}\mathbf{T}_{\mathbf{J}}$ represent the assembly of the subdomain terms $(\mathbb{K}^m)^{-1}\mathbf{T}_{\boldsymbol{\varphi}_i}^m$ and $(\mathbb{K}^m)^{-1}\mathbf{T}_{\mathbf{J}}^m$, for $1 \leq m \leq M$, respectively.

Let us also make some important remarks about the MSHDG implementation. Firstly, the use of Schur's complement leads to an efficient computation of all inverses except for $\mathbb{Z}^{-1}$, which is the global reduced problem and therefore should be the bottleneck of the algorithm. Furthermore, all local subelements can not only be parallelized but also classified in a way where only a very few of them ($\ll M$) are solved and then stored and reused. In particular, this storage is not expensive since although $N^{fm} + 1$ different right hand side vectors $\mathbf{T}_{\alpha}^m$ are required, only one single matrix $\mathbb{K}^m$ is inverted and stored per class of subelements. Table 3.1 summarizes the implementation steps.

3.4 Convergence test and cost analysis

In this section, a numerical experiment is presented in order to assess the performance and accuracy of the MSHDG method. To that end, we will solve 3.1 in a 3d cubic domain $\Omega = (-1, 1)^3$ with $a(\mathbf{x}) = c(\mathbf{x}) = 1$, and $b(\mathbf{x}) = \mathbf{J} = 0$. Furthermore, we will

Table 3.1: Implementation steps of MSCG method

1. For a representative of each subdomain $\Omega^m, 1 \leq m \leq M$,
   a. Compute local matrices matrices $\mathbb{A}^m$ to $\mathbb{I}^m$ and vectors $\boldsymbol{F}_i^m(\alpha)$
   b. Solve for $\mathbf{H}_{\mathbf{J}}^m, \mathbf{E}_{\mathbf{J}}^m, \widehat{\mathbf{E}}_{\mathbf{J}}^m$
   c. Solve for $\mathbf{H}_{\boldsymbol{\varphi}_i}^m, \mathbf{E}_{\boldsymbol{\varphi}_i}^m, \widehat{\mathbf{E}}_{\boldsymbol{\varphi}_i}^m$, $1 \leq i \leq N^{f^m}$
   d. Compute the subdomain global matrix $\mathbb{K}^m$ and load vectors $\mathbf{T}_\alpha^m$
2. Derive and assemble $\mathbb{Z}$ and $\mathbf{W}$ according to the described procedure
3. Solve $\mathbb{Z}\boldsymbol{\Lambda} = \mathbf{W}$
4. Compute $(\mathbf{e}_h, \mathbf{h}_h, \widehat{\mathbf{e}}_h) \in \mathbf{Y_h} \times \mathbf{Y_h} \times \mathbf{N_h}$ using 3.36

choose the boundary data $\mathbf{g}_D$ such that the exact solution is given by:

$$\mathbf{E}(x, y, z) = (\sin(\omega y), \sin(\omega x), 0). \tag{3.42}$$

Here, results for $\omega = 1$ are analyzed. We also consider a 3d tetrahedral mesh obtained by splitting a regular $n \times n \times n$ Cartesian 3d grid ($h = 1/n$). Once more, the original subdomain is split into $M = q \times q \times q$ cubic subdomains. The polynomial degree considered inside each subdomain is k. Table 3.2 shows the L^2 errors of the solution for both the MSHDG method as well as equivalent HDG discretization for $k = 1$ while table 3.3 shows the same errors for $k = 2$. As expected, a convergence of $\mathcal{O}(h^{p+1})$ is obtained and both methods provide errors of the same order.

Table 3.2: Convergence history of the MSHDG method and the HDG method for $k = 1$: $L^2(\Omega)$ error in the solution as a function of n, q.

Mesh	MSHDG				HDG	
n	$q=1$ error	$q=2$ error	$q=4$ error	$q=8$ error	error	order
8	$6.48 \cdot 10^{-1}$	$6.48 \cdot 10^{-1}$	$6.48 \cdot 10^{-1}$	$6.48 \cdot 10^{-1}$	$6.48 \cdot 10^{-1}$	–
16	$9.42 \cdot 10^{-1}$	$9.42 \cdot 10^{-1}$	$9.42 \cdot 10^{-1}$	$9.42 \cdot 10^{-1}$	$9.42 \cdot 10^{-1}$	2.79
32	$2.25 \cdot 10^{-2}$	$2.25 \cdot 10^{-2}$	$2.25 \cdot 10^{-2}$	$2.25 \cdot 10^{-2}$	$2.25 \cdot 10^{-2}$	2.06
64	$5.51 \cdot 10^{-3}$	$5.51 \cdot 10^{-3}$	$5.51 \cdot 10^{-3}$	$5.51 \cdot 10^{-3}$	$5.51 \cdot 10^{-3}$	2.00
128	$1.37 \cdot 10^{-3}$	$1.37 \cdot 10^{-3}$	$1.37 \cdot 10^{-3}$	$1.37 \cdot 10^{-3}$	$1.37 \cdot 10^{-3}$	2.01

Like the MSCG method, not only do we we get the same convergence order for all equivalent discretizations with different choices of q, but we also obtain exactly the same error. Given the choice of a discontinuous space for the multiscale interfaces, all discretizations are equivalent and provide the same solution:

Table 3.3: Convergence history of the MSHDG method and the HDG method for $k = 2$: $L^2(\Omega)$ error in the solution as a function of n, q.

Mesh	MSHDG				HDG	
n	$q = 1$ error	$q = 2$ error	$q = 4$ error	$q = 8$ error	error	order
8	$5.03 \cdot 10^{-2}$	$5.03 \cdot 10^{-2}$	$5.03 \cdot 10^{-2}$	$5.03 \cdot 10^{-2}$	$5.03 \cdot 10^{-2}$	--
16	$6.21 \cdot 10^{-3}$	$6.21 \cdot 10^{-3}$	$6.21 \cdot 10^{-3}$	$6.21 \cdot 10^{-3}$	$6.21 \cdot 10^{-3}$	3.04
32	$7.76 \cdot 10^{-4}$	$7.76 \cdot 10^{-4}$	$7.76 \cdot 10^{-4}$	$7.76 \cdot 10^{-4}$	$7.76 \cdot 10^{-4}$	3.01
64	$9.72 \cdot 10^{-5}$	$9.72 \cdot 10^{-5}$	$9.72 \cdot 10^{-5}$	$9.72 \cdot 10^{-5}$	$9.72 \cdot 10^{-5}$	2.99
128	$1.25 \cdot 10^{-5}$	$1.25 \cdot 10^{-5}$	$1.25 \cdot 10^{-5}$	$1.25 \cdot 10^{-5}$	$1.25 \cdot 10^{-5}$	3.00

$(\mathbf{h}_h, \mathbf{e}_h)^{mshdg} = (\mathbf{H}_h, \mathbf{E}_h)^{hdg}$.

It is also relevant to compare the degrees of freedom for the MSHDG and HDG methods. To that end, we focus on a uniform discretization of the 3d Maxwell's case (for more general analysis on the cost of HDG, see [70]). Let us assume that a total of $6n^3$ elements are present in the total discretization (that is, n subdivisions in each dimension times 6 tetrahedra per cube). For $k = 1$, the HDG method provides 4 degrees of freedom per element for each of the six components of $(\mathbf{H}_h, \mathbf{E}_h)$ and 3 degrees of freedom per face, for each component of $\widehat{\mathbf{E}}_h$. When $p = 2$, the HDG method uses 10 instead of 4 degrees of freedom per element and 6 instead 3 per face.

These same numbers also apply to the local MSHDG discretization considering that there are $6n^3/p^3$ elements per subdomain. Then, for the global traces considered of order $p = n/q$ when $k = 1$ or $p = 2n/q$ when $k = 2$ we obtain $(p + 1)^2$ degrees of freedom per interface, of which there are $3(q + 1)q^2$. Tables 3.4 and 3.5 provide the total numbers of degrees of freedom for the HDG discretization as well as the MSHDG for $k = 1$ and $k = 2$, respectively.

Note that the set of global degrees of freedom for the MSHDG method is always of smaller size when compared to the HDG method. Particularly, a good balance between the size of the local and global problem is sought in order to maximize the efficiency of the method. So, for instance, if we look at the last row of table 3.5, we would prefer to partition the domain in 8 subelements per direction and obtain a total of $1m$ degrees of freedom for $\widehat{\mathbf{e}}_h$ than to partition it only into 2 per direction,

Table 3.4: Comparison of the degrees of freedom between the MSHDG method and the HDG method using uniform meshes for $k = 1$.

	MSHDG						HDG	
n	$q = 2$			$q = 8$				
	M	$\mathcal{K}_{\text{dof}}^{\text{mshdg}}$	$\mathcal{N}_{\text{dof}}^{\text{mshdg}}$	M	$\mathcal{K}_{\text{dof}}^{\text{mshdg}}$	$\mathcal{N}_{\text{dof}}^{\text{mshdg}}$	$\mathcal{N}_{\text{dof}}^{\text{hdg,all}}$	$\mathcal{N}_{\text{dof}}^{\text{hdg,trace}}$
8	8	$11.5K$	$1.8K$	512	180	$3.4K$	$91.5K$	$30.6K$
16	8	$91.5K$	$5.8K$	512	$1.4K$	$31K$	$740K$	$246K$
32	8	$740K$	$20.8K$	512	$11.5K$	$86.4K$	$3.9m$	$1.9m$
64	8	$3.9m$	$78K$	512	$91.5K$	$280K$	$47m$	$15m$

Table 3.5: Comparison of the degrees of freedom between the MSHDG method and the HDG method using uniform meshes for $k = 2$.

	MSHDG						HDG	
n	$q = 2$			$q = 8$				
	M	$\mathcal{K}_{\text{dof}}^{\text{mshdg}}$	$\mathcal{N}_{\text{dof}}^{\text{mshdg}}$	M	$\mathcal{K}_{\text{dof}}^{\text{mshdg}}$	$\mathcal{N}_{\text{dof}}^{\text{mshdg}}$	$\mathcal{N}_{\text{dof}}^{\text{hdg,all}}$	$\mathcal{N}_{\text{dof}}^{\text{hdg,trace}}$
8	8	$27K$	$5.8K$	512	420	$31K$	$215K$	$62K$
16	8	$215K$	$20.8K$	512	$3.4K$	$86.4K$	$1.7m$	$492K$
32	8	$1.7m$	$78K$	512	$27K$	$280K$	$9.8m$	$3.8m$
64	8	$9.8m$	$304K$	512	$215K$	$1m$	$110m$	$30m$

where the local subproblems would we too large.

Furthermore, $\mathcal{K}_{dof}^{mshdg}$ represents the total number of local degrees of freedom for each of the HDG subproblems. Let us note that in fact, the actual size of the local systems of equations is smaller since we use static condensation to solve only for the HDG traces. Overall, there is a reduction of a factor equivalent to the one given between the last two columns (from all the HDG degrees of freedom to only those on the traces, $\widehat{\mathbf{E}}_h$).

Finally, we note that this comparison of degrees of freedom is for a uniform discretization where the subdomain decomposition and the global mesh have been matched to provide solutions of the same accuracy. However, for most of the problems of interest, the local meshes will be finer in order to capture the geometry. In these problems, the global discretization will be only determined by the frequencies of interest. The difference of degrees of freedom between MSHDG and HDG will be even greater.

3.5 Numerical results

In this section we present a collection of forward direct simulations obtained using the multiscale HDG method introduced in this chapter. The main objective is to show how the method allows for the accurate solution of large electromagnetic problems.

Firstly, we obtain the numerical solutions for 3d fibers that use either the concept of index guiding or, alternatively, that are made of a Photonic Crystal cross section. Then, we obtain the electric and/or magnetic field patterns for waveguides on Photonic Crystal slabs. For all these cases, a particular multiscale decomposition is described as well as the set of parameters $a(\mathbf{x}), b(\mathbf{x})$ and $c(\mathbf{x})$ defining the material properties.

3.5.1 Optical Fibers

Optical fibers have been a key development for telecommunications. They are long structures that have the ability of conducting electromagnetic energy with minimal losses. Typically, the cross section defines each fiber since they are then extended cylindrically in the longitudinal component. Such cross section traps the waves in the core region, around which there is a cladding that avoids energy losses.

The design of such cladding becomes crucial when it comes to assess the effectiveness of an optical fiber. Often, the core is just designed with a higher index material than the cladding so that the energy is confined by index guiding or total internal reflection [74]. More recently, Photonic Crystal fibers were formally introduced in [78] and have proven a better performance than index guiding fibers when other aspects besides optical communications -such as carrying more power, having multiple cores, dealing with higher nonlinearities...- are taken into account [137].

Firstly, we consider an optical fiber with a homogeneous core made of silicon ($\varepsilon = 11.8$). In this case and because of the total internal reflection phenomenon, when a planar wave is sent from one end of the fiber, all the energy is confined within the higher index material region and propagates along the fiber with very little losses. Figure 3.2 shows the longitudinal component of the magnetic field H_z, which is the most relevant for this scenario, for a wavelength considered to be 1.4 times the radius

of the optical fiber.

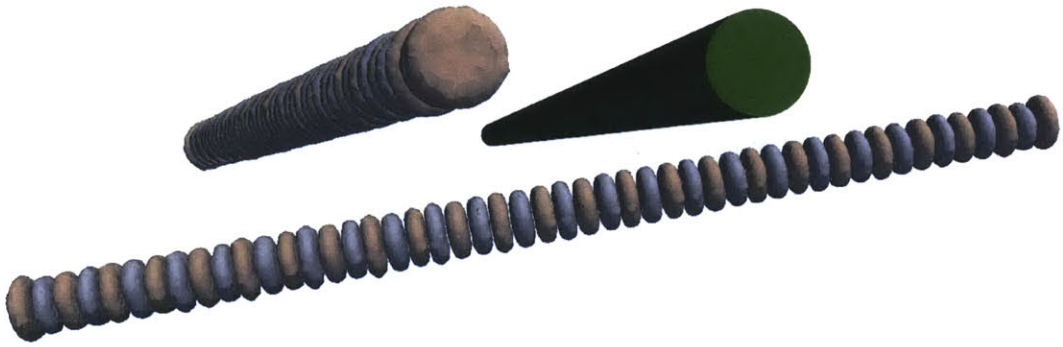

Figure 3.2: H_z wave field and geometry of a homogeneous $\varepsilon_{max} = 11.8$ cylindrical index guiding fiber. For a fiber with radius r the wavelength is $\lambda = 1.4r$.

Similarly, figure 3.3 shows the H_z field for an index guiding based optical fiber where the higher index material is distributed on a ring. By total internal reflection the propagated magnetic field is confined only to the ring. In this particular case, the internal radius corresponds to $0.8r$ where r is the external radius and the wavelength is $1.4r$.

Figure 3.3: H_z wave field and geometry of a homogeneous $\varepsilon_{max} = 11.8$ ring index guiding fiber. For a fiber with internal radius $0.8r$ being r the external one. The wavelength is $\lambda = 1.4r$.

For the MSHDG simulation of the two preceding examples we have decomposed the domain into $5\times5\times25$ subdomains of size $2r\times2r\times2r$. Each of the subdomains that satisfies $(3,3,i)$, $\forall i \in [4,22]\cap\mathbb{Z}$ is heterogeneous and contains a fine discretization to capture the geometry of the cylinder or the ring (about $60K$ discretization elements per subdomain). The surrounding subdomains (a,b,i), for $a \in \{2,4\}$, $b \in \{2,4\}$ and $i \in [4,22]\cap\mathbb{Z}$ are homogeneous and consider discretizations with about $5K$ elements. All the subdomains that lay on the boundary are considered as PML regions (plus all

those with $i = \{2, 3, 23, 24\}$) and have the same discretizations as the homogeneous ones. As a result, around $4m$ of elements are considered of polynomial approximation order of 2. The total number of HDG degrees of freedom for the Maxwell's forward simulation problem is around $40m$ for each of the 6 volumetric components of the fields $\mathbf{E}, \mathbf{H}$ and around $50m$ for the traces. (for order 2, the components defined on the traces have 6 degrees of freedom per face and those on the volumes have 10 degrees of freedom per element), so about $340m$ total degrees of freedom. Neglecting the local problem given the parallelization of HDG we would end up with a global system of $100m$ degrees of freedom for the traces. However, when using MSHDG we only solve on the interfaces of the subdomains where a polynomial approximation order of 10 has been considered and thus the total size of the vector $\mathbf{\Lambda}$ is around $300K$. The system for $\mathbf{\Lambda}$ is denser but given its size it will be easily solved by a sparse direct solver. Note that this particular scalings work for a polynomial approximation order of 2 locally and 10 globally but the contrast of degrees of freedom between statically condensed problems (like HDG or MSCG/MSHDG) and globally coupled methods (like CG) increases as the order grows, as shown in [70], since the traces are defined on 2d elements while the other variables over entire 3d volumes.

Let us consider the numerical simulation of a PC fiber. One class of Photonic Crystal fibers work as an extension of 1d Photonic bandgap structures. In this case, one dimensional multilayered structures are bended around a circular core to form the cladding. These type of fibers work well for the range of frequencies for which the multilayered structure offered a bandgap in 1d. In particular, the extensively used Bragg fibers [158] fall into this category.

More sophisticated PC fibers use the results from 2d Photonic Crystal structures to design the cladding. In particular, when squared or hexagonally symmetric lattices are considered, one can obtain wide ranges of frequencies for which the energy does not propagate. As a result, confinement can be obtained by considering a defect in the structure. Figure 3.4 shows the zoomed geometry and the longitudinal component of the magnetic field for a PC fiber obtained by using a frequency ($\omega a/2\pi c = 0.23$) that is inside the first (TE) gap of a hexagonally a-symmetric 2d Photonic Crystal

with holes of radius $0.3a$ drilled on a silicon core ($\varepsilon = 11.8$). The energy travels only through the homogeneous core in the center of the structure. The PC cladding avoids transverse losses.

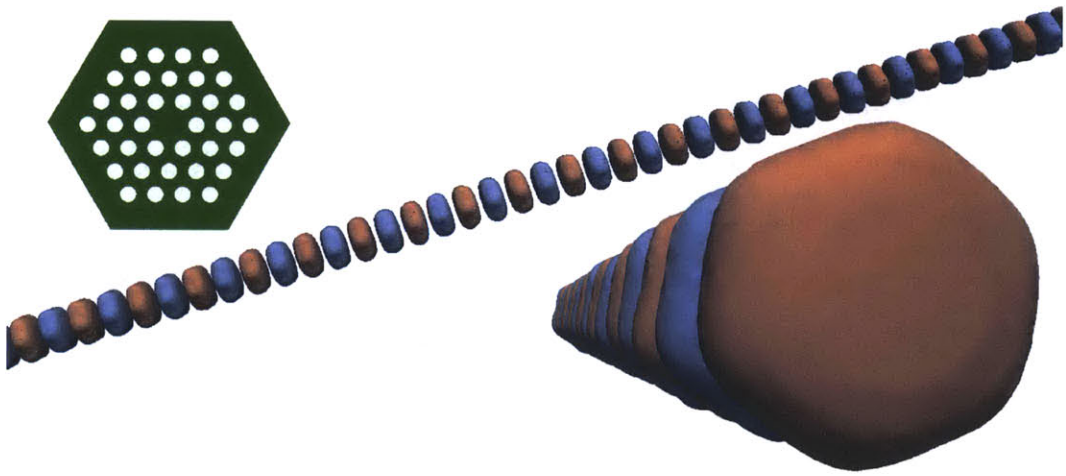

Figure 3.4: H_z wave field of a $\varepsilon_{max} = 11.8$ fiber with a core that is a hexagonally symmetric (period a) Photonic Crystal. Radius of the holes is $r = 0.3a$ and a frequency of $\omega a/2\pi c = 0.23$. In green is shown the zoomed geometry of the cross section.

This PC fiber has also been numerically solved using the MSHDG method. In this case, the domain has been decomposed into $9 \times 9 \times 35$ subdomains with regular cylindric extensions of 2d rhombi. The central layer of subdomains is homogeneous and with $\varepsilon = 11.8$. All surrounding subelements up to distance 3 have a cylindrical air hole drilled in the center of the subdomain and the rest of the elements are again discretized like the central ones (some are homogeneous with silicon, some are homogeneous with air and some correspond to the PMLs). Thus, about $1K$ subelements have holes and thus need around $5K$ HDG discretization elements of order 2 inside whereas the remaining $1.8K$ subelements will contain $1K$ order 2 elements. In total, if we considered an HDG discretization of the whole problem we would have around $70m$ degrees of freedom for each volumetric component of the solution vector and $82m$ for the traces, leading to $580m$ degrees of freedom, $160m$ of which correspond to the global unknowns $\boldsymbol{\Upsilon}$. When using the MSHDG with interfaces of order 6 we end up with a global system of equations of only about $450K$ degrees of freedom for $\boldsymbol{\Lambda}$.

3.5.2 Waveguides on 3d Photonic Crystal slabs

2d Photonic Crystal structures have already been numerically simulated in chapter 2. These are structures that when considered infinitely periodic offer frequency ranges or gaps for which propagation is not allowed. As a result, when linear defects are considered, one can obtain waveguides. However, when the problems are considered in 2d, they are equivalent to assuming that the third component is constant and infinite.

These 2d Photonic Crystals can be of great use for real applications if considered in 3d with a finite thickness. PC slabs can be used as waveguides that tend to offer higher effectiveness under sharp bends than index guiding based fibers [1, 31]. We are thus interested in being able to find the EM wave solutions for two dimensional periodic structures cylindrically extended in the third dimension on a slab with thickness d, typically of the order of a, the 2d period.

First, let us consider 2d structures that led to bandgaps in the TM polarization modes. If we consider a pattern with the symmetries of a square that contains higher index material rods on air, we obtained a 2d frequency gap for $\omega a/2\pi c \in \{0.27, 0.41\}$ if the higher index material was considered silicon $\varepsilon = 11.8$ and $r = 0.2a$. A similar TM-like gap will be obtained if considered on a 3d slab (gap size depends on the thickness d - optimal for $d \sim 2a$ [74, 75]).

Then, when a linear defect is considered in this fully periodic structure, the propagation of electromagnetic waves will only be allowed through it. Note however that the waves will propagate through the air region ($\varepsilon = 1$) and since we now have finite thickness, there will not be confinement on the third dimension and most of the energy will scape from above and below. In order to address this, one can include several layers of a higher index material in the vertical direction such that the frequencies of interest (those in the bandgap of the 2d PC slab) also fall in the gap of the multilayered pattern. Figure 3.5 shows the geometric description of such a slab. Alternatively, confinement could be obtained for specific frequencies if a line of rods of different radius was considered, as in [22].

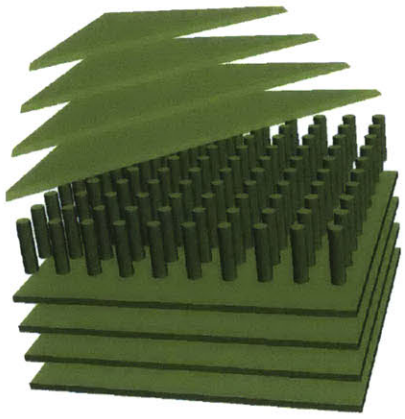

Figure 3.5: Geometric setting of a TM-like PC slab with a higher index material (green) squared lattice rodded structure and vertical confinement through a multi-layered pattern.

We can now use the MSHDG method to obtain the solution fields to Maxwell's equations for this configuration. Let us consider the geometry described in figure 3.5 surrounded by PMLs, where the material different to air is silicon. If one line of vertical rods is removed and a planar wave is sent from one end of the linear defect, we obtain the pattern shown in figure 3.6 for the relevant component E_z. We can see how surface losses show up in contrast to the 2d counterpart shown in figure 2.5. For this simulation, a unitary frequency of $\omega a/2\pi c = 0.35$ has been considered; the radius of the rods corresponds to $0.2a$ being a the periodicity of the 2d PC as well as the distance between centers of consecutive rods. The multilayered structure contains 5 layers of thickness $0.2a$ and periodicity or separation between centers of layers of $0.5a$. The bandgap of the 1d multilayered structure contains inside the bandgap of the 2d periodic Photonic Crystal.

Specifically, the computational domain has been decomposed into $11 \times 7 \times 22$ cubic subregions. Each of the subelements that satisfies $(i, 4, k)$, $\forall k \in [3, 20] \cap \mathbb{Z}$ is heterogeneous and contains a fine discretization to capture the cylindrical rod for $i \in \{2, 3, 4, 5, 7, 8, 9, 10\}$ (about $60K$ discretization elements) and is homogeneous through the line defect, *i.e.* for $i = 6$. All elements of the form (i, j, k), $\forall k \in [3, 20] \cap \mathbb{Z}$, $i \in [2, 10] \cap \mathbb{Z}$ and $j \in \{2, 3, 5, 6\}$ are heterogeneous to capture the multilayered structure. The rest of the surrounding elements correspond to the PML region. Except for

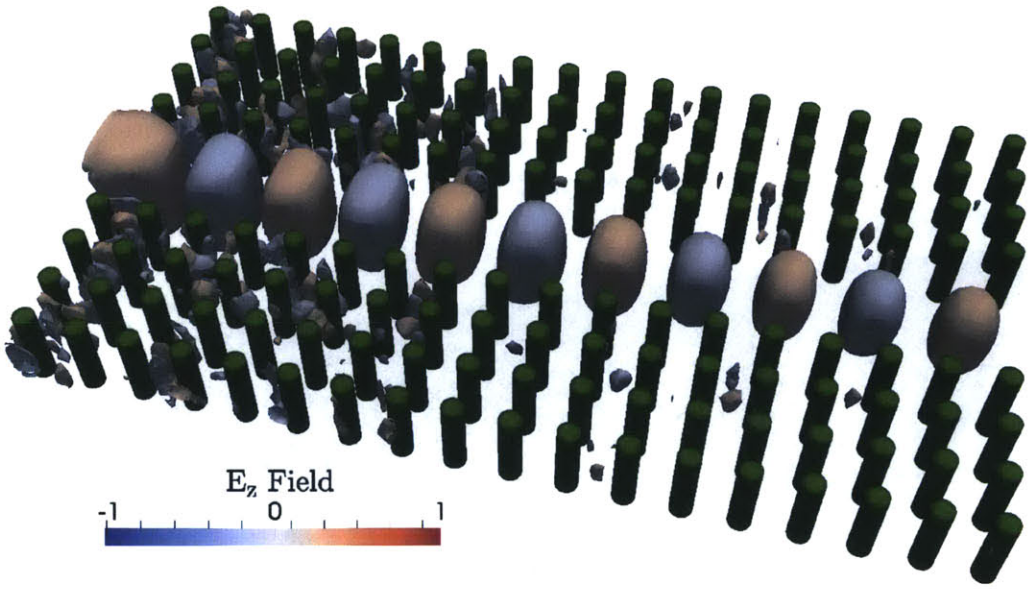

Figure 3.6: E_z wave field for a TM-like PC slab. Frequency $\omega a/2\pi c = 0.35$, $\varepsilon_{high} = 11.8$. Rod radius and multilayer thickness $0.2a$, multilayer period $0.5a$. The multilayered structure in the vertical component is not shown.

those containing a rod, all subdomains have a local discretization of $3K$ elements. In conclusion, an HDG equivalent discretization for the full problem would have around $6.2m$ elements of order 2, leading to $124m$ degrees of freedom per volumetric component of the solution and $148m$ for the traces. That means about $1b$ total degrees of freedom for the system of equations. Exploiting the structure of the HDG method we would actually only solve globally for the two traced components and thus about $300m$ degrees of freedom. Instead, the MSHDG method will solve only for $\mathbf{\Lambda}$ which is only defined on the interfaces of the subelements. There are $5,500$ such interfaces with polynomial approximation order of 10 leading to a total number of degrees of freedom of $1.4m$.

More interestingly we can consider slabs for hexagonally symmetric 2d Photonic Crystals. These periodic structures in 2d show wide bandgaps for TE modes and confine the energy in the higher index material rather than in air. Figure 3.7 shows the H_z wave propagation fields on a silicon PC slab with hexagonally drilled air holes of radius $r = 0.3a$. The thickness of the slab has been considered $d = a$ and the frequency shown in the figure is $\omega a/2\pi c = 0.23$, which falls into the corresponding bandgap.

The losses are minimal, even considering the finite thickness of the slab, which is surrounded by air and then PMLs. This figure shows both the total domain and geometry considered for computational purposes (including PMLs) and the magnetic field inside the real domain (removed inside the PMLs).

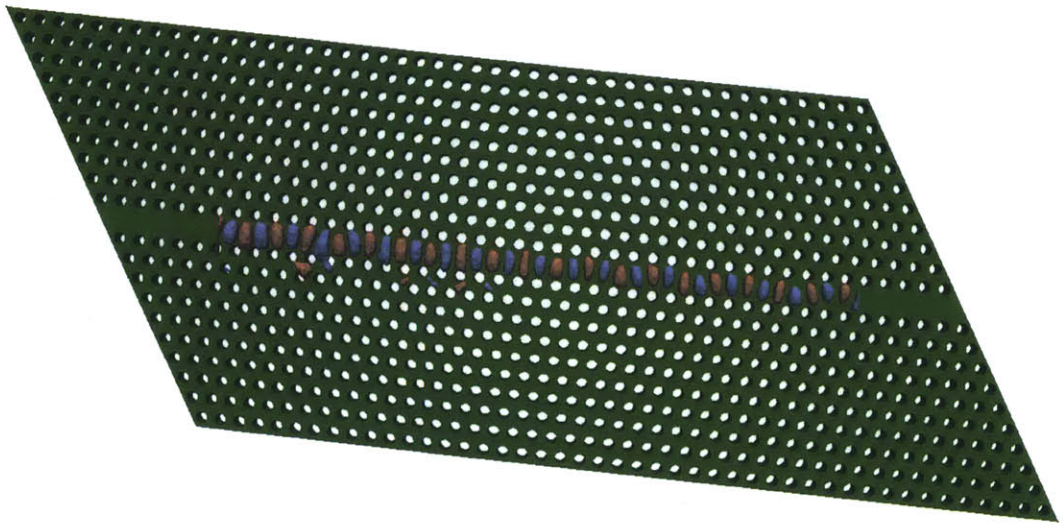

Figure 3.7: H_z wave field for a TE-like PC slab. Frequency $\omega a/2\pi c = 0.23$. Hole radius $0.3a$, slab thickness a. Green for $\varepsilon_{high} = 11.8$.

When actually solving the problem shown in figure 3.7 using the MSHDG method, we have defined a $21 \times 5 \times 45$ decomposition into cylindrical extensions of 2d rhombi that contain one cylindrical hole. The slab is surrounded by one layer of air (as thick as the slab itself) and then PMLs. Once more, if we count all the degrees of freedom for this problem corresponding to the full HDG discretization we end up with $620m$ that are statically condensed to around $150m$ through HDG only or further into $1.1m$ when solving the global problem of the MSHDG formulation.

Finally, in order to validate the numerical results given by the simulation scheme presented in this chapter we try to numerically reproduce some of the experimental results that have been reported in the literature. To that end, we will try to compare our simulation results to the experiments by Chow *et al.* in [30]. In particular, holes of $r = 0.3a$ are drilled on a GaAs slab of thickness $d = 0.5a$. Some frequencies that fall in the bandgap $\omega a/2\pi c \in (0.26 - 0.32)$ are imposed on the right hand side and the transmission fraction for each tested frequency is represented through circles and

squares in figure 3.8.

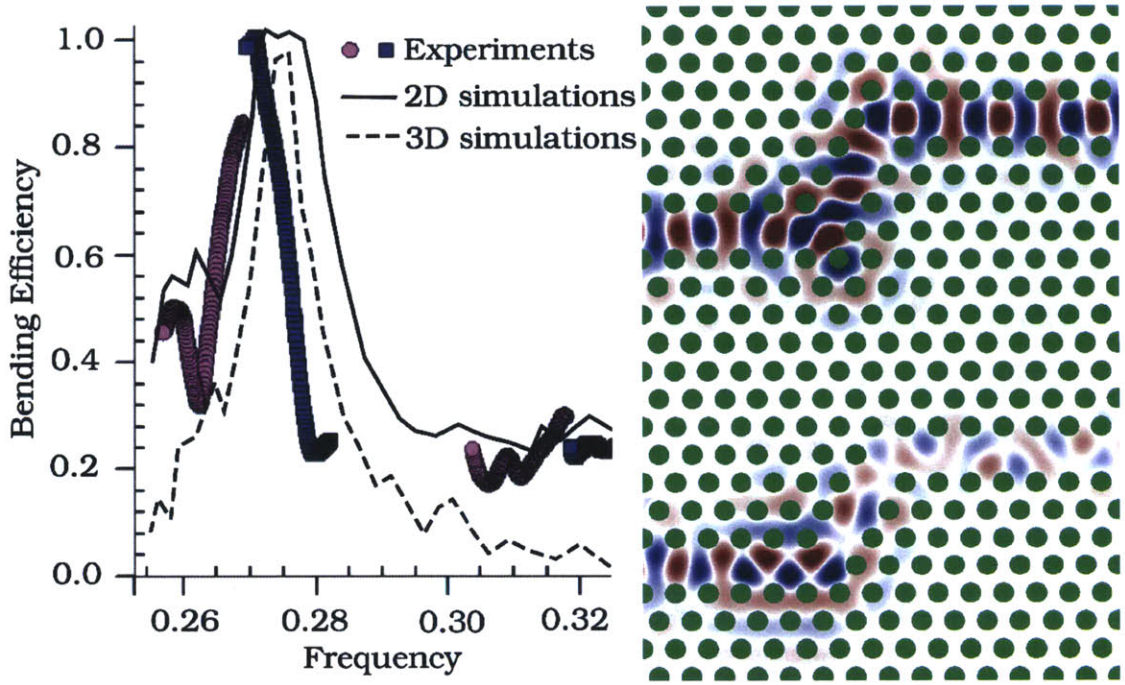

Figure 3.8: Experimental match of 2d and 3d multiscale simulations with respect to results reported in [30]. 3d slice of propagation patterns for $\omega = 0.278$ (top right) and $\omega = 0.30$ (bottom right).

In order to test our numerical approach we first perform 2d simulations of this scenario where the thickness of the slab is considered infinite. The values of the transmission fraction are shown in figure 3.8 through a solid line. Finally, a full 3d simulation is set up with the realistic slab thickness (note that a substrate of Al_xO_y present in the experiments is ignored for simplicity of the simulations). In this case, the transmission fraction, shown through a dashed line in the same figure, decreases from the 2d overestimate since we account for 3d effects and the planar losses above and below the slab.

3.6 Concluding Remarks

This chapter presents the MSHDG method for Maxwell's equations and thereby completes the set of multiscale methods for the simulation of wave propagation source problems in finite domains. Together with the MSCG method for Helmholtz's equations we have developed a collection of simulation tools that are able to provide

accurate numerical representations of wave solutions within acoustics and electromagnetics. In the case of 3d electromagnetics, the overall reduction of degrees of freedom by this two stage hybridization process results in a global system of equations of significantly smaller size than its CG or HDG counterpart. We only solve for two components ($\mathbf{\Lambda}$) on the 2d coarse (chosen for ω) interfaces in contrast to six ($\mathbf{E}, \mathbf{H}$) components on the 3d fine volumes (chosen for the geometry). Furthermore, and as an advantage to an HDG approach, the definition and identification of classes of subdomains at the *macro* discretization level, allows the method to only solve a few subproblems (also efficiently using HDG) and then reutilize the information many times.

We also present several examples where this methodology has been used to efficiently and accurately obtain the wave propagation fields. In particular, index guiding and Photonic Crystal fibers have been analyzed in 3d as well as both TE and TM based waveguides on PC slabs.

Chapter 4

Multiscale CG method for Eigenvalue Helmholtz's problems

> *Somewhere, something incredible is waiting to be known*
>
> **–Carl Sagan**

So far we have introduced multiscale techniques for the direct forward simulation of source problems for a specific frequency. However, waves can often be characterized through an eigenvalue analysis. In particular, a direct inspection of the eigenmodes in elasticity and acoustics provides information about vibrating resonance modes. Similarly, band diagrams in electromagnetics are obtained as solutions to eigenproblems. In this chapter we present an extension of the MSCG method for Helmholtz's equation to eigenvalue problems.

From a numerical linear algebra perspective, there are two classes of problems: solving systems of equations $\{\mathbf{x} \in \mathbb{R}^n : \mathbb{A}\mathbf{x} = \mathbf{f}\}$, and finding eigenvalues and eigenvectors $\{(\gamma, \mathbf{x}) \in \mathbb{R} \times \mathbb{R}^n : \mathbb{A}\mathbf{x} = \gamma\mathbf{x}\}$. The former is covered in chapters 2, 3 and albeit challenging for large problems (and thus our work on reducing the size of the problem exploiting the physics), there exist many algorithms that can find exact solutions in a finite number of steps [153]. The latter is inherently complex since it is as hard as finding roots of polynomials, and thus requires an iterative procedure in general for

sizes strictly larger than 4. As a result, we will develop a multiscale technique that can improve the scalability of eigenproblems so that larger, even 3d, problems can be efficiently solved.

We are interested in finding eigenvalues $\gamma \in \mathbb{R}$ that depend on the wavevector $\mathbf{k}$ and satisfy the following equation for some nonzero eigenfunction u.

$$\left.\begin{aligned} -\nabla \cdot (a(\mathbf{x})\nabla u) &= \gamma(\mathbf{k}) b(\mathbf{x}) u, \quad \text{in } \Omega \\ u &= g_D, \qquad\qquad\quad \text{on } \partial\Omega \end{aligned}\right\} \tag{4.1}$$

As for Helmholtz's equation in chapter 2, here $\Omega \subset \mathbb{R}^d$ is the physical domain with boundary $\partial\Omega$ where the problem is defined. The function g_D defines the Dirichlet boundary conditions, either taken as homogeneous ($g_D = 0$) or, as we shall analyze later, imposing periodicity. Furthermore, $a(\mathbf{x})$ and $b(\mathbf{x})$ are piecewise constant functions that define the material properties.

Let us first solve this eigenvalue problem through a traditional CG approach. To that end, we need to introduce a discretization $\mathcal{T}_h$ of the computational domain Ω and the approximation space given in 2.8. Then, solutions to problem 4.1 can be obtained as $(u_h, \gamma_h) \in X_h \times \mathbb{R}$ such that

$$-(a\nabla u_h, \nabla v)_\Omega = \gamma_h (b u_h, v)_\Omega, \quad \forall v \in X_h(0). \tag{4.2}$$

The algebraic description of this set of equations is given by $\mathbb{A}u_h = \gamma_h \mathbb{M} u_h$, where $\mathbb{A}$ and $\mathbb{M}$ are the CG diffusion and mass matrices, respectively. Furthermore, (ω_h, u_h) are a pair of eigenfrequency and eigenwave, being $\omega_h^2 = \gamma_h$.

The numerical resolution of this problem has been extensively studied for instance in [23,99]. Here, we develop a multiscale approach whereby the final eigenvalue problem is of much smaller size at the price of turning 4.1 into a nonlinear eigenvalue formulation. A similar technique was introduced in [38] where a hybridized representation of 4.1 is introduced. Nevertheless, this HDG-like discretization reduces the size of the final eigenproblem, but it does not exploit the physics of the problem nor reuses the local solutions.

4.1 Multiscale CG method

The main motivation of the multiscale CG method (NMSCG) for eigenvalues is shared with the introduction of this method for the source problem through Helmholtz's equation. We are particularly interested in the simulation of wave phenomena under the presence of discrete heterogeneities. In particular, it is often the case that certain patterns appear repeatedly in the physical domain. It is therefore desirable to have a numerical capability, like the MSCG method, that is able to reuse local substructure of the problem. This will significantly improve scalability and larger problems will be able to be solved for given computational resources.

Through the process of statically condensing all local subdomains (most of them reused) and thus reducing drastically the size of the global system of equations to solve, we traded-off density of the reduced system. However, in the case of eigenvalue problems, there is yet another price to pay: the original eigenvalue problem is transformed into a much smaller one that has a nonlinear dependence on the eigenvalues. As it has been shown in [38] for a similar HDG hybridization of the eigenvalue problem, the resulting nonlinear eigenproblem is guaranteed to converge to the right eigenmodes when the Newton process is started from the linearly approximated eigenmodes.

We now describe both the formulation and the implementation of the NMSCG method for finding eigensolutions of Helmholtz's equation.

4.1.1 Problem Formulation

First of all, let us note that if we write $f = \gamma b(\mathbf{x})u$, equation 4.1 can be written as:

$$\left.\begin{aligned} -\nabla \cdot (a(\mathbf{x})\nabla u) &= f, \quad \text{in } \Omega \\ u &= g_D, \quad \text{on } \partial\Omega \end{aligned}\right\} \tag{4.3}$$

which is a particular case of 2.1 for $k = 0$. This is a key observation since we will use the same derivations that we used in chapter 2 and later replace $f = \gamma b(\mathbf{x})u$. Let us define a collection of triangulations $\mathcal{T}_h^m$ with mesh size h at each subdomain Ω^m such that Ω is the union of all subdomains where the intersection of different subdomains

is a set of zero Lebesgue measure. Let us also introduce the space for the solution field and the flux at each subdomain as:

$$\begin{aligned} X_h^m &= \{v \in C^0(\Omega^m) \ : \ v|_K \in \mathcal{P}_p(K) \text{ for } K \in \mathcal{T}_h^m\}, \\ W_h^m &= \{w \in C^0(\partial\Omega^m) \ : \ w|_{\partial\Omega^m} = v|_{\partial\Omega^m} \text{ for } v \in X_h^m, \forall K \in \mathcal{T}_h^m\}. \end{aligned} \tag{4.4}$$

so that the total solution will be defined in Y_h as follows:

$$Y_h = \{v \in L^2(\Omega) \ : \ v \in C^0(\Omega^m), \text{ and } v|_K \in \mathcal{P}_p(K), \forall K \in \mathcal{T}_h^m, 1 \leq m \leq M\}, \tag{4.5}$$

and the global traces will lie on $V_h = \{\mu \in C^0(\mathcal{E}_h) \ : \ \mu|_e \in \mathcal{P}_p(e), \forall e \in \mathcal{E}_h\}$.

Note that, again, $X_h^m(\eta) = \{v \in X_h^m \ : v = \eta \text{ on } \partial\Omega^m\}$. The set of equations that defines 4.3 can be formulated in a discrete fashion as seeking an approximation $(U_h, \lambda, q_h) \in Y_h \times V_h(g_D) \times W_h$ that satisfies:

$$(a\nabla U_h, \nabla v)_\Omega - \sum_{m=1}^{M} \langle q_h, v\rangle_{\partial\Omega^m} = (f, v)_\Omega, \qquad \forall v \in Y_h, \tag{4.6a}$$

$$U_h = \lambda, \qquad \text{on } \mathcal{E}_h, \tag{4.6b}$$

$$\langle [\![q_h]\!], \mu\rangle_{\mathcal{E}_h} = \langle g_N, \mu\rangle_{\Gamma_N}, \quad \forall \mu \in V_h(0). \tag{4.6c}$$

Recall that this problem can be locally split into a set of Dirichlet problems in the subdomains if $\lambda \in V_h$ is known. Such λ is then obtained through the assembly of the local solutions into the global system. Similar to the multiscale CG method for the source problem presented (see theorem B.3), we arrive at the solution to the discretized formulation: $(U_h, \lambda) \in Y_h \times V_h$ satisfies

$$\begin{aligned} a_h(\lambda, \mu) &= b_h(\mu) \qquad \forall \mu \in V_h(0), \\ U_h &= U_\lambda + U_f. \end{aligned} \tag{4.7}$$

Here, $a_h(\mu, \eta) = (a\nabla U_\mu, \nabla U_\eta)_{\mathcal{T}_h}$ and $b_h(\mu) = (f, U_\mu)_{\mathcal{T}_h}$, for $\mu, \eta \in V_h$. Recall also that U_μ is the solution to the homogeneous source problem with Dirichlet boundary conditions $g_D = \mu$ on $\partial\Omega^m$ at each subdomain while U_f is the solution to the f-source problem with homogeneous Dirichlet boundary conditions. In addition, note that since $f \in L^2(\Omega)$ we can write $U_f = U_W f$, where $U_W : L^2(\Omega) \to Y_h$ is obtained like U_f but for the basis functions describing $L^2(\Omega)$. In other words, instead of directly

obtaining U_f in every subdomain as a solution to

$$\begin{aligned}(a\nabla U_f, \nabla v)_{\Omega^m} - \langle q_f, v\rangle_{\partial\Omega^m} &= (f, v)_{\Omega^m}, \quad \forall v \in X_h^m, \\ U_f &= 0, \qquad\qquad \text{on } \partial\Omega^m,\end{aligned} \tag{4.8}$$

we define $P_h^W f$ as the orthogonal projection of f into Y_h and then obtain $U_W f$ as

$$\begin{aligned}(a\nabla U_W f, \nabla v)_{\Omega^m} - \langle q_W f, v\rangle_{\partial\Omega^m} &= (P_h^W f, v)_{\Omega^m}, \quad \forall v \in X_h^m, \\ U_W f &= 0, \qquad\qquad \text{on } \partial\Omega^m.\end{aligned} \tag{4.9}$$

At this point we wonder whether replacing back $f = \gamma b(\mathbf{x})u$ will provide the expected solutions of the eigenproblem. We know that $a_h(\lambda, \mu) = (f, U_\mu)_{\mathcal{T}_h}, \forall \mu \in V_h$ provides the solution field on the condensed degrees of freedom for the source problem. One can thus think that the global multiscale formulation for the eigenvalue problem given by

$$a_h(\tilde{\lambda}^f, \mu) = \tilde{\gamma}_h (U_{\tilde{\lambda}^f}, U_\mu)_{\mathcal{T}_h}, \tag{4.10}$$

provides the eigenmodes on the reduced degrees of freedom. Note that the eigenvalue $\tilde{\gamma}_h$ lies on $\mathbb{R}$. Let us now compare the solutions given by 4.2 and 4.10. Firstly, both γ_h and $\tilde{\gamma}_h$ belong to $\mathbb{R}$. Also as expected, $u_h \in X_h$ and $\tilde{u}_h \in Y_h$ lie on different spaces, but they can be identified. Another difference appears when looking how many pairs of eigensolutions are given by each problem. The CG discretization provides significantly more pairs than the MSCG given its larger dimension. However, we will see that the multiscale solutions provide the pairs corresponding to the lowest frequency, which are always the meaningful ones.

Last but most important, formulation 4.10 is nonlinear given the fact that $U_{\tilde{\lambda}^f}$ depends on $f(\gamma_h, u_h)$. If this dependence is ignored (assume $f = 0$ only therein) we will obtain some linearized pairs $(\hat{\gamma}_h, \hat{u}_h)$ that will not necessarily coincide with the actual eigenpairs, but they will be used as initial guesses for the nonlinear problem that we now introduce.

Let us now deal with the nonlinearities of the multiscale eigenvalue problem. Note that $U_{\lambda^f} = U_{\lambda^0} + U_W f$, but f needs to be replaced according to $f = \gamma_h b U_h$. We end up with a nonlinear eigenvalue problem (NMSCG) that provides the same lowest frequency pairs $(\gamma_h, u_h) \in \mathbb{R} \times Y_h$ as problem 4.2, through a much smaller set of

equations. These equations are given by (see theorem B.6 in appendix B for the derivations):

$$\begin{aligned} a_h(\lambda,\mu) &= \gamma_h((I-\gamma_h b U_W)^{-1}U_\lambda, U_\mu) \quad \forall \mu \in V_h \\ u_h &= (I-\gamma_h b U_W)^{-1}U_\lambda \end{aligned} \tag{4.11}$$

Note that the dependence on γ_h is nonlinear and therefore the resolution of this set of equations is not trivial. However, as it is proved in [38] for the HDG approach of the eigenvalue problem, the approximation obtained from solving the linear multiscale eigenvalue formulation $\hat{\gamma}_h$ provides a good approximation to the actual eigenvalue γ_h, *i.e.* $|\hat{\gamma}_h - \gamma_h|$ is bounded. In particular, $\hat{\gamma}_h$ will be used as initial guess for the Newton process to solve 4.11.

4.1.2 Implementation

In this section we provide an implementation guide of the NMSCG method for the eigenvalue Helmholtz's equation. As we have discussed before, the problem formulation 4.11 includes a nonlinear eigenvalue equation. However, we have accurate approximations to the eigenmodes provided by the linear eigenproblem 4.10. It is therefore viable to use standard locally convergent methods, such as Newton's method, in order to solve 4.11. Here, we describe the algebraic formulation of the NMSCG as well as the algorithmic approach.

Let us start by denoting with $\mathbb{A}$ the discretization of the bilinear form $a_h(\mu,\eta) = (a\nabla U_\mu, \nabla U_\eta)_\Omega$, where $\mu,\eta \in V_h$ and by $\mathbb{B}(\gamma)$ the matrix corresponding to the right hand side in 4.11 for a given γ. Thus, if $\{\varphi_i\}_{i=1}^N$ denotes the basis functions defining the space V_h, we write:

$$\begin{aligned} \mathbb{A}_{ij} &= (a\nabla U_{\varphi_i}, \nabla U_{\varphi_j})_\Omega, & 1 \le i,j \le N, \\ \mathbb{B}_{ij}(\gamma) &= ((I-\gamma b U_W)^{-1}U_{\varphi_i}, U_{\varphi_j})_\Omega, & 1 \le i,j \le N. \end{aligned} \tag{4.12}$$

Note that if $(\overline{\gamma},\overline{\lambda}) \in \mathbb{R}\times V_h$ is a pair of functions defining an eigensolution of $a_h(\overline{\lambda},\mu) = \overline{\gamma}_h((I-\overline{\gamma}_h b U_W)^{-1}U_{\overline{\lambda}}, U_\mu)$ for all $\mu \in V_h$, then the following equality also holds:

$$\mathbb{A}\overline{\lambda} = \overline{\gamma}\mathbb{B}(\overline{\gamma})\overline{\lambda} \tag{4.13}$$

We will add the condition that the norm of the eigenmodes needs to be one in order to reduce the number of eigenvectors for each eigenvalue from infinity to one. In conclusion, if $\mathbb{M}$ denotes the mass matrix, we can formulate the nonlinear eigenvalue problem as seeking a pair $(\gamma, \lambda) \in \mathbb{R} \times V_h$ such that

$$\mathbf{F}(\gamma, \lambda) = \begin{pmatrix} \mathbb{A}\lambda - \gamma\mathbb{B}(\gamma)\lambda \\ \lambda\mathbb{M}\lambda - 1 \end{pmatrix} = \mathbf{0}. \tag{4.14}$$

If we now consider that we are at a given state (γ_0, λ_0), we can find the next iterate (γ, λ) using Newton's method as

$$\begin{pmatrix} (\mathbb{A} - \gamma_0\mathbb{B}(\gamma_0)(\lambda - \lambda_0) - (\gamma - \gamma_0)\mathbb{C}(\gamma_0)\lambda \\ 2\lambda_0\mathbb{M}(\lambda - \lambda_0) \end{pmatrix} = -\mathbf{F}(\gamma_0, \lambda_0), \tag{4.15}$$

where $\mathbb{C}(\gamma) = \mathbb{B}(\gamma) + \gamma d\mathbb{B}(\gamma)/d\gamma$, which can also be described through:

$$\mathbb{C}_{ij}(\gamma) = ((I - \gamma b U_W)^{-2} U_{\varphi_i}, U_{\varphi_j})_\Omega, \quad 1 \leq i, j \leq N. \tag{4.16}$$

Finally, if we assume that the initial iterate satisfies $\lambda\mathbb{M}\lambda = 1$ (if it doesn't, it can be normalized), we can obtain the next iterate (γ, λ) in 4.15 as:

$$\begin{aligned} (\mathbb{A} - \gamma_0\mathbb{B}(\gamma_0))\lambda &= (\gamma - \gamma_0)\mathbb{C}(\gamma_0)\lambda_0, \\ \lambda_0\mathbb{M}\lambda &= 1. \end{aligned} \tag{4.17}$$

This is the basis of the algorithm. Note that in the first equation above, we see a linear dependence between λ and γ and thus we can decouple both equations, which will simplify the methodology as shown in table 4.1. Note that Newton's method has a quadratic convergence rate provided that we are close enough to the zero sought. Therefore, given the quality of the initial guess, we will get to the correct pair (γ, λ) within a few iterations of the step 3 of the algorithm.

This algorithm provides the eigenpair (γ, λ) around a given initial guess (γ_0, λ_0). Therefore, one needs to apply algorithm 4.1 for every desired mode given by the linear problem 4.10. In order to ensure that all the obtained modes are right, and especially for those that share the eigenvalue (multiplicity larger than 1), it is important to compute the eigenmodes in increasing order (starting from the lowest frequency), and

Table 4.1: Implementation steps of NMSCG method

1. Form and store the matrices $\mathbb{A}$ and $\mathbb{M}$ and get $\mathbb{B}(0)$
2. Get the initial approximation (γ_0, λ_0) from 4.10 as:
$$\mathbb{A}\lambda_0 = \gamma_0 \mathbb{B}(0)\lambda_0$$
3. For $n = 0, 1, 2, 3...$ until convergence, do:
   (a) Form the matrices $\mathbb{B}(\gamma_n)$ and $\mathbb{C}(\gamma_n)$
   (b) Compute $\widehat{\lambda}$ by solving the top equation in 4.17 as:
$$(\mathbb{A} - \gamma_n \mathbb{B}(\gamma_n))\widehat{\lambda} = \mathbb{C}(\gamma_n)\lambda_n$$
   (c) Set $\delta_\gamma = 1/(\widehat{\lambda}\mathbb{M}\lambda_n)$
   (d) Update the eigenvalue as $\gamma_{n+1} = \gamma_n + \delta_\gamma$
   (e) Update the eigenfunction as $\lambda_{n+1} = \delta_\gamma \widehat{\lambda}$

check two things after every solution: (a) the obtained eigenvalue is larger or equal to the previous one $\gamma^n \geq \gamma^{n-1}$ and the distance to the initial guess is small, and (b) the eigenmode is orthogonal to every other previous eigenmode, *i.e.* $u^n \mathbb{M} u^k = 0, \forall k < n$.

4.2 Numerical examples

This section aims to illustrate how the multiscale CG method works for several homogeneous and heterogeneous examples in 2d and 3d. The convergence and accuracy of the method is verified after it has been applied to a homogeneous square $\Omega = (0, 1)^2$ with Dirichlet boundary conditions $g_D = 0$ for which the eigenpairs $\gamma^{mn} = \pi^2(m^2+n^2)$ and $u^{mn} = \sin(m\pi x)\sin(n\pi y)$ are analytically known.

Let us look now at the performance of this algorithm for some examples in 2d. In particular, we first look at the solutions to problem 4.1 for $\Omega = (0, 1)^2 \setminus (0.4, 1)^2$ and $g_D = 0$. Figure 4.1 shows some lowest frequency modes obtained using algorithm 4.1. The color map shows the value $+1$ of the solution field u^n with dark blue and -1 with dark red. Note how all the modes are perpendicular and with increasing frequency, as expected. In fact, as it can be found in the literature, e.g. [74], the eigenproblem 4.1 can also be formulated as the minimization of the Rayleigh quotient, whereby one seeks the smallest resonance frequency such that it is orthogonal to all the existing modes.

This eigenproblem has been solved using the NMSCG method with 5 square subdomains of equal geometry and material properties. Each of this subregions has been

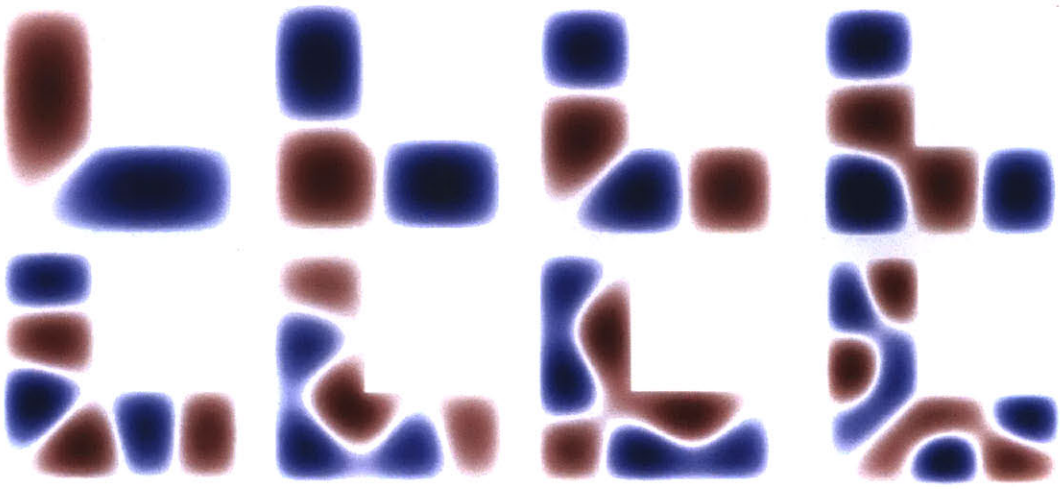

Figure 4.1: Eigenmodes [2, 3, 4, 5; 6, 7, 8, 9] of an homogeneous L shaped domain.

discretized through a structured triangular mesh with 200 elements of order 2. For the traces at the *macro* discretization level, we have used polynomial approximations of order 10. Newton's method reduces the error to machine precision in 3 to 4 iterations for all the 8 eigenpairs computed.

Similarly, in figure 4.2 we show the 8 lowest frequency modes on a square domain $\Omega = (0, 1)^2$. Here, we have considered a heterogeneous medium formed after including a higher propagation speed material in a squared ring inside the domain. In particular $a(\mathbf{x})_{high} = 20$ has been chosen for the ring inside a lower speed material $a(\mathbf{x})_{low} = 1$. The energy thus tends to concentrate inside the intermediate region.

Note how all eigenmodes are perpendicular to each other and they go from low (mode 1) to higher frequency (mode 8). Also, given the symmetry of the domain, we obtain the same eigenvalue or frequency for those modes with multiplicity. In particular, modes 2 and 3 are equivalent and correspond to a 90 degrees shift. Either of them can be considered the second or the third eigenmodes because the frequency is the same. They are clearly orthogonal between them so both are valid eigenmodes. The same thing happens for modes 7 and 8.

The example shown in figure 4.2 has been obtained through the NMSCG method with a 5×5 subdomain decomposition. All subelements are discretized with a structured triangular mesh with 200 elements of order 2. The global traces $\lambda \in V_h$ consider

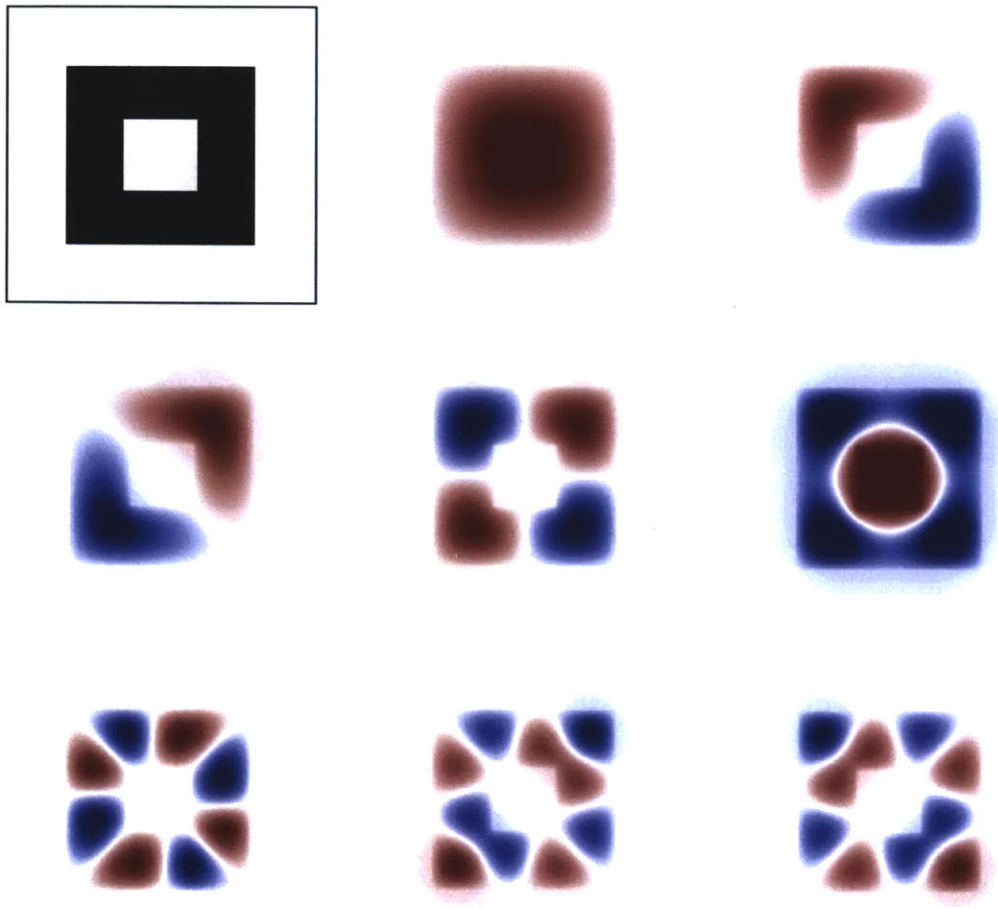

Figure 4.2: Geometry and lowest frequency eigenmodes $[1,2;3,4,5;6,7,8]$ for the heterogeneous square in square in square 2d eigenvalue problem. Black has higher index $a(\mathbf{x})_{high} = 20a(\mathbf{x})_{low}$.

a polynomial approximation order of 10. Overall, the total degrees of freedom are reduced from over $10K$ with a classic CG approach to 660 with NMSCG.

Let us now move forward and use the NMSCG method for 3d problems. The subdomains are cubes discretized into tetrahedra, while the *macro* mesh considers the faces between subelements as squares that are characterized by 2d shape functions.

The first 3d example is a homogeneous cube $\Omega = (0,1)^3$ with homogeneous Dirichlet boundary conditions. The eigenfunctions and eigenvalues for this problem are known analytically and correspond to $u^{lmn} = \sin(l\pi x)\sin(m\pi y)\sin(n\pi z)$ and $\gamma^{lmn} = \pi^2(l^2+m^2+n^2)$, respectively. As a result, the convergence of all eigenmodes can be trivially checked. Figure 4.3 shows several of the lowest (and not so low)

frequency modes obtained using the NMSCG method introduced in this chapter.

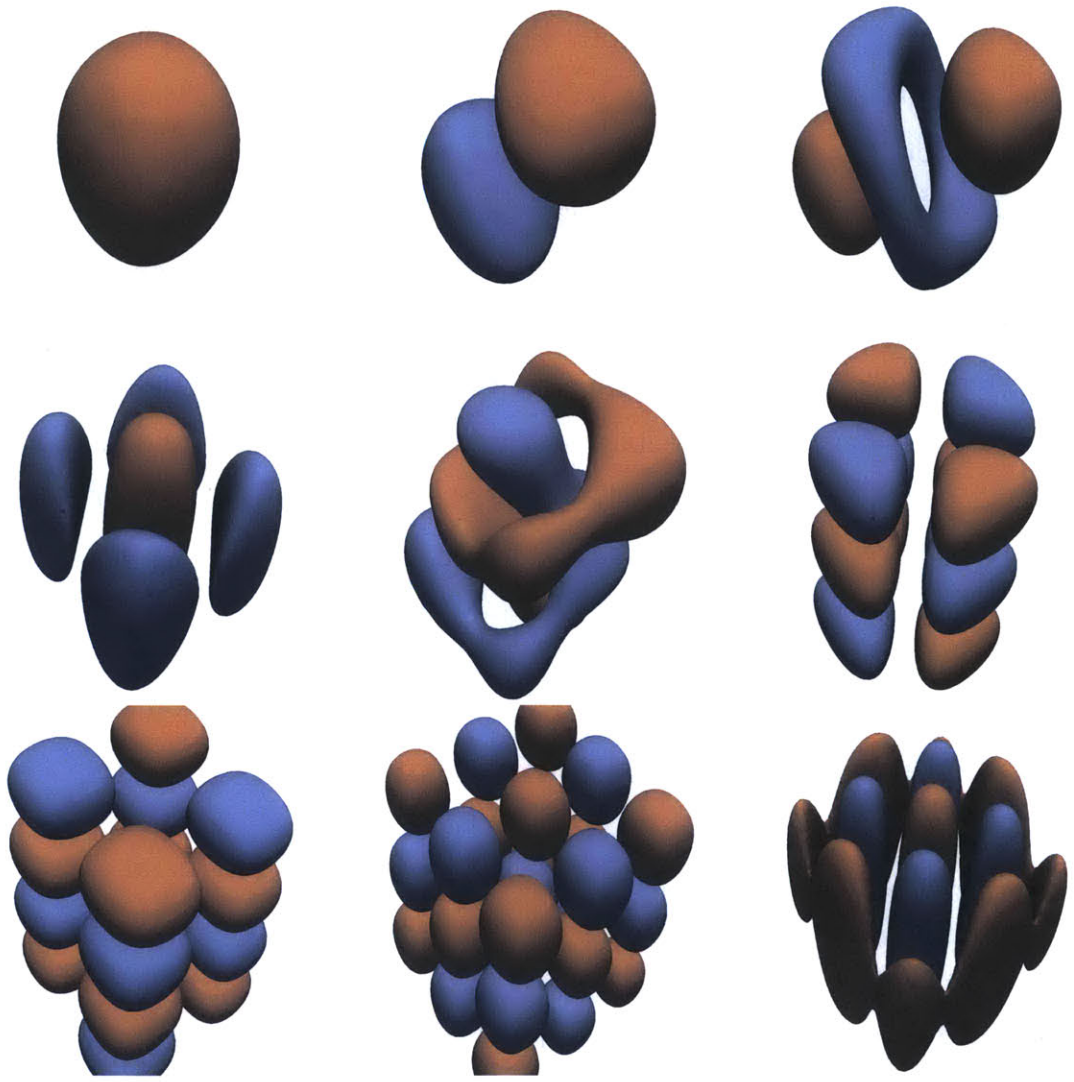

Figure 4.3: Eigenfunctions corresponding to modes $[1, 2, 6; 10, 13, 24; 36, 45, 50]$ on a homogeneous cube. Red/blue contours show the level sets $+0.5/-0.5$, respectively.

In this example, we have considered a *macro* discretization of the domain Ω with $5 \times 5 \times 5$ subdomains, each of which considers a local discretization of 10^3 hexahedra with six tetrahedra per hexahedron. Every subdomain consists of $6K$ elements of order 2 while the global level considers 450 faces of order 10, leading to $55K$ condensed degrees of freedom. Additionally, Newton's method converges quadratically and thus reduces the error of the eigenmodes down to machine precision within only 4 iterations of step 3 in algorithm 4.1.

Finally, we consider an example in 3d with heterogeneous materials. More specifically, let us include a hollow cube of higher propagation speed $a(\mathbf{x}) = 20$ in the host material $a(\mathbf{x}) = 1$. The exact structure is of following form: insert a $1 \times 1 \times 1$ host material cube in a $3 \times 3 \times 3$ higher propagation speed material, which at the same time is fit inside a $5 \times 5 \times 5$ host material cube. It actually corresponds to the natural 3d extension of the problem shown in figure 4.2.

This example is then solved using the NMSCG method with the exact same discretization as the $(0,1)^3$ homogeneous cube of the previous example. However, two different representatives of local problems need to be solved and stored: an homogeneous $a(\mathbf{x}) = 1$ subelement as well as an homogeneous $a(\mathbf{x}) = 20$ subdomain. After assembling them accordingly and solving equations 4.11 with the NMSCG method, we obtain the resonance modes for the 12 lowest frequencies that are shown in figure 4.3. Note how the eigenfunctions concentrate in the higher propagation speed material since it requires less energy than expanding into the host material.

4.3 Eigenvalues for periodic problems

Another eigenvalue problem of significant interest for the acoustics and electromagnetics community involves considering a periodic setting. In particular, heterogeneous geometries that show discrete translational symmetries offer remarkable capabilities, such as bandgaps, or ranges of frequencies that do not allow transmission. More specifically, if $a(\mathbf{x})$ is the inhomogeneous material property of interest, we will say that the geometry offers discrete translational symmetry in direction $\widehat{\boldsymbol{\alpha}}$ if there exists $\alpha \in \mathbb{R}$ such that $a(\mathbf{x}) = a(\mathbf{x} + n\boldsymbol{\alpha})$, for all $n \in \mathbb{Z}$ where $\boldsymbol{\alpha} = \alpha\widehat{\boldsymbol{\alpha}}$.

Under these circumstances, one can use Bloch's theorem to reduce the solution waves of interest to a segment in direction $\widehat{\boldsymbol{\alpha}}$ representative of all the space, *i.e.* essentially all points in a segment of length α in direction $\widehat{\boldsymbol{\alpha}}$. Equivalently, one can define the reciprocal lattice to be the reduced set of wavevectors $\mathbf{k}$ that provide different Bloch states. Note that whenever equation 4.1 is solved for wavevectors $\mathbf{k}_1, \mathbf{k}_2$ that satisfy $\mathbf{k}_1 \cdot \widehat{\boldsymbol{\alpha}} = \mathbf{k}_2 \cdot \widehat{\boldsymbol{\alpha}} + m(2\pi/\alpha)$, for $m \in \mathbb{Z}$, we obtain the same solutions.

In addition, when rotational and mirror symmetries are considered, one can further

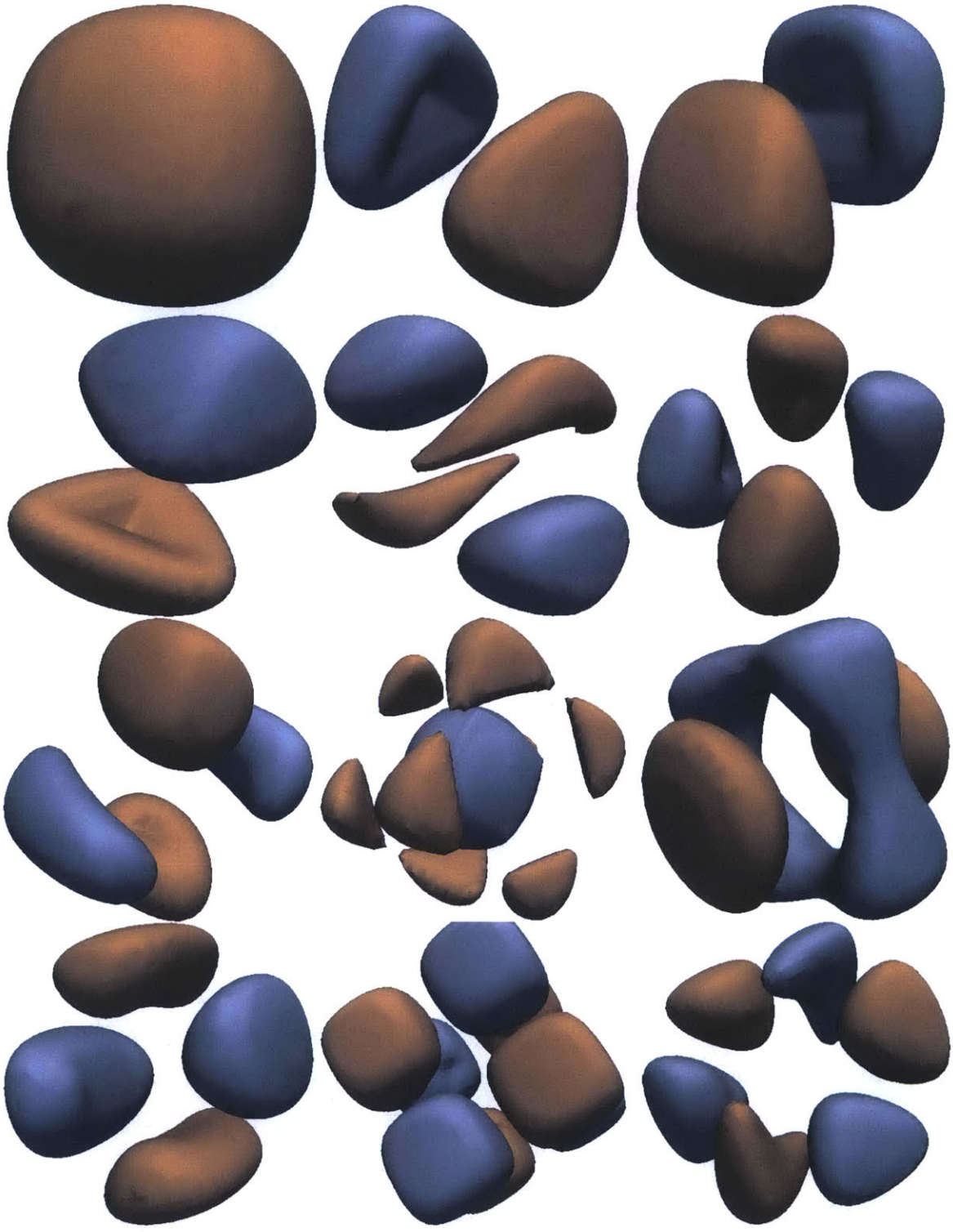

Figure 4.4: Eigenfunctions corresponding to modes $[1, 2, 3; 4, 5, 6; 7, 8, 9; 10, 11, 12]$ on a heterogeneous cube (cube in $a(\mathbf{x}) = 20$ cube in cube). Red/blue contours show the level sets $+0.5/-0.5$, respectively.

reduce the reciprocal lattice to what is called the irreducible Brillouin zone, which is the only region where solutions are different. Any other reciprocal lattice point $\mathbf{k}$ can be then trivially derived. Finally, it has been shown that obtaining the solutions for lattice points $\mathbf{k}$ that lay on the boundary of the irreducible Brillouin zone is enough to characterize all solutions, see for instance [74].

In order to solve equation 4.1 for different values of the wavevector $\mathbf{k}$ in the reciprocal lattice, we use the Bloch's wave decomposition $u(\mathbf{x}) = e^{i\mathbf{k}\cdot\mathbf{x}}u_{\mathbf{k}}(\mathbf{r})$ and solve for $u_{\mathbf{k}}$ instead. When plugging this identity in equation 4.1 one obtains a new PDE that can be written as

$$-(\nabla + i\mathbf{k}) \cdot (a(\mathbf{x})(\nabla + i\mathbf{k})u_{\mathbf{k}}) = \gamma_{\mathbf{k}} b(\mathbf{x}) u_{\mathbf{k}}. \tag{4.18}$$

We thus observe that solving for each Bloch's state $u_{\mathbf{k}}$ is equivalent to solving for the original field u provided that the PDE operator ∇ is switched for the $\mathbf{k}$ dependent operator $\nabla + i\mathbf{k}$. In order to show how the actual implementation changes, let us first note that 4.18 can also be written as:

$$-\nabla \cdot (a(\mathbf{x})\nabla u_{\mathbf{k}}) + 2i\mathbf{k}a(\mathbf{x})\nabla u_{\mathbf{k}} - k^2 a(\mathbf{x})u_{\mathbf{k}} = \gamma_{\mathbf{k}}(\mathbf{k})b(\mathbf{x})u_{\mathbf{k}} \tag{4.19}$$

where $k = |\mathbf{k}|$. Then, after considering the multiscale discretization procedure we obtain 4.7 where $a_h(\mu, \eta)$ now takes the following expression:

$$a_h(\mu, \eta) = (a(\mathbf{x})\nabla U_\mu, \nabla U_\eta)_{\mathcal{T}_h} + 2i(a(\mathbf{x})\nabla U_\mu, U_\eta)_{\mathcal{T}_h} \cdot \mathbf{k} - k^2 (a(\mathbf{x})U_\mu, U_\eta)_{\mathcal{T}_h}. \tag{4.20}$$

As a result, the matrix $\mathbb{A}_{ij}$ previously introduced will now consider the extra terms derived from the discrete translational symmetry. If we denote by $\mathbb{K}_{ij} = (\nabla U_{\varphi_i}, \nabla U_{\varphi_j})_\Omega$ the diffusion matrix, by $\mathbb{T}_{ij} = (\nabla U_{\varphi_i}, U_{\varphi_j})_\Omega$ the convection matrix and by $\mathbb{M}_{ij} = (U_{\varphi_i}, U_{\varphi_j})_\Omega$ the mass matrix, for all $1 \leq i, j \leq N$, we can obtain $\mathbb{A}^{\mathbf{k}} = a(\mathbf{x})[\mathbb{K} + 2i\mathbb{T} \cdot \mathbf{k} - k^2\mathbb{M}]$ and thus the eigenvalue problem can be again written as:

$$\mathbb{A}^{\mathbf{k}} u_{\mathbf{k}} = \gamma_{\mathbf{k}} \mathbb{M} u_{\mathbf{k}}. \tag{4.21}$$

After fixing a given $\mathbf{k}$ on the boundary of the irreducible Brillouin zone, we form the previous equation and proceed with algorithm 4.1 to find the eigenpair $\gamma_{\mathbf{k}}, u_{\mathbf{k}}$

corresponding to the Bloch's states.

Let us now show some 2d examples of band diagrams obtained with NMSCG for periodic settings. In particular, we have obtained the dispersion relations for two cases that are well known in the literature: rods on a square and on a hexagonally symmetric lattice. More specifically, figure 4.5 shows the dispersion relation as well as some TM polarized lower resonance modes in the case of a $\varepsilon = 8.9$ rods on air distributed according to the symmetries of the square. Analogously, figure 4.6 shows again some TM lower eigenmodes together with the dispersion relation of the a hexagonally symmetric distribution of rods.

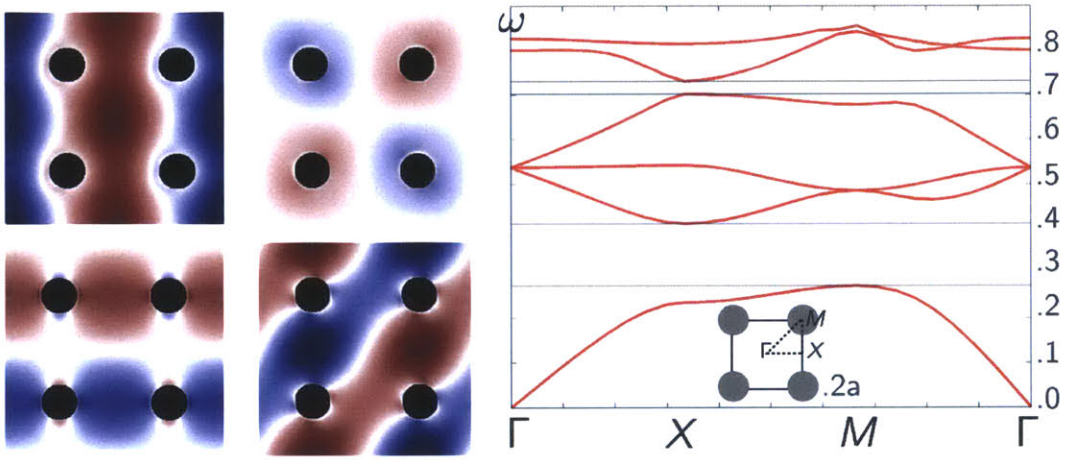

Figure 4.5: Left: some low frequency eigenmodes at M and X. Right: band diagram of a periodic structure with aluminum rods of radius $0.2a$ on a square lattice. E field for TM polarized modes. Inset shows the IBZ and corner points Γ, M, X.

4.4 Concluding Remarks

In this chapter we have extended the multiscale CG methodology for the numerical solution of eigenvalue problems. In particular, we have seen how the same numerical technique that in chapter 2 has been introduced for the source problem, provides a nonlinear eigenvalue formulation. The size of the eigenproblem is significantly reduced due to the static condensation technique presented at a price of turning the eigenproblem nonlinear. However, since good initial guesses are obtained through the linearized eigenvalue formulation 4.10, the nonlinear problem in 4.11 can be efficiently

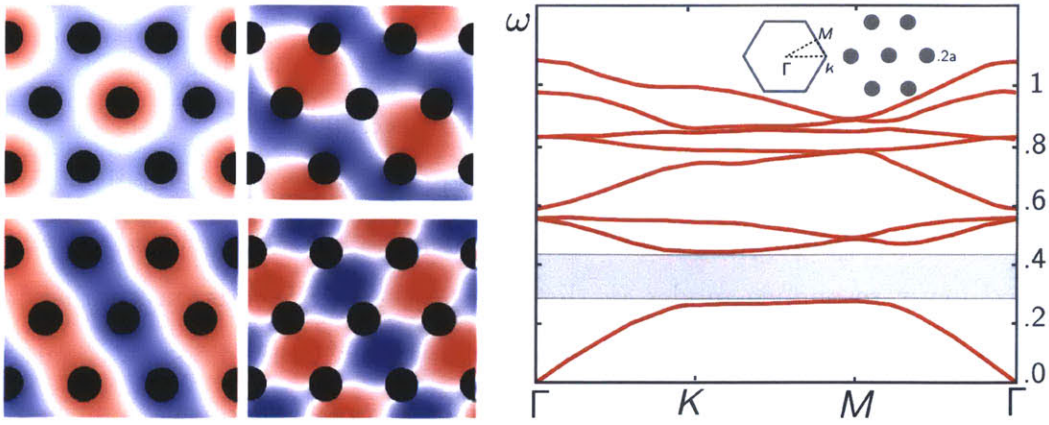

Figure 4.6: Left: some low frequency eigenmodes at M and K. Right: band diagram of a periodic structure with aluminum rods of radius $0.2a$ on a hexagonal lattice. E field for TM polarized modes. Inset shows the IBZ and corner points Γ, K, M.

solved using just a few iterations of Newton's method.

Note that the cost of algorithm 4.1 is determined by (a) solving the linear eigenproblem, which is computationally cheaper than the original CG eigenvalue formulation 4.2 given its reduced size, and (b) performing a few Newton iterations where the inverse of $(I - \gamma b U_W)$ as well as a system resolution are required every time. In particular, we can see how the inverse can be computed efficiency given the block structure of U_W, which is independent for each subdomain. In addition, the system resolution is only defined on the degrees of freedom on the *macro* discretization traces V_h and hence can be solved efficiently for relatively large problems.

Furthermore, the NMSCG method has also been extended for eigenvalue formulations that consider periodic boundary conditions and thus use Bloch's theorem. In this case, the derivative operator is changed according to $\nabla \leftarrow (\nabla + i\mathbf{k})$, where $\mathbf{k}$ is the wavevector, and eigenpairs can be found for all values of $\mathbf{k}$ in a given irreducible Brillouin zone. This analysis allows us to obtain band diagrams for different heterogeneous periodic settings and thereby numerically estimate photonic or phononic bandgaps. Similarly, we could obtain band diagrams for 3d Photonic Crystals but Maxwell's equations in 3d cannot be reduced to Helmholtz. The nonlinear multiscale methodology could be extended for these problems using the multiscale HDG method presented in chapter 3, but this work is beyond the scope of this thesis.

Finally, we have shown the performance of this methodology through the simulation of an homogeneous L shape in 3d and a cube in 3d, where some low frequency modes (and not so low) have been accurately found. Similarly, the eigensolutions on a 2d square in a 3d cube with heterogeneous inclusions have also been analyzed. The NMSCG for a 2d periodic setting has been considered in order to obtain the dispersion relations of TM polarized structures with rods in both square and hexagonal symmetries.

Chapter 5

Binary Optimization for Wave Propagation

> *Tell me, and I'll forget. Show me, and I may remember. Involve me, and I'll understand.*
>
> **–Chinese Proverb**

Wave phenomena in acoustics, elastodynamics and electromagnetics have been widely studied in the last two decades. These phenomena have found numerous applications in many domains of engineering. The family of problems related to wave propagation has lately increased due to the growing interest in *meta*material design. However, when trying to design manufacturable and realizable *meta*materials and other structured materials, physical and mathematical intuition are insufficient by themselves. One is therefore led to consider optimization-based approaches to design. Very often, the optimization problems that arise are of a discrete nature, leading to binary or mixed-integer optimization models. Indeed, in considering design variables that correspond to a finite set of pixels, the optimization problem is to choose between two given materials for each pixel, hence the typical application problem results in the need to solve discrete optimization models. In this chapter, a binary optimization model that combines local search approximations with reduced basis is presented. Solutions obtained using this methodology tend to produce local optima that improve the objective function value at least two orders of magnitude. Our approach utilizes

a reduced basis projected problem [12] and binary generalized gradients to ensure feasibility of all solutions.

This chapter is organized as follows. First, we describe the optimization procedure as a coordinate descent method where the computation of the binary gradient is discussed. Then, a reduced basis method is introduced in order to increase the efficiency of the algorithm while ensuring a satisfactory level of accuracy. Finally, two illustrative examples are shown: a 1d frequency filter and an optimal 2d heat exchanger.

5.1 Coordinate Descent method

Let us consider ε to be the property defining each material. Since the problem will be governed by a Partial Differential Equation of the form $F(u(\varepsilon), \varepsilon) = 0$, the discretized PDE (with N_{el} discretized elements) can be expressed as a system of the form $\mathbb{A}(\boldsymbol{\varepsilon})\mathbf{u} = \mathbf{f}$ in the linear case. Moreover, using the multiscale numerical methodology, the system matrix can be written as $\mathbb{A}(\boldsymbol{\varepsilon}) = \sum_{q=1}^{N_{el}} \varepsilon^q \mathbb{A}_q$. More generally, if at the subdomain level the material distribution is still heterogeneous, then the terms $\varepsilon^q \mathbb{A}_q$ become $\mathbb{A}_q(\varepsilon^q)$. In any case, $\boldsymbol{\varepsilon}$ is piecewise constant and the local discretization (CG or HDG) will therein use an equivalent linear decomposition. Let $J(\mathbf{u}(\boldsymbol{\varepsilon}), \boldsymbol{\varepsilon})$ be the objective function measuring the deviation to a desired and known solution -often just $J(\mathbf{u}(\boldsymbol{\varepsilon}), \boldsymbol{\varepsilon}) = \mathbb{I}_{\Omega_{obj}} ||\mathbf{u}(\boldsymbol{\varepsilon}) - \mathbf{u}_0||_2^2$ and denoted by $J(\mathbf{u}(\boldsymbol{\varepsilon}))$; $\mathbb{I}_{\Omega_{obj}}$ is the indicator function-, then the structured material design optimization problem can be written in the following general form:

$$\begin{aligned} \min_{\boldsymbol{\varepsilon}, \mathbf{u}} \quad & J(\mathbf{u}(\boldsymbol{\varepsilon}), \boldsymbol{\varepsilon}) \\ \text{s.t.} \quad & \left(\sum_{q=1}^{N_{el}} \varepsilon^q \mathbb{A}_q \right) \mathbf{u} = \mathbf{f} \\ & \boldsymbol{\varepsilon} \in \{\varepsilon_{min}, \varepsilon_{max}\}^{N_{el}} \end{aligned} \tag{5.1}$$

Problem 5.1 arises in many areas of applied engineering such as inverse problems, shape optimization, topology optimization, optimal design and optimal control. However, the PDE constraints and the nature of the design variables often pose several

significant challenges for contemporary optimization methods. First, the problem is nonlinear and non-convex due to the dependence of the objective function on the design variables through the underlying PDEs. Second, the problem is large-scale since the discretization of the PDEs leads to a large system of equations, which often involves up to several hundreds of millions of degrees of freedom for some 3d problems. And third, if some (or all) design variables can only take on integer or discrete values then problem 5.1 becomes a mixed-integer nonlinear optimization problem. Unfortunately, while discrete variables are common in practice, their presence causes the optimization problem to be NP-hard in general. It is therefore necessary to develop a suitable approximation of the problem in order to achieve computational tractability in practice.

In the context of developing an approximation and in order to solve the optimization problem stated in 5.1 we first need to devise an optimization method that ensures that the binary constraints $\boldsymbol{\varepsilon} \in \{\varepsilon_{\min}, \varepsilon_{\max}\}^{N_{el}}$ are satisfied. To that end, we introduce the notion of binary gradient.

5.1.1 Computation of the Binary Gradient

Gradients are crucial for optimization purposes since they provide information about sensitivities or variations in the objective function when arbitrarily small changes in each of the design variables are taken. Nevertheless, since we want to maintain binary solutions throughout the optimization process, we will only allow directional changes that leave a current pixel as is, or that flip componentwise $\varepsilon_{\min}$ to $\varepsilon_{\max}$ or *viceversa*. This can be done by defining the sensitivities of our objective function according to unitary changes instead of differential changes. To accomplish this we introduce the following binary generalized gradient:

$$G_m(\boldsymbol{\varepsilon}) = \frac{\Delta J(\mathbf{u}(\boldsymbol{\varepsilon}))}{\Delta \varepsilon} = \frac{J(\mathbf{u}(\boldsymbol{\chi}^m)) - J(\mathbf{u}(\boldsymbol{\varepsilon}))}{\varepsilon_{\max} - \varepsilon_{\min}}, \tag{5.2}$$

for $m = 1, \ldots, N_{el}$, where $\boldsymbol{\chi}^m$ just changes the m^{th} component of $\boldsymbol{\varepsilon}$ from $\varepsilon_{\min}$ to $\varepsilon_{\max}$ or *vice versa*. We then choose the descent direction that provides the smallest value of $\mathbf{G}(\boldsymbol{\varepsilon})$ and advance in that descent direction iteratively, as in any steepest descent

algorithm for continuous optimization. This amounts to changing one pixel at a time.

This binary notion of a gradient differs from the natural one in the sense that infinitesimal perturbations are no longer considered. The smallest change considered for the design variables is already $|\boldsymbol{\varepsilon}| \in \mathcal{O}(1)$, and therefore, there are no analytic guarantees that, unless $G_m = 0$ for every direction, there exists a direction for which $G_m < 0$ and thus the objective function value can be locally decreased. However, if the size of the pixels could be arbitrarily small, we recover a differential definition of the topological gradient as discussed in [67]. All in all, we can rely on this gradient providing an improvement direction when it exists for the resolution of the pixelization. As a result, different pixel discretizations may lead to totally different directions.

5.1.2 Coordinate Descent Binary Optimization Algorithm

To sum up the foregoing, table 5.1 provides the optimization algorithm. Let p be the number of pixels considered, $\boldsymbol{\varepsilon}(i)$ represent the i^{th} state of the optimal design and $\mathbf{u}_j$ the solution for the current design variable state $\boldsymbol{\varepsilon}(i)$ changing its j^{th} coordinate from ε_{max} to ε_{min} or viceversa.

Table 5.1: Flowchart of the binary optimization algorithm

1-	Start with an initial guess $\boldsymbol{\varepsilon}(0)$,
2-	Obtain the objective function value $J(\mathbf{u}(\boldsymbol{\varepsilon}(0)))$,
3-	Compute the solutions $\mathbf{u}_1 \cdots \mathbf{u}_p$ exactly,
4-	Compute the binary sensitivities G_m using 5.2,
5-	If $G_m \geq 0, \forall m$, end.
	Else, pick $\bar{m} = \arg\min_m G_m$ and set $\boldsymbol{\varepsilon}(0) \leftarrow \boldsymbol{\chi}^{\bar{m}}$,
6-	Go to 2,

Note that this algorithm is actually a local search approach to the binary optimization problem 5.1. The complexity of binary optimization problems is in general NP-hard, which implies that whenever the variable set is large, the problem is intractable. In our case, the parameter space is very large, typically about 500 for 2d problems and over a thousand for 3d problems, so branch and bound or branch and cut algorithms would have a computational cost of $\mathcal{O}(2^{1,000}s) \simeq \mathcal{O}(10^{300}s)$, where

$\mathcal{O}(s)$ is the cost of a single simulation. Local search methods are approximation algorithms that are commonly used to solve these problems for the balance they offer between cost and optimality. However, they are only able to guarantee local minima, the quality of which really depend on the size and quality of the neighborhoods considered.

Material design optimization is yet harder, since unless the local search neighborhoods are very small, the computational burden of the local search methodology itself is excessive. Note that p full numerical simulation problems need to be solved every time step 3 of algorithm 5.1 is reached. In developing an approximation to the problem 5.1, we want to be able to efficiently compute the true objective function value at neighboring states. That is, for a given value of the design variables $\boldsymbol{\varepsilon}'$ that is close to already known states $\boldsymbol{\varepsilon}$, we want to compute $\mathbf{u}(\boldsymbol{\varepsilon}')$ inexpensively and then obtain $J(\mathbf{u}(\boldsymbol{\varepsilon}'))$. To that end, we will solve the PDE through a reduced basis approach, as introduced in section 5.2.

5.1.3 Exploiting the Multiscale simulations

The constraint defining the physics of the problem through a PDE becomes a large system of equations that needs to be satisfied for every parameter state $\boldsymbol{\varepsilon}$. This PDE is enforced through a discretization using the multiscale methods described in chapter 2. Note that every time that a solution $\mathbf{u}(\boldsymbol{\varepsilon})$ is calculated, the discretized system needs to be formed, assembled and solved for the corresponding $\boldsymbol{\varepsilon}$. This set of operations can require significant resources, both in memory and time. As a consequence, a clever organization and storage of data becomes crucial.

The multiscale discretization methods previously presented offer the possibility of computing and storing solutions to one representative of each local problem class. Moreover, $\boldsymbol{\varepsilon}$ is piecewise constant and thus it can be pulled out from the local contributions to the assembled global matrix. Since most of the time we are interested in solving problems corresponding to neighboring solutions, only a handful of components of $\boldsymbol{\varepsilon}$ will change to form $\boldsymbol{\varepsilon}'$, say that subdomain q^* changes from ε_1 to ε_2. In this way, forming $\mathbb{A}(\boldsymbol{\varepsilon}')$ only requires considering the local subproblem that changes,

and then performing the following operation:

$$\mathbb{A}(\boldsymbol{\varepsilon}') = \mathbb{A}(\boldsymbol{\varepsilon}) + (\varepsilon_2 - \varepsilon_1)\mathbb{A}_{q^*}, \tag{5.3}$$

in contrast to recomputing all of the local matrices and assembling $\mathbb{A}(\boldsymbol{\varepsilon}')$ from scratch. This approach will thus reduce significantly the computational work for the local problem solution and global system assembly; the solution of the global system of equations is still required.

Similarly, other optimization problems will focus on one subelement as a design region (say q^*) and the pixelization will be therein. For these problems, computing the solution at a neighbor requires changing ε inside the local problem, either the CG or HDG solver. In this case, we can formulate the global assembly as:

$$\mathbb{A}(\boldsymbol{\varepsilon}) = \sum_{q=1, q\neq q^*}^{N_{el}} \mathbb{A}_q(\varepsilon^q) + \mathbb{A}_{q^*}(\varepsilon^{q^*}) =: \overline{\mathbb{A}} + \mathbb{A}_{q^*}(\varepsilon^{q^*}) \tag{5.4}$$

In this manner, the first term ($\overline{\mathbb{A}}$) is always the same for all possible problems considered in the simulation and we thus store $\overline{\mathbb{A}}$ once. Then, for every neighbor solution, the corresponding $\mathbb{A}_{q^*}(\varepsilon^{q^*})$ needs to be obtained and added to $\overline{\mathbb{A}}$ in order to get the global assembled matrix. Obtaining $\mathbb{A}_{q^*}(\varepsilon^{q^*})$ can be done inexpensively, since the same trick applies at the CG/HDG level given that ε^{q^*} will also be elementwise constant there. Once more, the global system needs to be solved.

5.2 A Reduced Basis method

The reduced basis (RB) method can be used to provide an accurate, reliable and efficient solution of parametrized PDEs, see [6, 24] and further references therein. Material design or optimal control problems involve large numbers of parameters, and thus computing sensitivities or solutions for the entire family of parameters is seldom achievable.

Let $n \leq p \leq N_{el}$ be the number of regions where a material parameter needs to be chosen and $k < n$ be a certain positive integer corresponding to the reduced basis size. For a given feasible pattern $\boldsymbol{\varepsilon} \in \{\varepsilon_{\min}, \varepsilon_{\max}\}^n$, let $\overline{\mathbf{u}}_1 = \mathbf{u}(\boldsymbol{\varepsilon})$, and define

$k-1$ neighbors $\boldsymbol{\varepsilon}^j$ by just perturbing a small number of pixels from either $\varepsilon_{\min}$ to $\varepsilon_{\max}$ or *vice versa*, and then compute their corresponding solutions $\overline{\mathbf{u}}_j = \mathbf{u}(\boldsymbol{\varepsilon}^j)$ for $j = 2, \ldots, k$. We now define the reduced basis as $\overline{\boldsymbol{\Phi}} = span[\overline{\mathbf{u}}_1, \overline{\mathbf{u}}_2, \ldots, \overline{\mathbf{u}}_k] \in \mathbb{R}^{N_{el} \times k}$, so that we can then obtain an approximate version of any given $\mathbf{u}(\boldsymbol{\varepsilon})$ as $\tilde{\mathbf{u}}(\boldsymbol{\varepsilon})$ through:

$$\tilde{\mathbf{u}}(\boldsymbol{\varepsilon}) = \sum_{j=1}^{k} \alpha_j(\boldsymbol{\varepsilon}) \overline{\mathbf{u}}^k = \overline{\boldsymbol{\Phi}} \boldsymbol{\alpha}(\boldsymbol{\varepsilon}). \tag{5.5}$$

The discretized system can now be approximately solved as $\overline{\boldsymbol{\Phi}}^t \mathbb{A}(\boldsymbol{\varepsilon}) \overline{\boldsymbol{\Phi}} \boldsymbol{\alpha}(\boldsymbol{\varepsilon}) = \overline{\boldsymbol{\Phi}}^t \mathbf{f}$. Finally, let us define $\tilde{\mathbb{A}}_q = \overline{\boldsymbol{\Phi}}^t \mathbb{A}_q \overline{\boldsymbol{\Phi}} \in \mathbb{R}^{k \times k}$, for $1 \leq q \leq n$ and also $\tilde{\mathbf{f}} = \overline{\boldsymbol{\Phi}}^t \mathbf{f} \in \mathbb{R}^k$. We will be able to approximately solve the governing system as:

$$\left(\sum_{q=1}^{n} \tilde{\mathbb{A}}_q(\varepsilon^q) \right) \boldsymbol{\alpha} = \tilde{\mathbf{f}} \tag{5.6}$$

which is a $k \times k$ system in contrast to the original $N_{el} \times N_{el}$ system. We finally recover $\tilde{\mathbf{u}}(\boldsymbol{\varepsilon}) = \overline{\boldsymbol{\Phi}} \boldsymbol{\alpha}(\boldsymbol{\varepsilon})$.

Once the RB-approximations are computed for all neighbors, we can compute $\tilde{G}_m$ as a computationally less expensive approximation of G_m as follows:

$$\tilde{G}_m(\boldsymbol{\varepsilon}) = \frac{\Delta J(\tilde{\mathbf{u}}(\boldsymbol{\varepsilon}))}{\Delta \varepsilon} = \frac{J(\tilde{\mathbf{u}}(\boldsymbol{\chi}^m)) - J(\mathbf{u}(\boldsymbol{\varepsilon}))}{\varepsilon_{\max} - \varepsilon_{\min}}. \tag{5.7}$$

The quality of the reduced basis approximation is defined by the error indicator $||\mathbf{u} - \tilde{\mathbf{u}}||_2^2$. However, the analytic bounds available for this class of problems are often very conservative [12]. For the equations of interest in this thesis, we will rely on approximating parameter states that are very close in order to keep the error indicator as low as possible. In addition, the quality of the approximation will be checked at each iteration and, if not sufficient, the basis will be enhanced with more empirical solution states.

5.2.1 Optimization Algorithm with Reduced Basis

Now that reduced basis approximations have been introduced, we can use this method to help improve the efficiency of algorithm 5.1 by computing the binary gradient using a RB-approximate solution instead of full size simulations. Table 5.2 summarizes the

optimization algorithm based on the ideas described above. Let $l \leq k$ be the size of the initial basis computed around a starting guess $\boldsymbol{\varepsilon}(0)$ and let the subindex of $\boldsymbol{\varepsilon}$ denote the vector position in the basis Φ.

Table 5.2: Binary Optimization algorithm with Reduced Basis

1-	Start with an initial guess $\boldsymbol{\varepsilon}(0)$,
2-	Obtain the objective function value $J(\mathbf{u}(\boldsymbol{\varepsilon}(0)))$,
3-	Pick $\boldsymbol{\varepsilon}_1, \boldsymbol{\varepsilon}_2, \cdots, \boldsymbol{\varepsilon}_l$ neighbors of $\boldsymbol{\varepsilon}(0)$ randomly,
4-	Compute solutions $\mathbf{u}_1 \cdots \mathbf{u}_l$ for $\boldsymbol{\varepsilon}_1 \cdots \boldsymbol{\varepsilon}_l$ exactly,
5-	Form $\Phi(\boldsymbol{\varepsilon}(0)) = [\mathbf{u}(\boldsymbol{\varepsilon}_1) \cdots \mathbf{u}(\boldsymbol{\varepsilon}_l))]$ and obtain $\tilde{u}(\boldsymbol{\varepsilon}(0))$,
6-	If $size\{\Phi(\boldsymbol{\varepsilon}(0))\} = p > k$, remove the $m = p - k$ elements with smallest values of $\alpha_m(\boldsymbol{\varepsilon}(0))$,
7-	Orthonormalize Φ using Gram-Schmidt,
8-	If $\|\|\tilde{\mathbf{u}}(\boldsymbol{\varepsilon}(0)) - \mathbf{u}(\boldsymbol{\varepsilon}(0))\| > 10^{-2}$ Replace r basis elements with smallest $\alpha_r(\boldsymbol{\varepsilon})$, Go to 5,
9-	Compute binary sensitivities $\tilde{G}_m$ using 5.7,
10-	If $\tilde{G}_m \geq 0, \forall m$, end. Else, pick $\bar{m} = \arg\min_m \tilde{G}_m$ and set $\boldsymbol{\varepsilon}(0) \leftarrow \boldsymbol{\chi}^{\bar{m}}$,
11-	Compute l_0 random neighbors and update $\Phi(\boldsymbol{\varepsilon}(0)) \leftarrow [\Phi(\boldsymbol{\varepsilon}(0))\ \mathbf{u}(\boldsymbol{\varepsilon}_1) \cdots \mathbf{u}(\boldsymbol{\varepsilon}_{l_0}))]$, Go to 6,

Note that in contrast to algorithm 5.1, in algorithm 5.2 $\tilde{\mathbf{G}}$ is computed through approximate values of the objective function $J(\tilde{\mathbf{u}}(\boldsymbol{\varepsilon}))$. Sensitivity information in the binary gradient will be reliable provided the quality of the basis is acceptable, which is checked at step 8. We expect the reduced basis to work well for neighbors $\boldsymbol{\varepsilon}'$ that only differ from the current state $\boldsymbol{\varepsilon}$ in one single pixel if it provides accurate approximations for that state itself. In addition, note that step 6 removes the least relevant components of the basis to keep its size constant, and step 7 uses a Gram-Schmidt orthonormalization process to improve the quality of the basis, or equivalently, to reduce the condition number of Φ, which will help obtain $\tilde{\mathbf{u}}$ through 5.6. In addition, r is a small number (typically less than the number of cores available, so that the cost is equivalent to only one simulation given the trivial parallelization) that corresponds to the exact solutions computed every time the basis needs to be updated.

By joining together the multiscale simulation properties and the reduced basis

theory, we seek a balance wherein the approximate local search algorithm will find local optima of quality with tractable computational cost. Several starting guesses, as well as further enhancements - like letting the solution worsen slightly to avoid getting stuck at a bad local optima - might be required for some applications. It is also important to point out that stages 4, 9 and 11 of algorithm 5.2 are completely parallelizable.

5.2.2 Eigenvalue Optimization algorithm

In chapter 4 the multiscale techniques have been extended to a nonlinear solver of Helmholtz's eigenvalue formulation. This equation governs the same family of problems but now considers the frequency as unknown and looks for the resonance modes or eigenmodes. Many desired materials within the wave propagation context may also be designed for a certain behavior or properties of their eigenmodes and eigenvalues. This is the case of PC bandgap optimization [96], among many others.

The binary optimization algorithm introduced herein can easily be extended to problems governed by the eigenvalue Helmholtz equation, provided an efficient solver is available. Given the parallelisms of the multiscale techniques for force and eigenvalue problems, all the discussed methodologies (binary gradient and reduced basis) can be trivially extended. All in all, we now seek to solve:

$$\begin{aligned} \min_{\boldsymbol{\varepsilon},\mathbf{u},\lambda} \quad & J(\mathbf{u}(\boldsymbol{\varepsilon}),\lambda(\boldsymbol{\varepsilon}),\boldsymbol{\varepsilon}) \\ \text{s.t.} \quad & \left(\sum_{q=1}^{N_{el}} \mathbb{A}_q(\varepsilon^q)\right)\mathbf{u} = \lambda\left(\sum_{q=1}^{N_{el}} \mathbb{M}_q(\varepsilon^q)\right)\mathbf{u} \\ & \boldsymbol{\varepsilon} \in \{\varepsilon_{min},\varepsilon_{max}\}^{N_{el}} \end{aligned} \tag{5.8}$$

Once more, the subdomain decomposition will let us write $\mathbb{A}(\boldsymbol{\varepsilon}) = \mathbb{A}_q(\varepsilon^q)$, where ε^q could be a single value if the entire subdomain is homogeneous, or, equivalently to the previous case, a piecewise constant function if the pixels are considered inside each subelement. In addition, for these kind of design optimization problems, the objective function will typically seek to maximize or minimize certain eigenvalues or combinations of them, thereby resulting in the dependence of J on λ.

The implementation of the binary eigenvalue optimization algorithm is equivalent to table 5.1 if reduced basis are not used or to table 5.2 if they are used. Note however, that step 3 of the former and 4 of the latter will now require the resolution of a nonlinear eigenvalue problem using the methodology introduced in chapter 4.

5.3 Examples

The full power of this methodology shows up especially when combined with the simulation methods introduced in chapters 2, 3, and 4, since structured materials for large wave propagation problems can be designed. Some of them are analyzed deeply in chapter 6. However, in order to show the effectiveness of the reduced basis coordinate descent optimization procedure we show two illustrative examples. First, we have applied the methodology described herein to the design of one-dimensional frequency filters. In particular, we have succeeded in designing a binary material that is able to totally reflect a given frequency considering the finiteness of the domain. This phenomenon is well-known if the pattern is considered periodic and therefore infinite but is not so well-known for finite structures. And second, we apply the same optimization procedure to a 2-dimensional problem governed by the heat transfer equation.

5.3.1 1d Frequency Filter

Frequency filters are devices that, when set for a given specific frequency or range of frequencies, are able to completely reflect the incoming waves (prohibiting propagation) while not affecting (or just allowing some propagation for) other frequencies. These devices are well known within the electromagnetics community. They have been of crucial use for the design of important novel devices and applications such as waveguides, switches, fibers and optical buffers, see for instance [97]. However, most of the results reported in the literature so far have ignored the discrete nature of the the design variables, thereby often leading to either suboptimal or impractical designs.

For the case of PC, frequency filters are a particular case of photonic bandgap

problems. Luckily, when seeking materials that show photonic bandgaps, optimal solutions assuming infinite periodicity turn out to be binary, as observed by Lord Rayleigh as early as 1888 [131]. Nevertheless, if we are interested in extending the conceptual ideas introduced by the photonic bandgap to other wave phenomena or want to consider finite domains, we need to mitigate the non-binary nature of the continuously relaxed optimal solution. Consequently, if we want to obtain satisfactory solutions −especially fabricability−, we must effectively constrain solutions to be binary.

Figure 5.1: Frequency filter geometry in 1d. C is the pixelized design region and B is the objective subdomain.

Figure 5.1 outlines the 1d frequency filter application. We focus here on the case of electromagnetic waves, for which the governing equation in the frequency domain is exactly the Helmholtz equation. Furthermore, ε^{-1} is the inverse permittivity or the square of the speed of light for TM modes. Equivalently, if we were to consider TE modes in electromagnetics or acoustic problems, the definition of ε would have another meaning. The formulation of the optimization problem can be written as follows:

$$\begin{aligned} \min_{\boldsymbol{\varepsilon},\mathbf{u}} \quad & J(\mathbf{u}(\boldsymbol{\varepsilon}),\boldsymbol{\varepsilon}) \\ \text{s.t.} \quad & \left(\sum_{q=1}^{N_{el}} \varepsilon^q \mathbb{A}_q\right)\mathbf{u} = \mathbf{f} \\ & \boldsymbol{\varepsilon} \in \{\varepsilon_{min}, \varepsilon_{max}\}^n \end{aligned} \tag{5.9}$$

where $J(\mathbf{u}(\boldsymbol{\varepsilon}),\boldsymbol{\varepsilon}) = \mathbb{I}_B||\mathbf{u}(\boldsymbol{\varepsilon})||_2^2$. The first set of constraints corresponds to the numerical discretization using the multiscale CG method of Helmholtz's equation governing the TM modes of electromagnetic waves:

$$\begin{aligned} \nabla \cdot \varepsilon \nabla u + k^2 u = 0 \quad & \text{in } \Omega \\ \nabla u \cdot \mathbf{n} - iku = \nabla u^{inc} \cdot \mathbf{n} - iku^{inc} \quad & \text{on } \partial\Omega \end{aligned} \tag{5.10}$$

and the two chosen materials have permittivities $\varepsilon_{min} = 1$ and $\varepsilon_{max} = 13$. In addition,

the incident frequency corresponds to a wavelength of 1/3 the width of the design region. Note that here, for simplicity, first-order absorbing boundary conditions have been considered where u^{inc} corresponds to the incident wave.

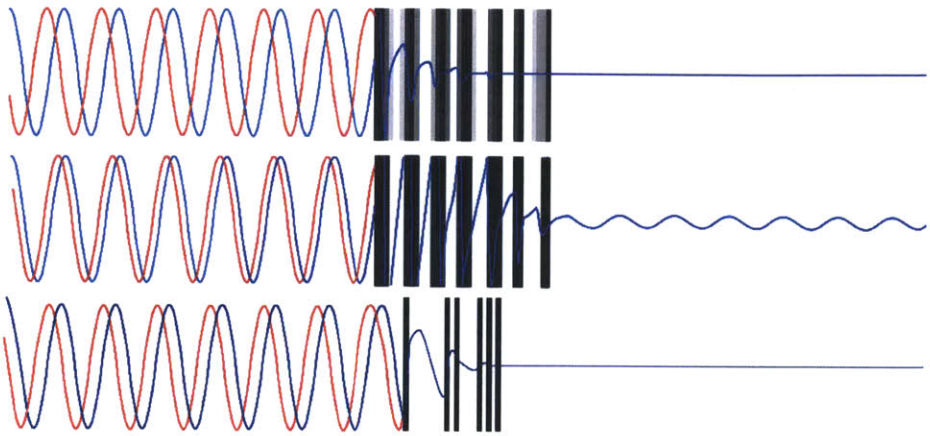

Figure 5.2: 1-dimensional frequency filter. Right-propagating wave color coded in blue, reflecting left-propagating wave in red. Top: continuous optimum; Center: Discrete projection; Bottom: binary optimum. Frequency corresponding to 3 wavelengths fitting the design region.

Figure 5.2 shows the optimized structures obtained with (top) the standard adjoint method with relaxation of the integer constraints, see [139] for the full derivations regarding the adjoint method for this particular example, (center) the adjoint method with enforcement of the integer constraints via projection into the closest binary value, and (bottom) our proposed method. Our method produces exactly (up to machine precision error) an optimal binary solution within only six iterations, whereas the standard adjoint method computes an optimal solution which is not binary (and thus not fabricable nor acceptable) and the projected adjoint method produces a binary solution which is not optimal (and thus is an inferior design).

The multiscale discretization considered for this problem has 500 high order elements (order 3 providing 15 inner and boundary degrees of freedom per element) of which the central 100 constitute the 50 pixels we seek to design (each subelement is the rectangle formed by combining two discretization triangles). All possible combinations of solutions would lead to $2^{50} > 10^{13}$ problems and thus would be intractable to solve. In spite of the high material and solution field contrasts, grid convergence

of the discretization has been achieved thanks to the high order used in the MSCG method.

This computational result is especially encouraging since the basis need only contain about 10 solution vectors to guarantee a very good approximation of the exact solutions. As a result, the systems of equations used to compute the binary gradient never exceeded a 10×10 system. Furthermore the binary gradient computation which is of order $\mathcal{O}(n)$ (recall n is the number of pixels or more generally the parameter space size) took less time than one single MSCG computation took. It is also encouraging that the binary gradient computations are extremely accurate, with values of the error indicator $||\mathbf{G} - \tilde{\mathbf{G}}||_1 \in \mathcal{O}(10^{-7})$.

5.3.2 Heat transfer problem

In a similar setting but in a 2-dimensional context we consider a heat transfer problem. In this case, the governing equation is not Helmholtz's or Maxwell's and does not represent a hyperbolic solution or a wave. However, this elliptic and coercive equation provides useful insights on the optimization procedure since solutions are smoother and less sensitive to parameter changes. Easily, we can just adapt Helmholtz's equation's formulation by removing the term $-k^2u$. The problem we want to solve can be written as:

$$\begin{aligned} -\nabla \cdot \varepsilon \nabla u &= f \quad \text{in } \Omega = [0,1]^2 \\ u &= 0 \quad \text{on } \partial\Omega \end{aligned} \tag{5.11}$$

where ε represents the thermal conductivity of the material and f is the source term, which has been chosen to be $f = 2\pi^2 \sin(\pi x)\sin(\pi y)$. We seek a 2-dimensional pattern maximizing the heat transferred from the Dirichlet boundaries of a square plate into the center point. Note that if we do not include an extra volume constraint, the optimum will be obtained when the material used everywhere corresponds to the one holding a larger thermal conductivity. Therefore the overall setting of the optimization problem for this case will be slightly modified by the volume constraint. If we choose $0 \leq \beta \leq 1$ as the volume fraction that we are allowed to change, the problem can be written as:

$$
\begin{aligned}
\min_{\boldsymbol{\varepsilon},\mathbf{u}} \quad & J(\mathbf{u}(\boldsymbol{\varepsilon}),\boldsymbol{\varepsilon}) \\
\text{s.t.} \quad & \left(\sum_{q=1}^{N_{el}} \varepsilon^q \mathbb{A}_q\right)\mathbf{u} = \mathbf{f} \\
& \frac{1}{N_{el}}\sum_{q=1}^{N_{el}} \frac{\varepsilon^q - \varepsilon_{\min}}{\varepsilon_{\max} - \varepsilon_{\min}} \leq \beta \\
& \boldsymbol{\varepsilon} \in \{\varepsilon_{min}, \varepsilon_{max}\}^{N_{el}}
\end{aligned}
\tag{5.12}
$$

A square domain with a 20 by 20 pixelization has been considered with $\varepsilon_{\min} = 1$ and $\varepsilon_{\max} = 2$. Firstly, the problem has been solved considering the continuous relaxation $\boldsymbol{\varepsilon} \in [\varepsilon_{\min}, \varepsilon_{\max}]^{N_{el}}$ through the Adjoint method. In a very similar way to the frequency filter problem and analogously derived as in [139], the Adjoint method provides us with the sensitivities and thus the direction to take at each iterate. We can then pick a small enough step size (using a line search), take the step, and iterate until we reach the final optimal and feasible solution determined by the volume constraint. Such a constraint can also be dualized into the objective function and one can instead solve the new optimization problem with the modified objective:

$$
J(\mathbf{u}(\boldsymbol{\varepsilon}),\boldsymbol{\varepsilon}) = ||\mathbf{u}(\boldsymbol{\varepsilon})||_2^2 + \lambda\left(\sum_{q=1}^{N_{el}} \frac{\varepsilon^q - \varepsilon_{\min}}{\varepsilon_{\max} - \varepsilon_{\min}} - \beta N_{el}\right) \tag{5.13}
$$

and the original set of constraints. If the value of λ is chosen large enough, both strategies lead to the same solutions since the volume constraint (or dualized penalization) is satisfied with equality (or becomes zero, respectively).

Note that for the homogeneous case with $\varepsilon = 1$ the analytical solution $u = \sin(\pi x)\sin(\pi y)$ to 5.11 provides a squared volume of $J(u(1)) = 0.5$, whereas if we pick the homogeneous material with $\varepsilon = 2$ the objective drops down to the value $J(u(2)) = 0.0625$, which would be the optimal solution had not we considered the volume constraints.

Results have been computed for $\beta = 0.44$ and $\beta = 0.58$ and are shown in Figure 5.3. We can observe how the continuous optimal solutions provide a non-binary solution that after projection into $\boldsymbol{\varepsilon} \in \{1,2\}^{N_{el}}$ and respecting the volume constraint, the resulting solution is suboptimal. In fact, for the case $\beta = 0.44$ the optimal

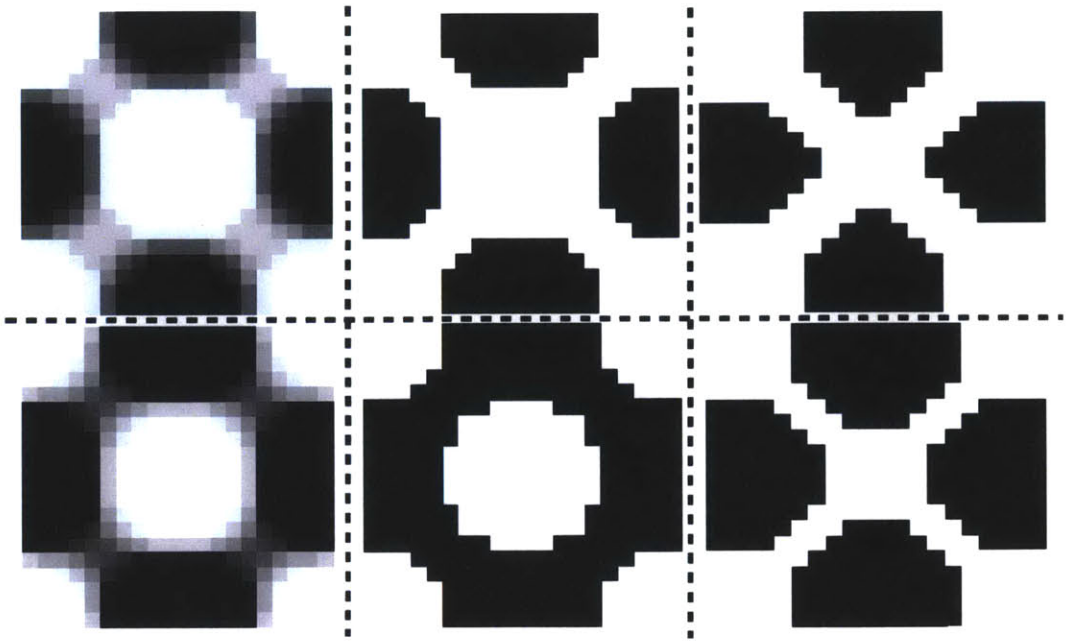

Figure 5.3: 2-dimensional heat transfer problem. Top figures correspond to $\beta = 0.44$ and bottom figures to $\beta = 0.58$. Left figures show the continuous solutions obtained through the Adjoint method, middle figures the projected binary solutions, and right figures show the binary solutions after using our proposed method.

objective value is $J(\mathbf{u}(\boldsymbol{\varepsilon}_{cont})) = ||\mathbf{u}||_2^2 = 0.0973$ in the continuous case, and once projected it increases to $J(\mathbf{u}(\varepsilon_{proj})) = 0.1020$. We can do better, as our binary optimum demonstrates, obtaining $J(\mathbf{u}(\boldsymbol{\varepsilon}_{bin})) = 0.0991$. Table 5.3 summarizes the different values obtained for each case. Note how our methodology decreases the solution gap with respect to the continuous optima [21] from 4.83% to 1.85% when $\beta = 0.44$ and from 6.06% to 1.08% for $\beta = 0.56$. However, since the lowest solution gap or integrality gap is unknown for this problem, we do not know if there exist solutions that could yet reduce the gap further with this pixelization.

Table 5.3: Results for the Heat transfer problem

β	J_{cont}	J_{proj}	Gap	J_{bin}	Gap
0%	0.5	0.5	0%	0.5	0%
44%	0.0973	0.1020	4.83%	0.0991	1.85%
58%	0.0825	0.0875	6.06%	0.0834	1.08%
100%	0.0625	0.0625	0%	0.0625	0%

Note how the binary optimum is more than 2.5 times closer to the continuous

optima than the projected binary solution for $\beta = 0.44$ and more than 5.5 times closer for $\beta = 0.58$. With a given material allowance we have thus been able to provide a binary pattern, easily fabricable, which is very close to the non-fabricable continuous optimum for the same volume of material.

Moreover, regarding this last example, the computational cost is $\mathcal{O}(k{\cdot}m{\cdot}s_n)$, where k is the number of iterations, m the size of the neighborhood and $\mathcal{O}(s_n)$ is the cost of solving the numerical problem for a given combination of the n pixels. In contrast, the theoretical complexity of this problem is NP hard and the computational cost is given by $\mathcal{O}(\exp(s_n))$, if the complete binary search/enumeration is performed. More specifically the number of pixels can be reduced to $n = 50$ exploiting the symmetries of the problem. The proposed algorithm provides the reported binary solutions after $k \simeq 20$ iterations. In addition, for every single system resolution (there are $m = \mathcal{O}(n)$ of those) the computational complexity of a classic FE method is $\mathcal{O}(s_n) = \mathcal{O}(n^2)$ while the proposed reduced basis approach reduces the total cost from $\mathcal{O}(m \cdot s_n) = \mathcal{O}(n^3)$ to a few resolutions ($r << n$) of the exact system $\mathcal{O}(r \cdot n^2)$ plus m solutions of the reduced $r \times r$ system, so $\mathcal{O}(m \cdot r^2)$. As a result, since $r = \mathcal{O}(1)$ the RB method computational cost is $\mathcal{O}(n^2)$. To sum up, table 5.4 summarizes the computational costs and properties of the different optimization algorithms.

Table 5.4: Summary of optimization algorithms

Algorithm	Cost	Comments
Branch and Bound	$\mathcal{O}(\exp(s_n))$	global optimum but totally intractable
Local Search w/o RB	$\mathcal{O}(k \cdot n \cdot s_n)$	deterministic local optimum, often intractable
Local Search w/ RB	$\mathcal{O}(k \cdot s_n)$	randomized local optimum, typically tractable

Heat transfer as an eigenvalue problem

This same problem can also be formulated in terms of eigenvalues. In this way, we will also illustrate how the binary optimization algorithm works for eigenproblems. Note that minimizing $||\mathbf{u}(\boldsymbol{\epsilon})||_2^2$ is equivalent to maximizing the heat that gets transferred through a square domain, from the center out or *vice versa*. In conclusion, maximizing all the eigenvalues of the heat equation 5.11 will equivalently maximize

the transmission of heat or also minimize the value of $||\mathbf{u}(\boldsymbol{\varepsilon})||_2^2$ in the domain for a given initial Dirichlet source.

All in all, let us first organize the eigenvalues of the heat equation in increasing order:

$$\omega_{n-1} \geq \omega_{n-2} \geq \cdots \geq \omega_2 \geq \omega_1 \geq 0 \tag{5.14}$$

and define an auxiliary variable λ such that $0 \leq \lambda \leq \omega_1$. In this way, increasing λ will push the smallest eigenvalue up, and subsequently all of them. Now we can formulate the optimization problem as:

$$\begin{aligned} \max_{\boldsymbol{\varepsilon},\mathbf{u},\lambda} \quad & \lambda \\ \text{s.t.} \quad & \mathbb{A}(\boldsymbol{\varepsilon})\mathbf{u} = \lambda \mathbb{M}\mathbf{u} \\ & \frac{1}{N_{el}} \sum_{q=1}^{N_{el}} \frac{\varepsilon^q - \varepsilon_{\min}}{\varepsilon_{\max} - \varepsilon_{\min}} \leq \beta \\ & \boldsymbol{\varepsilon} \in \{\varepsilon_{min}, \varepsilon_{max}\}^{N_{el}} \end{aligned} \tag{5.15}$$

Problem 5.15 can now be solved using the binary eigenvalue optimization algorithm and the solution obtained matches exactly those obtained when solving 5.12. Similarly, the linear relaxation (that is replacing the binary constraints by $\varepsilon_{\min} \leq \varepsilon^q \leq \varepsilon_{\max}$, for all q) can be solved using SDP techniques, see [119], and the the same continuous optima have been obtained for each value of β, as expected.

When the binary optimization methodology has been used in the heat transfer problem, both for the source problem formulation as well as the dual eigenvalue formulation, the same optimal pattern has always been obtained, independently of the starting guess. This indicates two things: first, that the local optimum obtained for each β value is likely to be the binary global optimum (note that this is not guaranteed since the optimization problem is not necessarily convex); and second, that coercive dissipative problems such as those governed by Poisson's equation work very well and robustly with reduced basis and local search algorithms, as already expected [12]. When these methodologies are applied to wave equations, obtaining optimal patterns with this level of quality and robustness will not be easy, but this is precisely what will make the contributions more relevant.

5.4 Concluding Remarks

This chapter provides a practical optimization technique for the design of materials under wave propagation scenarios. The design of such materials poses several challenges mostly regarding computational complexity. For manufacturing reasons, it is often the case that gray solutions are not realizable and thus black/white distributions need to be found. However, global optimization algorithms for discrete programming are seldom practical because the problems are typically large and formulations theoretically NP hard. Generic heuristic methods, like genetic algorithms or simulated annealing, are some of the few approaches that can actually perform some sort of optimization in order to find improved solutions. Nevertheless, they do not use any knowledge of the physics inherent to the problem.

The methodology introduced in this chapter combines the notion of topology optimization through a binary gradient calculation, with the use of reduced basis, which takes advantage of the physics of the problem (close configurations provide similar enough solutions). Overall, a practical iterative algorithm has been presented, whereby until convergence is reached, every iteration tries to identify the direction of largest improvement at a cost on the order of solving only one full simulation problem.

In addition to its practicality, the inherent randomness of the algorithm provided by the choice of elements for the reduced basis is also helpful. Note that different local optima are reached, even starting from the same initial guess. This property helps the algorithm avoid getting stuck at poor local optima. Moreover, after several different local optima have been found and given that they are all feasible, the best of all is chosen.

Chapter 6

Applications

> *Let there be light:*
> *and there was light.*
>
> **–Genesis 1:3**

So far we have focused the efforts on introducing a numerical simulation technique and a topological optimization tool for the design of structured materials. As a consequence, we now seek to show how this new paradigm actually provides some new, effective and unintuitive patterns for several relevant wave propagation applications. Firstly, we try to find discrete patterns that can hide an object and thereby provide a solution for the cloaking problem. Next, we focus on the design of highly efficient sharp bends for electromagnetic and acoustic waveguides, both in 2d and 3d.

6.1 Designing an invisibility Cloak

Electromagnetic cloaks are devices that render an object, illuminated by electromagnetic or acoustic waves of certain frequencies, invisible to an observer. In order to develop cloaking devices, it is necessary to design their material properties and be able to fabricate these properties. The distribution of the material properties of cloaks can be theoretically derived by transformation optics [122]. However, since these patterns possess continuous, anisotropic, and extreme (even infinite) material properties, the practical realization of such cloaks is not possible. In this section we show the design

results of applying the optimization methodology introduced in chapter 5.

6.1.1 Problem description and formulation

Let us first discuss the formulation of the problem. The performance of a cloak is typically measured by the amplitude or intensity of the scattered wave field from a given object surrounded by the cloak after it is illuminated by electromagnetic or acoustic waves of certain wavelengths. A cloak performs perfectly if it can produce a scattered field with zero amplitude (equivalently, zero intensity) in a given target region around the cloak (ideally, the entire space). The problem of designing the layout of a perfect cloak can be rigorously addressed by formulating a discrete optimization problem for the parameters that represent the material properties and geometry of the cloak.

Consider the design of a cloak device as shown in figure 6.1. The circular cylinder at the center (D) represents an ideal metallic structure that contains an object to be made invisible by the cloak. The ring structure in light gray color represents the cloak (namely, the design domain C) which is composed of m pixels of dielectric material with relative permittivity ε_{min} or ε_{max}. The whole structure is illuminated by an incident plane wave $u^0 = e^{ikx}$ propagating in the positive x direction, where k is the free space wave number and $i = \sqrt{-1}$. Furthermore, the infinite domain is truncated by using first-order absorbing boundary conditions as an approximation to the Sommerfeld radiation condition on the outer boundary Γ_{out}, see appendix A for further details. A perfect electric conducting condition is applied on the inner boundary $\Gamma_{\text{in}} = \partial D$. Due to the invariance of the electromagnetic or acoustic properties along the out-of-plane direction, the problem can be formulated in two dimensions. If we consider optics in two dimensions, there are also two possible polarizations of the magnetic and electric fields, namely, transverse electric (TE) polarization and transverse magnetic (TM) polarization. We assume that the optical cloak operates in the TM mode and that the materials are nonmagnetic (their relative permeability equals one). The extension of the proposed method to design an optical cloak operating in the TE case is straightforward. For the acoustic case, ε_j^2 represents the inverse of the

speed of sound of medium j.

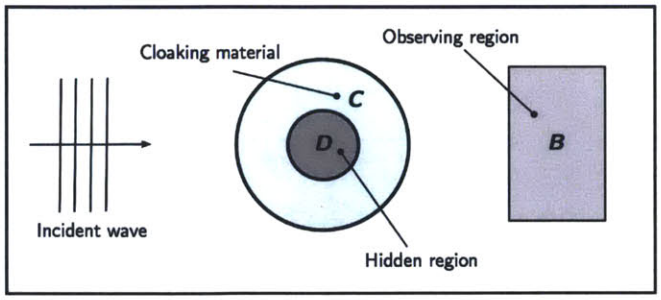

Figure 6.1: Geometric description of the cylinder cloaking problem.

In order to render the circular cylinder invisible to an observer, the optical cloak device should be designed to minimize the amplitude of the scattered field u^s in region B surrounding the observer. Therefore, the discrete optimization problem for the optical cloak design is formulated as follows:

$$\begin{aligned}
\min_{\varepsilon,u} \quad & ||u-u^0||_B^2 = \int_B (u-u^0)^*(u-u^0)dxdy & \\
\text{s.t.} \quad & \nabla^2 u + k^2\varepsilon(x,y)u = 0, & \text{in } \Omega\backslash D \\
& \nabla u\cdot\mathbf{n} - iku = \nabla u^0\cdot\mathbf{n} - iku^0, & \text{on } \partial\Omega \\
& \nabla u\cdot\mathbf{n} = 0, & \text{on } \partial D \\
& \varepsilon(x,y)\in\{\varepsilon_{min},\varepsilon_{max}\}, & \forall (x,y)\in C \\
& \varepsilon(x,y) = \varepsilon_{min}, & \forall (x,y)\in \Omega\backslash(C\cup D)
\end{aligned} \tag{6.1}$$

Note that the total solution field corresponds to the addition of the scattered and incident fields: $u = u^s + u^0$. In addition, * denotes the complex conjugate. Problem 6.1 corresponds to the continuous formulation (in terms of the objective and the PDE constraint) of the design optimization problem.

Similarly, we also consider the design of a carpet cloak such as the one in figure 6.2. An object in region D is sought to be hidden underneath the carpet that needs to be designed for region C such that the scattering of the oblique (45 degrees) illumination coming from the top left corner is minimized in region B.

In practice, the above discrete optimization problem is solved by discretizing the full domain $\Omega\backslash D$ into finite elements (here a MSCG discretization with only one subelement is used since the problem is computationally tractable) and then nu-

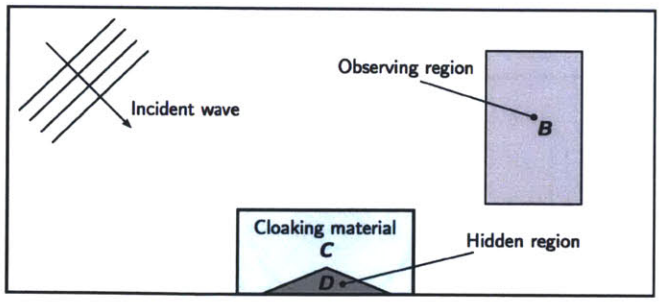

Figure 6.2: Geometric description of the carpet cloaking problem.

merically solving the Helmholtz equation. The relative permittivity function $\varepsilon(x, y)$ will be piecewise constant defined as a given value ε^j in each discretization element ($j = 1 \dots N_{el}$). We then assume that the design domain C consists of m pixels on which the relative permittivity function $\varepsilon(x, y)$ takes the values from the set $\{\varepsilon_{min}, \varepsilon_{max}\}$. Note that each pixel will consider several discretization elements together. All in all, the discrete version of 6.1 can be written as:

$$\begin{aligned} \min_{\boldsymbol{\varepsilon},\mathbf{u}} \quad & (\mathbf{u}-\mathbf{u}^0)^*\mathbb{M}\mathbb{I}_B(\mathbf{u}-\mathbf{u}^0) \\ \text{s.t.} \quad & \left(\sum_{q=1}^{N_{el}} \varepsilon^q \mathbb{A}_q\right)\mathbf{u} = \mathbf{f}, \\ & \varepsilon^q = \varepsilon_{min} + \sum_{p=1}^{m} (\rho^p - \varepsilon_{min})\mathbb{I}_q^p, \quad \forall q = 1 \dots N_{el} \\ & \rho^p \in \{\varepsilon_{min}, \varepsilon_{max}\}, \qquad\qquad \forall p = 1 \dots m \end{aligned} \tag{6.2}$$

where $\mathbb{M}$ is the mass matrix obtained through the MSCG discretization derived in chapter 2, $\mathbb{A}_q$ represents the local contributions to the discretized matrix from each subelement q, $\mathbf{f}$ contains information from the boundary conditions, $\boldsymbol{\rho}$ defines the permittivity of each pixel and $\boldsymbol{\varepsilon}$ represents the permittivity at each discretization element. In addition, $\mathbb{I}_B$ is an indicator function of region B and $\mathbb{I}_q^p$ will be one if the discretization element q belongs to pixel p or zero otherwise. Note that $\mathbf{u} \in \mathbb{C}^{\mathcal{N}_{dof}}$, being $\mathcal{N}_{dof}$ the total number of degrees of freedom.

This optimization problem is highly non-convex and nonlinear. Furthermore, what makes the problem extremely difficult is the presence of the discrete constraints, for which there are no known efficient and rigorous optimization algorithms for solving any problem of this kind.

6.1.2 Design results for 2d cylindrical cloaks

First, we tackle the problem of designing a cylindrical cloak. In this case, when we illuminate a circular (in 2d) object with a planar wave coming from the left side of the domain, the total and scattered wave fields are as shown in figure 6.3. In this particular case, the interference of the wave with the object creates a shadow behind the cylinder that hides the original acoustic or electromagnetic signal. Note how the scattered field corresponds to the subtraction of the total field from the incident field, which in this case is a collection of vertical stripes alternating $+1$ and -1, represented by red and blue, respectively.

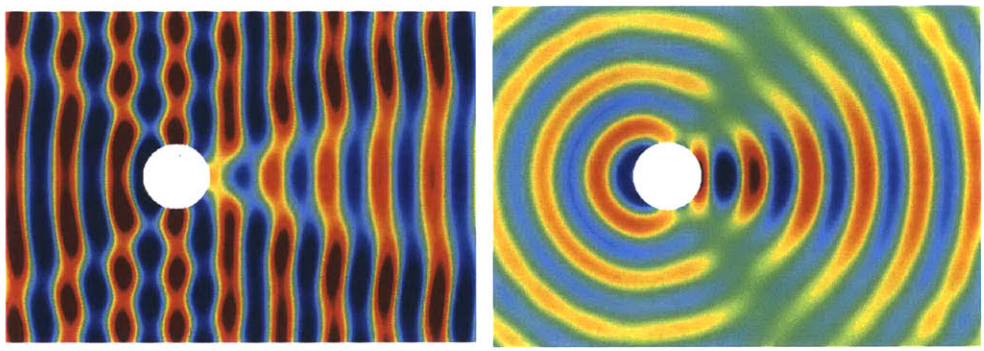

Figure 6.3: Total (left) and scattered (right) wave field in the absence of a cloak.

Let us for this example focus on electromagnetic waves with TM polarization and choose a material that is rather common when manufacturing this sort of devices: Polyimide (PI), with $\varepsilon_{max} = 3.4\varepsilon_{min}$, where ε_{min} is the permittivity of air, namely $\varepsilon_{min} = 1$. Also, denote the radius of the object to cloak by R, and let us pick a wavelength that corresponds to $2R$. We also define a rectangular domain that is large enough to fit all the features of the problem and a radius of the cloak that is $2.5R$.

In terms of the design discretization, we will choose a set of pixels $\{p_i\}_{i=1}^{m}$ without intersection and covering the entire cloak design region. Given the symmetry of the problem (horizontal axis along the center of the domain) only half of the pixels are chosen independently. In order to minimize potential manufacturing limitations, the design space has been discretized into circular segments of $\pi/20$ radians and $0.1R$.

We can now numerically design a cloak defined by problem 6.2 using the simulation technique in chapter 2 and the optimization methodology introduced in chapter 5. After considering several initial guesses and optimization procedures, we obtain a collection of locally optimal patterns. First, note that every single state of materials in the optimization procedure is feasible. This is actually a very important property and thus we will save the best-so-far solution, since the procedure might allow for local increases of the objective function to avoid getting stuck at suboptimal local minima. Furthermore, it is also important to note the randomized nature of the optimization algorithm 5.2: the choice of the members of the reduced basis is random, potentially leading to different descent directions. Finally, the optimization procedure assumes a given starting guess and therefore the method will compute different local optima when starting from alternative states. The same problem will be solved several times being led to different local minima. After the fact, the best-of-all minima will be chosen.

Figure 6.4 shows two different local optima for the cylinder cloaking problem. In the first case, shown in the left side figures, the pattern obtained is able to decrease the objective function value by 99.92%. In other words, this pattern reduces the wave field scattered by the cylindrical object by a factor of $1,300$. The objective region, in this case, is shown through a black rectangle and it is centered behind the object, at a distance of $7R$, with a width of $2R$ and a height of $4R$. If we now seek a pattern that is able to hide the same frequency on a larger target domain, the right side figures show another pattern obtained with the same method. In this latter case, the target domain has doubled in each direction, so it has increased the area by a factor of 4 and the objective function value has still been reduced by a 99.5%, *i.e.*, a factor 200. This second solution might seem less optimal but is also a lot more practical, since it is able to cloak the object, essentially everywhere behind it.

Ideally, we would want to have the cloak to be as thin as possible; however, for a successful cloak such thickness depends on the contrast of the materials as well as the size of the pixels. If we fix the materials to be PI and air and the size of the pixels the same as above, figure 6.5 shows how the quality of the pattern improves as we increase

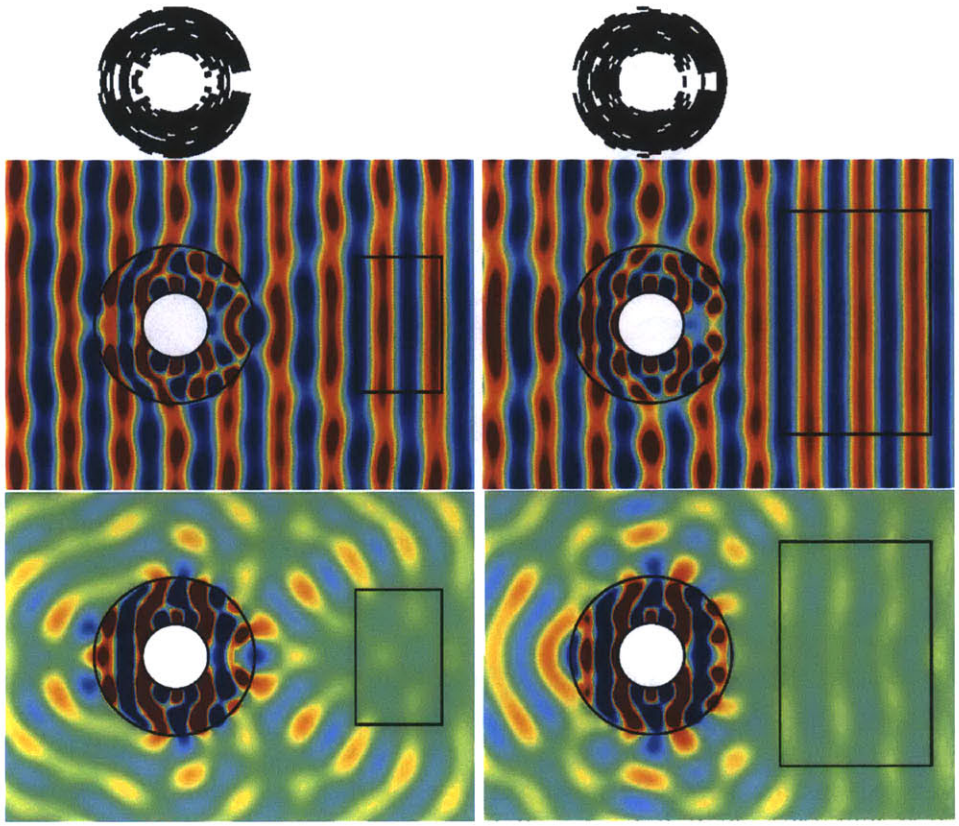

Figure 6.4: Material distribution (top); total (center) and scattered (bottom) wave field patterns in presence of a cloak. Left: optimality of 99.92%, right: optimality of 99.5% for a larger target region.

the size of the cloak. For wavelengths that are of the order of the object, typically a cloak of $2.5R$ to $3R$ obtained through our methodology is enough for reductions above 99% of the scattered field for a given frequency. In optimization terms, when we increase the size of the feasible region, the objective function can only improve. Indeed, for the four cases below, their feasible sets satisfy $\mathcal{F}_1 \subset \mathcal{F}_2 \subset \mathcal{F}_3 \subset \mathcal{F}_4$ and therefore it is clear that the objective function values satisfy $Z_1 \geq Z_2 \geq Z_3 \geq Z_4$. In fact, $|\mathcal{F}_1| = 0, |\mathcal{F}_2| = 100, |\mathcal{F}_3| = 200$ and $|\mathcal{F}_4| = 300$. The results shown in this figure correspond to the same frequency and materials previously analyzed.

Validation of the Reduced Basis

The binary gradient used within the optimization algorithm relies on the accuracy of the Reduced Basis approximations for the solution field. The error bounds that the literature provides for RB approximations under non coercive elliptic operators are

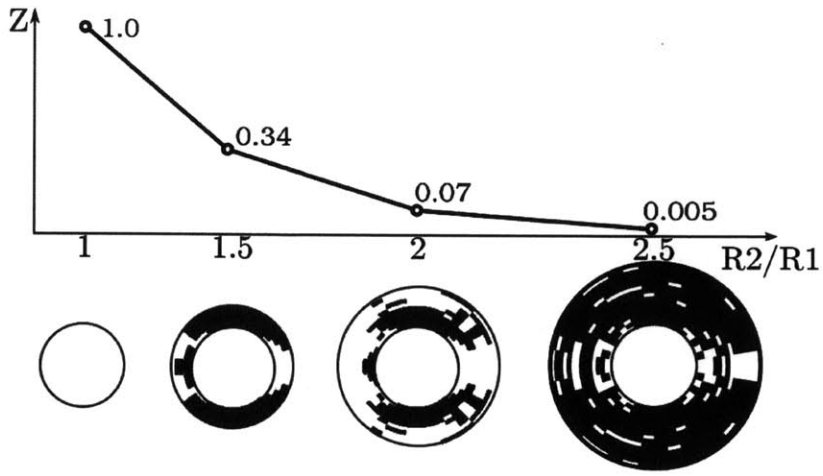

Figure 6.5: Optimality of different cloak patterns as the size of the cloak is increased.

very conservative. However, since we are only interested in computing the solution field at close-by neighbors (they only differ by one single pixel from a given state), the approximations are typically accurate.

Figure 6.6 illustrates the use of reduced basis in the cylinder cloaking setting. Let us assume that we want to form a basis around the pattern in subfigure (j). First, we randomly pick 30 neighbors by replacing one single pixel of the pattern −a subset (8) of them are shown in (a) to (h)− and we then compute the corresponding solution fields to form the basis. If we now want to approximate the solution to pattern (i), the errors are of order 1; however, when comparing the accuracy of the full simulation for (j) with the corresponding RB approximation, the error is of order 10^{-5}.

Similarly, we can compute the approximate solutions to the remaining neighbors (a total of 270 for the chosen pixelization) with acceptable accuracy levels. Figure 6.7 shows the approximation error value when changing each pixel from state (j) in figure 6.6. Note that for the elements in the basis, the error is exactly zero (color coded with dark blue). In this case, the neighbors that are worst approximated still have an L_2 approximation error of around 10^{-3} (color coded in dark red) with respect to the solution provided by the full size simulation.

In terms of computational effort, when using RB approximations, only around five full simulations are computed and added to update the basis; then, 300 very small

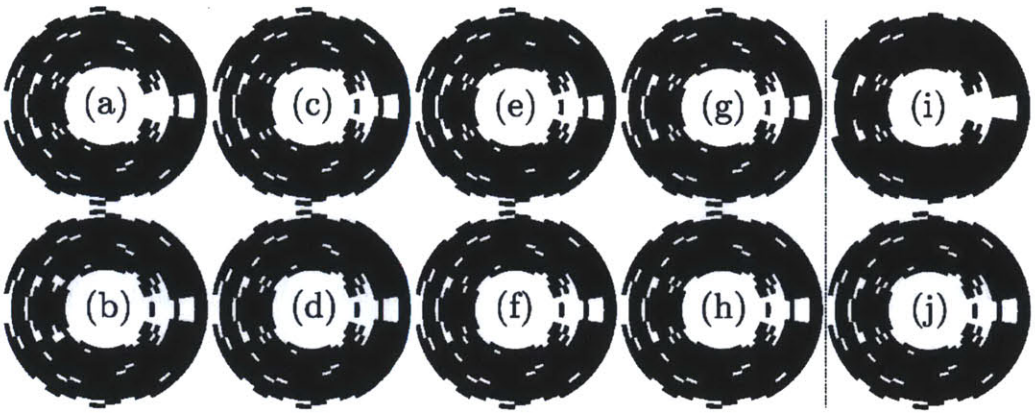

Figure 6.6: Permittivity states for the cloaking region. Subfigures (a)-(h) show patterns the solutions to which form the basis around state (j). The solution to pattern (i) is poorly approximated by this basis.

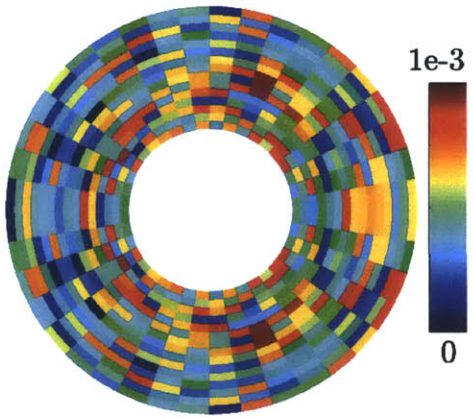

Figure 6.7: Error value of the RB approximate solution using basis in figure 6.6 with respect to the full simulation when changing each pixel.

systems of 30×30 are solved. If RB approximations were not used, the full size simulations of the 300 neighbors would be required at each iteration. Moreover, the randomized nature of the basis together with these tolerable approximation errors might lead the algorithm to pick a descent direction that might not actually be the same as if the basis was different. This behavior in fact improves the quality of heuristic binary optimization methods [46] since it avoids systematically getting stuck at poor local optima.

6.1.3 Design results of 2d carpet cloaks

Similarly to the previous section, in this one we discuss the design of a carpet cloak. When illuminating a solid wall that is totally reflective, the wave fronts reflect with the same angle as the incident wave with respect to the surface, according to Snell's law. However, in the presence of an object on the surface, the resultant reflected wave will be altered.

If we consider the binary optimization previously introduced, we seek a material distribution around the scattering object laying on the solid wall such that the reflected wave is minimized inside some target region of interest. Firstly, a Cartesian discretization of the parametric space has been considered, therefore the solution is always the union of square pixels, which are easily manufacturable. Figure 6.8 shows the total and scattered fields for the homogeneous case without a cloak as well as the optimal design for a frequency corresponding to 15 wavelengths per unit of length (the domain size is $[-1, 1] \times [0, 1]$). The alternative material to air $\varepsilon_{min} = 1$ that has been considered in this case is aluminum, $\varepsilon_{max} = 8.9$. An overall reduction of the scattered field of 96% has been achieved for this frequency and this set of materials.

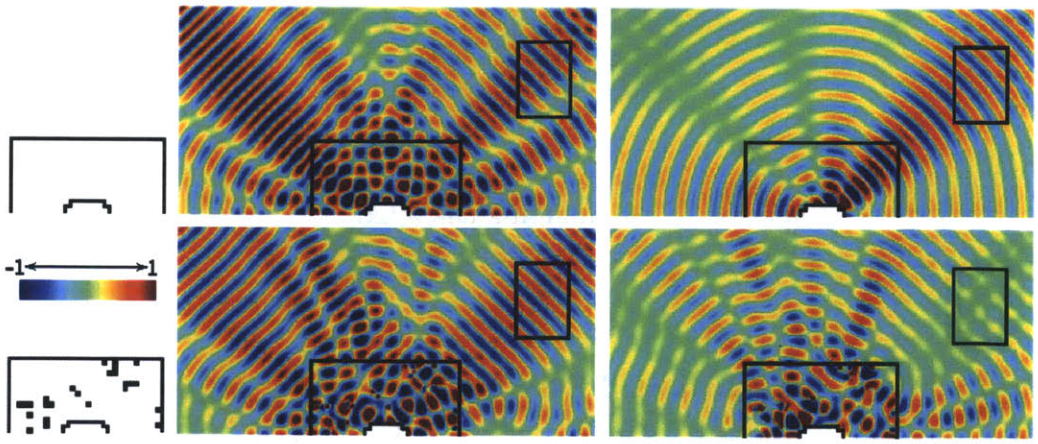

Figure 6.8: Carpet cloaking. Top figures show solutions without a cloak whereas in the bottom an optimal cloak case is shown. Left: material patterns; center: total wave field; right: scattered wave field

Overall, the binary optimization method has been effectively used to devise patterns that provide desired cloaking properties while addressing the main difficulties

that arise when designing cloaks: continuous distributions of materials and singular values of the material properties. We are able to provide designs that can cloak a wavelength of the order of the object through material patterns that are described by a set of pixel inclusions of a prescribed isotropic material on air. Moreover, these patterns are discrete and thus address one of the main manufacturing requirements.

6.2 Optimization of Helmholtz waveguide bends

Waveguides are devices that allow the controlled propagation of waves for very long distances (from tens to millions of wavelengths). Fibers are a particular case of waveguides that offer a cross sectional 1d or 2d geometry that is able to trap a given frequency, or a range, in the inner core. Thus, when these geometries are extended cylindrically in the third dimension, the energy will mainly (except from undesired losses) travel along the center of the fiber.

In the case of optics, general waveguides as well as fibers are typically designed based on two phenomena: index guiding or Photonic Crystals. The equivalent physics for acoustics produces sound waveguides. The first phenomenon is explained as follows: when a high index material is surrounded by a lower index material, and the wave hits the boundary between the two with a large enough angle, then from Snell's law there will be total internal reflection (TIR) and the energy will stay in the higher index material. For this reason, a simple homogeneous cylindrical piece of higher index material will serve as the simplest fiber. The latter will use the idea of Photonic (or Phononic for acoustics) bandgap, which does not allow propagation of energy within a certain range of frequencies for a given periodic geometry. If a linear defect is included in this geometry, then energy propagation is only allowed through such a defect. Figure 6.9 shows a PC and an index guiding waveguide.

High quality waveguides and fibers are those that have minimal losses and thus allow waves to travel long distances without jeopardizing the quality of the signal. However, when these waveguides or fibers are long, bends (sometimes sharp) are often required and such bends typically become a source of high losses for existing designs. In this section we address this issue and try to find designs that minimize losses on

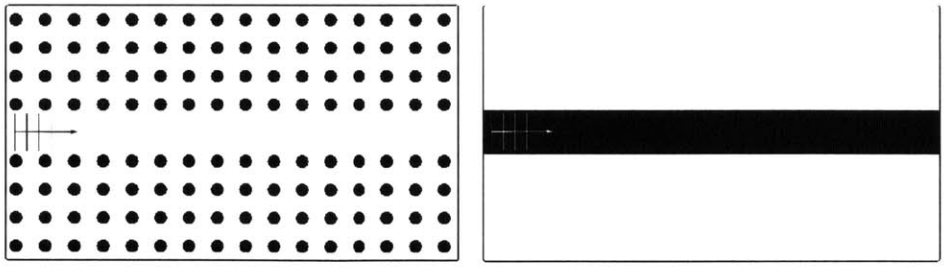

Figure 6.9: Example geometries of a Photonic/Phononic Crystal waveguide (left) and an index guiding fiber (right).

waveguide and fiber bends, both in 2d and also 3d.

6.2.1 Problem description

In order to design waveguides or fibers with highly efficient sharp bends we will apply the aforementioned binary optimization methodology to the corner object together with the multiscale simulation procedure. Note that for the particular example of Photonic Crystals, the multiscale simulation methods introduced in chapters 2 and 3 become crucial given the multiple repetition of highly detailed patterns.

The main aim of this section is to formulate the optimization problem that will then be applied to the design of a 90 degree Photonic Crystal bend in 2d in section 6.2.2 and to the design of a 90 degree bend in a 3d fiber in section 6.2.3. Then, we will extend the design formulation to 3d Maxwell's equations and obtain optimal patterns for a Y bend on a TE polarized PC slab.

Let Ω represent the domain of the problem. This domain includes a certain upstream length of the waveguide from the bend as well as a similar downstream length and thus will be rectangular in 2d and a rectangular parallelepiped in 3d. The incoming waveguide enters the domain from the left side boundaries and then bends downwards 90 degrees escaping the domain across the bottom boundary. For this reason, Perfectly Matched Layers (or PMLs) will be included at the left and bottom boundaries, at least. The corner area will be considered the design region and the last layer of waveguide before exiting the domain will form the objective region. Figure 6.10 shows the 2d geometric representation of the problem. The extension to a 3d TIR fiber becomes natural.

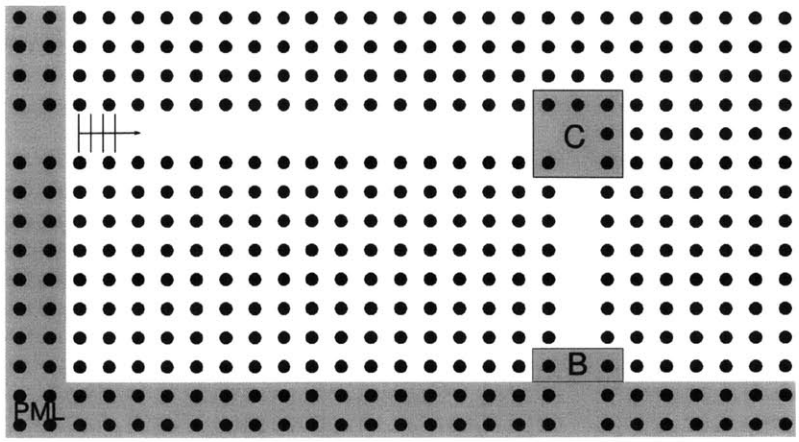

Figure 6.10: Geometry of the 90 degrees bend design for a 2d PC waveguide. PML refers to the region of Perfectly Matched Layers, B forms the objective region and C the design pixelization. In black are the rods of a dielectric material on air.

The simulation of this kind of problem for Helmholtz's equation has already been discussed in the multiscale simulation method presented in chapter 2. In order to formulate the optimization problem using the binary programming algorithm previously introduced, two things need to be defined: the objective function, and the pixelization of the design region (region C in the figure).

Firstly, we shall discuss the choice of the objective function J. In contrast to the cloaking problem, for the waveguide bend design we are not interested in directly matching an outcoming wave since the phase of the wave is irrelevant. What we certainly want is to preserve as similar as possible the amplitude of the incoming wave. Furthermore, we want the wave to propagate exactly in the direction of the bent waveguide. For these reasons, the goal is to maximize the transmission, or equivalently, to match the power or energy exiting the waveguide with the power or energy entering the waveguide. Information about the power transmission is found in the Poynting vector, which in electromagnetics can be computed as $\mathbf{S} = \mathbf{E} \times \mathbf{H}$, when averaged over a period.

Furthermore, given that the waveguide exits the domain through the bottom boundary, we are only interested in the vertical component of the time-averaged Poynting vector in the exit region and we compare it with the horizontal component of the same vector in a region prior to the bend.

All in all, the objective function can be computed as the ratio between the output power and the input power:

$$T = \frac{P_{out}}{P_{in}}, \tag{6.3}$$

where each one of these powers is obtained from averaging all the vertical/horizontal components of the Poynting vector for each element in the objective region B as:

$$P = \int_B \mathbf{S} \cdot \mathbf{n}\, dA. \tag{6.4}$$

Furthermore, note that $S = |\mathbf{S}|$, when averaged over a period can be computed in terms of the frequency domain solution as discussed in [73]:

$$S = \frac{1}{2}\omega \mathcal{I}m(u^* \nabla u). \tag{6.5}$$

Now that a suitable objective function has been described, we need to define the pixelization of the design region. In this case, the most natural choice is just a partition of the corner element in a square/cubic grid. Figure 6.11 shows the discretizations considered for the simulation problem when the corner is assumed to be a naive extension of the rodded structure (left); or when prepared for the optimization method (right) through a triangulation that fits 20×20 squares as a pixel decomposition.

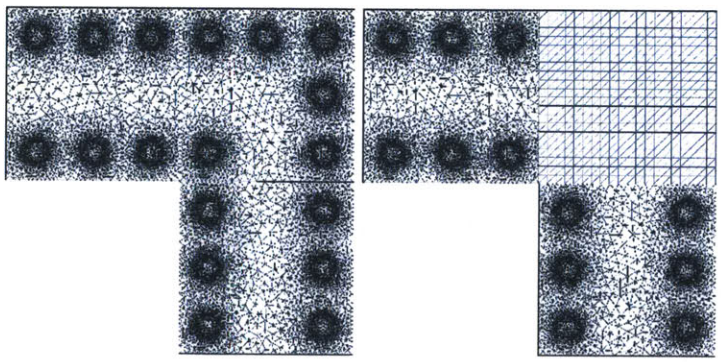

Figure 6.11: Multiscale discretization examples for the corner of a 2d PC waveguide. Discretizations of a naive geometry (left) and a square pixelization of the design region for the optimization procedure (right).

In conclusion and with all the aforementioned considerations, the optimization problem for the waveguide bend can be written as below. Note that maximizing the

transmission fraction is equivalent to simply maximizing the power in B since the denominator of T remains constant. All in all, we want to solve:

$$\begin{aligned}
\max_{\varepsilon,u} \quad & |P_B(u)| = \left| \int_B \mathbf{S}(u) \cdot \mathbf{n} dx dy \right| \\
\text{s.t.} \quad & \nabla^2 u + k^2 \varepsilon(x,y) u = 0, && \text{in } \Omega \\
& \nabla u \cdot \mathbf{n} - iku = \nabla u^0 \cdot \mathbf{n} - iku^0, && \text{on } \Gamma_{\text{in}} \\
& \varepsilon(x,y) \in \{\varepsilon_{min}, \varepsilon_{max}\}, && \forall (x,y) \in C \\
& \varepsilon(x,y) = \varepsilon_{known}, && \forall (x,y) \in \Omega \backslash C
\end{aligned} \tag{6.6}$$

Note that ε is set to ε_{known} outside the design domain C since the distribution of permittivity values there is known, fixed and piecewise constant. In addition, Γ_{in} corresponds to an interboundary condition that will account for the incoming planar wave. It is also important to highlight that the governing equation will be modified in Ω_{PML} as described in appendix A. The multiscale method will be used to discretize 6.6 into:

$$\begin{aligned}
\max_{\varepsilon,\mathbf{u}} \quad & \left| \int_B \frac{1}{2} \omega \mathcal{I}m \left(\mathbf{u}^* \mathbb{B} \mathbf{u} \cdot \mathbf{n} \right) dx dy \right| \\
\text{s.t.} \quad & \left(\sum_{q=1..N_{el}}^{q \neq C} \mathbb{A}_q(\boldsymbol{\varepsilon}^q) + \mathbb{A}_C(\boldsymbol{\varepsilon}^C) \right) \mathbf{u} = \mathbf{f}, \\
& \boldsymbol{\varepsilon}^q = \boldsymbol{\varepsilon}^q_{known} \in \{\varepsilon_{min}, \varepsilon_{max}\}^{n_q}, && \forall q = 1 \ldots N_{el}, q \neq C \\
& \varepsilon^C_s = \varepsilon_{min} + \sum_{p=1}^{m} (\rho^p - \varepsilon_{min}) \mathbb{I}^s_p, && \forall s = 1 \ldots |\boldsymbol{\varepsilon}^C| \\
& \rho^p \in \{\varepsilon_{min}, \varepsilon_{max}\}, && \forall p = 1 \ldots m
\end{aligned} \tag{6.7}$$

Here $\mathbb{B}$ is the convection matrix obtained through the MSCG discretization derived in chapter 2, $\mathbb{A}_q$ represents the subproblem contributions to the discretized matrix, $\mathbf{f}$ contains information from the boundary conditions and $\boldsymbol{\varepsilon}^q$ is now a function for each *macro* element q that represents the elementwise constant permittivity at each discretization element therein. $\boldsymbol{\varepsilon}^q$ is known at all subelements and has the corresponding size n_q but is unknown for the design region C where it is organized into m pixels with material properties to be chosen between ε_{min} or ε_{max}. In addition, $\boldsymbol{\rho}$ is the vector of design variables that takes the value of the material chosen for each pixel and $\mathbb{I}^s_p$ takes the value 1 only when the discretization element s belongs to pixel

p. Finally, $\mathbf{u} \in \mathbb{C}^{\mathcal{N}_{dof}}$, where $\mathcal{N}_{dof}$ is the total number of degrees of freedom.

6.2.2 Design of a 2d PC waveguide bend

Let us now focus on the design of a highly efficient 90 degree bend for a 2d Photonic Crystal waveguide. In particular, the reflection at the T junctions of 2d PC waveguides has also been minimized using topology optimization methods in [72,73] and we thus seek to compare how our approach performs. For the numerical simulation of this problem we have discretized the entire domain Ω into square subdomains containing 3×3 arrays of aluminum ($\varepsilon = 8.9$) rods of radius $r = 0.2a$ respecting the symmetries of a square, a being the periodicity of the structure or equivalently the distance between the center of every two consecutive rods. Note that for this geometry, the first bandgap shows up for unitary frequencies such that $\omega a/2\pi c \in (0.26, 0.41)$ as discussed in chapter 4 and shown in figure 4.5 therein.

Hence, any frequency strictly inside this bandgap will be completely reflected by the described pattern (except for evanescent modes in the boundaries that decay exponentially, see [74] for further details). Then, after including a linear defect that then bends 90 degrees, we expect the wave to propagate only through the waveguide created.

We now seek to design an optimal pattern that is able to maximize the transmission power for a given frequency after the bend. So let us pick $\omega a/2\pi c = 0.34$, which is inside the described bandgap. If we first compute the transmission rate with a naive approach consisting of designing the corner by just removing the rods from an L shaped waveguide, we obtain a transmission fraction of 0.96, which is okay if we accept losses of a 4% in every 90 degrees bend of the waveguide. Some related work also asserts that higher efficiency can be achieved if the bend is smoothed out by breaking it into two consecutive 45 degree bends. In this case and for the chosen frequency, the transmission ratio increases to 0.98, or equivalently, a 2% of loss.

In order to set up the design optimization problem we replace the discretization of the corner subelement by a square pixelization consisting of $20 \times 20 = 400$ pixels embedded in a finer mesh for simulation purposes. Figure 6.11-right shows the mesh

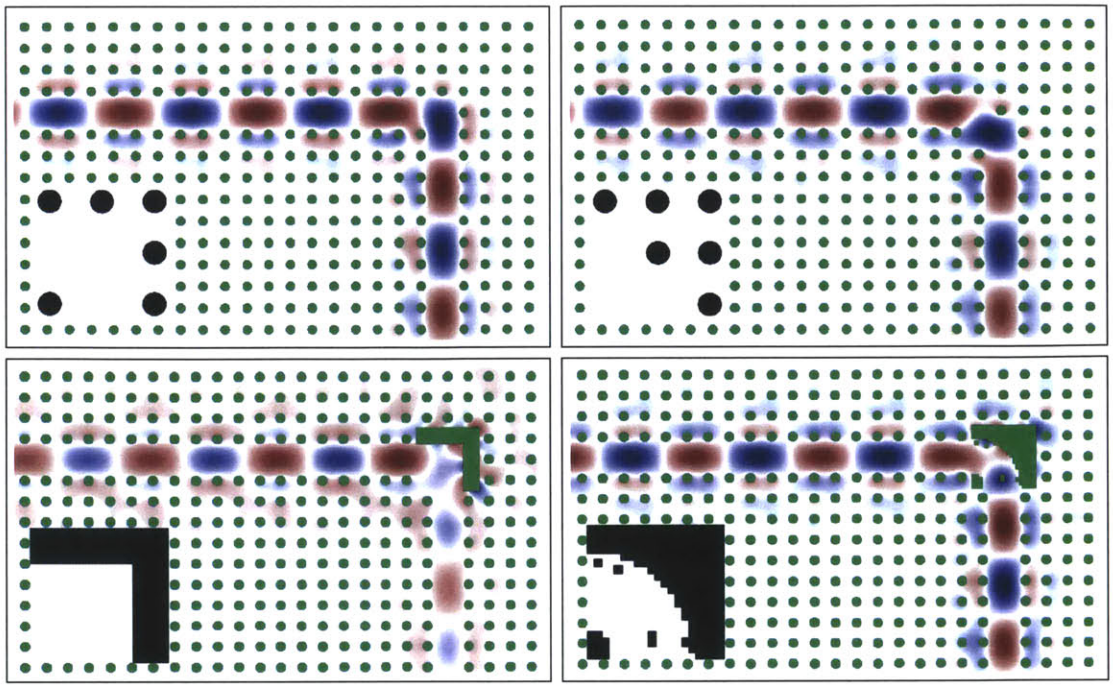

Figure 6.12: Wave propagation patterns through a 2d PC waveguide with a 90 degree bend for $\omega a/2\pi c = 0.34$. Naive approaches (top), initial guess (bottom left) and optimized pattern (bottom right). Insets show the exact geometry at the corners.

chosen for design purposes. Then a starting guess needs to be chosen, and just by physical intuition and without any hope of getting a decent transmission rate we pick two solid rectangles of the higher index material forming an L shape in the outer corner of the bend, surrounded by the lower index material. For this configuration, as expected, the transmission rate decreases all the way to 0.78 for the same design frequency.

Nevertheless, we are now ready to start the optimization procedure introduced in chapter 5 and further described for this specific problem in the previous section. The final optimal pattern that has been obtained is shown -together with the naive and initial guess approaches- in figure 6.12, and provides a transmission fraction of 0.997 so only 0.3% of the energy is lost after a the waveguide faces a 90 degrees bend.

All in all, we have been able to design an alumina/air pattern for the bend region that is able to reduce the losses by a factor of 7 and 13 with respect to naive rod based approaches. These factors are obtained as value losses for each of the naive geometries divided by the losses provided by the optimized pattern. This reduction

is particularly relevant for practical purposes, since long waveguides have multiple bends. Table 6.1 summarizes these results.

Table 6.1: Summary of results for the 2d waveguide bend.

Pattern	Naive #1	Naive #2	Initial guess	Optimized
Transmission %	96	98	78	99.7
Factor over naive #1	·	2	< 0	13

An alternative approach for the design of these two dimensional structures is topology optimization. In fact, for the problem of designing PC waveguide bends in 2d, topology optimization has shown very good performance as shown in [72, 73] since the objective function is relatively binary by nature as well as not too sensitive and especially tractable (in 2d). Results reported in [72] also offer a pattern that for TM polarizations with square symmetries containing rods of radii $r = 0.18a$ and refractive index $n = 3.4$. This pattern provides significant transmission fractions for any frequency in the gap $\omega a/2\pi c \in (0.32, 0.44)$. We have also validated our methodology by numerically simulating this geometry and matching the numerical results reported in [72], see figure 6.14. Furthermore, we have optimized the geometry further for a specific frequency and obtained better results, as shown in figure 6.13.

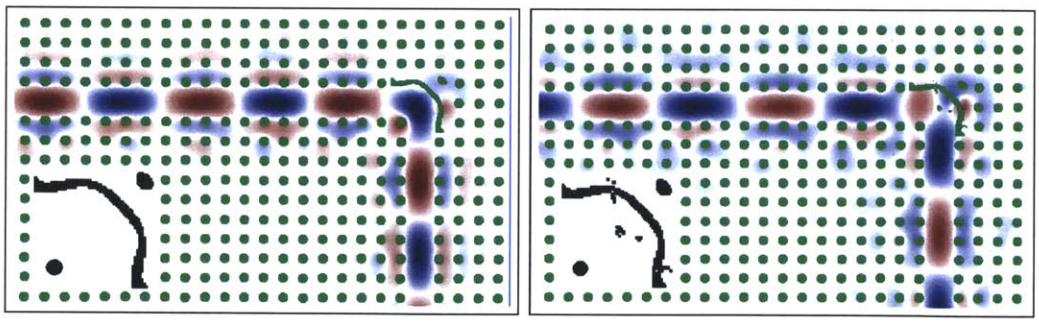

Figure 6.13: Wave propagation patterns through a 2d PC waveguide with a 90 degree bend for $\omega a/2\pi c = 0.34$. Solution given in [72] through topology optimization (left); and our optimum obtained starting from there (right).

Despite our method not being capable of improving this pattern for the full range of frequencies, we are able to further reduce the losses for a single frequency. In particular, we target the frequency with poorest transmission $\omega a/2\pi c = 0.34$, for which the naive approach only provides a transmission fraction of 0.971, the topology

optimization pattern results in $T = 0.995$ and our method is able to increase the fraction to $T = 0.9998$, when taking as initial guess the optimum given in [72].

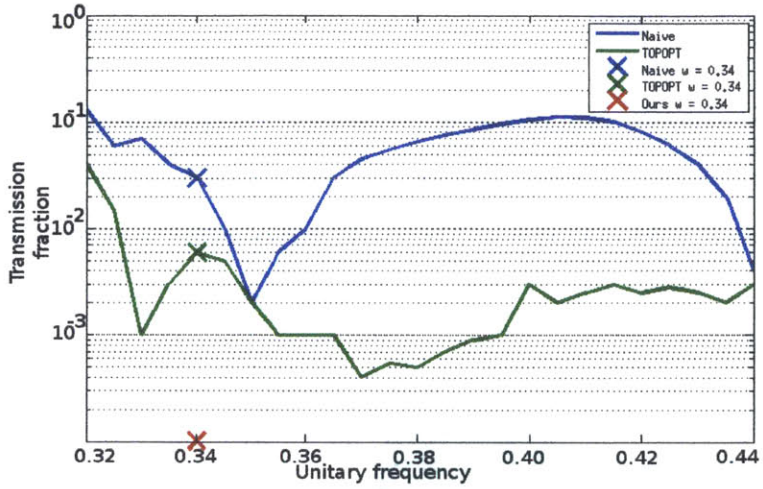

Figure 6.14: Transmission fraction value (logarithmic) for frequencies in the lowest bandgap for the naive approach, optimum in [72] and our optimum for $\omega = 0.34$

6.2.3 Design of a 3d fiber bend

After the successful design of highly efficient two dimensional Photonic Crystal waveguide bends, we shall try the extension of this methodology to 3d fibers. The three dimensional problem is especially challenging for two main reasons explained below.

Firstly, the simulation problem involves a significantly higher complexity, given the increase of degrees of freedom as well as their connectivities. This first challenge has been already discussed in chapters 2 and 3 and the multiscale methodologies offer a rather efficient solution given the scalability and parallelizability of the methods.

In addition, the optimization problem requires a great deal more simulation runs than in the 2d case. Note that the pixelization is now in three dimensions, and hence the set of design pixels that are considered is significantly larger. That means that the neighborhoods, which are chosen to be on the order of the number of pixels $\mathcal{O}(n)$, are larger, requiring more Reduced Basis simulations per iteration as well as a larger basis to ensure accuracy of the approximations. Also, since the set of pixels is larger, the optimal solution might take longer to be reached, *i.e.*, more global optimization iterations.

Overall, the complexity of the problem increases very significantly because not only will more global optimization iterations be required, but each one of which will also take significantly longer because there are more neighbors, the basis is larger and every simulation inherently takes longer. In spite of the aforementioned challenges, optimal 3d bends can be found taking advantage of both the simulation and design optimization techniques presented in this thesis.

Let us consider a 3d cylindrical fiber, where the cross section is a homogeneous disc with $a(\mathbf{x}) = 11.8$. Figure 6.15 shows the geometry for which we want to design a bend that minimizes losses.

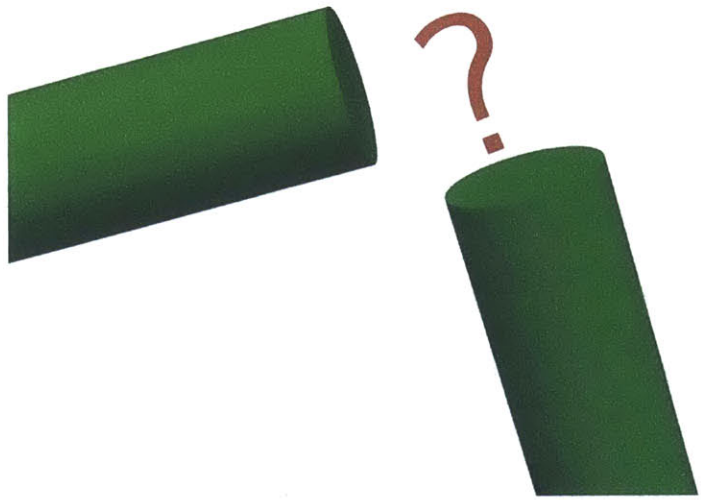

Figure 6.15: Geometric problem setting for the 3d fiber bend optimization.

By total internal reflection or index guiding, waves sent along the cylinder with a frequency ω_0 will not escape and can thus be guided. This frequency ω_0 has been chosen to be the one given by $\lambda = 4R$, where λ is the wavelength and R the radius of the fiber. However, a sharp bend (90 degrees) will have significant losses since some of the wave hitting the bend will not be guided (the internal reflection will not be total). This is the reason why the naive approach obtained by intersecting two straight cylinders will only provide a transmission fraction of 0.35 with up to 65% in loss.

In order to set up the optimization problem, a corner cube of the domain is removed and replaced by a new subelement in the multiscale simulation that embeds

a $10 \times 10 \times 10$ cubic pixelization; this is not too fine because of the 3d nature of the problem but already challenging given its large size ($1,000$ pixels). An initial guess needs to be chosen and the projection of the two straight rods into the new pixelization is chosen for simplicity. For this case, the transmission fraction drops down to 0.19 with 81% losses. However, after we let the optimizer work from there, it takes the design into a pattern that provides, for the targeted frequency, a transmission ratio of 0.88 and thus reduces the losses to only 12%, which is a significant improvement, especially given that it is a sharp bend in 3d. Figure 6.16 shows the three geometries and the corresponding solutions for ω_0, and table 6.2 summarizes these results.

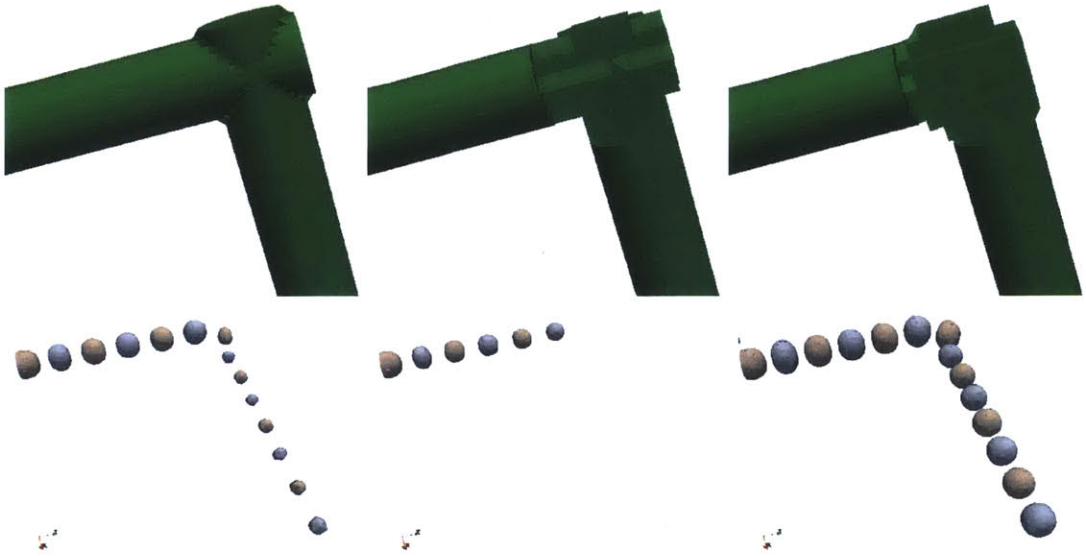

Figure 6.16: Zoomed alternative geometries for the 3d waveguide bend (top) and corresponding wave propagation patterns showing the level sets ± 0.3 (bottom). Naive approach (left), initial guess (center) and optimized pattern (right).

Table 6.2: Summary of results for the 3d fiber bend.

Pattern	Naive	Initial guess	Optimized
Transmission %	35	19	88

6.3 Optimization of Maxwell's waveguide bends

We can formulate a design optimization problem for a Y waveguide bend on a 3d Photonic Crystal slab. This application is relevant since this kind of bend are regularly

used in PC waveguides when a signal is sought to be split in two. Not only will we solve the problem in 2d assuming infinite thickness of the slab, but also in 3d with finite thickness. For this latter case, full Maxwell's 3d simulations will be required and to that end, we will use the MSHDG method developed in chapter 3.

6.3.1 Problem formulation

Figures 6.17 and 6.18 show the geometry of the problem that we are here interested in solving. A hexagonal lattice is considered with holes of radius $0.3a$ on a material with a certain permittivity, a being the periodicity or the distance between the centers of consecutive holes. For three dimensional slabs with this in-plane structure, a Photonic bandgap appears for the H_z modes (note we consider the TE-like polarization) when the thickness of the slab is around a, see [74] for further details.

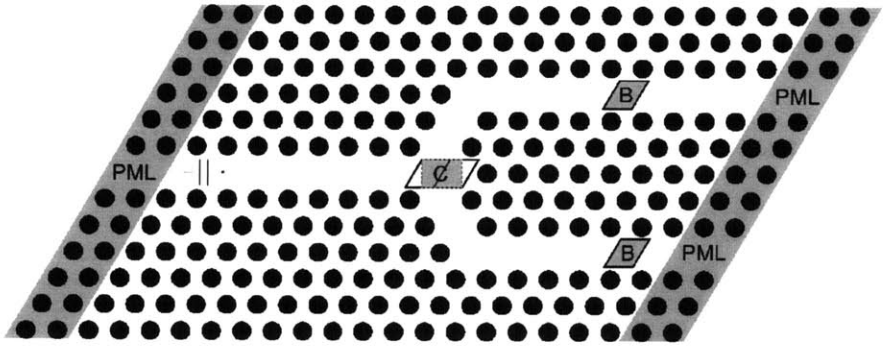

Figure 6.17: Geometric problem setting of the Y bend design for a 2d/3d slab PC waveguide. PML refers to the region of Perfectly Matched layers, B forms the objective region and C the design pixelization. Black represent the air holes on a slab of a certain homogeneous material.

Figure 6.17 shows in black the holes drilled across the slab, assumed to be made of silicon ($\varepsilon = 11.8$). Note that the shaded areas correspond to the PML (see appendix A for further details), both areas B form the objective region and C corresponds to the design region. A rectangular domain with 27×20 pixels will be considered therein. Additionally, figure 6.18 shows two 3d visualizations of the geometry considered.

All in all, note that if HDG is considered as a numerical scheme for the subelement problems, then the Poynting vector will be computed as $\mathbf{S} = \mathbf{E} \times \mathbf{H}$. Furthermore, we consider Maxwell's equations as constraints and the corresponding interelement

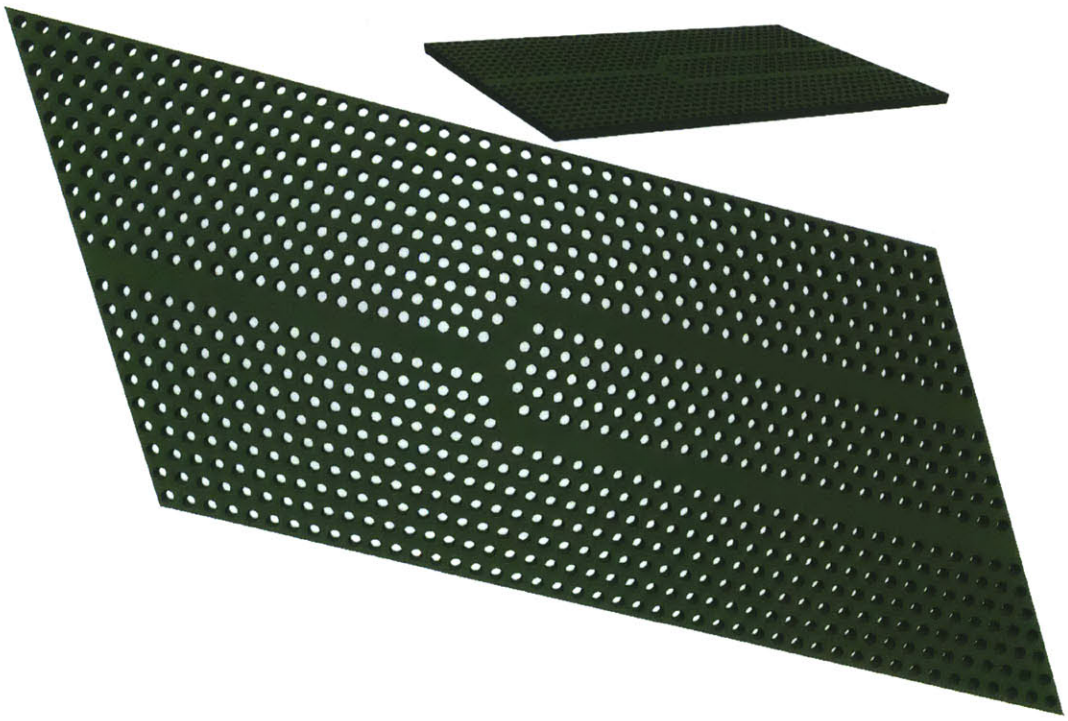

Figure 6.18: Geometric description of the Y waveguide bend on a PC slab. Air holes of radius $0.3a$ are accordingly drilled on a higher permittivity material slab of thickness a.

condition for the incoming field. We can thus write the binary optimization problem for the following continuous formulation:

$$\begin{aligned}
\max_{\varepsilon,\mathbf{E},\mathbf{H}} \quad & |T_B(\mathbf{E},\mathbf{H})| = \left| \int_B \mathbf{S}(\mathbf{E},\mathbf{H}) \cdot \mathbf{n} dx dy \right| & \\
\text{s.t.} \quad & \nabla \times \mathbf{H} - (i\omega\varepsilon(x,y,z) + \sigma)\mathbf{E} = \mathbf{J}, & \text{in } \Omega \\
& \nabla \times \mathbf{E} + i\omega\mu\mathbf{H} = 0, & \text{in } \Omega \\
& \mathbf{n} \times \mathbf{H} - ik\mathbf{n} \times \mathbf{E} \times \mathbf{n} = \mathbf{g}_0, & \text{on } \Gamma_{\text{in}} \\
& \varepsilon(x,y,z) \in \{\varepsilon_{min}, \varepsilon_{max}\}, & \forall (x,y,z) \in C \\
& \varepsilon(x,y,z) = \varepsilon_{known}, & \forall (x,y,z) \in \Omega \backslash C
\end{aligned} \tag{6.8}$$

where ε is set as known in all the subdomains except for C. Note that Γ_{in} corresponds to an interboundary where the incoming wave is imposed through a Robin boundary condition for $\mathbf{g}_0 = \mathbf{n} \times \mathbf{H^0} - ik\mathbf{n} \times \mathbf{E^0} \times \mathbf{n}$, with an initial field obtained as $\mathbf{H}^0 = (0, 0, H_z^0)$, where $H_z^0 = e^{i\omega x}$, given that a TE-like polarization is assumed. After the MSHDG discretization of Maxwell's equations is considered, we are able to formulate

the design optimization problem as follows:

$$
\begin{aligned}
\max_{\boldsymbol{\varepsilon},\mathbf{U}} \quad & \left| \int_B \mathbf{S}(\mathbf{U}) \cdot \mathbf{n}\, dxdy \right| \\
\text{s.t.} \quad & \left(\mathbb{A}_0 + \sum_{q=1..N_{el}}^{q \neq C} \mathbb{A}_q(\boldsymbol{\varepsilon}^q) + \mathbb{A}_C(\boldsymbol{\varepsilon}^C) \right) \mathbf{U} = \mathbf{F}, \\
& \boldsymbol{\varepsilon}^q = \boldsymbol{\varepsilon}^q_{known} \in \{\varepsilon_{min}, \varepsilon_{max}\}^{n_q}, \qquad \forall q = 1 \ldots N_{el}, q \notin C \\
& \varepsilon^c_s = \varepsilon_{min} + \sum_{p=1}^{m} (\rho^p - \varepsilon_{min}) \mathbb{I}^s_p, \qquad \forall s = 1 \ldots |\boldsymbol{\varepsilon}^c|, \forall c \in C \\
& \rho^p \in \{\varepsilon_{min}, \varepsilon_{max}\}, \qquad \forall p = 1 \ldots m
\end{aligned}
\tag{6.9}
$$

where $\mathbf{U} = (\mathbf{H}, \mathbf{E}, \boldsymbol{\Upsilon}, \boldsymbol{\Lambda})$ and then the Poynting vector can be recovered from the definition to obtain the objective function. $\mathbb{A}_0$ represents the portion of the MSHDG discretization matrix that is independent of all values of permittivity, and $\mathbb{A}_q(\boldsymbol{\varepsilon}^q)$ for $q \notin C$ provides the terms of the MSHDG discretization matrix that corresponds to all subelements except from those in region C. Finally, $\mathbb{A}_C(\boldsymbol{\varepsilon}^C)$ will be the term corresponding to the subelements in C. Note that $\mathbb{A}_0$ and the sum of all $\mathbb{A}_q$ for $q \notin C$ will only be computed once, added and stored.

6.3.2 Design of a Y waveguide on a PC slab

Let us first focus on the two dimensional setting where the slab is assumed to have infinite thickness. For the parameters chosen (materials, radius, symmetry) a Photonic bandgap appears for frequencies in the range $\omega a/2\pi c \in (0.19, 0.27)$, as described for instance in [74]. Let us choose $\omega = 0.225$ and analyze the transmission fraction obtained with a naive approach for the Y bend, where a defect is created with the shape of a Y. The H_z solution field can be found at the top of figure 6.19. For this configuration, a total of 13% of the incoming energy goes into undesired losses. Similarly, we can now project the corner rod into our pixelization and compute the solution field, shown in the center of the same figure, for which the losses increase to 16%. Finally, this state is taken as a starting guess and the optimization procedure is considered, which after about $1,000$ iterations and several runs reaches the binary pattern shown in the bottom of the figure for which the losses are reduced to 5%.

Once the 2d problem has been solved, we are ready to approach the 3d model. In

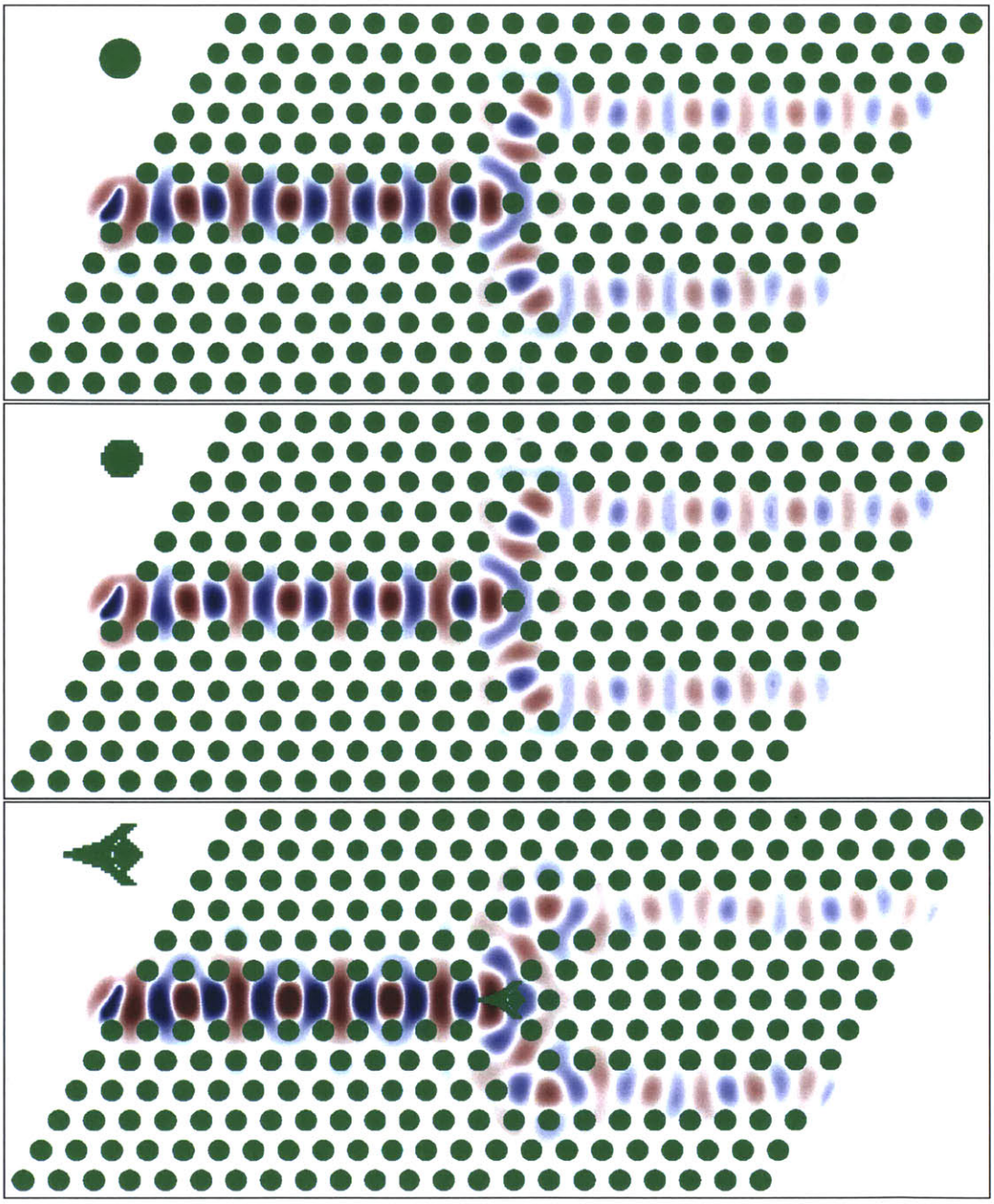

Figure 6.19: H_z solution field for a 2d representation of a TE polarized PC slab waveguide with a Y bend for $\omega a/2\pi c = 0.225$ and holes of radii $0.3a$ on a $\varepsilon = 11.8$ material. Naive approach (top), initial guess through projection (center) and optimized pattern (bottom). Insets show the exact geometry at the Y corner.

this case, the thickness of the slab has been considered to be $d = a$ and the geometry shown in figure 6.18 has been surrounded by a PML region. All in all, the total number of degrees of freedom for the forward simulation problem before the MSHDG

reduction is around 600 million, considering the nodal points times the components of $\mathbf{U}$.

The cylindrical extension of the same three patterns discussed so far has been considered within the 3d simulation setting. As expected, the performance of all the patterns is significantly worse. However, the 2d optimized pattern still provides a much higher efficiency than either the naive hole. Figure 6.20 shows the H_z solution states on a cut over the horizontal plane corresponding to half of the thickness respectively for the solution states with each one of the three geometries: the rounded hole, its projection into our pixelized domain and the 2d optimal pattern. The color map has been changed to facilitate the identification of the propagated field.

The perfectly rounded hole drilled on the silicon slab will now have only 0.32 as transmission fraction and thus yields 68% in losses. Similarly, the projected hole onto the pixelized domain increases the losses up to 75%. On the other hand, the 2d optimized pattern will maintain a decent performance with only 39% of losses.

Table 6.3 summarizes the transmission fraction values for each case. Note that the pattern optimized for the 2d case improves the transmission in the 3d case by a factor of two.

Table 6.3: Summary of results for the 2d/3d Y waveguide bend.

Pattern	Rounded Hole	Pixel Projection	2d Optimized
Transmission (2d) %	87	84	95
Transmission (3d) %	32	25	61

6.4 Concluding Remarks

This chapter has presented several optimal designs that have been computed by bringing together the numerical simulation capability and the design optimization tool. We have thereby illustratively proven the validity of this new design paradigm by obtaining practical patterns. It is particularly remarkable that discrete optimization has been carried out on problems which are already challenging just to simulate numerically. Furthermore, the computational efficiency of these methods has allowed us to

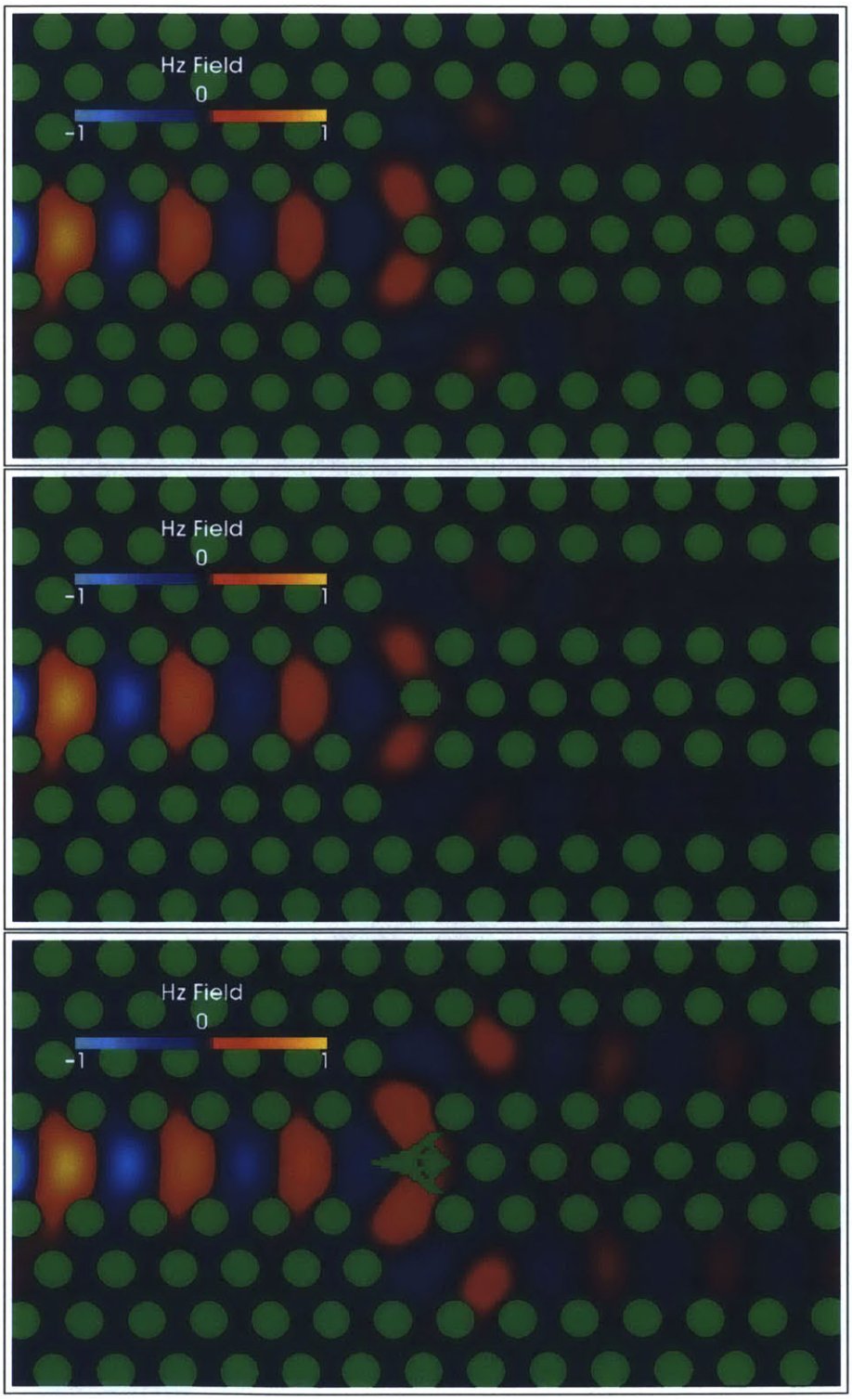

Figure 6.20: H_z solution field for a 3d TE polarized PC slab waveguide with a Y bend for $\omega a/2\pi c = 0.225$. The radii of the holes are $0.3a$ and the thickness of the $\varepsilon = 11.8$ slab is a. Naive approach (top), initial guess through projection (center) and 2d optimized pattern (bottom).

choose fine enough pixelizations to describe the design region with up to a couple of thousand pixels, both in 2d and 3d.

Firstly, we have focused on the design of an invisibility cloak in 2d. Optimal patterns with reductions of the scattered field of over 97% have been found for both cylindric and carpet cloaks. The materials (PI and aluminum) as well as the shapes of the pixels for each pattern have been chosen to facilitate as much as possible their fabrication.

In addition to the cloaking problem, the design of improved sharp waveguide bends has also been considered. In a two dimensional setting, we have found a discrete pattern that reduces the transmission losses down to 2% for specific frequencies around a 90 degree bend of a TM polarized squarely symmetric PC waveguide. Analogously, full 3d optimal patterns have been found for sharp bends on cylindric fibers, for which the transmission fraction has risen to 0.88.

Moreover, the same techniques have been used for a 3d Y waveguide bend on a TE polarized PC slab. The simulations in 3d consider Maxwell's equations instead. The optimal patterns have been obtained in 2d and tested through the 3d simulations offering improvements of the transmission fraction from 0.32 to 0.61 in the 3d setting and for specific frequencies. In order to improve this results even further, we could consider the optimization of the upper and lower 60 degree bends as well as the inner sides of the Y.

Similarly, additional applications within electromagnetics, acoustics and elasticity could also benefit from this design capability. Besides, more relevant patterns would be found if robustness constraints were included in the design formulation, both with respect to the material properties as well as the targeted frequency.

Chapter 7

Summary and Future Work

> *Science never solves a problem without creating ten more.*
>
> **–George Bernard Shaw**

Last but not least, this chapter summarizes the work presented in this thesis pointing out the main contributions as well as listing potential future lines of research. Also, several physical applications are discussed that have not been considered here and that could benefit from this research.

7.1 Conclusions

The main goal of the research presented in this thesis has been to devise a capability for the automatic, robust and practical design of materials that present desired features for wave propagation control. Such capability has been obtained by developing a set of multiscale methods for the numerical simulation of wave propagation problems together with a binary optimization algorithm for design.

Firstly, the numerical simulation capability by itself is one of the main contributions. The organized division of the computational domain into equivalent subdomains allows for a static condensation of the degrees of freedom that reduces the size of the global problem from $\mathcal{O}(n)$ to $\mathcal{O}(n^{1/2})$ in 2d and $\mathcal{O}(n^{2/3})$ in 3d. For given computational resources, this approach allows for the simulation of larger problems in 2d and

in 3d. This technique has been implemented for Helmholtz's and Maxwell's equations providing a robust, convergent and efficient procedure for the numerical computation of wave propagation problems in the context of acoustics and electromagnetics. Moreover, the same techniques have been adapted for a nonlinear hybridized resolution of wave eigenvalue problems, again in 2d and 3d. As a result, problems with a total of up to several hundred million degrees of freedom have been solved without the use of supercomputers. The key advantage of these methodologies lie in the re-use of the local solutions. Note that the static condensation of the volumetric degrees of freedom into the boundary traces is carried out only for a handful of subelements. In contrast to other parallelization strategies, including efficient direct solvers, we exploit the physics and only solve one representative of each class.

In addition, we have developed a binary optimization procedure. This design approach goes beyond the classical heuristics of discrete optimization since it takes advantage of the actual physics of the problem. The use of reduced basis approximations lets us take advantage of the inherent physics and helps us further reduce the computational cost at each iteration. Furthermore, this approach guarantees the binary nature of all the solutions found, bringing a rather common and often intractable manufacturability constraint into the formulation of the design problem. Note that this optimization technique helps improve given patterns and therefore can always be used as a post-processing methodology for any candidate material obtained through any alternative technique.

The combination of the aforementioned techniques results in the most relevant contribution of this thesis. In fact, bringing together a numerical technique efficient enough that makes design optimization possible, even in 3d, with a binary optimization method that numerically obtains patterns that meet this basic manufacturing constraint, is novel, unique and promising. On top of that, the optimization algorithm benefits greatly from the multiscale methodology since, at each iteration, none or just a few subelements need to be recomputed (depending on the definition of the subelements) and the reassembly of the global matrix is modified only locally, for a handful of nonzero entries of the global matrix.

Finally, the validity and effectiveness of this approach has been proved by actually designing patterns that are not intuitive yet very effective in terms of optimality criteria. In particular, circular and carpet cloaks as well as low loss acoustic and electromagnetic waveguide bends, in 2d and remarkably in 3d, have been found. The design of these novel devices are of high interest in the structured materials and *meta*materials communities and therefore they have been designed with a focus on accurately meeting most fabrication requirements pointed out by experimentalists. These include the choice of the component materials for each application, the ranges of frequencies of interest, the size of the patterns, the shape of the pixels, and of the domains of interest. In conclusion, all these patterns are not only unintuitive but they also provide the desired features optimally, while maintaining their discrete nature.

7.2 Summary of contributions

The contributions of this thesis can be synthesized as:

- Development of multiscale numerical methods that take advantage of repeated geometries to enable the resolution of larger problems for given computational resources:
  - formulation and implementation of a multiscale CG methodology in 2d and 3d for Helmholtz's equation,
  - formulation and implementation of a multiscale HDG methodology for Helmholtz's and Maxwell's equations in 2d/3d;
- Development of a nonlinear multiscale numerical method for eigenvalue problems with repeated patterns:
  - formulation and implementation of a nonlinear multiscale CG methodology for the eigenvalue Helmholtz's equation in 2d/3d,
  - extension of the code for periodic problems imposing Bloch's theorem;
- development of a tractable algorithm for the discrete design optimization of heterogeneous materials:

  - introduction of a binary gradient coordinate descent heuristic approach,
  - use of reduced basis approximation to improve the efficiency,
  - combination with the simulation tools to enhance the design method;

- demonstration of the design capability for circular and carpet electromagnetic cloaks in 2d; and

- demonstration of the design capability on the creation of patterns for highly efficient sharp bends in 2d PC waveguides and 3d fibers and PC slabs.

7.3 Future Work

Many avenues for further research relating to these methods are apparent. Firstly, we list the ideas that could potentially enhance the multiscale simulation methodology. We then look at future work involving the optimization procedure and finally conclude by listing several applications that could potentially benefit from this research.

7.3.1 Numerical simulation

We begin by discussing future lines of research regarding the numerical simulation of wave propagation problems. These include the consideration of high order meshes, the extension to nested multiscale methods, the parallelized implementation of the method, the formulation of the MSHDG method for eigenvalues and extending the techniques to other equations.

Use of high-order curved meshes

Most of the problems of interest contain geometric details at very different scales. That is partially the reason why multiscale methods are a powerful approach for their numerical resolution. Nevertheless, the local discretizations that have been considered throughout the work presented in this thesis do not use high-order descriptions of the geometries. This is currently a very active field of research by itself and different methodologies have been successfully implemented, such as linear elas-

ticity deformation of meshes [125] as well as more advanced techniques that can truly describe complex high-order geometries both in 2d [133, 134], as well as in 3d [63].

The consideration of this methodologies could further reduce the degrees of freedom of the local problems, which most of the times are overdimensioned in order to ensure a good description of the geometry. Moreover, the development of higher quality meshes, especially for 3d problems, would also help reduce the total number of degrees of freedom of the local problems, potentially leading to choices of larger subelements.

Furthermore, we have only considered structured *macro*discretizations. The extension of the multiscale methodologies for unstructured subdomain decompositions would generalize the simulation methods. In particular, note that for linear PDEs the Jacobian does not depend on the position or the solution fields and thus it can be pulled out from the integrals. Then, by properly defining the map from each subelement into a reference element, only one representative of each class of reference subelements needs to be solved.

Extension to nested multiscale approaches

The multiscale methods provide equivalent numerical approximations to their local solvers (CG and HDG respectively) with considerable savings in the computational effort. This is achieved by decomposing the governing equation on a bounded domain into a number of local subproblems on subdomains and introducing the Lagrange multipliers to glue the approximation across subdomain interfaces. As we have seen, only a few local subproblems need to be solved and are trivially parallelizable. Thus, the main computational effort comes when solving the global system. It is therefore desired that the size of the subelements is as large as possible (then the amount of Lagrange multipliers is reduced), but if they are chosen too large, then the local problems become limiting in terms of computational effort.

Similarly to how nested multigrid methods work [141], the implementation of a nested multiscale approach could provide an even more considerable reduction of the computational effort since several levels of *macro*discretization could be considered. In

the presence of repeated patterns (as an example, recall the PC waveguides) one could devise a first level of *macro*decomposition into subelements that contain 8×8 rods. These local problems might seem too large to solve by direct solvers and could already be limiting the computational effort; nevertheless, if each of the representatives is also solved through another level of *macro*discretization into 2×2 rods, a global reduction of the degrees of freedom could be achieved.

This is a very interesting area of further research, but note that the decision of how many levels of discretization minimize the computational effort seems to be very problem dependent. Therefore, a somehow automated manner of making such decision could certainly enhance the multiscale approach. Furthermore, when choosing the size of the subproblems there is a trade-off between the total number of degrees of freedom (the larger the subdomains, the less degrees of freedom) and the density of the system of equations (the larger the subdomains, the higher the order considered and thus the denser the system becomes) that should be carefully analyzed in order to find optimal sizes of subelements.

Extend the implementation with parallelization and iterative solvers

All the simulation results that have been presented here have been obtained through direct solvers using Matlab®. For the large 3d problems with over $500m$ degrees of freedom, a single linux machine with four eight-core AMD Opteron 6320 CPUs, each one with a clock frequency of $2.8GHz$, $24MB$ of cache and a total memory of $512GB$ has been used. The 32 cores allow for the absolutely parallel resolution of the local problems. Nevertheless, the limiting factor that does not let us go to larger problems is the RAM required for solving the global system of equations. Going to more powerful computers is not really a solution to this issue given the poor scalability of the size of the system with respect to the size of the problem (especially in 3d). However, a parallel implementation of the multiscale methods as well as the use of iterative solvers with preconditioners could allow the resolution of significantly larger problems if one is willing to trade off wall-clock time. The parallel implementation through the use of iterative solvers on the CPU has already been successfully developed for implicit

DG methods [126] as well as the HDG method [135]. An equivalent extension for the multiscale methods presented here would significantly contribute to the resolution of even larger wave propagation problems. It might be necessary to consider the time dependent wave equation since devising preconditioners for Helmholtz's and Maxwell's equations in 3d is inherently complicated. Furthermore, the static condensation carried out from each local subelement into the global system may also be challenging to consider in parallel.

Develop a nonlinear MSHDG for 3d Maxwell's eigenproblem

Chapter 4 introduces the extension of the multiscale CG method presented in chapter 2 for Helmholtz's equations in 2d and 3d. Similarly, the MSHDG method that has been developed in chapter 3 could also be adapted to solve the eigenvalue Maxwell's equations also in 3d. The eigenproblem formulation of Maxwell's equation would be analogously converted into a nonlinear formulation in exchange of a significant reduction of the size of the problem.

In fact, the electromagnetics community has also shown a big interest on band diagrams for 3d problems. In this case, TE and TM modes cannot be decoupled and finding bandgaps that simultaneously impede the transmission of electric and magnetic pulses becomes harder. In particular, full 3d Photonic Crystals have only recently captured the attention of the community because such gaps are narrow for simple structures.

Extend the techniques to other equations

The multiscale methods introduced in this thesis have been developed and implemented for frequency domain waves described by Helmholtz's and Maxwell's equations. This capability could be easily extended to time domain wave equations as well as nonlinear wave equations. Firstly, elastic wave equations would allow us to model computational mechanics and thus design materials for the seismic wave mitigation as well as devices for the ultrasonic wave control. This equation is linear and describes the propagation of waves in an elastic medium. Similarly, there are several wave equations in the context of fluid dynamics. In particular, the shallow water

equations are a set of nonlinear hyperbolic equations that describe the flow below a pressure surface in a fluid (wavelength much larger than depth). These equations model tides, tsunamis, waves incoming ports and other large length scale waves on fluids. The design of submerged ports as well as tsunami dispersers could be obtained using these equations.

Furthermore, although multiscale methods have already been implemented for other equations such as elliptic coercive equations for flow in porous media [69] or computational mechanics [71], problems governed by other physics could greatly benefit from the adoption of the approach presented in this thesis. Firstly, the clever identification and choice of a *macro*discretization with equivalent subelements can help reduce the global number of degrees of freedom compared to any CG, DG or HDG based discretization considered, without jeopardizing the quality of the approximation. This technique could not only be especially suitable for the numerical computation of flows in porous media (note the pattern repetition therein), but it could also be very helpful for problems with homogeneous materials, such as Navier-Stokes equations for aerodynamics or aeroacoustics, for instance.

Special attention needs to be paid for nonlinear equations since the reuse of the local subelement information might be complicated given the presence of a Jacobian that is no longer independent of the solution field. If the local subelements are not reused, these multiscale techniques would not differ significantly from the already existing domain decomposition techniques, e.g. [135].

7.3.2 Binary design optimization methods

We now point out the main areas of future research in terms of the design optimization methodology. Mainly, we discuss the inclusion of other manufacturability constraints, the design optimization over ranges of frequencies and the consideration of pixel adaptive approaches.

Include further manufacturability constraints

It is often the case that the computed optimal solution of an optimization problem cannot be implemented directly, irrespective of data accuracy, due to either technological limitations, the deliberate simplification of a model to keep it tractable, and/or human factors. Fabricability constraints are typically very difficult to include in the optimization formulations because of their complexity and ambiguity, yet they are crucial for the optimal patterns to be valid and practical. A fabrication adaptivity methodology has been introduced in [95], whereby a conservative but robust optimal solution is sought that allows the robust optimum to be manually tunable according to manufacturability concerns.

The extension of the work presented in [95] or other robust design ideas as the ones presented in [15, 20] to the binary design optimization algorithm would make the results more realizable. Solution patterns are already binary, which is one of the main fabrication concerns, but it might be the case that suspended pixels show up in the solution. Similarly, the precision at which pixels can be fabricated is bounded but not zero and the current optima do not have any guarantee of performance if the patterns are not matched exactly.

Extend methodologies for optimization of frequency ranges

The optimization algorithm that has been presented in this thesis considers objective functions that involve the solution field $u(\mathbf{x}, \varepsilon)$ for a fixed frequency ω_0. When designing patterns for wave propagation control it is often the case that the devices sought are more interesting if valid for a range of frequencies. Incorporating solutions u for a few similar frequencies in the objective function as in [60] can be done at a computational cost factor of $\mathcal{O}(n_\omega)$ where n_ω is the number of targeted frequencies.

Robust optimization ideas with respect to the frequency ω instead of the design parameters $\boldsymbol{\varepsilon}$ could also enhance the optimization methodology significantly. Similarly, the use of reduced basis could also be considered, since close enough frequencies never provide arbitrarily different responses. Alternatively, the objective function could include terms towards the minimization of the sensitivities of the solution $\partial u / \partial \omega$.

Pixel adaptivity

The illustrative examples presented in chapter 6 have considered pixelizations of the design domain that try to be as close as possible to fabricable patterns. It has already been discussed why for computational practicality the number of pixels needs to be relatively small. There is a trade-off between the number of pixels considered (the more, the potentially better quality pattern) and the computational cost of getting an optimal solution (more iterations required plus each iteration is more expensive). It would thus be desired to follow an adaptive methodology: start from several random initial guesses on a rather coarse pixelization; then, the best solution is chosen, the pixelization is refined around the boundaries of the current pattern and the optimization restarted from the projection of the previous optimal state into the refined pixelization. In this manner, the number of pixels could be consistently kept at around a thousand whereas the precision of the pattern could be enhanced.

7.3.3 Potential applications of interest

Finally, let us now mention some of the physical applications that have not been considered for design in this thesis and that could greatly benefit from the methodologies developed herein. The simulation of superlenses [47, 56, 166] or *nano* and *micro*cavities [2, 88, 157] have been included in chapter 2 and all these applications could also use the binary optimization procedure for design. Furthermore, acoustic holography devices [89] could be designed. These are materials that can control the phase at which an acoustic wave is reflected based on the angle of incidence. Similarly, the design of claddings for Photonic Crystal fibers as in [78] could also be enhanced through the methodology here presented. Also, the design of sound bullets [148] for terrain inspection and medical purposes, ultrasound focusing devices [165] or *nano*antennas with improved optical performance [79] is of high interest. There are also natural extensions of this field to the heat equation, with particular interest in the design of thermodynamic cloaks and heat flux concentrators [65, 140].

Also, there are problems where periodicity can be assumed and only the simulation and design optimization of a certain unit cell is needed. The multiscale forward

simulation tool can also be used there (the eigenvalue solver of chapter 4) as well as the binary design optimization procedure for their design process. Examples of these problems are photonic/acoustic/elastic bandgap as in [68,96,98], among many others.

Within the last few years, as an extension of Photonic Crystals and electronics, Plasmonics has attracted attention from researchers within the wave propagation community. Plasmonics studies the coupling of light to charges (like electrons) in metals. This coupling allows breaking the diffraction limit through geometric details at the subwavelength scale [118], unlike Photonic Crystals, which need to be several wavelengths long. Applications of Plasmonics to photovoltaic devices [7], nanolithography [150] and *nano*optical devices [93] have also raised the interest of this field.

Additionally, there is also a large set of potential uses of structured materials for wave propagation in elastic media that are beyond the scope of this thesis. Some examples are earthquake filters [77], nonlinear shock dispersers [61,68] or elastic cloaks [58]. Moreover, negative Poisson's ratio materials, first introduced in [84, 85], are *meta*materials that can offer remarkably large volumetric changes under small stresses [55, 149, 155, 156, 159].

All the applications that have just been mentioned are a small representation of possible wave control applications of interest. They all require the simulation of a large, finite domain and the optimization of a subregion therein, and therefore should benefit from this work.

> *The important thing is*
> *never to stop questioning.*
>
> **–Albert Einstein**

Appendix A

Perfectly Matched Layers for Multiscale methods

Wave propagation problems often occur in unbounded domains. However, for the numerical solution of these problems, a finite and bounded computational domain needs to be defined. In particular, the choice of boundary conditions is not trivial if all reflections want to be avoided. All in all, the boundary conditions of a wave propagation problem modeled through Helmholtz's equation should be considered as Sommerfeld radiation conditions [146]:

$$\left.\begin{array}{rl} \nabla \cdot (a(\mathbf{x})\nabla u) + k^2 b(\mathbf{x}) u = f & \text{in } \mathbb{R}^d \\ \lim\limits_{|\mathbf{x}|\to\infty} |\mathbf{x}|^{\frac{d-1}{2}} \left(\dfrac{\partial u}{\partial |\mathbf{x}|} - iku \right) = 0 & \forall \mathbf{x} = \hat{\mathbf{x}}|\mathbf{x}| \end{array}\right\} \tag{A.1}$$

where a, b are define once the material properties and the frequency are fixed, $d \in \{2, 3\}$ represents the dimension of the physical domain and $i = \sqrt{-1}$ denotes the imaginary unit.

The truncation of this boundary condition at a given external non infinite boundary corresponds to the so-called first-order absorbing boundary conditions. These type of boundary conditions can be accurate for some scattered field problems but clearly provide a significant source of error, especially if the boundaries are not too faraway, in terms of wavelengths, from the regions of interest.

An alternative boundary conditions treatment for wave propagation problems is given by Perfectly Matched Layers, or just PMLs. The main purpose of these artificial layers of computational domain is to avoid reflections by damping the physical

solution to zero before it reaches the actual boundaries. J. Berenger proposed in [17] a methodology whereby creating a transformation of the derivative operators that included imaginary values, the solution field was damped.

More specifically, if we want to consider PMLs that absorb waves propagating in the x direction, the following transformation of the derivative operator through a change of variables needs to be included in the equation for that part of the domain:

$$\frac{\partial}{\partial x} \rightarrow \frac{1}{s_x}\frac{\partial}{\partial x} = \frac{1}{1-\frac{i\sigma(x)}{\omega}}\frac{\partial}{\partial x} \tag{A.2}$$

and equivalently for directions y or z. Note that ω is the frequency and $\sigma(x)$ some auxiliary function that only depends on the spatial variable x and that will define the damping. Also note that wherever $\sigma > 0$, waves propagating in x are attenuated. For notation purposes, let us now define

$$\tilde{\nabla} = \left(\frac{\partial}{\partial \tilde{x}}, \frac{\partial}{\partial \tilde{y}}, \frac{\partial}{\partial \tilde{z}}\right) = \left(\frac{1}{s_x}\frac{\partial}{\partial x}, \frac{1}{s_y}\frac{\partial}{\partial y}, \frac{1}{s_z}\frac{\partial}{\partial z}\right) \tag{A.3}$$

and now the Helmholtz problem defined by A.1 can be truncated at a domain of interest Ω_0 plus several layers of PML around it Ω_{pml} to form a computational domain $\Omega = \Omega_0 \cup \Omega_{pml}$. Then, the equation that governs the problem in Ω_0 corresponds to $(\sigma_x, \sigma_y, \sigma_z) = (0,0,0)$, whereas the one on the right and left sides of Ω_{pml} will consider $\sigma_x > 0$, the ones on the top and bottom sides of Ω_{pml} will take $\sigma_y > 0$ and the front and back sides of Ω_{pml} will have $\sigma_z > 0$. Similarly, the areas where two PML regions intersect will have the corresponding two components of $\boldsymbol{\sigma}$ positive and for the corner regions, the three components will be greater than zero.

All in all, the problem can be written as:

$$\left.\begin{array}{rl} \nabla \cdot (a\Gamma\nabla u) + bs_x s_y s_z u = f, & \text{in } \Omega \subset \mathbb{R}^d \\ \text{anything, e.g. : } u = 0 & \text{on } \partial\Omega \end{array}\right\} \tag{A.4}$$

where

$$\Gamma = \begin{bmatrix} s_y s_z s_x^{-1} & 0 & 0 \\ 0 & s_x s_z s_y^{-1} & 0 \\ 0 & 0 & s_x s_y s_z^{-1} \end{bmatrix}. \tag{A.5}$$

The thickness of the layers could be arbitrarily small if the values of σ are chosen

large enough. However, a very large contrast of values of σ leads to reflections at those points. It is therefore essential to choose $\sigma_x(|x-x_0|), \sigma_y(|y-y_0|)$ and $\sigma_z(|z-z_0|)$ to be non constant functions that slowly and smoothly increase with the distance to the PML boundary position.

Furthermore, the exact same transformation on the derivative operators needs to be considered for the PMLs when Maxwell's equations are solved. All in all, we replace $\nabla \leftarrow \tilde{\nabla}$, which can also be written analogously to equation A.4 as:

$$\left.\begin{aligned} \Gamma\nabla\times\mathbf{H} - (i\omega a(x)+b(x))s_x s_y s_z \mathbf{E} &= \mathbf{J}, \quad \text{in } \Omega \\ \Gamma\nabla\times\mathbf{E} + i\omega c(x) s_x s_y s_z \mathbf{H} &= 0, \quad \text{in } \Omega \\ \text{anything, e.g. : } \mathbf{n}\times\mathbf{E} &= 0, \quad \text{on } \partial\Omega \end{aligned}\right\}. \tag{A.6}$$

More advanced PMLs have been devised in [83] for the case of heterogeneous materials or more precisely PC waveguides. The choice of the functions s presented there allow for a reduction of the PML width of 50% to 80% taking advantage of the heterogeneity of the waveguides and the output wave pattern [83]. When considering the Perfectly Matched Layers formulations within the multiscale methodologies, this dependence of the stretching functions s on the distance to the PML boundary can jeopardize the efficiency of the method. This approach can easily be included within the Multiscale methodologies, although in this case, every extra subelement used in the PML region needs to be solved separately.

Recall that we will only be solving a few different local problems, corresponding to representatives of each class of geometry. However, for every PML subelement, the governing equation is different (note that $x-x_0$ is different for every subelement, and equivalently for $y-y_0$, $z-z_0$). In order to be able to reuse the resolution of local subelements many times, firstly we choose the local discretization of all the subelements forming the PML region to be the same. For this specific case, note that all subelements aligned along the vertical column of the right side boundary of Ω_0 belong to the same class and thus only one representative needs to be solved. That can be extended to every of the 4 boundary edges in 2d or the 6 faces in 3d. One more element per corner needs to be included.

One more consideration to have in mind is the fact that the thickness of the PML needs to be of the order of several wavelengths, to avoid reflections that may affect the solution field in Ω_0. This would lead us to include more than one layer of subelements one next to the other. Note that every layer would require one more representative to be solved, since every layer has a different function s (there the name PM-Layers). It is though preferable to create a wider element that can take the desired amount of wavelengths than to consider multiple layers of subelements.

Finally, sometimes the domain boundaries $\partial\Omega_0$ might not be aligned with the wave direction $\mathbf{k}$. In this situation, it is preferable to inscribe Ω_0 inside a rectangle aligned with $\mathbf{k}$ and then attach to it Ω_{pml}.

All these tricks might depend on the specific problem that we want to solve but it is important that these considerations are taken into account in order to minimize the computational cost increase produced by the use of PMLs. In all the examples simulated in this thesis, the number of local subelements required for the problem itself plus the PML never exceeds 15, which makes them fully parallelizable provided 16 or more cores are available.

Appendix B

Multiscale methods

This appendix provides some theoretical results, theorems and proofs corresponding to the multiscale simulation methods. The intention is to complete the statements and derivations of chapters 2, 3 and 4 as well as facilitating their reading.

Firstly, let us show the existence and uniqueness of the MSCG approximate solution, as well as the relationship between the solutions to this method and a classical CG approach. The equivalent theorem and proof for the MSHDG method can also be derived.

Theorem B.1 *There exists a unique function (U_h, λ, q_h) in the space $Y_h \times V_h(g_D) \times W_h$ satisfying the primal formulation 2.14. Moreover,*

$$U_h = u_h \text{ on } \Omega, \qquad \lambda = u_h \text{ on } \mathcal{E}_h \tag{B.1}$$

where $u_h \in X_h(g_D)$ is the solution to formulation 2.9.

Proof Since $\lambda \in V_h(g_D)$ and $U_h \in Y_h$, it follows from (2.14b) that $U_h \in X_h(g_D)$. Moreover, since $X_h(0) \in Y_h$, by 2.14a and 2.15 we have

$$(a\nabla U_h, \nabla v)_\Omega + (bU_h, v)_\Omega - \langle [\![q_h]\!], v\rangle_{\mathcal{E}_h} = (f, v)_\Omega, \quad \forall v \in X_h(0). \tag{B.2}$$

We next note from the definition of the space $V_h(0)$ that $\mu = v|_{\mathcal{E}_h}$ belongs to $V_h(0)$ whenever $v \in X_h(0)$. Hence, the jump condition (2.14c) implies that

$$\langle [\![q_h]\!], v\rangle_{\mathcal{E}_h} = \langle g_N, v\rangle_{\Gamma_N}, \quad \forall v \in X_h(0). \tag{B.3}$$

It thus follows from B.2 and B.3 that

$$(a\nabla U_h, \nabla v)_\Omega + (bU_h, v)_\Omega = (f, v)_\Omega + \langle g_N, v\rangle_{\Gamma_N}, \quad \forall v \in X_h(0). \tag{B.4}$$

By the uniqueness of the approximate solution of the CG method, we immediately obtain that $U_h = u_h$ and, as a consequence, that $\lambda = u_h$ on $\mathcal{E}_h$.

It remains to prove that the function q_h exists and is unique. By (2.14a) and the uniqueness of U_h, this is equivalent to proving that the trivial solution is the only solution of

$$\sum_{m=1}^{M} \langle q_h, v \rangle_{\partial\Omega^m} = 0, \quad \forall v \in Y_h. \tag{B.5}$$

Since $q_h \in W_h$, there is a $w \in Y_h$ such that $q_h|_{\partial\Omega^m} = w|_{\partial\Omega^m}$ for all $\Omega^m \in \mathcal{T}_\Omega$. Taking $v = w$ in the above equation, we have that $q_h = 0$. □

Let us now state and prove that the decomposition considered for the multiscale methods indeed provides the solution to the combined problem.

Theorem B.2 *Let u_f and u_η be solutions of the following problems, respectively.*

$$\left.\begin{aligned} -\nabla \cdot (a\nabla u_f) + bk^2 u_f &= f, \quad \text{in } \Omega^m \\ u_f &= 0, \quad \text{on } \partial\Omega^m \end{aligned}\right\}, \tag{B.6}$$

$$\left.\begin{aligned} -\nabla \cdot (a\nabla u_\eta) + bk^2 u_\eta &= 0, \quad \text{in } \Omega^m \\ u_\eta &= \eta, \quad \text{on } \partial\Omega^m \end{aligned}\right\}. \tag{B.7}$$

Then, $u = u_f + u_\eta$ is the solution of:

$$\left.\begin{aligned} -\nabla \cdot (a\nabla u) + bk^2 u &= f, \quad \text{in } \Omega^m \\ u &= \eta, \quad \text{on } \partial\Omega^m \end{aligned}\right\}. \tag{B.8}$$

Proof Let us consider $u =_f + u_\eta$ and plug it in equation B.8.

$$\left.\begin{aligned} -\nabla \cdot (a\nabla u_f + u_\eta) + bk^2 (u_f + u_\eta) &= f, \quad \text{in } \Omega^m \\ u_f + u_\eta &= \eta, \quad \text{on } \partial\Omega^m \end{aligned}\right\}. \tag{B.9}$$

Now the first line, we use linearity of the operator ∇ as well as bk^2 to split it into two additive blocks. In the second equation we use that $u_f = 0$ on $\partial\Omega$ and $u_\eta = \eta$ on $\partial\Omega$ from equations B.6 and B.7. All in all,

$$\left.\begin{aligned} [-\nabla \cdot (a\nabla u_f) + bk^2 u_f] + [-\nabla \cdot (a\nabla u_\eta) + bk^2 u_\eta] &= f, \quad \text{in } \Omega^m \\ 0 + \eta &= \eta, \quad \text{on } \partial\Omega^m \end{aligned}\right\}. \tag{B.10}$$

Finally, let us use again B.6 and B.7 to replace $[-\nabla\cdot(a\nabla u_f)+bk^2u_f]$ by f and $[-\nabla\cdot(a\nabla u_\eta)+bk^2u_\eta]$ by 0 to obtain an identity, proving the statement. □

We now prove the uniqueness of the solution for the weak dual formulation of the MSCG. This result could equivalently be proven for the MSHDG method.

Theorem B.3 *Let (U_h,λ,q_h) be the solution of the primal formulation 2.14. Then*

$$U_h = U_\lambda + U_f, \quad \textit{and} \quad q_h = q_\lambda + q_f. \tag{B.11}$$

Moreover, the Lagrange multiplier $\lambda\in V_h(g_D)$ is the unique solution of

$$a_h(\lambda,\mu) = b_h(\mu), \quad \forall\mu\in V_h(0), \tag{B.12}$$

where

$$\begin{aligned} a_h(\eta,\mu) &= (a\nabla U_\eta,\nabla U_\mu)_\Omega + (bU_\eta,U_\mu)_\Omega\,,\\ b_h(\mu) &= (f,U_\mu)_\Omega + \langle g_N,\mu\rangle_{\Gamma_N}\,. \end{aligned} \tag{B.13}$$

Proof We first note from (2.16a) and (2.18a) that

$$\begin{aligned} &(a\nabla(U_\lambda+U_f),\nabla v)_\Omega + (b(U_\lambda+U_f),v)_\Omega\\ &\qquad - \langle[\![q_\lambda+q_f]\!],v\rangle_{\mathcal{E}_h} = (f,v)_\Omega, \quad \forall v\in X_h(0). \end{aligned} \tag{B.14}$$

This equation and Theorem 1 immediately yield the first result (B.11).

The first result implies that (2.14c) can be rewritten as

$$\langle[\![q_\lambda+q_f]\!],\mu\rangle_{\mathcal{E}_h} = \langle g_N,\mu\rangle_{\Gamma_N}\,, \quad \forall\mu\in V_h(0). \tag{B.15}$$

We next note from (2.18b) and (2.18a) that

$$\begin{aligned} \langle[\![q_\lambda]\!],\mu\rangle_{\mathcal{E}_h} &= \langle[\![q_\lambda]\!],U_\mu\rangle_{\mathcal{E}_h}\\ &= (a\nabla U_\lambda,\nabla U_\mu)_\Omega + (bU_\lambda,U_\mu)_\Omega\,. \end{aligned} \tag{B.16}$$

Similarly, from (2.18b), (2.16a), (2.18a), and (2.16b) we have

$$\begin{aligned} \langle[\![q_f]\!],\mu\rangle_{\mathcal{E}_h} &= \langle[\![q_f]\!],U_\mu\rangle_{\mathcal{E}_h}\\ &= -(f,U_\mu)_\Omega + (a\nabla U_f,\nabla U_\mu)_\Omega + (bU_f,U_\mu)_\Omega\\ &= -(f,U_\mu)_\Omega + \langle[\![q_\mu]\!],U_f\rangle_{\mathcal{E}_h}\\ &= -(f,U_\mu)_\Omega. \end{aligned} \tag{B.17}$$

The second result (B.12) follows from (B.15)-(B.17). This completes the proof. □

Also, equivalent results can also be stated for non-conforming discretizations. Proofs for theorems B.4 and B.5 are analogous to theorems B.1 and B.3.

Theorem B.4 *There exists a unique function* $(U_h^{\text{non}}, \lambda^{\text{non}}, q_h^{\text{non}})$ *in the space* $Y_h^{\text{non}} \times V_h^{\text{non}}(g_D) \times W_h^{\text{non}}$ *satisfying the primal formulation (2.43). Moreover,*

$$U_h^{\text{non}} = u_h^{\text{non}} \text{ on } \Omega, \qquad \lambda^{\text{non}} = u_h^{\text{non}} \text{ on } \mathcal{E}_{\text{e}}. \tag{B.18}$$

Theorem B.5 *Let* $(U_h^{\text{non}}, \lambda^{\text{non}}, q_h^{\text{non}})$ *be the solution of the primal formulation 2.14. Then*

$$U_h^{\text{non}} = U_{\lambda^{\text{non}}}^{\text{non}} + U_f^{\text{non}}. \tag{B.19}$$

Moreover, the Lagrange multiplier $\lambda^{\text{non}} \in V_h^{\text{non}}(g_D)$ *is the unique solution of*

$$a_h^{\text{non}}(\lambda^{\text{non}}, \mu) = b_h^{\text{non}}(\mu), \quad \forall \mu \in V_h^{\text{non}}(0), \tag{B.20}$$

where a_h^{non} *and* b_h^{non} *are given by*

$$\begin{aligned} a_h^{\text{non}}(\eta, \mu) &= (a \nabla U_\eta^{\text{non}}, \nabla U_\mu^{\text{non}})_\Omega + \left(b U_\eta^{\text{non}}, U_\mu^{\text{non}}\right)_\Omega, \\ b_h^{\text{non}}(\mu) &= (f, U_\mu^{\text{non}})_\Omega + \langle g_N, \mu \rangle_{\Gamma_N}, \end{aligned} \tag{B.21}$$

for all $\eta, \mu \in V_h^{\text{non}}$.

Finally, let us algebraically obtain the nonlinear expression that is used for the MSCG method when the eigenvalue Helmholtz's equation wants to be solved.

Theorem B.6 *There exists* $\gamma_h \in \mathbb{R}$ *independent of the polynomial degree of approximation that satisfies*

$$a_h(\lambda, \mu) = \gamma_h((\mathbb{I} - \gamma_h U_W)^{-1} U_\lambda, U_\mu) \quad \forall \mu \in V_h \tag{B.22}$$

and such that (γ_h, u_h) *is a valid eigenpair of problem 4.1.*

Proof (sketch) Skipping all functional analysis details we sketch-prove here the derivation of B.22. Firstly, recall that we can write $U_h = U_\lambda + U_W f$ so that 4.10 holds. Let us then set $f = \gamma_h U_h$ and, as a result, $U_h = U_\lambda + U_W(\gamma_h U_h)$. Rearranging terms we obtain $U_h = (I - \gamma_h U_W)^{-1} U_\lambda$, converting 4.10 into B.22. □

Bibliography

[1] Y. Akahane, T. Asano, B.S. Song, and S. Noda. High-q photonic nanocavity in a two-dimensional photonic crystal. *Nature*, 425(6961):944–947, 2003.

[2] H. Altug, D. Englund, and J. Vučković. Ultrafast photonic crystal nanocavity laser. *Nature Physics*, 2(7):484–488, 2006.

[3] J. Andkjær, N.A. Mortensen, and O. Sigmund. Towards all-dielectric, polarization-independent optical cloaks. *Applied Physics Letters*, 100(10):101106, 2012.

[4] J. Andkjær and O. Sigmund. Topology optimized low-contrast all-dielectric optical cloak. *Applied Physics Letters*, 98(2):021112, 2011.

[5] I. Andronov, F. Molinet, and D. Bouché. *Asymptotic and hybrid methods in electromagnetics*. IET, 2005.

[6] H. Antil, M. Heinkenschloss, R. H. Hoppe, and D. C. Sorensen. Domain decomposition and model reduction for the numerical solution of PDE constrained optimization problems with localized optimization variables. *Computing and Visualization in Science*, 13:249–264, 2010.

[7] H. A Atwater and A. Polman. Plasmonics for improved photovoltaic devices. *Nature materials*, 9(3):205–213, 2010.

[8] M. Augustin, H. Fuchs, D. Schelle, E. Kley, S. Nolte, A. Tünnermann, R. Iliew, C. Etrich, U. Peschel, and F. Lederer. Highly efficient waveguide bends in photonic crystal with a low in-plane index contrast. *Optics Express*, 11(24):3284–3289, 2003.

[9] I. Babuška, G. Caloz, and J. E. Osborn. Special finite element methods for a class of second order elliptic problems with rough coefficients. *SIAM Journal of Numerical Analysis*, 31(4):945–981, 1994.

[10] I. Babuška and M. Zlamal. Nonconforming elements in the finite element method with penalty. *SIAM Journal of Numerical Analysis*, 10(5):863–875, 1973.

[11] H. Bao, J. Bielak, O. Ghattas, L.F. Kallivokas, D.R. O'Hallaron, J. R. Shewchuk, and J. Xu. Large-scale simulation of elastic wave propagation in heterogeneous media on parallel computers. *Computer Methods in Applied Mechanics and Engineering*, 152(1):85–102, 1998.

[12] M. Barrault, Y. Maday, N.C. Nguyen, and A.T. Patera. An 'empirical interpolation' method: application to efficient reduced-basis discretization of partial differential equations. *Journal of Computational Physics*, 229(10):3706–3725, 2010.

[13] F. Bassi and S. Rebay. A high-order accurate discontinuous finite element method for the numerical solution of the compressible Navier-Stokes equations. *Journal of Computational Physics*, 131(2):267–279, 1997.

[14] C. Baumann and J. Oden. A discontinuous hp finite element method for convectio-diffusion problems. *Computer Methods for Applied Mechanical Engineering*, 175:311–341, 1999.

[15] A. Ben-Tal and A. Nemirovski. Robust optimization–methodology and applications. *Mathematical Programming*, 92(3):453–480, 2002.

[16] M.P. Bendsoe and O. Sigmund. Material interpolation schemes in topology optimization. *Archive of Applied Mechanics*, 69:635–654, 1999.

[17] J.P. Berenger. A Perfectly Matched Layer for the absorption of electromagnetic waves. *Journal of Computational Physics*, 114:185–200, 1994.

[18] C. Bernardi, Y. Maday, and A. T. Patera. Domain decomposition by the mortar element method. In *Asymptotic and Numerical Methods for Partial Differential Equations with Critical Parameters*, pages 269–286. Springer, 1993.

[19] C. Bernardi, Y. Maday, and A. T. Patera. A new nonconforming approach to domain decomposition: The mortar element method. In *Nonlinear Partial Differential Equations and their Applications*, volume 299, pages 13–51. Longman, New York, 1994.

[20] D. Bertsimas, O. Nohadani, and K. M. Teo. Robust optimization for unconstrained simulation-based problems. *Operations Research*, 58(1):161–178, 2010.

[21] D. Bertsimas and R. Weismantel. *Optimization over integers*. Dynamic Ideas, 2005.

[22] P. Bienstman, S. Assefa, S.G. Johnson, J.D. Joannopoulos, G.S. Petrich, and L.A. Kolodziejski. Taper structures for coupling into photonic crystal slab waveguides. *JOSA B*, 20(9):1817–1821, 2003.

[23] D. Boffi, F. Brezzi, and L. Gastaldi. On the problem of spurious eigenvalues in the approximation of linear elliptic problems in mixed form. *Mathematics of Computation of the American Mathematical Society*, 69(229):121–140, 2000.

[24] S. Boyaval, C. Le Bris, T. Lelivre, Y. Maday, N. C. Nguyen, and A. Patera. Reduced basis techniques for stochastic problems. *Archives of Computational Methods in Engineering*, 17:435–454, 2010.

[25] W. Cai, U.K. Chettiar, A.V. Kildishev, and V.M. Shalaev. Optical cloaking with metamaterials. *Nature Photonics*, 1(4):224–227, 2007.

[26] E. Cances, C. Le Bris, N.C. Nguyen, Y. Maday, A. T. Patera, and G.S.H. Pau. Feasibility and competitiveness of a reduced basis approach for rapid electronic structure calculations in quantum chemistry. In *Proceedings of the Workshop for Highdimensional Partial Differential Equations in Science and Engineering (Montreal)*, 2007.

[27] Y. Cao, S. Li, L. Petzold, and R. Serban. Adjoint sensitivity analysis for differential algebraic equations: The adjoint dae system and its numerical solution. *SIAM Journal on Scientific Computing*, 24(3):1076–1089, 2003.

[28] Filippo Casadei. *Multiscale analysis of wave propagation in heterogeneous structures.* PhD thesis, Georgia Institute of Technology, 2012.

[29] Q. Cheng, T.J. Cui, X. Jian, and B.G. Cai. An omnidirectional electromagnetic absorber made of metamaterials. *New Journal of Physics*, 12:063006, 2010.

[30] E. Chow, S.Y. Lin, S.G. Johnson, J.D. Joannopoulos, J. Bur, and P.R. Villeneuve. Demonstration of high waveguide bending efficiency ($> 90\%$) in a photonic-crystal slab at 1.5μm wavelengths. In *Proceedings of SPIE*, volume 4283, page 454, 2001.

[31] E. Chow, S.Y. Lin, S.G. Johnson, P.R. Villeneuve, J.D. Joannopoulos, J.R. Wendt, G. A Vawter, W. Zubrzycki, H. Hou, and A. Alleman. Three-dimensional control of light in a two-dimensional photonic crystal slab. *Nature*, 407(6807):983–986, 2000.

[32] P. G. Ciarlet. *The Finite Element Method for Elliptic Problems.* North-Holland, Amsterdam, 1978.

[33] B. Cockburn, B. Dong, and J. Guzmán. A superconvergent LDG-hybridizable Galerkin method for second-order elliptic problemsrkin method for second-order elliptic problemsalerkin method for second-order elliptic problems. *Mathematics of Computation*, 77:1887–1916, 2008.

[34] B. Cockburn, B. Dong, and J. Guzmán. A hybridizable and supercovergent discontinuous Galerkin method for biharmonic problems. *SIAM Journal on Scientific Computing*, 40(1-3):141–187, 2009.

[35] B. Cockburn, B. Dong, J. Guzmán, M. Restelli, and R. Sacco. A hybridizable discontinuous Galerkin method for steady-state convection-diffusion-reaction problems. *SIAM Journal of Scientific Computing*, 31(5):3827–3846, 2009.

[36] B. Cockburn and J. Gopalakrishnan. A characterization of hybridized mixed methods for second order elliptic problems. *SIAM Journal of Numerical Analysis*, 42(1):283–301, 2004.

[37] B. Cockburn, J. Gopalakrishnan, and R. Lazarov. Unified hybridization of discotinuous Galerkin, mixed and continuous Galerkin methods for second order elliptic problems. *SIAM Journal of Numerical Analysis*, 47:1319–1365, 2009.

[38] B. Cockburn, J. Gopalakrishnan, F. Li, N.C. Nguyen, and J. Peraire. Hybridization and postprocessing techniques for mixed eigenfunctions. *SIAM Journal on Numerical Analysis*, 48(3):857–881, 2010.

[39] B. Cockburn, J. Gopalakrishnan, N. C. Nguyen, J. Peraire, and F.J. Sayas. Analysis of HDG methods for stokes flow. *Mathematics of Computation*, 80(274):723–760, 2010.

[40] B. Cockburn, J. Gopalakrishnan, and F.J. Sayas. A projection-based error analysis of HDG methods. *Mathematics of Computation*, 79:1351–1367, 2010.

[41] B. Cockburn, J. Gopalakrishnan, and H. Wang. Locally conservative fluxes for continuous Galerkin method. *SIAM Journal of Numerical Analysis*, 45(4):1742–1776, 2007.

[42] B. Cockburn, J. Gopalakrishnan, and H. Wang. Locally conservative fluxes for the continuous galerkin method. *SIAM Journal of Numerical Analysis*, 45(4):1742–1776, 2007.

[43] B. Cockburn, J. Guzmán, and H. Wang. Superconvergent discontinuous Galerkin methods for second-order elliptic problems. *Mathematics of Computation*, 78:1–24, 2009.

[44] B. Cockburn and C. W. Shu. The local discontinuous Galerkin method for convection-diffusion systems. *SIAM Journal of Numerical Analysis*, 35:2440–2463, 1998.

[45] B. Cockburn and C.W. Shu. Runge-Kutta discontinuous Galerkin methods for convection-dominated prolbems. *Journal of Scientific Computing*, 16(3):173–261, 2001.

[46] M. Conforti, G. Cornuejols, and G. Zambelli. *Integer Programming.* To be published, 2014.

[47] E. Cubukcu, K. Aydin, and E. Ozbay. Subwavelength resolution in a two-dimensional Photonic-Crystal-based superlens. *Physical Review Letters*, 20:207401, 2003.

[48] S.A. Cummer and D. Schurig. One path to acoustic cloaking. *New Journal of Physics*, 9(3):45, 2007.

[49] X. Dang, J. Qi, M.T. Klug, P.Y. Chen, D.S. Yun, N.X. Fang, P.T. Hammond, and A.M. Belcher. Tunable localized surface plasmon-enabled broadband light harvesting enhancement for high-efficiency panchromatic dye-sensitized solar cells. *Nanoletters*, 13(2):637–642, 2013.

[50] L. Demkowicz and J. Gopalakrishnan. A class of discontinuous Petrov-Galerkin methods. part i: the transport equation. *Computer Methods for Applied Mechanical Engineering*, 199:1558–1572, 2010.

[51] L. Demkowicz and J. Gopalakrishnan. A class of discontinuous Petrov-Galerkin methods. part ii: optimal test functions. *Numerical Methods for Partial Differential Equations*, 27:70–105, 2011.

[52] L. Demkowicz and L. Vardapetyan. Modeling of electromagnetic absorption/scattering problems using¡ i¿ hp¡/i¿-adaptive finite elements. *Computer Methods in Applied Mechanics and Engineering*, 152(1):103–124, 1998.

[53] B. Engquist and A. Majda. Absorbing boundary conditions for the numerical simulation of waves. *Mathematics of Computation*, 31:629–651, 1977.

[54] R.M. Errico. What is an adjoint model? *Bulletin of the American Meteorological Society*, 78:2577–91, 1997.

[55] K.E. Evans, M.A. Nkansah, and I.J. Hutchinson. Modeling negative Poisson ratio effects in network-embedded composites. *Acta Metallurgica et Materialia*, 40(9):2463–2469, 1992.

[56] N. Fang, H. Lee, C. Sun, and S. Zhang. Sub–diffraction-limited optical imaging with a silver superlens. *Science*, 308:534–537, 2005.

[57] M. Farhat, S. Enoch, S. Guenneau, and A. B. Movchan. Broadband cylindrical acoustic cloak for linear surface waves in a fluid. *Physical Review Letters*, 101:134501, 2008.

[58] M. Farhat, S. Guenneau, S. Enoch, and A.B. Movchan. Cloaking bending waves propagating in thin elastic plates. *Physical Review B*, 79, 2009.

[59] M. Farhat, S. Guenneau, A.B Movchan, and S. Enoch. Achieving invisibility over a finite range of frequencies. *Optics Express*, 16(8):5656–5661, 2008.

[60] L.H. Frandsen, P.I. Harpoth, P.I. Borel, M. Kristensen, J.S. Jensen, and O. Sigmund. Broadband photonic crystal waveguide 60 degrees bend obtained utilizing topology optimization. *Optics Express*, 12(24):5916–5921, 2004.

[61] F. Fraternali, M. A. Porter, and C. Daraio. Optimal design of composite granular protectors. *Mechanics of Advanced Materials and Structures*, 17:1–19, 2010.

[62] W.R. Frei, D.A. Tortorelli, and H.T. Johnson. Topology optimization of a photonic crystal waveguide termination to maximize directional emission. *Applied Physics Letters*, 86:111114, 2005.

[63] A. Gargallo-Peiró, X. Roca, and J. Sarrate. A surface mesh smoothing and untangling method independent of the CAD parameterization. *Computational Mechanics*, pages 1–23, 2013.

[64] A. Greenleaf, Y. Kurylev, M. Lassas, and G. Uhlmann. Cloaking devices, electromagnetic wormholes, and transformation optics. *SIAM Review*, 51(1):3–33, 2009.

[65] S Guenneau, C. Amra, and D. Veynante. Transformation thermodynamics: cloaking and concentrating heat flux. *Optics Express*, 20(7):8207–8218, 2012.

[66] C. Guiffaut and K. Mahdjoubi. A parallel fdtd algorithm using the mpi library. *Antennas and Propagation Magazine, IEEE*, 43(2):94–103, 2001.

[67] M. Hassine, S. Jan, and M. Masmoudi. From differential calculus to 0-1 topological optimization. *SIAM Journal on Control and Optimization*, 45(6):1965–1987, 2007.

[68] E.B. Herbold, J. Kim, V.F. Nesterenko, S. Wang, and C. Daraio. Tunable frequency bandgap and pulse propagation in a strongly nonlinear diatomic chain. *Acta Mechanica*, 205(1-4):85–103, June 2009.

[69] T. Y. Hou and X. H. Wu. A multiscale finite element method for elliptic problems in composite materials and porous media. *Journal of Computational Physics*, 134(1):169–189, 1997.

[70] A. Huerta, A. Angeloski, X. Roca, and J. Peraire. Efficiency of high-order elements for continuous and discontinuous galerkin methods. *International Journal for Numerical Methods in Engineering*, 96(9):529–560, 2013.

[71] T. JR Hughes, G. R. Feijóo, L. Mazzei, and J.B. Quincy. The variational multiscale method–a paradigm for computational mechanics. *Computer Methods in Applied Mechanics and Engineering*, 166(1):3–24, 1998.

[72] J.S. Jensen and O. Sigmund. Systematic design of photonic crytsal structures using topology optimization: Low-loss waveguide bends. *Applied Physics Letters*, 84(12):2022–2024, 2004.

[73] J.S. Jensen and O. Sigmund. Topology optimization of photonic crystal structures: a high-bandwidth low-loss T-junction waveguide. *Journal of the Optics Society of America B*, 22(6):1191–1198, 2005.

[74] J.D. Joannopoulos, S.G. Johnson, J.N. Winn, and R.D. Meade. *Photonic crystals: molding the flow of light.* Princeton University Press, 2008.

[75] S.G. Johnson, S. Fan, P.R. Villeneuve, J.D. Joannopoulos, and L.A. Kolodziejski. Guided modes in photonic crystal slabs. *Physical Review B*, 60(8):5751, 1999.

[76] J. B. Keller and R. M. Lewis. Asymptotic methods for partial differential equations: the reduced wave equation and Maxwell's equations. In *Surveys in applied mathematics*, pages 1–82. Springer, 1995.

[77] S.H. Kim and M.P. Das. Seismic waveguide of metamaterials. *Modern Physics Letters B*, 26(17):1250105, 2012.

[78] J.C. Knight, T.A. Birks, P. J. Russell, and D.M. Atkin. All-silica single-mode optical fiber with photonic crystal cladding. *Optics Letters*, 21(19):1547–1549, 1996.

[79] D.K. Ko, A. Kumar, K.H. Fung, R. Ambekar, N. X. Fang, and K.C. Toussaint. Nonlinear optical response from arrays of Au bowtie nanoantennas. *Nanoletters*, 11(1):61–65, 2011.

[80] R.V. Kohn, D. Onofrei, and M.I. Weinstein. Cloaking via change of variables for the Helmholtz equation. *Communications on Pure and Applied Mathematics*, pages 973–1016, 2010.

[81] D. Komatitsch, R. Martin, J. Tromp, M.A. Taylor, and B.A. Wingate. Wave propagation in 2-d elastic media using a spectral element method with triangles and quadrangles. *Journal of Computational Acoustics*, 9(02):703–718, 2001.

[82] D. Komatitsch and J.P. Vilotte. The spectral element method: An efficient tool to simulate the seismic response of 2d and 3d geological structures. *Bulletin of the Seismological Society of America*, 88(2):368–392, 1998.

[83] M. Koshiba, Y. Tsuji, and S. Sasaki. High-performance absorbing boundary conditions for photonic crystal waveguide simulations. *IEE Microwave and Wireless Components Letters*, 11(4):152–154, 2001.

[84] R. Lakes. Foam structures with a negative poisson's ratio. *Science*, 235:1038–1040, February 1987.

[85] R. Lakes. Deformation mechanisms in negative poisson's ratio materials: structural aspects. *Journal of Materials Science*, 26:2287–2292, 1991.

[86] N. Landy and D.R. Smith. A full-parameter unidirectional metamaterial cloak for microwaves. *Nature Materials*, 12(1):1476–1122, 2013.

[87] J. Li and J.B. Pendry. Hiding under the carpet: a new strategy for cloaking. *Physical Review Letters*, 101(20):203901, 2008.

[88] X. Liang and S.G. Johnson. Formulation for scalable optimization of microcavities via the frequency-averaged local density of states. *Optics Express*, 21(25):30812–30841, 2013.

[89] C. Lindsey and D.C. Braun. Basic principles of solar acoustic holography. *Solar Physics*, 192(1-2):261–284, 2000.

[90] C. Luo, S. G. Johnson, J. D. Joannopoulos, and J. B. Pendry. All-angle negative refraction without negative effective index. *Physical Review B*, 65(20):201104, May 2002.

[91] C. Luo, S. G. Johnson, J. D. Joannopoulos, and J. B. Pendry. Subwavelength imaging in photonic crystals. *Physical Review B*, 68(4):045115, Jul 2003.

[92] Y. Luo, H. Zhu, T. Nissen-Meyer, C. Morency, and J. Tromp. Seismic modeling and imaging based upon spectral-element and adjoint methods. *The Leading Edge*, 28(5):568–574, 2009.

[93] S.A. Maier, M.L. Brongersma, P.G. Kik, S. Meltzer, A. Requicha, and H. Atwater. Plasmonics–a route to nanoscale optical devices. *Advanced Materials*, 13(19):1501–1505, 2001.

[94] A. Mekis, J.C. Chen, I. Kurland, S. Fan, P.R. Villeneuve, and J.D. Joannopoulos. High transmission through sharp bends in photonic crystal waveguides. *Physical Review Letters*, 77(18):3787, 1996.

[95] H. Men, R.M. Freund, N.C. Nguyen, J. Saa-Seoane, and J. Peraire. Fabrication-adaptive optimization with an application to photonic crystal design. *Operations Research*, 62(2):418–434, 2014.

[96] H. Men, N.C. Nguyen, R.M. Freund, P.A. Parrilo, and J. Peraire. Bandgap optimization of two-dimensional photonic crystals using semidefinite programming and subspace methods. *Journal of Computational Physics*, 229:3706–3725, 2010.

[97] H. Men, N.C. Nguyen, R.M. Freund, R.M. Lim, P.A. Parrilo, and J. Peraire. Design of photonic crystals with multiple and combined band gaps. *Physical Review E*, 83(4), 2011.

[98] H. Men, N.C. Nguyen, J. Saa-Seoane, R.M. Freund, and J. Peraire. Designing phononic crystals with conic convex optimization. In *International Mechanical Engineering Congress and Exposition*, 2013.

[99] B. Mercier, J. Osborn, J. Rappaz, and P.A. Raviart. Eigenvalue approximation by mixed and hybrid methods. *Mathematics of Computation*, 36(154):427–453, 1981.

[100] C. Morency and J. Tromp. Spectral-element simulations of wave propagation in porous media. *Geophysical Journal International*, 175(1):301–345, 2008.

[101] N.A. Mortensen, O. Sigmund, and O. Breinbjerg. Prospects for poor-man's cloaking with low-contrast all-dielectric optical elements. *Journal of the European Optical Society*, 4, 2009.

[102] J.C. Nédélec. Mixed finite elements in $\mathbb{R}^3$. *Numerische Mathematik*, 35(3):315–341, 1980.

[103] C. Nguyen, X. Roca, D. Moro, and J. Peraire. A hybridized multiscale discontinuous galerkin method for compressible flows. In *51st AIAA Aerospace Sciences Meeting including the New Horizons Forum and Aerospace Exposition*, 2013.

[104] H.M. Nguyen. Cloaking via change of variables for the Helmholtz equation in the whole space. *Communications on Pure and Applied Mathematics*, pages 1505–1524, 2010.

[105] N. C. Nguyen. A multiscale reduced-basis method for parametrized elliptic PDEs with multiple scales. *Journal of Computational Physics*, 227(23):9807–9822, 2008.

[106] N.C. Nguyen and J. Peraire. Hybridizable discontinuous Galerkin methods for partial differential equations in continuum mechanics. *Journal of Computational Physics*, 231(18):5955–5988, 2012.

[107] N.C. Nguyen, J. Peraire, and B. Cockburn. An implicit high-order hybridizable discontinuous Galerkin method for linear convection-diffusion equations. *Journal of Computational Physics*, 228:3232–3254, 2009.

[108] N.C. Nguyen, J. Peraire, and B. Cockburn. An implicit high-order hybridizable discontinuous Galerkin method for nonlinear convection-diffusion equations. *Journal of Computational Physics*, 228:8841–8855, 2009.

[109] N.C. Nguyen, J. Peraire, and B. Cockburn. A comparison of HDG methods for Stokes flow. *Journal of Scientific Computing*, 45:215–237, 2010.

[110] N.C. Nguyen, J. Peraire, and B. Cockburn. A hybridizable discontinuous Galerkin method for Stokes flow. *Computer Methods in Applied Mechanics and Engineering*, 199:582–597, 2010.

[111] N.C. Nguyen, J. Peraire, and B. Cockburn. A hybridizable discontinuous Galerkin method for the incompressible Navier-Stokes equations. In *Proceedings of the 48th AIAA Aerospace Sciences Meeting and Exhibit*, pages 2010–362, 2010.

[112] N.C. Nguyen, J. Peraire, and B. Cockburn. High-order implicit hybridizable discontinuous Galerkin methods for acoustics and elastodynamics. *Journal of Computational Physics*, 230(10):3695–3718, 2011.

[113] N.C. Nguyen, J. Peraire, and B. Cockburn. Hybridizable discontinuous Galerkin methods. In *Spectral and High Order Methods for Partial Differential Equations*, volume 76, pages 63–84, 2011.

[114] N.C. Nguyen, J. Peraire, and B. Cockburn. Hybridizable discontinuous Galerkin methods for the time-harmonic Maxwell's equations. *Journal of Computational Physics*, 230(19):7151–7175, 2011.

[115] N.C. Nguyen, J. Peraire, and B. Cockburn. An implicit high-order hybridizable discontinuous Galerkin method for the incompressible Navier-Stokes equations. *Journal of Computational Physics*, 230:1147–1170, 2011.

[116] A.F. Oskooi, C. Kottke, and S.G. Johnson. Accurate finite-difference time-domain simulation of anisotropic media by subpixel smoothing. *Optics Letters*, 34(18):2778–2780, 2009.

[117] A.F. Oskooi, D. Roundy, M. Ibanescu, P. Bermel, J. D. Joannopoulos, and S.G. Johnson. MEEP: A flexible free-software package for electromagnetic simulations by the FDTD method. *Computer Physics Communications*, 181:687–702, 2010.

[118] E. Ozbay. Plasmonics: merging photonics and electronics at nanoscale dimensions. *Science*, 311(5758):189–193, 2006.

[119] P. A. Parrilo and S. Lall. Semidefinite programming relaxations and algebraic optimization in control. *European Journal of Control*, 9(2-3):307–321, 2003.

[120] A. T. Patera. A spectral element method for fluid dynamics: laminar flow in a channel expansion. *Journal of computational Physics*, 54(3):468–488, 1984.

[121] J. B. Pendry. Negative refraction makes a perfect lens. *Physical Review Letters*, 85(18):3966–3969, Oct 2000.

[122] J.B. Pendry, D. Schurig, and D.R. Smith. Controlling electromagnetic fields. *Science*, 312:1780–1782, 2006.

[123] J. Peraire, N.C. Nguyen, and B. Cockburn. A hybridizable discontinuous Galerkin method for the compressible Euler and Navier-Stokes equations. In *Proceedings of the 48th AIAA Aerospace Sciences Meeting and Exhibit*, pages 2010–363, 2010.

[124] J. Peraire and P.O. Persson. The compact discontinuous Galerkin (CDG) method for elliptic problems. *SIAM Journal of Scientific Computing*, 30(4):1806–1824, 2008.

[125] P.O. Persson and J. Peraire. Curved mesh generation and mesh refinement using Lagrangian solid mechanics. In *47th AIAA Aerospace Sciences Meeting and Exhibit, Orlando, Florida, AIAA-2009-949*, 2009.

[126] P.O.O. Persson and J. Peraire. Newton-GMRES preconditioning for discontinuous Galerkin discretizations of the navier-stokes equations. *SIAM Journal on Scientific Computing*, 30(6):2709–2733, 2008.

[127] D. Peter, D. Komatitsch, Y. Luo, R. Martin, N. Le Goff, E. Casarotti, P. Le Loher, F. Magnoni, Q. Liu, C. Blitz, et al. Forward and adjoint simulations of seismic wave propagation on fully unstructured hexahedral meshes. *Geophysical Journal International*, 186(2):721–739, 2011.

[128] J.S. Peterson. The reduced basis method for incompressible viscous flow calculations. *SIAM Journal of Scientific Statistic Computations*, 10(4):777–786, 1989.

[129] B.I. Popa and S.A. Cummer. Cloaking with optimized homogeneous anisotropic layers. *Physical Review A*, 79(2):023806, 2009.

[130] B.I. Popa, L. Zigoneanu, and S.A. Cummer. Experimental acoustic ground cloak in air. *Physical Review Letters*, 106(25):253901, 2011.

[131] Lord Rayleigh. On the maintenance of vibrations by forces of double frequency, and on the propagation of waves through a medium endowed with a periodic structure. *Philosophical Magazine*, 24(147):145–159, 1887.

[132] B. Recht, M. Fazel, and P.A. Parrilo. Guarranteed minimum-rank solutions of linear matrix equations via nuclear norm minimization. *SIAM Review*, 52(3):471–501, February 2008.

[133] J.F. Remacle, T. Toulorge, and J. Lambrechts. Robust untangling of curvilinear meshes. In *Proceedings of the 21st International Meshing Roundtable*, pages 71–83. Springer, 2013.

[134] X. Roca, A. Gargallo-Peiró, and J. Sarrate. Defining quality measures for high-order planar triangles and curved mesh generation. In *Proceedings of the 20th International Meshing Roundtable*, pages 365–383. Springer, 2012.

[135] X. Roca, N.C. Nguyen, and J. Peraire. Scalable parallelization of the hybridized discontinuous galerkin method for compressible flow. In *21st AIAA Computational Fluid Dynamics Conference*, 2013.

[136] Z. Ruan, M. Yan, C. W. Neff, and M. Qiu. Ideal cylindrical cloak: Perfect but sensitive to tiny perturbations. *Physical Review Letters*, 99(11):113903, 2007.

[137] P. Russell. Photonic crystal fibers. *Science*, 299(5605):358–362, 2003.

[138] M. Ruzzene. Frequency wavenumber domain filtering for improved damage visualization. *Smart Materials and Structures*, 16(6):2116, 2007.

[139] J. Saa-Seoane. Simulation and design optimization for linear wave phenomena on metamaterials. Master's thesis, Master's Thesis, MIT, 2011.

[140] J. Saa-Seoane, N.C. Nguyen, H. Men, R. Freund, and J. Peraire. Binary optimization techniques for linear PDE-governed material design. *Applied Physics A*, 109(4):1023–1030, 2012.

[141] M. Schinnerl, J. Schoberl, and M. Kaltenbacher. Nested multigrid methods for the fast numerical computation of 3d magnetic fields. *Magnetics, IEEE Transactions on*, 36(4):1557–1560, 2000.

[142] D. Schurig, J. J. Mock, B. J. Justice, S. A. Cummer, J. B. Pendry, A. F. Starr, and D. R. Smith. Metamaterial electromagnetic cloak at microwave frequencies. *Science*, 314:1780–1782, 2006.

[143] J.A. Sethian. Evolution, implementation, and application of level set and fast marching methods for advancing fronts. *Journal of Computational Physics*, 169(2):503–555, 2001.

[144] R. P. Shaw. Boundary integral equation methods applied to wave problems. *Developments in boundary element methods*, pages 121–153, 1979.

[145] D. Shin, Y. Urzhumov, Y. Jung, G. Kang, S. Baek, M. Choi, H. Park, K. Kim, and D.R. Smith. Broadband electromagnetic cloaking with smart metamaterials. *Nature Communications*, 3, 2012.

[146] A. Sommerfeld. *Partial Differential Equations in Physics.* Academic Press. New York, 1949.

[147] S.C. Soon, B. Cockburn, and H. K. Stolarski. A hybridizable discontinuous galerkin method for linear elasticity. *International Journal of Numerical Methods in Engineering*, 80(8):1058–1092, 2009.

[148] A. Spadoni and C. Daraio. Generation and control of sound bullets with a nonlinear acoustic lens. *Proceedings of the National Academy of Sciences*, 107(7230), 2010.

[149] A. Spadoni and M. Ruzzene. Elasto-static micropolar behavior of a chiral auxetic lattice. *Journal of the Mechanics and Physics of Solids*, 60(1):156–171, 2012.

[150] W. Srituravanich, N. Fang, C. Sun, Q. Luo, and X. Zhang. Plasmonic nanolithography. *Nanoletters*, 4(6):1085–1088, 2004.

[151] A. Tandaechanurat, S. Ishida, D. Guimard, M. Nomura, S. Iwamoto, and Y. Arakawa. Lasing oscillation in a three-dimensional photonic crystal nanocavity with a complete bandgap. *Nature Photonics*, 5(2):91–94, 2011.

[152] D. Torrent and J. Sánchez-Dehesa. Acoustic cloaking in two dimensions: a feasible approach. *New Journal of Physics*, 10(6):063015, 2008.

[153] L.N. Trefethen and D. Bau III. *Numerical linear algebra*, volume 50. Siam, 1997.

[154] V. G Veselago. The electrodynamics of substances with simultaneously negative values of ϵ and μ. *Soviet Physics Uspekhi*, 10:509–514, 1968.

[155] H. Wan, H. Ohtaki, S. Kotosaka, and G Hu. A study of negative poisson's ratios in auxetic honeycombs based on a large deflection model. *European Journal of Mechanics A*, 23:95–106, 2004.

[156] Y. Wang, Z. Luo, N. Zhang, and Z. Kang. Topological shape optimization of microstructural metamaterials using a level set method. *Computational Materials Science*, 87:178–186, 2014.

[157] R. Watahiki, T. Shimada, P. Zhao, S. Chiashi, S. Iwamoto, Y. Arakawa, S. Maruyama, and Y. K. Kato. Enhancement of carbon nanotube photoluminescence by photonic crystal nanocavities. *Applied Physics Letters*, 101(14):141124, 2012.

[158] Y. Xu, R. K. Lee, and A. Yariv. Asymptotic analysis of bragg fibers. *Optics Letters*, 25(24):1756–1758, 2000.

[159] D.U. Yang, S Lee, and F.Y. Huang. Geometric effects on micropolar elastic honeycomb structure with negative poisson's ratio using the finite element method. *Finite Elements in Analysis and Design*, 39:187–205, 2003.

[160] Y.Nesterov. A method for unconstrained convex minimization problem with the rate of convergence $o(1/k^2)$. *Doklady*, 269:543–547, 1983.

[161] Y.Nesterov. *Introductory Lectures on Convex Optimization.* Kluwer, 2004.

[162] H.C. Yu, H. Chen, and K. Thornton. Extended smoothed boundary method for solving partial differential equations with general boundary conditions on complex boundaries. *Modelling and Simulation in Materials Science and Engineering*, 20(7):075008, 2012.

[163] Z. Yu, Y. Feng, X. Xu, J. Zhao, and T. Jiang. Optimized cylindrical invisibility cloak with minimum layers of non-magnetic isotropic materials. *Journal of Physics D*, 44(18):185102, 2011.

[164] S. Zhang, C. Xia, and N. Fang. Broadband acoustic cloak for ultrasound waves. *Physical Review Letters*, 106(2):24301, 2011.

[165] S. Zhang, L. Yin, and N. Fang. Focusing ultrasound with an acoustic metamaterial network. *Physical Review Letters*, 102(19):194301, 2009.

[166] X. Zhang and Z. Liu. Superlenses to overcome the diffraction limit. *Nature Materials*, 7:435–441, 2008.

[167] S. Zhou, W. Li, G. Sun, and Q. Li. A level-set procedure for the design of electromagnetic metamaterials. *Optics Express*, 18(7):6693–6702, 2010.